MODELLING OF SOLUTE TRANSPORT PAST A DISORDERED UPTAKE FIELD

A thesis submitted to The University of Manchester
for the degree of Doctor of Philosophy
in the Faculty of Science and Engineering

2022

George Frederick Price
Department of Mathematics
School of Natural Sciences

Contents

Abstract **15**

Declaration **16**

Copyright Statement **17**

Acknowledgements **18**

1 Introduction **19**

1.1 Relevant examples of solute transport within disordered domains 19

1.2 Mathematical approaches for modelling solute transport 21

1.2.1 Continuum-based models 22

1.2.2 Individual-based models 23

1.2.3 Example: A one-dimensional individual- to continuum-based model for solute transport through a disordered domain 25

1.2.4 Spatial averaging and homogenization techniques 27

1.3 Mathematical modelling of flow and transport within porous media and other disordered domains 30

1.3.1 Modelling flow through disordered domains 31

1.3.2 Modelling solute transport through disordered domains 33

1.4 The genesis of this thesis 35

1.5 Objectives and structure of the thesis 36

2 Characterising uncertainty for one-dimensional solute transport in a spatially disordered domain **38**

2.1 Model 39

2.1.1 Asymptotic regimes in $(\mathrm{Pe}_l, \mathrm{S})$-parameter space 40

2.2 Methods 42

2.2.1 Monte Carlo realisations . . . 43
2.2.2 Constructing an expansion . . . 43
2.2.3 Advection-dominated solute transport . . . 50
2.3 Results . . . 54
2.3.1 Monte Carlo realisations . . . 55
2.3.2 Corrections to the homogenized solution . . . 57
2.3.3 Advection-dominated solute transport . . . 65
2.4 Discussion . . . 72

3 A moments-based approach to characterise uncertainty for solute transport past a discrete sink distribution 77
3.1 Model . . . 79
3.2 Developing a moments-based approach for characterising uncertainty . . . 83
3.3 Moments of the sink function . . . 86
3.3.1 Normally-perturbed sink locations . . . 86
3.3.2 Uniformly-random sink locations . . . 88
3.4 Calculating a free-space Green's function . . . 91
3.4.1 One-dimensional free-space Green's function . . . 92
3.4.2 Two-dimensional free-space Green's function . . . 94
3.4.3 Three-dimensional free-space Green's function . . . 97
3.5 Characterising uncertainty using corrections to the homogenized solution . . . 99
3.5.1 Corrections accounting for periodic sink locations . . . 99
3.5.2 Moments of corrections accounting for normally-perturbed sink locations 106
3.5.3 Moments of corrections accounting for uniformly-random sink locations . 112
3.6 Discussion . . . 117

4 Solute transport past sink distributions represented by Gaussian processes 123
4.1 Model . . . 124
4.2 Methods . . . 127
4.2.1 The moments-based approach . . . 128
4.2.2 Calculating an effective uptake term . . . 130
4.3 One-dimensional results . . . 132
4.3.1 Expectation of corrections and using an effective uptake parameter . . . 133
4.3.2 Using the (co)variance of the leading-order concentration . . . 135
4.4 Calculating an effective uptake parameter in two and three dimensions . . . 139
4.4.1 Two-dimensional effective uptake parameter . . . 139

4.4.2 Three-dimensional effective uptake parameter . . . 141
4.5 Summary of effective uptake parameters in n dimensions . . . 142
4.6 Calculating an effective uptake parameter for a discrete uptake function with uniformly-random sink locations . . . 144
4.7 Discussion . . . 147

5 Conclusions **152**
5.1 Summary . . . 152
5.2 Further work . . . 155

A Chapter 2 appendices **158**
A.1 Numerical method for solving the governing equations . . . 158
A.2 Classical approach to homogenization . . . 160
A.3 Leading-order behaviour of the homogenized solution and Green's function . . . 163
A.3.1 Useful calculations involving the product of the homogenized solution and Green's function . . . 164
A.4 Calculation of the covariance for normally-perturbed sink locations . . . 165
A.5 Tracking the cumulative distribution function in the limit of advection-dominated transport . . . 167

B Chapter 3 and 4 appendices **170**
B.1 Exact Green's function in one dimension . . . 170
B.2 Finite-difference scheme . . . 172
B.2.1 One dimension . . . 172
B.2.2 Two dimensions . . . 172
B.3 Integral solver . . . 173
B.4 Evaluating useful integrals . . . 173
B.5 Integrating the homogenized solution combined with the one-dimensional free-space Green's function . . . 175
B.6 Eigenvalue decomposition . . . 177
B.7 Considering a log-normal Gaussian process in one dimension . . . 178

Word count 54154

List of Tables

1.1 Table summarising the differences between volume averaging and multiscale asymptotics, which closely follows Table 1 in Davit et al. (2013). 29

2.1 Table containing the required balances of parameters for different effects to dominate, where A, U and D represent advection, diffusion and uptake respectively. . 41

2.2 Table showing the conditions of validity for different regimes when sinks are normally perturbed from a periodic configuration (NP) and order statistics from a uniform distribution (UR). 74

3.1 Table showing how the (expected) correction to the homogenized solution in the vicinity of $\mathbf{x} = \mathbf{e}_{\mathbf{i}_n}$ depends on $\lambda, \varsigma, \sigma, \mathrm{Pe}_L$ and Da for $\mathrm{Pe}_L \gg \max(1, \sqrt{\mathrm{Da}})$ in the limit $\varsigma \to 0$. These are given for periodic, normally-perturbed and uniformly-random sink locations in (3.5.13), (3.5.24) and (3.5.36) respectively. 119

4.1 Table showing the different values of $\mathrm{Da}_{\mathrm{eff}}$ in the limit $\ell \to 0$ when using a Gaussian and exponential covariance function. Results are obtained by taking the limit $\ell \to 0$ for Gaussian [exponential] covariance functions in one, two and three dimensions in (4.3.1) [(4.3.2)], (4.4.6) [(4.4.7)] and (4.4.9) [(4.4.10)] respectively. . 143

List of Figures

1.1 (a) Anatomy of fetal and maternal circulation in the human placenta (Serov et al., 2015). (b) Anatomy of pulmonary vessels and airways in the human lung (Gray, 1918). 20

1.2 Illustration depicting the stochastic hopping of particles using M sites which are a distance d apart, where site i contains n_i particles. Particles can move to neighbouring sites and move to the right at a rate p^+ and to the left at a rate p^-. Located at N sites are sinks, which demonstrate a removal process through the domain, where the j^{th} sink has a strength S_j. For illustrative purposes, $k = 1$ and $\Delta_N = M - 1$ are used for the first and final sink locations respectively, although sink locations can be distributed randomly throughout the domain. . . 26

1.3 (a) Cross section of the villous trees in a human placenta (Chernyavsky et al., 2011). (b) Cross section of the parenchyma in a human lung (Lande and Mitzner, 2006). 31

2.1 (a) Depiction of asymptotic regions in $(\mathrm{Pe}_l, \mathrm{S})$-parameter space, where $\varepsilon \ll 1$. D, A, U and UA represent regions where diffusion, advection, uptake and both advection and uptake dominate over the domain length respectively, with diffusion dominating on the inter-sink length. Alternatively, A^I, U^I and UA^I represent regions where advection, uptake and both advection and uptake dominate on the domain and inter-sink length respectively. The blue region shows the area of parameter space considered in Russell and Jensen (2020). The green region shows the area of parameter space considered in this chapter. The red region shows when the homogenized solution found in Section 2.2.2 is seen to fail (Chernyavsky et al., 2011). (b) Different concentration profiles for varying values of Pe_l and S, which correspond to markers (1) - (5) in figure (a). Each profile is scaled using the concentration at the inlet ($C(0)$) and is calculated using the numerical method outlined in Appendix A.1 with $N = 19$ periodically located point sinks (i.e. $\varepsilon = 0.05$). 41

2.2 Comparison between the numerical solution of (2.1.2) [$C(x)$, solid black], the asymptotic approximation of the homogenized solution [$C_H(x)$, given in (2.2.5), dot-dashed blue], the use of a correction term which accounts for a periodic sink distribution [$C_H(x) + \widehat{C}_a(x)$, given in (2.2.5) and (2.3.1), dashed yellow], the leading-order solution using a classical approach to homogenization [$C^{(0)}(x)$, given in (A.2.6), dot-dashed purple], the second-order solution using a classical approach to homogenization [$C^{(0)}(x) + \varepsilon C^{(1)}(x)$, given in (A.2.6) and (A.2.13), dashed green] and the homogenized solution calculated by replacing $\sum_{j=1}^{N} \delta(x - \xi_j)$ with the exact spatial average $N/(N+1)$ [$\check{C}_H$, calculated by replacing S with $(N/(N+1))$S in 2.2.5, dot-dashed red]. Here, $N = 19$ periodic point sinks are used (i.e. $\varepsilon = 0.05$) and $(\mathrm{Pe}_l, \mathrm{S}) = (1, \varepsilon)$. Depicted in the inset is the relative error between each approximation and the numerical solution using (2.2.7), where $N \in \{1, \ldots, 300\}$. 45

2.3 A contour plot of the Green's function [$G(x, y)$] using the leading-order approximation given in (2.2.11), where $(\mathrm{Pe}_l, \mathrm{S}) = (1, \varepsilon)$ and $\varepsilon = 0.05$ are used. 48

2.4 Depiction of a concentration profile in the vicinity of one point sink $x = \xi_j$, where the concentration upstream and downstream of the sink are given by C_{j-1} and C_j respectively. The solid line represents when diffusion is still present, whereas the dashed line represents when diffusion is negligible, causing the boundary-layer thickness to become infinitesimally small. 51

2.5 (a) & (c) Multiple realisations of concentration profiles [grey] with the sample mean [$\hat{\mu}$, dashed red], sample Gaussian-based 95% credible intervals [$\hat{\mu} \pm 1.96\hat{\sigma}$ (where $\hat{\sigma}$ represents the sample standard deviation), solid blue], sample median [$\hat{\mu}_{0.5}$, dashed green], the sample 95% credible intervals [$\hat{\mu}_{0.5\pm0.475}$, solid cyan] and a single realisation [solid magenta]. (b) & (d) Depiction of the sample covariances [$\hat{K}[x, y]$]. Figures (a) and (b) use a normally-perturbed sink distribution with $\xi_j \sim \mathcal{N}(j, \sigma^2)$, where $\sigma = 0.194$. Figures (c) and (d) use order statistics from a uniform distribution $\mathcal{U}(0, \varepsilon^{-1})$ as the sink locations. All figures use 10^4 Monte Carlo simulation for $N = 19$ point sinks (i.e. $\varepsilon = 0.05$), where $(\mathrm{Pe}_l, \mathrm{S}) = (1, \varepsilon)$. . 56

2.6 Depiction of the Y-domain separation, where A, B, C, D, E and F represent the domains $[0, \frac{1}{2}]$, $[\frac{1}{2}, k - \frac{1}{2}]$, $[k - \frac{1}{2}, x]$, $[x, k + \frac{1}{2}]$, $[k + \frac{1}{2}, \varepsilon^{-1} - \frac{1}{2}]$ and $[\varepsilon^{-1} - \frac{1}{2}, \varepsilon^{-1}]$ respectively. 58

2.7 Comparison between the sample variance for 10^5 Monte Carlo simulations [$\hat{\sigma}^2$, solid blue] and the expression for the variance of the correction [$\mathrm{Var}[\widehat{C}_b(x)]$, dashed red]. Here, $N = 19$ point sinks (i.e. $\varepsilon = 0.05$) and $(\mathrm{Pe}_l, \mathrm{S}) = (1, \varepsilon)$. (a) Variance of solute concentration when sinks are normally perturbed from a periodic arrangement with $\sigma = 0.01$, where the variance of $\widehat{C}_b(x)$ is given in (2.3.11). (b) Variance of solute concentration when sinks are given by order statistics from a uniform distribution, where the variance of $\widehat{C}_b(x)$ is given in (2.3.19). Also shown is the variance calculated using the exact values of $C_H(x)$ and $G(x, y)$ given in (2.2.3) and (2.2.10) respectively. These are used to solve for $\mathcal{K}[\widehat{C}_b(x), \widehat{C}_b(x)]$ given in (2.3.14) [$\mathrm{Var}_{\mathrm{exact}}[\widehat{C}_b(x)]$, dot-dashed green], where the integral solver given in Shampine (2008) is used. The convergence of both $\mathrm{Var}[\widehat{C}_b(x)]$ and $\mathrm{Var}_{\mathrm{exact}}[\widehat{C}_b(x)]$ to the sample variance can be seen in the inset for $N \in \{0, \ldots, 50\}$. 62

2.8 (a) Depiction of the probability density functions $\pi_{\xi_j}(x)$ when sink locations are prescribed as order statistics taken from a uniform distribution. Here, $j = 1, \ldots, N$ and $N = 9$ (i.e. $\varepsilon = 0.1$) are used. (b) Shown are the functions $\varepsilon I_2(x)^2$ [blue], $I_3(x, x)$ [red] and $I_3(x, x) - \varepsilon I_2(x)^2$ [yellow], where I_2 and I_3 are defined in (2.3.5) and (2.3.15) respectively. Solid lines are calculated using the integral solver given in Shampine (2008) with the exact values of the homogenized solution and Green's function given in (2.2.3) and (2.2.10) respectively. Dashed lines use the approximations of $I_3(x, x)$ and $I_2(x)^2$ given in (2.3.17) and (2.3.18) respectively. Here, $N = 19$ ($\varepsilon = 0.05$) and $(\mathrm{Pe}_l, \mathrm{S}) = (1, \varepsilon)$ are used. 62

2.9 Cumulative distribution functions for $N = 19$ sink locations. (a) normally-perturbed sink locations with a standard deviation $\sigma = 0.194$, with the cdf given in (2.3.21). (b) uniformly-random sink locations, with the cdf given in (2.3.22). . 66

2.10 Comparison between the sample variance [$\hat{\sigma}^2$, solid blue] and the expression for the variance found using (2.2.24) [Var$[C(x)]$, dashed red]. Insets show a comparison between the sample mean [$\hat{\mu}$, solid blue] and the expectation found using (2.2.23) [$\mathbb{E}[C(x)]$, dashed red]. Here, 10^5 Monte Carlo simulations with (2.2.22) are used, where $N = 19$ (i.e. $\varepsilon = 0.05$) and $\mathrm{S} = \varepsilon$ in the limit of infinite Pe_l. (a) normally-perturbed sink locations with $\sigma = 0.194$, where the expectation and variance are given in (2.3.24) and (2.3.25) respectively. (b) uniformly-random sink locations with the expectation and variance given in (2.3.29) and (2.3.30) respectively. Also plotted is the variance given in (2.3.19) in the limit where $\mathrm{Pe}_l \to \infty$ [$\mathrm{Var}_{\mathrm{Pe}_l \to \infty}[C(x)]$, dot-dashed green]. 68

2.11 Depiction of 10^4 concentration profiles [grey] using (2.2.22), the expectation [$\mathbb{E}[C(x)]$, dashed red], Gaussian-based 95% credible intervals [$\mathbb{E}[C(x)] \pm 1.96\sqrt{\mathrm{Var}[C(x)]}$, solid blue], median [$CI(x; 0.5)$, dashed green], cdf 95% credible intervals [$CI(x; 0.5 \pm 0.475)$, solid cyan] and a single realisation [solid magenta]. Here, there are $N = 19$ point sinks (i.e. $\varepsilon = 0.05$) and $\mathrm{S} = \varepsilon$ in the limit of infinite Pe_l. (a) Sink locations are normally-perturbed with a standard deviation $\sigma = 0.194$, where (2.3.24) and (2.3.25) give the expectation and variance respectively and (2.3.28) gives the median and cdf 95% credible interval. The inset shows a magnification of one unit-cell. (b) Sink locations are uniformly random, where (2.3.29) and (2.3.30) give the expectation and variance respectively and (2.3.33) gives the median and cdf 95% credible interval. 69

2.12 Depiction of 10^4 concentration profiles [grey] using (2.2.21), the sample mean [$\hat{\mu}$, dashed red], sample Gaussian-based 95% credible intervals [$\hat{\mu} \pm 1.96\hat{\sigma}$ (where $\hat{\sigma}$ represents the sample standard deviation), solid blue], median [$CI(x; 0.5)$, dashed green], cdf 95% credible intervals [$CI(x; 0.5 \pm 0.475)$, solid cyan] and a single realisation [solid magenta]. Here, there are $N = 19$ point sinks (i.e. $\varepsilon = 0.05$) with $\mathrm{Pe}_l = \varepsilon^{-1}$ and $\mathrm{S} = \varepsilon$. (a) Sink locations are normally-perturbed with a variance $\sigma = 0.194$, where the median and cdf 95% credible interval are calculated using (2.3.28). The inset shows a magnification of one unit-cell. (b) Sink locations are uniformly random, with the median and cdf 95% credible interval are calculated using (2.3.33). 72

3.1 Two-dimensional solute concentration, where (a)-(c) show realisations with sinks appearing as spots, (d)-(e) show sample expectations and (f)-(g) show sample variances. Panel (a), panels (b), (d), (f) and panels (c), (e), (g) represent periodic, normally-perturbed according to a standard deviation $\sigma = 0.02$ and uniformly-random sink locations respectively. Realisations are found using (3.1.2) with Appendix B.2 and sample moments are calculated using 10^4 realisations. All figures use $\mathcal{D}_2^s = [0,1] \times [-0.5, 0.5]$, $\lambda = 0.2$, $(\mathrm{Pe}_L, \mathrm{Da}) = (20, 10)$ and $\varsigma = 0.01$. 82

3.2 Two-dimensional solute concentration for uniformly-random sinks located in a domain $\mathcal{D}_2^s = [0,1] \times [-2.5, 2.5]$. Here, (a) shows a single realisation, (b) shows the sample expectation and (c) shows the sample variance. Realisations are found using (3.1.2) with Appendix B.2 and sample moments are calculated using 10^4 realisations. All figures use $\lambda = 0.2$, $(\mathrm{Pe}_L, \mathrm{Da}) = (20, 10)$ and $\varsigma = 0.01$. 84

3.3 Covariance $\mathcal{K}_{\hat{g}}[x_1, y_1]$ of the one-dimensional sink function $\hat{g}$. (a) normally-perturbed sink locations calculated using (3.3.12) and (3.3.13) with (3.3.5). (b) uniformly-random sink locations calculated using (3.3.20). Both figures use $(\mathrm{Pe}_L, \mathrm{Da}) = (20, 10)$, $\lambda = 0.2$ and $\varsigma = 0.01$, with (b) using $e_i = (2i-1)/2N$ as the mean sink locations for $i = 1, \ldots, N$. 89

3.4 (a) Contour plot of the free-space Green's function $\mathcal{G}_1(x_1 - x_1')$ in one dimension. (b) Contour plot showing the difference between the exact and free-space Green's function $(G(x_1, x_1') - \mathcal{G}_1(x_1 - x_1'))$. Here, the free-space and exact Green's function are given in (3.4.9) and (B.1.2) respectively, with both figures using $(\mathrm{Pe}_L, \mathrm{Da}) = (20, 10)$. Note the similarities in structure when compared to Figure 2.3 from Chapter 2, which uses an exact Green's function with different parameter values. 93

3.5 (a) Contour plot of the free-space Green's function $\mathcal{G}_2(\mathbf{x} - \mathbf{x}')$ in two dimensions. (b) Plot of the free-space Green's function $\mathcal{G}_2(\mathbf{x} - \mathbf{x}')$ along $x_2 = 0$. Both figures use $(\mathrm{Pe}_L, \mathrm{Da}) = (20, 10)$ and $\mathbf{x}' = (0.5, 0)$. 94

3.6 (a) Depiction of the lengthscales involved in the Green's function for a sink located at $\mathbf{x} = \mathbf{x}'$ [red dot] and the asymptotic shape of the wake [solid blue], where $\mathrm{Pe}_L \gg \max(1, \sqrt{\mathrm{Da}})$. (b) The region of influence [dashed green] about the point $\mathbf{x} = \mathbf{y}$ [black dot]. Sinks located outside of this region will have weak influence on the concentration at $\mathbf{x} = \mathbf{y}$. Here, red dots represent sink locations $\mathbf{x} = \mathbf{x}'$ and blue ellipses represent the asymptotic shapes of the wake about each sink. 96

3.7 Concentration in one dimension, where $\mathbb{E}[C(x_1;\omega)]$ represents the sample expectation from 10^6 Monte Carlo realisations. Insets show the difference between each approximation and the sample expectation. Figure (a) uses periodic sink locations, whereas figure (b) uses normally-perturbed sink locations according to a standard deviation $\sigma = 0.02$. All figures use $\lambda = 0.2$, $(\mathrm{Pe}_L, \mathrm{Da}) = (20, 10)$ and $\varsigma = 0.01$. 102

3.8 Depiction of the relevant angles and lengths created by $\mathbf{x}, \mathbf{x}'$ and $\mathbf{e}_{\mathbf{i}_n}$ in two and three dimensions. 103

3.9 Concentration in two dimensions, where figures in column (a) use periodic sinks locations and figures in column (b) use normally-perturbed sink locations with a standard deviation $\sigma = 0.02$. For periodic and normally-perturbed sink locations row (i) shows the numerical concentration $C(\mathbf{x})$ and expected concentration $\mathbb{E}[C(\mathbf{x};\omega)]$ (the central sink-row from Figures 3.1(a) and 3.1(d) respectively), (ii) shows the homogenized solution for both cases, (iii) shows the correction $\widehat{C}_1(\mathbf{x})$ and expected correction $\mathbb{E}[\widehat{C}_1(\mathbf{x};\omega)]$ and (iv) the combination of the homogenized solution with the correction $\widehat{C}_1(\mathbf{x})$ and the expected correction $\mathbb{E}[\widehat{C}_1(\mathbf{x};\omega)]$ respectively in one strip of the domain where $x_2 \in [-0.1, 0.1]$. Row (v) shows the results from (i), (ii), (iv), (3.5.3) and (3.5.19) with $x_2 = 0$, where the inset shows the difference between each approximation and the numerical or expected concentration. All sample expectations are calculated using 10^4 realisations with Appendix B.2. All figures use $\lambda = 0.2$, $\varsigma = 0.01$, $(\mathrm{Pe}_L, \mathrm{Da}) = (20, 10)$ and $\mathcal{D}_2^s = [0, 1] \times [-0.5, 0.5]$. 105

3.10 Variance of the concentration in one dimension, where (a) uses normally-perturbed sink locations and (b) uses uniformly-random sink locations. Here, $\mathrm{Var}[C(x_1;\omega)]$ represents the sample variance from 10^6 Monte Carlo realisations, $\mathrm{Var}[\widehat{C}(x_1;\omega)]$ is calculated using (3.3.10) and (3.3.11) with (3.3.5) in (3.5.15) for (a) and (3.5.26) for (b) and $\mathrm{Var}_{\varsigma\to 0}[\widehat{C}(x_1;\omega)]$ is calculated using (3.5.20) for (a) and (3.5.38) for (b). All figures use $\lambda = 0.2$, $(\mathrm{Pe}_L, \mathrm{Da}) = (20, 10)$ and $\varsigma = 0.01$, with figure (a) using $\sigma = 0.02$. 110

3.11 Variance of the concentration in two dimension, where columns (a) and (b) use normally-perturbed and uniformly-random sink locations respectively. Figures (i) and (ii) show the sample variance (taken from Figures 3.1(f) and 3.2(c)) $[\mathrm{Var}[C(\mathbf{x};\omega)]]$ and the δ-function approximation of the variance $[\mathrm{Var}_{\varsigma\to 0}[C(\mathbf{x};\omega)]]$ respectively in one strip of the domain where $x_2 \in [-0.1, 0.1]$. To calculate δ-function approximations we uses (3.5.20) and (3.5.38) for normally-perturbed and uniformly-random sink locations respectively. Figure (a)(iii) shows both the sample variance and δ-function approximation with $x_2 = 0$, whereas figure (b)(iii) shows a cloud plot of the sample variance for $x_2 = -2, -1.996, \ldots, 2$ from Figure 3.2(c), the average of these variances over x_2 $[\langle \mathrm{Var}[C(\mathbf{x};\omega)]\rangle_{x_2}]$ and the δ-function approximation of the variance from (3.5.38) $[\mathrm{Var}_{\varsigma\to 0}[\widehat{C}_1(x_1, 0;\omega)]]$. All figures use $\lambda = 0.2$, $(\mathrm{Pe}_L, \mathrm{Da}) = (20, 10)$ and $\varsigma = 0.01$ and sample variances are calculated from 10^4 Monte Carlo realisations. Figure (a) uses $\mathcal{D}_2^s = [0, 1] \times [-0.5, 0.5]$ and $\sigma = 0.02$ whereas figure (b) uses $\mathcal{D}_2^s = [0, 1] \times [-2.5, 2.5]$. 111

3.12 Expected concentrations for uniformly-random sink locations, where circles, squares and diamonds represent one-, two- and three-dimensional domains respectively. Figure (a) uses dashed and dot-dashed lines to represent the homogenized solution $[C_H(x_1)]$ and the approximation found using the expected correction $\mathbb{E}[\widehat{C}_2(\boldsymbol{x};\omega)]$. The solid lines represent the sample expectation, where in one dimension we use 10^6 realisations $[\mathbb{E}[\widehat{C}_2(x_1;\omega)]]$ and in two dimensions we use 10^4 realisations with $\mathcal{D}_2^s = [0, 1] \times [-2.5, 2.5]$ and then take the average over $x_2 = -2, -1.996, \ldots, 2$ $[\langle \mathbb{E}[\widehat{C}_2(x_1, x_2;\omega)]\rangle_{x_2}]$. Figure (b) shows the difference between sample expectations and each correction. Throughout we use $\lambda = 0.2$, $\varsigma = 0.01$ and $(\mathrm{Pe}_L, \mathrm{Da}) = (20, 10)$, with the expectation of $\widehat{C}_2(x_1, x_2;\omega)$ being approximated using (3.5.34). 116

4.1 Two-dimensional realisations of the sink function $\hat{g}(\mathbf{x};\omega)$ using a Gaussian [(a), (b), (c)] and exponential [(d), (e), (f)] covariance function from (4.1.2) and (4.1.3) respectively. Here, (a) & (d), (b) & (e) and (c) & (f) use $\ell = 0.01$, $\ell = 0.1$ and $\ell = 1$ respectively, with all realisations using $\sigma = 0.2$ and eigenvalue decomposition from Appendix B.6. 126

4.2 Difference between the sample mean $[\mathbb{E}_{\{G,E\}}[C(x_1;\omega)]]$ and the homogenized solution from (4.2.2) $[C_H(x_1)]$, the expected second-order correction from (4.2.15) $[\mathbb{E}_{\{G,E\}}[\widehat{C}_2(x_1;\omega)]]$ and using the approximation given in (4.2.17) $[\mathbb{E}^{\ell\to\infty}[\widehat{C}_2(x_1;\omega)]]$. Here, $(\mathrm{Pe}_L, \mathrm{Da}) = (20, 40)$, $\ell = 10$ and $\sigma = 0.2$ are used, the subscript G and E notation represents using a Gaussian and exponential covariance function respectively and the sample means are calculated using 10^7 realisations. 133

4.3 Difference between the sample mean $[\mathbb{E}_{\{G,E\}}[C(x_1;\omega)]]$ and the homogenized solution $C_H(x_1)$ from (4.2.2), using the expected correction $\widehat{C}_2(x_1;\omega)$ from (4.2.15) $[C_H(x_1)+\mathrm{Da}^2\,\mathbb{E}_{\{G,E\}}[\widehat{C}_2(x_1;\omega)]]$ and using the effective uptake parameters $\mathrm{Da}^G_{\mathrm{eff}}$ and $\mathrm{Da}^E_{\mathrm{eff}}$ from (4.3.1) and (4.3.2) respectively in (4.2.21) $[C_H^{\{G,E\}}(x_1)]$. Here, $(\mathrm{Pe}_L, \mathrm{Da}) = (20, 40)$, $\ell = 0.01$ and $\sigma = 0.2$ are used throughout, the subscript (and superscript) G and E notation represents using a Gaussian and exponential covariance function respectively and 10^7 realisations are used to calculate sample expectations. 135

4.4 Column (a) depicts the sink covariance function $\mathcal{K}^G_{\hat{g}}(x_1, x_2)$ from (4.1.2) whereas column (b) depicts the solute covariance in terms of the correction $\mathcal{K}^G_{\widehat{C}_1}[x_1, x_2]$ from (4.2.12). Here, $\ell = 0.01, 0.1, 1, 10$ is used in rows (i), (ii), (iii) and (iv) respectively. The correction $\mathcal{K}^G_{\widehat{C}_1}[x_1, x_2]$ is calculated using (4.2.12) with the integral solver described in Appendix B.3, with $(\mathrm{Pe}_L, \mathrm{Da}) = (20, 40)$, $\sigma = 0.2$ being used throughout. 137

4.5 Column (a) depicts the sink covariance function $\mathcal{K}^E_{\hat{g}}(x_1, x_2)$ from (4.1.3) whereas column (b) depicts the solute covariance in terms of the correction $\mathcal{K}^E_{\widehat{C}_1}[x_1, x_2]$ from (4.2.12). Here, $\ell = 0.01, 0.1, 1, 10$ is used in rows (i), (ii), (iii) and (iv) respectively. The correction $\mathcal{K}^E_{\widehat{C}_1}[x_1, x_2]$ is calculated using (4.2.12) with the integral solver described in Appendix B.3, with $(\mathrm{Pe}_L, \mathrm{Da}) = (20, 40)$, $\sigma = 0.2$ being used throughout. 138

4.6 A plot showing the variances calculated using (4.3.6), (4.2.12) and (4.3.5) for $\ell \to \infty$, $\ell = [10, 1, 0.1, 0.01]$ and $\ell \to 0$ respectively. Here, solid and dotted lines are used to represent a Gaussian and exponential covariance function respectively. The asymptotes for small and large ℓ are represented by red dashed lines with squares and circles respectively, where the asymptote for $\ell \to 0$ is calculated using $\ell = 0.01$. This figures uses $(\mathrm{Pe}_L, \mathrm{Da}) = (20, 40)$, $\sigma = 0.2$. A second-order Simpson rule is used to evaluate (4.2.12). 139

4.7 Difference between Da and $\mathrm{Da}_{\mathrm{eff}}$ as the parameters Pe_L, Da, σ and ℓ change, as shown by figures (a), (b), (c) and (d) respectively, with insets showing log-log plots. Here, the difference is shown in one dimension (1D), two dimensions (2D) and three dimensions (3D) with solid and dashed lines representing a Gaussian and Exponential covariance function respectively. Figures (b), (c) and (d) use $\mathrm{Pe}_L = 20$, Figures (a), (c) and (d) use $\mathrm{Da} = 20$, Figures (a), (b) and (d) use $\sigma = 1$ and Figures (a), (b) and (c) use $\ell = 0.01$. Effective uptake parameters for Gaussian [exponential] covariance functions are given in one, two and three dimensions in (4.3.1) [(4.3.2)], (4.4.6) [(4.4.7)] and (4.4.9) [(4.4.10)] respectively. . 144

4.8 (a) Approximations of the expected concentration for uniformly-random sink locations in two and three dimensions, as given in Figure 3.12(a). Added are the two- and three-dimensional effective uptake approximations in magenta and black respectively. (b) Difference between sample expectations and each correction in two dimensions. Throughout we use $\lambda = 0.2$, $\varsigma = 0.01$ and $(\mathrm{Pe}_L, \mathrm{Da}) = (20, 10)$ with squares and diamonds representing two- and three-dimensional domains respectively. Effective concentrations are calculated using (4.6.3) with Table 4.1 and (4.2.22). 146

4.9 (a) Images of fetal tissue obtained using electron microscopy, where the top left image shows a single mitochondria. Images are courtesy of Michelle Desforges [unpublished]. (b) Distribution of mitochondria (grey) in the vasculosyncytial membrane, where the figure includes epithelium and capillaries (magenta), cytotrophoblast (orange) and the nuclei of syncytiotrophoblast (green). The outlining orange cuboid has dimensions $147\,\mu\mathrm{m} \times 305\,\mu\mathrm{m} \times 100\,\mu\mathrm{m}$ and the figure is courtesy of Tomass Vaivods [unpublished] using data from Michelle Desforges [unpublished]. 150

B.1 (a) & (c) Realisations of one plus the sink function on a log-scale [grey] with the sample mean [dashed red] and a single realisation [solid magenta]. (b) & (d) Realisations of concentration profiles [grey] with the sample mean [$\hat{\mu}$, dashed red], sample Gaussian-based 95% credible-intervals [$\hat{\mu} \pm 1.96\hat{\sigma}$ (where $\hat{\sigma}$ represents the sample standard deviation), solid blue], sample median [$\hat{\mu}_{0.5}$, dashed green], sample 95% credible-intervals [$\hat{\mu}_{0.5 \pm 0.475}$, solid cyan] and one single realisation [solid magenta]. Figures (a)-(b) and (c)-(d) use a Gaussian and exponential covariance function for $z(x_1)$ in (B.7.1) respectively. All figures use 10^4 Monte Carlo simulation with $(\mathrm{Pe}_L, \mathrm{Da}) = (10, 40)$, $\sigma = 1$ and $\ell = 0.1$. 179

The University of Manchester

George Frederick Price
Doctor of Philosophy
Modelling of Solute Transport Past a Disordered Uptake Field
January 14, 2022

Solute transport often takes place in spatially complex domains with inherently heterogeneous structures, such as in biological tissue and geophysical flows. Due to the complexity of transport networks a variety of mathematical problems exist across a range of lengthscales. We seek to characterise the effect of disordered multiscale spatial structures on solute uptake in the presence of advection and diffusion.

We first examine a one-dimensional advection-diffusion-uptake model for solute transport past an array of point sinks with first-order kinetics. When an advection-diffusion balance exists on the microscale we quantify the impact of disordered sink locations on the solute concentration by finding corrections to a deterministic homogenized solution using a Green's function method. This non-standard approach to homogenization characterises uncertainty in the solute concentration due to disordered sink locations and captures influences from multiple lengthscales. When advection dominates on the microscale, a staircase structure is exhibited by individual concentration profiles due to boundary layers forming upstream of sink locations. This causes concentration profiles to be non-Gaussian, resulting in moments being poor predictors of disorder in solute concentration. Therefore, we calculate the median and credible intervals for the concentration using the inverse of the cumulative distribution function for sink locations. Credible intervals preserve the staircase structure exhibited by individual concentration profiles and capture their non-Gaussian behaviour.

Next, we consider a more direct approach that quantifies the impact of a disordered sink function on solute concentration in one, two and three spatial dimensions. The sink function is represented by an ensemble of discrete sink locations with each sink having finite width. We develop a 'moments-based' approach, which gives a direct mapping between the first two moments of the sink distributions and the first two moments of the solute concentration. Non-local corrections to a deterministic homogenized solution are found by successively inverting linear operators using an appropriate Green's function, with a region of influence being given by inverting this Green's function. For asymptotically small sink widths we find that periodic corrections scale with the sink width according to corresponding singularities in the Green's function. By normally perturbing sinks from a periodic arrangement we find that disorder smooths out singularities when taking averages. By prescribing sink locations using a uniform distribution we find that the dominant correction varies smoothly in space but is amplified by asymptotically small sink widths in two- and three-dimensional domains.

Finally, we consider using a continuous sink function described by a Gaussian process with both Gaussian and exponential covariance functions in one, two and three dimensions. For asymptotically large correlation lengths, non-local corrections in the moments-based approach are readily evaluated and provide an upper bound on the variance of solute distributions. For asymptotically small correlation lengths the (co)variance of corrections is simplified using a δ-function approximation, allowing an effective uptake parameter to be used to predict the expected concentration. As the covariance function for uniformly-random sink locations is Gaussian in two and three spatial dimensions we calculate an effective uptake parameter. Its use is illustrated for two applications: solute transport within maternal blood through the intervillous space of the placenta and oxygen uptake by mitochondria within placental tissue.

Declaration

No portion of the work referred to in the thesis has been submitted in support of an application for another degree or qualification of this or any other university or other institute of learning.

Copyright Statement

i. The author of this thesis (including any appendices and/or schedules to this thesis) owns certain copyright or related rights in it (the "Copyright") and s/he has given The University of Manchester certain rights to use such Copyright, including for administrative purposes.

ii. Copies of this thesis, either in full or in extracts and whether in hard or electronic copy, may be made **only** in accordance with the Copyright, Designs and Patents Act 1988 (as amended) and regulations issued under it or, where appropriate, in accordance with licensing agreements which the University has from time to time. This page must form part of any such copies made.

iii. The ownership of certain Copyright, patents, designs, trade marks and other intellectual property (the "Intellectual Property") and any reproductions of copyright works in the thesis, for example graphs and tables ("Reproductions"), which may be described in this thesis, may not be owned by the author and may be owned by third parties. Such Intellectual Property and Reproductions cannot and must not be made available for use without the prior written permission of the owner(s) of the relevant Intellectual Property and/or Reproductions.

iv. Further information on the conditions under which disclosure, publication and commercialisation of this thesis, the Copyright and any Intellectual Property and/or Reproductions described in it may take place is available in the University IP Policy (see http://documents.manchester.ac.uk/DocuInf-o.aspx?DocID=487), in any relevant Thesis restriction declarations deposited in the University Library, The University Library's regulations (see http://www.manchester.ac.uk/library/aboutus/regulations) and in The University's Policy on Presentation of Theses.

Acknowledgements

I would first like to thank Prof. Oliver Jensen, where your continued support, vast knowledge, insightful guidance, dedication and incredible patience have been vastly appreciated throughout our time together. I'd like to thank my co-supervisor Dr. Igor Chernyavsky, your hard work, expertise and advice were instrumental towards the research undertaken. A noticeable mention should go to the wider mathematical community at The University of Manchester, who have aided my research and made the past four years so incredibly enjoyable. In particular, I would like to thank everyone in office 1.134 and who I've socialise with on the ATB bridge, you've all been a fantastic support network in which I've formed some wonderful friendships.

A huge thank you is owed to my parents, you have offered helpful advice, kind words and loving support through some difficult moments of my studies. I'd like to thank Laura, for her emotional support, and all my friends and family, who have played football, disc golf, D&D and board games, attended gigs, festivals, holidays, walks and sporting events, socialised in bars, pubs, clubs and restaurants and even just done nothing at all with me. Last, but most certainly not least, I would like to thank Bruce, who is the most amazing house rabbit and hasn't complained once about the countless attention I demand from him.

Chapter 1

Introduction

Solute transport in the natural world often takes place in spatially complex and heterogeneous systems with inherently random structures. This transport is an essential part of life and is often seen in both physiological and geophysical systems. Due to occurring over multiple lengthscales the transport often becomes complex, posing difficulties in capturing the impact of fine-scale effects on the effective macroscopic description. To further complicate matters, disorder within systems can require corrections to (and fluctuations about) the mean to characterise solute transport. This is a topic of broad interest, with applications to geophysical flows, biological tissue (e.g. placentas, lungs, tumours and plant roots), industry (e.g. filtration, biofilms and lithium-ion batteries) and composite materials to name a few. This thesis will seek to characterise the effects of disordered multiscale spatial structures on the solute concentration within these complex transport networks, focusing in particular on the role of spatially non-uniform solute uptake.

1.1 Relevant examples of solute transport within disordered domains

Consider the example of solute transport within a human placenta. Here, blood gases and nutrients are exchanged between fetal and maternal circulatory systems via complex, three-dimensional disordered vascular networks. On the fetal side, blood exits the fetus via two umbilical arteries, which separate into multiple branches and form complex tree-like structures

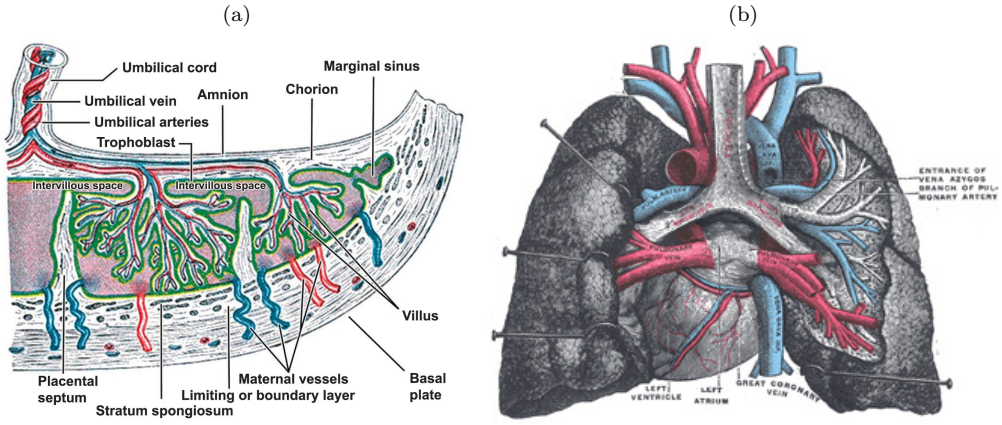

Figure 1.1: (a) Anatomy of fetal and maternal circulation in the human placenta (Serov et al., 2015). (b) Anatomy of pulmonary vessels and airways in the human lung (Gray, 1918).

known as villous trees, see Figure 1.1(a). These trees protrude out of the fetal plate and invade the intervillous space (IVS), which contains a pool of maternal blood. This allows solute exchange between the fetal and maternal circulatory systems to occur at terminal villi, which are located at the peripheral branches of villous trees. Due to the complexity of transport networks a variety of mathematical problems exist across a range of lengthscales, as shown in Erian et al. (1977), Aifantis (1978) and Jensen and Chernyavsky (2019).

The respiratory system is another well-documented biological example, where air is inhaled into the lung through a network of complicated bifurcating airways. Air travels through the branching network until it reaches terminal alveoli, which provide a large surface area and contain pulmonary capillaries for gas exchange to occur, see Figure 1.1(b). The alveoli exchange oxygen for waste carbon dioxide with pulmonary capillaries via diffusion, from where oxygen is then transported through a branching network of pulmonary veins into the systemic circulatory system. Numerous mathematical models of gas exchange in the human lung exist, with many focusing on the complexity of transport due to the airway and vascular structure, see Zhang and Kleinstreuer (2001), Freitas and Schröder (2008) and Kleinstreuer and Zhang (2010) for example.

Biofilms consist of syntrophic microorganisms (often including bacteria) which live in colonies. Hall-Stoodley et al. (2004) found that the complex structure of these colonies aid a biofilm's ability to survive in hostile environments. Biofilms are of great interdisciplinary interest due to being found in two-thirds of bacterial infections (Del Pozo et al., 2008), being responsible for the

biocorrosion of metals (Beech and Sunner, 2004) and being used to adsorb and metabolise pollutants during sewage treatment (Flemming, 1993). The transport of chemical species through biofilms is a complex process due to it occurring over multiple lengthscales in a disordered domain (Costerton, 1999; Dalwadi et al., 2018).

Filters can be found throughout industry, where they are used for removing impurities when treating surface water (Zularisam et al., 2006), processing and preserving food without chemical treatment (Rektor and Vatai, 2004) and removing excess waste and water from blood during kidney dialysis (Lakshmi et al., 2014). Here, non-periodic structures can be seen to improve filtration of solute by reducing the likelihood of blockage whilst maintaining the rate of solute removal (Datta and Redner, 1998; Dalwadi et al., 2015). Similarly for lithium-ion batteries, the electrode's complex porous structure has been shown to impact the efficiency, reliability and life expectancy of modern batteries (Garcia and Chiang, 2007).

For the examples above, transport occurs over multiple lengthscales in domains that often have an inherently random structure. This causes difficulty when modelling transport mathematically or computationally as the complex structure of the domain requires fine grid spacing and the disorder can require multiple realisations to be produced. We will now outline some well-documented mathematical techniques for modelling transport, along with the benefits and drawbacks of each approach. Following this, we outline how homogenization and spatial averaging can be used to find macroscopic solutions which include effects from the microscopic structure. The techniques of volume averaging and homogenization will be considered, both of which prevent the need for solving the mathematical problem in full.

1.2 Mathematical approaches for modelling solute transport

Existing mathematical models of solute transport will be divided into two broad categories: continuum- and individual-based. Continuum models are commonly used due to being less computationally expensive and allowing existing methods of analysis to be applied, although do neglect effects due to individual interactions and properties (Panasenko and Volpert, 2016). Therefore consideration is required before modelling systems using either approach, with some studies opting to couple individual- and continuum-based models (Smith and Yates, 2018).

1.2.1 Continuum-based models

Most continuum-based models consist of a system of ordinary differential equations (ODEs) or partial differential equations (PDEs), which are used to govern the system's behaviour, such as the flow of a fluid or the transport of a solute. Many continuum-based models study the quantity of interest using the continuity equation, which takes the general three-dimensional form

$$\frac{\partial \rho}{\partial t} + \nabla \cdot \mathbf{j} = \sigma, \tag{1.2.1}$$

where ρ, $\mathbf{j}$, t and σ represent the quantity per unit volume, the flux per unit area, time and the generation or removal of the quantity per unit volume respectively. When considering the transport of a solute, ρ, $\mathbf{j}$, t and σ commonly have the dimensions mol$\times$m^{-3}, mol$\times$m$^{-2}\times$s^{-1}, s and mol$\times$m$^{-3}\times$s^{-1} respectively. When $\sigma > 0$ (i.e. quantity is generated) the final term in (1.2.1) is referred to as a source and when $\sigma < 0$ (i.e. quantity is removed) it is referred to as a sink. Advective and diffusive fluxes are often considered for solute transport, which will be represented by $\mathbf{j}_A$ and $\mathbf{j}_D$ respectively. Advective flux represents the transport of solute by bulk motion and is given by $\mathbf{j}_A = \mathbf{u}\rho$, where $\mathbf{u}$ is the flow velocity vector field. The diffusive flux represents the net movement of particles from a higher to a lower concentration due to random motion. It is often given by Fick's law, which states that the flux of a solute (relative to the bulk motion) in the system is proportional to the local concentration gradient (Fick, 1855). Fick's law gives the diffusive flux term as $\mathbf{j}_D = -\mathsf{D}\nabla\rho$, which assumes that particles diffuse according to a Markovian process. Here, D represents a diffusion tensor for anisotropic media but is simplified to a constant coefficient D for isotropic media. Although this form is used widely when modelling transport processes, it should be noted that non-Fickian diffusion can be observed within solids (Shewmon, 1963), porous media (Berkowitz et al., 2006; De Anna et al., 2013; Alim et al., 2017) and other structures, therefore an alternative approach may be required.

When modelling solute transport through porous media, advective and diffusive fluxes are often used, i.e. $\mathbf{j} = \mathbf{j}_A + \mathbf{j}_D$. By assuming Fickian diffusion occurs, (1.2.1) takes the well-known form of the advection-diffusion-reaction equation. Let ρ from (1.2.1) represent the concentration of solute per unit volume, notated by $C(\mathbf{x}, t)$. Also, let solute uptake $\sigma(\mathbf{x}, C)$ be dependent on the concentration at a given $\mathbf{x}$ location, then (1.2.1) reduces to

$$\frac{\partial C}{\partial t} + \nabla \cdot (-\mathsf{D}\nabla C + \mathbf{u}C) = \sigma(\mathbf{x}, C), \tag{1.2.2}$$

which is dependent upon the flow velocity $\mathbf{u}$ (m$\times$s^{-1}), the diffusion tensor D (m$^2\times$s^{-1}) and the

sink term $\sigma(\mathbf{x}, C)$ (mol$\times$m$^{-2}\times$s^{-1}). Equation (1.2.2) says that the rate at which concentration changes inside a volume is given by the flow and diffusion into and out of the volume, along with the creation and consumption of concentration inside the volume. The velocity $\mathbf{u}$ may be known, or may depend on other differential equations which are coupled with (1.2.2). The advection-diffusion-reaction equation given in (1.2.2) has a variety of applications, such as modelling car traffic flow (Lighthill and Whitham, 1955), population dynamics (Sibert et al., 1999; Adam and Sibert, 2002; Petrovskii and Li, 2003) and chemotaxis observed in bacteria (Dillon et al., 1995; Ford and Harvey, 2007) to mention a few.

When modelling flow through natural disordered media, $\mathbf{u}$, D and σ are often functions of the environment. If they involve multiple lengthscales or spatial disorder, these variables can become highly complex. This results in computational methods becoming inefficient and (1.2.2) being potentially hard to solve, both analytically and numerically. Therefore upscaling or averaging techniques are commonly used to find a simple effective description. When upscaling the advection-diffusion-reaction equation, one aim is to find effective macroscopic parameters, for which a large number of methods exist (Cushman et al., 2002). One example is the Taylor dispersion effect, where shear flow with transverse diffusion can increase a solute's effective axial diffusivity (Taylor, 1953). The shear smears out solute concentration in the direction of the flow, causing the rate at which solute spreads in the flow direction to increase. This principle has been generalised to flows through periodic porous media (Brenner, 1980; Edwards et al., 1991; Salles et al., 1993; Auriault and Adler, 1995). Another example is given in Pavliotis and Stuart (2008), who upscale the advection-diffusion equation for a spatially oscillating velocity field.

Some studies consider the convergence of the upscaled descriptions, where it is found that sufficiently strong spatial disorder leads to macroscopic descriptions becoming insufficient, meaning a stochastic system of equations is instead required (Bal, 2011). It is therefore beneficial to study models with both spatial disorder and lengthscale separation to quantify fluctuations caused when discrete-to-continuous homogenization is used. Work on this has begun, for example, solute transport past a one-dimensional array of spatially disordered point sinks has been investigated (Chernyavsky et al., 2011, 2012; Russell et al., 2016; Russell and Jensen, 2020).

1.2.2 Individual-based models

For individual-based models, the primary concern is the quantity of an individual entity, which could represent a particle, molecule, animal, etc. Some models adopt a deterministic approach

whilst others allow the behaviour of an individual to be probabilistic by using a stochastic approach. By considering spatial hopping on a lattice, models often describe the time evolution of probability in terms of a master equation, which ensures that probability is conserved. This is done by assuming the probability of being in a state n depends on the transition rate of individuals from a different state to the state n and from the state n to a different state. These states can represent the number of particles in a spatial location, the quantity of a species in an ecosystem, etc. The master equation is commonly given by (Van Kampen, 1992)

$$\frac{\mathrm{d}P_n(t)}{\mathrm{d}t} = \sum_{m \neq n} \Big[W_{m \to n}(t) P_m(t) - W_{n \to m}(t) P_n(t) \Big], \tag{1.2.3}$$

where $P_n(t)$ represents the probability of being in a state n at a time t and $W_{i \to j}(t)$ the transition rate (probability per unit time) from a state i to a state j at a time t. When all $W_{i \to j}$ are independent of time the transition rates are treated as a memoryless property, which represents a kinetic scheme with Markovian dynamics. Thus, at any given time, the future state only depends on the current state with the past state being neglected. A classic example of a Markovian process is Fickian diffusion, which describes the movement of a solute from a region of high to low concentration at a rate proportional to the concentration gradient and independent of previous states.

When transition rates are dependent on time and so have a memory of the system's previous states the process is known as non-Markovian. If diffusion has non-Markovian dynamics we find that anomalous (non-Fickian) diffusion takes place. This can often be described using a power law, showing how the mean squared displacement ($\sigma_r{}^2$) relates to the diffusion coefficient (D). For $\sigma_r{}^2 \sim Dt^{\alpha}$, when $\alpha = 1$ this represents typical (Fickian) diffusion, when $\alpha < 1$ this represents sub-diffusion and when $\alpha > 1$ this represents super-diffusion. Anomalous diffusion has recently received attention in literature for crowded systems, which has applications to porous media (Berkowitz et al., 2006; Fomin et al., 2011; De Anna et al., 2013). The crowded systems see regions of slow and rapid flow due to fluid being 'trapped' in sections of the domain (Havlin and Ben-Avraham, 2002), which results in intermittent transport due to a non-uniform flow field. This is of particular interest when modelling geophysical flows (Scher and Montroll, 1975; Havlin and Ben-Avraham, 2002; Cushman et al., 2002; Berkowitz et al., 2006) and is often described using a continuous-time random walk (CTRW) model (Montroll and Weiss, 1965). Here, processes have arbitrary waiting times and varying jump lengths between states, with a generalised master equation being used to account for the system's history.

One method commonly used for simulating transport using (1.2.3) is the Gillespie algorithm, as developed in Gillespie (1976, 1977), although other stochastic simulation algorithms exist, see

Gillespie (2007) for a review. However, these approaches become computationally expensive when a system becomes large, such as for transport over multiple lengthscales. Although this can be mitigated by deriving asymptotic descriptions in terms of differential equations, see Van Kampen (1992) and Gardiner (2009), these approaches remain considerably more expensive to compute and harder to analyse when compared to adopting a continuum approach.

Hybrid models which combine the two approaches exist, which allow an individual-based model to be used for regions of the spatial domain which require high-resolution, with a continuum-based model being used elsewhere. These approaches offer a fine-grained computationally expensive description when required, with a coarse-grained computationally cheaper description elsewhere (Flekkøy et al., 2000; Delgado-Buscalioni and Coveney, 2003; Alpkvist et al., 2006). Hybrid models have gained popularity in recent years due to offering good agreement when compared to using a full individual-based model, but have a significant reduction in computational cost (Smith and Yates, 2018).

For illustrative purposes, let us now consider an individual-based model for the evolution of solute particles at a single site in a one-dimensional disordered domain. This will then be generalised to a continuum-based model, which describes the evolution of particles throughout the domain. This example will be used to outline how continuum descriptions are derived and assumptions that are required for their validity.

1.2.3 Example: A one-dimensional individual- to continuum-based model for solute transport through a disordered domain

Consider modelling solute transport through a porous medium using an individual-based model in one dimension, as done in Russell et al. (2016). Let there be M discrete sites on a lattice of length L, where sites are periodically located and set a distance d apart, see Figure 1.2. Consider one species of particles moving through the domain and let n_i represent the number of particles at the site i at a time t, where $i = 1, 2, \ldots, M$. Let each particle hop one space to the right at a constant rate p^+ and one space to the left at a constant rate p^- with there being no particle-particle interactions. Assume that particles flow into the system at a rate q and are allowed to leave the system at the left and right boundaries respectively. The total hopping rate travelling right from a site i is $p^+ n_i$ and travelling left from a site i is $p^- n_i$, see Figure 1.2. It will be assumed that particles at a site i can only travel to the sites $i - 1$ and $i + 1$.

Let particles be removed from the system at N randomly located sites, known as point sinks,

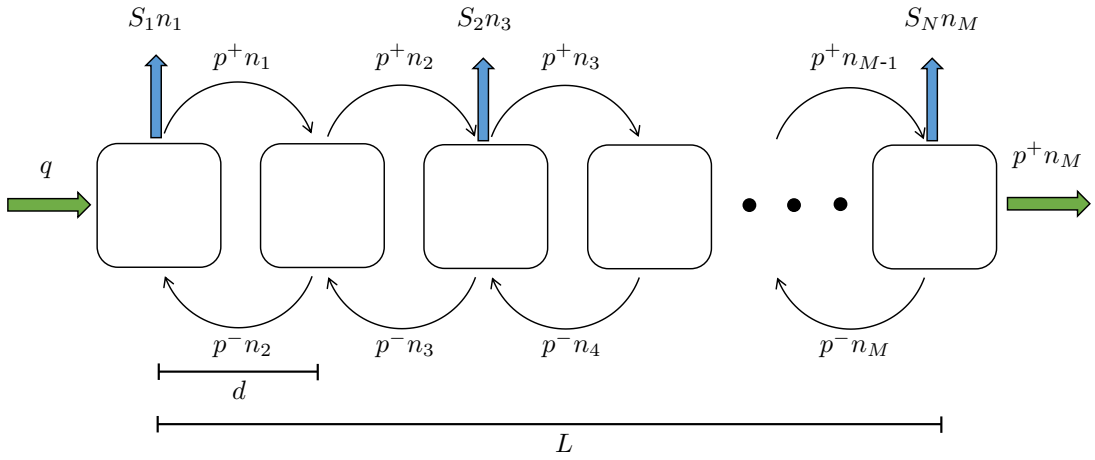

Figure 1.2: Illustration depicting the stochastic hopping of particles using M sites which are a distance d apart, where site i contains n_i particles. Particles can move to neighbouring sites and move to the right at a rate p^+ and to the left at a rate p^-. Located at N sites are sinks, which demonstrate a removal process through the domain, where the j^{th} sink has a strength S_j. For illustrative purposes, $k = 1$ and $\Delta_N = M - 1$ are used for the first and final sink locations respectively, although sink locations can be distributed randomly throughout the domain.

using first-order uptake kinetics (i.e. uptake will depend linearly on the number of particles at each sink location). Sinks will be located at sites $k + \Delta_j$, where the k^{th} site contains the first sink and the random variable Δ_j represents the number of sites away from k the j^{th} sink lies, with $j = 1, 2, \ldots, N$ and $k + \Delta_N \leq M$. Let sink j have a strength S_j, so particles are removed by the j^{th} sink at a rate $S_j n_{k+\Delta_j}$. Then the rate at which particles vary at a site i is given by

$$\frac{\mathrm{d}n_i}{\mathrm{d}t} = p^+(n_{i-1} - n_i) + p^-(n_{i+1} - n_i) - \sum_{j=1}^{N} \delta(i - k - \Delta_j) S_j n_i, \tag{1.2.4}$$

where δ represents the Dirac delta function (δ-function). This takes the form of the master equation given in (1.2.3), using $P_n(t) = n_i$ and the transition rates as

$$W_{\alpha\to\beta}(t) = \begin{cases} p^- & \text{if } \alpha - \beta = 1 \\ p^+ & \text{if } \alpha - \beta = -1\,, \\ 0 & \text{otherwise} \end{cases} \tag{1.2.5}$$

modified by an additional sink term that is introduced to remove particles when located at a site $i = k + \Delta_j$ for $j = 1, \ldots, N$.

The model (1.2.4) describes the evolution of particles at each site i. This can be generalised to a continuum-based model which instead describes the evolution of particles throughout the

domain. Let n_i represent the concentration of a solute at a point x for a given time t, i.e. $n_{i-1} = C(x-d,t)$, $n_i = C(x,t)$ and $n_{i+1} = C(x+d,t)$. Also let $x = \xi_j$ represent sink locations for $j = 1, \ldots, N$. Then by assuming M is asymptotically large we can generalise the individual-based model given in (1.2.4) to a continuum-based model. By using (1.2.4), Taylor expanding both $C(x+d,t)$ and $C(x-d,t)$ about x and allowing d to be asymptotically small compared to the average inter-sink distance we obtain

$$\begin{aligned}\frac{\partial}{\partial t}C(x,t) =& p^+(C(x-d,t) - C(x,t)) + p^-(C(x+d,t) - C(x,t)) \\ & - C(x,t)\sum_{j=1}^{N}\delta(x-\xi_j)S_j \\ =& p^+\left(-dC_x(x,t) + \frac{1}{2}d^2C_{xx}(x,t) + \ldots\right) + p^-\left(C_x(x,t) + \frac{1}{2}d^2C_{xx}(x,t) + \ldots\right) \\ & - C(x,t)\sum_{j=1}^{N}\delta(x-\xi_j)S_j.\end{aligned}$$

Then by letting

$$U = (p^+ - p^-)d \quad \text{and} \quad D = \frac{1}{2}(p^+ + p^-)d^2 \tag{1.2.6}$$

be the mean advective velocity and the diffusion coefficient respectively gives

$$C_t = -UC_x + DC_{xx} - C\sum_{j=1}^{N}\delta(x-\xi_j)S_j, \tag{1.2.7}$$

where $\mathcal{O}(d^3)$ terms have been neglected. Note that (1.2.7) recovers a one-dimensional version of the advection-diffusion-reaction equation given in (1.2.2) with a uniform advective velocity U.

Many methods exist for solving advection-diffusion-reaction equations, although due to the complexity of disordered media, $\mathbf{u}$, D and σ in (1.2.2) are often complex functions. This makes it unlikely for an exact solution to exist, with computational methods often becoming inefficient. It is therefore beneficial to use spatial averaging and homogenization techniques to approximate a system's leading-order behaviour without fully evaluating $C(\mathbf{x},t)$ given in (1.2.2).

1.2.4 Spatial averaging and homogenization techniques

Spatial averaging and homogenization have proven to be useful tools for modelling solute transport due to capturing the system's leading-order behaviour without the need to solve the system of equations in full. This is often advantageous for problems with multiple lengthscales, as averaging vastly reduces the computational cost but allows effects from the fine-scale structure

to impact the macroscale solution. The two most common methods are volume averaging (Rubinstein and Torquato, 1988; Quintard and Whitaker, 1988) and homogenization via multiscale asymptotics (Papanicolau et al., 1978). Both methods are outlined in the review by Davit et al. (2013) and can be used for systems described by ordinary differential equations (ODEs), partial differential equations (PDEs) and stochastic differential equations (SDEs) among others. Note that a variety of other methods exist, such as mixture theory (Hassanizadeh and Gray, 1979, 1980), moment methods (Brenner, 1980, 2013) and central limit methods (Bhattacharya, 1982) to name a few. For a broad review of spatial averaging and homogenization techniques, see Cushman et al. (2002) and Pavliotis and Stuart (2008).

Let us now summarise the methodology behind volume averaging and homogenization. At the core of volume averaging lies the decomposition of the problem into two components, both defining macroscale variables via spatial averaging and later including contributions from perturbations. To find the spatial average, a common approach is to use the moving volume average. Denote $\nu(\mathbf{x})$ as the averaging set at a point $\mathbf{x}$ and V its volume (i.e. $V = \int_{\nu(\mathbf{x})} \mathrm{d}V$). Then for any ψ, the moving volume average is given by

$$\langle \psi(\mathbf{x}, t) \rangle = \frac{1}{V} \int_{\xi \in \nu(\mathbf{x})} \psi(\xi, t) \, \mathrm{d}V. \tag{1.2.8}$$

Using this notation, we can decompose some concentration $C(\mathbf{x}, t)$ into

$$C(\mathbf{x}, t) = \langle C \rangle(\mathbf{x}, t) + \widetilde{C}(\mathbf{x}, t), \tag{1.2.9}$$

where $\langle C \rangle$ is the moving volume average and $\widetilde{C}$ is a perturbation correction to be found. So here we need to find a representative volume element (RVE) for $\langle C \rangle$, which gives a portion of the domain over which parameter fields are spatially quasi-stationary. This is followed by solving over unit-cells to find the correction $\widetilde{C}$. Note that the RVE and unit-cells can differ, where a unit-cell does not have to be a subset of the domain and can be found using images of porous media (Davit et al., 2013).

Although volume averaging gives effective transport equations and coefficients without assuming periodicity of the medium, it requires closure assumptions using heuristic estimates for terms in the governing equation. These closure assumptions normally assume the perturbations given by $\widetilde{C}$ in (1.2.9) is small in comparison to the average $\langle C \rangle$ (Whitaker, 1999), an assumption which can become problematic when large spatial heterogeneity exists. One drawback to the volume averaging approach is that corrections of higher order than $\langle C \rangle$ are neglected, which may be of importance when multiple lengthscales exist (Pavliotis and Stuart, 2008).

For the multiscale asymptotic approach, the underpinning methodology is to let l and L characterise the microscale and macroscale respectively. We assume a periodic micro-structure and then consider the limit $\varepsilon \to 0$, where $\varepsilon = l/L$. To begin, the concentration $C(\mathbf{x}, t)$ is assumed to have two-scale dependence on a short lengthscale $\mathbf{x}$ and a long lengthscale $\mathbf{X} = \varepsilon\mathbf{x}$, i.e. $C(\mathbf{x}, t) = \widehat{C}(\mathbf{x}, \mathbf{X}, t)$. This has been shown to construct uniformly valid approximations of functions (Johnson et al., 2011) and is often referred to as the method of multiple scales. A formal two-scale expansion of $C(\mathbf{x}, t)$, given by

$$C(\mathbf{x}, t) = \widehat{C}(\mathbf{x}, \mathbf{X}, t) = C^{(0)}(\mathbf{x}, \mathbf{X}, t) + \varepsilon C^{(1)}(\mathbf{x}, \mathbf{X}, t) + \varepsilon^2 C^{(2)}(\mathbf{x}, \mathbf{X}, t) + \ldots, \tag{1.2.10}$$

is then assumed, treating $\mathbf{x}$ and $\mathbf{X}$ as independent variables, where $C^{(n)}(\mathbf{x}, \mathbf{X}, t) = \mathcal{O}(1)$ for $n = 0, 1, 2, \ldots$ as $\varepsilon \to 0$. So by assuming the two lengthscales are independent, along with breaking the domain into multiple unit-cells of width ε and assuming periodicity over each unit-cell, the problem can be separated into a sequence of sub-problems for different orders of ε and solved independently. Throughout this thesis, this approach will be referred to as the classical approach to homogenization.

One drawback of using the classical approach is that it requires the assumption of two-scale dependence. When more than two lengthscales exist, such as when boundary layers are present, this approach may fail to capture influences at the appropriate order. The assumption of unit-cell periodicity can also be a cause for concern, with some studies modifying the classical approach by relaxing this assumption, thereby allowing the cell size to vary on the macroscopic scale (Van Noorden and Muntean, 2011; Chapman and McBurnie, 2011). However, when modelling transport through strongly disordered porous media there may be no such unit-cell structure present, resulting in an alternate approach being required. A summary of the two spatial averaging approaches can be found in Table 1.1.

	volume averaging	Multiscale asymptotics
Expansion	$C(\mathbf{x}, t) = \langle C \rangle(\mathbf{x}, t) + \widetilde{C}(\mathbf{x}, t)$	$C(\mathbf{x}, t) = \sum_i \varepsilon^i C^{(i)}(\mathbf{x}, \mathbf{X}, t)$
Scalings	Appropriate for all scalings	Appropriate for one scaling
Set up	One problem	Successive problems
Averaging volumes	A representative volume element followed by unit-cells	Unit-cells
Drawbacks	Neglects higher order terms	Assumes two-scale dependence

Table 1.1: Table summarising the differences between volume averaging and multiscale asymptotics, which closely follows Table 1 in Davit et al. (2013).

One disadvantage for both approaches is how disordered domains cannot be accounted for without considering complicated extensions. Consider perturbing the velocity and concentration

away from their means by some random variable for the multiscale asymptotic approach, i.e. $\mathbf{u} = \langle \mathbf{u} \rangle + \widehat{\mathbf{u}}$ and $C = \langle C \rangle + \widehat{C}$. Then the mean of $\mathbf{u}C$ is given by

$$\langle \mathbf{u}C \rangle = \langle (\langle \mathbf{u} \rangle + \widehat{\mathbf{u}})(\langle C \rangle + \widehat{C}) \rangle = \langle \langle \mathbf{u} \rangle \langle C \rangle \rangle + \langle \langle \mathbf{u} \rangle \widehat{C} \rangle + \langle \widehat{\mathbf{u}} \langle C \rangle \rangle + \langle \widehat{\mathbf{u}} \widehat{C} \rangle = \langle \mathbf{u} \rangle \langle C \rangle + \langle \widehat{\mathbf{u}} \widehat{C} \rangle,$$

where the mean of each perturbation $\widehat{\mathbf{u}}$ and $\widehat{C}$ is zero by definition. So when considering the advection term in (1.2.2), we obtain

$$\nabla \cdot (\mathbf{u}C) = \nabla \cdot (\langle \mathbf{u} \rangle \langle C \rangle) + \nabla \cdot (\langle \widehat{\mathbf{u}} \widehat{C} \rangle). \tag{1.2.11}$$

This shows that large perturbations of $\mathbf{u}$ and C may have a large impact on the concentration field. So when the perturbations $\widehat{\mathbf{u}}$ and $\widehat{C}$ become large due to spatial disorder on the microscale, non-standard approaches to homogenization are required. One alternate approach to classical homogenization is a weak disorder expansion (Dagan, 1984; Russell and Jensen, 2020), which includes the influence of disorder using an integral approach to homogenization. For a more complete review of alternative homogenization and spatial averaging methods, see Pavliotis and Stuart (2008).

We will now discuss some mathematical methods for modelling flow and transport within porous media and other disordered domains. Due to the domain's structure, the multiple lengthscales present and the spatial disorder, modelling flow and transport in porous media has given rise to a variety of problems with a vast range of applications.

1.3 Mathematical modelling of flow and transport within porous media and other disordered domains

Flow and transport through porous media are of particular interest due to their diverse applications. A porous medium consists of a matrix, an often complex structure, and pores, which are voids typically filled with fluid. It is commonly characterised by its porosity, permeability and stiffness among other features. Porous media have a variety of applications, including modelling geophysical flows (such as aquifers, groundwater flow and oil reservoirs (Bear, 2013)), blood flow in the human placenta (Erian et al., 1977; Aifantis, 1978; Chernyavsky et al., 2010), airflow in the human lung (Lande and Mitzner, 2006; Kuwahara et al., 2009; Miguel, 2012) and solute removal in filters (Datta and Redner, 1998; Dalwadi et al., 2015). Models are often concerned with the flow of a fluid, transport of a solute or the transfer of heat through the medium (Vafai, 2015).

From Figure 1.3 we see the porous structure, multiple lengthscales and spatial heterogeneity

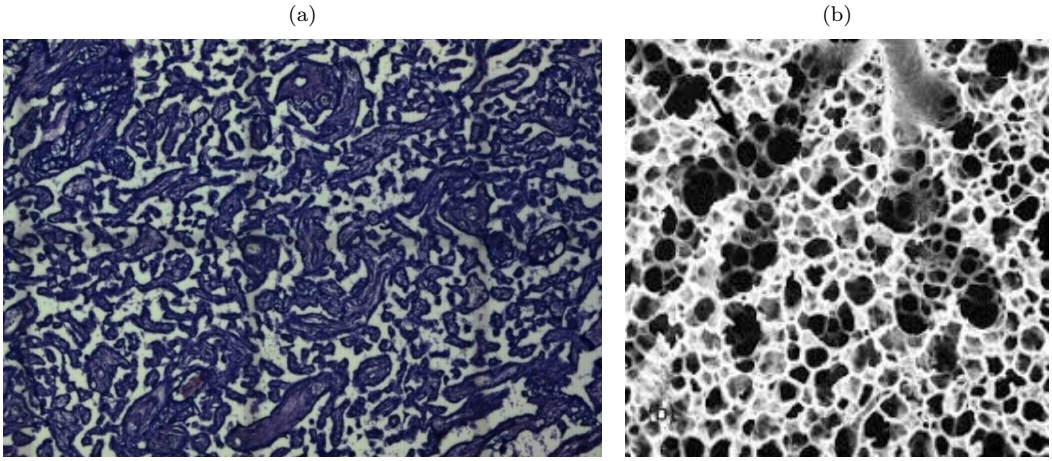

Figure 1.3: (a) Cross section of the villous trees in a human placenta (Chernyavsky et al., 2011). (b) Cross section of the parenchyma in a human lung (Lande and Mitzner, 2006).

of both the human placenta and lung. In the human placenta solute is transported within maternal blood through the intervillous space via advection and diffusion, with solute exchange occurring at the site of terminal villi where the vasculosyncytial membrane is thinnest (Wang, 2010). Figure 1.3(a) shows a cross section of the intervillous space, demonstrating the complex structure of villous networks. This structure is often treated as a porous medium due to its multiscale nature, where pores represent the intervillous space (IVS) and the matrix represents villous trees. Similarly, in the human lung air is transported through airways, which branch approximately 20 times (Kleinstreuer and Zhang, 2010) before reaching peripheral alveoli. The alveoli are the site for gas exchange between the lung and circulatory system, where the lungs of an adult are thought to have over 100 million alveoli (Ochs et al., 2004) with the alveolar walls being less than $10\,\mu$m thick (Tsunoda et al., 1974). Figure 1.3(b) shows a cross section of the human lung parenchyma and demonstrates its porous structure and the multiple lengthscales over which transport occurs.

1.3.1 Modelling flow through disordered domains

When concerned with the flow of a fluid through a porous medium, models commonly adopt Darcy's law. This was originally developed experimentally for the flow of water through sand by Darcy (1856) and states that an incompressible fluid flowing through pores has a linear relation between the volume-averaged velocity and pressure gradient. This can be expressed mathematically as the mass conservation incompressibility condition

$$\nabla \cdot \mathbf{u} = 0,$$

and the momentum conservation equation (Darcy, 1856)

$$\mathbf{u} = -\frac{K}{\mu}\nabla P,$$

where $\mathbf{u}$, μ, P and K represent the volume-averaged flow velocity, viscosity of the fluid, pressure of the fluid and the average hydraulic permeability of the medium respectively. Darcy's law can be derived directly from the Navier-Stokes equations using various techniques, including volume averaging (Whitaker, 1986; Rubinstein and Torquato, 1988) and homogenization via a two-scale expansion (Keller, 1977; Burridge and Keller, 1981). However, derivations often involve identifying a representative, periodic unit-cell or volume element to perform spatial averaging and use the assumption of periodicity at the microscale. Although Darcy-like models have been used for disordered porous media (Rubinstein and Torquato, 1989; Beliaev and Kozlov, 1996; Du and Ostoja-Starzewski, 2006), studies usually perform ensemble averaging (as opposed to spatial averaging) over a representative volume element and assume that disorder impacts the microscale and not the macroscale.

Adaptations of Darcy's law for modelling flow through porous media do exist. Two examples are proposed in Forchheimer (1901) and Brinkman (1949), which again assume the fluid is incompressible but give the relations

$$\left(1 + \frac{\rho}{\mu}\beta|\mathbf{u}|^{n-1}\right)\mathbf{u} = -\frac{K}{\mu}\nabla P \tag{1.3.1}$$

and

$$\mathbf{u} = -\frac{K}{\mu}\left(\nabla P - \mu_b \nabla^2 \mathbf{u}\right) \tag{1.3.2}$$

respectively, where ρ, β, n and μ_b are the density of the fluid, Forchheimer drag coefficient, Forchheimer velocity exponent and Brinkman effective viscosity respectively. Here, both β and μ_b are given as functions of the average hydraulic permeability K and the volume fraction ϕ of the medium. Forchheimer's equation given in (1.3.1) is commonly used for weak inertia flows, whereas Brinkman's equation given in (1.3.2) offers a coupling of Darcy with Stokes flow and is commonly used near the boundaries of porous media. When poroelasticity is of importance, one common method is presented in Biot (1941), which couples Darcy's law for the fluid with the linear elasticity of the medium. This is normally done for an isotropic and homogeneous porous medium with an incompressible fluid. Biot (1941) found that, for small deformations of the medium, the leading-order problem for the fluid becomes independent of the elasticity problem. We should note that, as for the Darcy approach, models presented in Forchheimer (1901) and Biot (1941) have been obtained via homogenization techniques which again require the assumption of periodicity on the microscale (Mei and Auriault, 1991; Balhoff et al., 2010;

Auriault and Sanchez-Palencia, 1977; Burridge and Keller, 1981). However, the model presented in Brinkman (1949) is derived phenomenologically, with Nield et al. (2006) claiming the model is only appropriate when the volume fraction of the medium is suitably small.

Some models focus on calculating estimates of an effective viscous drag term when considering flow past an array of impenetrable spheres and cylinders. This has been done using a Green's function approach with Stokes equation (Hasimoto, 1959) and using lubrication theory (Keller, 1964) among other methods. In contrast, a vast amount of studies have been concerned with the effect of spatially varying porosity on the flow rate through porous media (Du Plessis and Masliyah, 1991; Sahimi, 1993; Keller, 2001). This is of particular interest in geophysical flows, where complex networks are formed between pores which create regions of slow and rapid transport. Russell (2017) considered the macroscopic flow quantities in porous media using a collection of impenetrable cylinders in a two-dimensional domain. When introducing weak disorder to cylinder locations they found changing a cylinder's size had a longer-range impact than changing its location or shape. For strong disorder, they found rapid-flow channels appeared within the domain. These results demonstrate how microscopic flow properties can influence the far-field behaviour of velocity fields, meaning caution is required when assuming two-scale dependence and Darcy's flow in disordered media. For a more detailed overview of flow in porous media, see Sahimi (2011).

1.3.2 Modelling solute transport through disordered domains

Solute transport within porous media often occurs over a variety of lengthscales. As a result, mathematical models commonly use spatial averaging to find macroscopic solutions when a fine microscopic structure exists, as discussed in Section 1.2.4. One popular method is to use homogenization theory, where classic results were originally developed for porous media with a periodic microstructure (Bakhvalov, 1975; Berdichevsky, 1975; Papanicolau et al., 1978; Sánchez-Palencia, 1980), but were then generalised to spatially homogeneous random media (Keller, 1977; Kozlov, 1979; Papanicolaou, 1979). However, these methods are usually based on a two-scale expansion and assume unit-cell periodicity, which can cause drawbacks when transport occurs over multiple lengthscales through disordered media.

Solute transport through porous media with spatially varying porosity is an area of active research, where a filter having porosity that decreases with depth is thought to be more efficient at removing solute from a fluid than one with a strictly periodic structure (Dalwadi et al., 2015, 2016). The optimal design for a filtration membrane is unknown, but Pereira et al. (2021)

predicted it to depend on the angle, position, thickness and permeability of the membrane. Using a combination of numerical and asymptotic approaches, they found the optimal membrane has pores either centred and diagonal across, or angled and in the corner of, the domain. Iliev et al. (2020) found that a classical approach to homogenization for a reactive flow through a catalytic membrane in the limit of strong reaction fails. Therefore an alternative approach to homogenization involving an auxiliary eigenvalue problem was developed. These studies considered solute transport through porous media when multiple lengthscales are involved. However, they did not consider the impact of a disordered microstructure on the macroscopic transport, where corrections to (and fluctuations about) the mean need to be considered.

When modelling nutrient uptake by bacteria, Dalwadi et al. (2018) considered a chemical species diffusing through a colony of locally periodic bacteria with a spherical structure and finite size. Bacteria were treated as sinks with the effective uptake described by first-order kinetics and scaling with the bacteria's size. Via a homogenization approach with a relaxed periodicity assumption, it was found how the effective uptake scaled. When the sink volume is of the same order as the inter-sink distance the effective uptake scales with the sink volume for weak uptake and with the surface area for strong uptake. However, when the sink volume is asymptotically small in comparison to the inter-sink distance the effective uptake is bounded above as the uptake rate grows without bound. This approach was extended in Dalwadi and King (2020), where uptake within colonies of bacteria were prescribed by a non-linear function of the solute concentration, with a general partition coefficient being used across the bacterial membrane. It was catalogued how different behaviour on the microscale impact the effective uptake, with different properties sometimes resulting in the same observed uptake. When homogenizing, both studies relax the assumption of a periodic microstructure and consider the influence of spatially varying uptake from sinks. However, neither study considers the impact of disordered bacteria locations or when the two-scale assumption becomes invalid.

The mechanisms of water transport in plant roots sees water being exchanged between earth and roots using a complex three-dimensional root system. This allows for a greater yield of water and nutrients to be transferred between roots and soil (Craine, 2006) and again gives rise to a diverse set of mathematical models that often use multiscale analysis (Marciniak-Czochra and Ptashnyk, 2008; Roose and Schnepf, 2008; Piatnitski and Ptashnyk, 2017; King et al., 2021). Many other notable applications which motivate mathematical models using multiscale analysis for porous media exist. Three examples are the thermal modelling of a porous electrode in a lithium-ion battery (Garcia and Chiang, 2007; Hunt et al., 2020), the nutrient and drug

transport in vascular tumours (Shipley and Chapman, 2010; Jones and Chapman, 2012; Penta and Ambrosi, 2015) and the physics of composite materials (Bakhvalov, 1975; Bensoussan et al., 1978; Zhikov et al., 1979; Chapman and McBurnie, 2011; Anantharaman and Le Bris, 2011). We will now consider the genesis of this thesis and how disordered structures can influence the transport of a solute, which may be of relevance to the examples we have already considered.

1.4 The genesis of this thesis

In the human placenta solute is advected through the IVS within maternal blood and is lost to fetal blood at the site of terminal villi (or vice versa). A variety of complex mathematical problems exist due to the inherent disorder and structure of villous networks (Jensen and Chernyavsky, 2019), where terminal villi have irregular locations with variable uptake strengths and the Péclet number (which gives the ratio of advection to diffusion) is commonly high for a variety of solutes in maternal blood. Models which capture these effects allow the influence of spatial disorder on both the flow and transport of a solute to be quantified.

Chernyavsky et al. (2010) modelled maternal blood flow through the IVS using Darcy's equation, where solute transport is modelled via a homogenized advection-uptake equation with a uniform uptake coefficient. However, oxygen transport in the placenta is sensitive to the geometry of villous trees (Lin et al., 2016). Therefore, in an attempt to quantify the impact of disordered terminal villi locations, Chernyavsky et al. (2011, 2012) reduced villous branches to an array of randomly located point sinks which were distributed along a line, with an advection-diffusion equation describing the solute transport between sinks. Here, each point sink represents the location of a single terminal villus and was prescribed with zeroth-order uptake kinetics (i.e. the solute uptake at sinks was independent of the solute concentration). The studies highlighted errors due to spatial disorder across the porous medium, where fluctuations about the mean showed long-range spatial correlation. Chernyavsky et al. (2012) also showed how error margins depended on the model parameters and statistical properties of the sink distribution, such that if stochastic sink-to-sink variation on the microscale began to dominate the macroscale solution then the homogenization approximation was shown to fail.

Russell et al. (2016) extended the work done in Chernyavsky et al. (2011, 2012) by allowing sinks to have variable strengths (but periodic locations) and first-order kinetics (i.e. uptake depends linearly on the solute concentration). For weak disorder, it was found that individual sink contributions can be evaluated independently using a Green's function, followed by assembling

all contributions using the central limit theorem to demonstrate the overall impact of disordered sink strengths on the solute concentration. The use of a Green's function accommodated variation on both the short and long lengthscales. It was shown that a classical homogenization approach can be a biased estimator of the true mean solute concentration. Following this, Russell and Jensen (2020) used an alternate Green's function approach to find explicit fluctuation predictions to the concentration profiles caused due to both weak and strong disorder of sink locations (but identical sink strengths), making predictions that were valid across large regions of parameter space. This paper again highlighted errors in the mean concentration profile when using the classical approach to homogenization. Chapter 2 of this thesis will aim to further this study by considering when an advection-diffusion balance exists on the microscale (a regime not addressed in Russell and Jensen (2020)), which causes wavy concentration profiles and complicates the evaluation of integrals. The chapter also considers a more extreme limit when advection dominates on the microscale, which leads to concentration boundary-layers forming upstream of each sink, making statistical moments poor descriptors of the solute field.

1.5 Objectives and structure of the thesis

In Chapter 2, a one-dimensional advection-diffusion-uptake model for solute transport will be considered. Uptake of the solute will occur at disordered point sink locations with first-order kinetics, where the strength of each sink is uniformly fixed. The Green's function approach proposed in Russell and Jensen (2020) is used to find corrections to a homogenized solution that account for random sink locations. The model is extended by considering when an advection-diffusion balance exists on the microscale, causing the Green's function to become non-smooth due to an internal boundary layer. Therefore integrals must be solved directly (as opposed to using Riemann sums), a regime which wasn't considered in Russell and Jensen (2020). This non-standard approach proves helpful in characterising the uncertainty in net solute transfer associated with the inherent spatial disorder within porous media by calculating moments of the random concentration fields.

We also consider when advection dominates diffusion on the microscale in Chapter 2, which causes a staircase structure to form within concentration profiles due to boundary layers forming upstream of sink locations. As a result, concentration profiles become non-Gaussian, resulting in moments being poor descriptors of the impact disordered sink locations have on the solute field. An alternative approach is instead developed, which involves calculating the median and credible intervals of the concentration using the cumulative distribution function (cdf) of sink

distributions. This is found to better capture the impact of disordered sink locations on the solute concentration.

A more direct 'moments-based' approach for quantifying the impact of disordered sink locations on the solute concentration is presented for one, two and three dimensions in Chapter 3. This moments-based approach offers a direct mapping between the first two moments of the sink distribution and the first two moments of the solute distribution, where both continuous and discrete sink distributions can be considered. Due to singularities appearing in the Green's function in two and three dimensions, we allow discrete sinks to have a finite width ς. Non-local corrections to a deterministic homogenized solution are sought by successively inverting linear operators using an appropriate Green's function, where a region of influence at a location can be found by inverting this Green's function. For uniformly-random sink locations the mean correction is seen to vary only in the advective direction, with the impact of individual sink locations being smeared out.

In Chapter 4 the moments-based approach is used for a continuous sink distribution represented by a Gaussian process. When the correlation length of the sink function isn't small the corrections to the mean concentration are non-local, meaning a similar approach to Chapter 3 is adopted. However, when the correlation length is small and the mean corrections are more local in character we find replacing the uptake function with an effective uptake parameter becomes sufficient. This is also seen to be sufficient for suitably many discrete, uniformly-random sink locations in two- and three-dimensions.

To finish the thesis, given in Chapter 5 is a summary of the material presented in previous chapters. This includes how each chapter relates to (and differs from) existing literature and concludes with a discussion as to how the work presented in this thesis can be extended for further studies.

Chapter 2

Characterising uncertainty for one-dimensional solute transport in a spatially disordered domain

This chapter will consider a one-dimensional model of solute transport through a disordered medium, as stated in Section 2.1. First, a similar method to that presented in Russell and Jensen (2020) will be developed in Section 2.2.2, which allows corrections to a deterministic homogenized solution to be calculated. The corrections presented are non-distribution specific and will be used to account for both periodic and disordered point sink locations in Section 2.3.2. When sinks have periodic locations a correction to the homogenized solution is explicitly calculated, whereas for random sink locations we examine the moments of the correction to characterise the impact of disorder. This approach, first developed in Russell and Jensen (2020), will be used in a parameter regime that causes concentration profiles to become non-smooth, a regime not previously explored. This leads to boundary-layers appearing in a relevant Green's function which results in non-smooth moments of the concentration.

Following this, in Section 2.2.3 an alternate approach to quantify disorder when transport is advection-dominated is developed. In this regime we see sharp boundary-layers appearing in concentration profiles, which result in statistical moments failing to capture disorder in the concentration adequately. This failure is due to concentration profiles being distributed in a

non-Gaussian manner about the mean. To deal with this, the alternative approach uses a reconstructed staircase to allow credible intervals to be calculated using the cumulative distribution function (cdf) of sink locations. As a result, the cdf credible intervals are shown to better capture the non-Gaussian behaviour of concentration profiles in Section 2.3.3, with the additional benefit of preserving the microscale structures present in individual concentration profiles.

2.1 Model

Consider a one-dimensional model of solute transport in a steady flow past a linear array of N randomly located point sinks. Sinks have prescribed first-order uptake kinetics, with a fixed strength per unit concentration S_0. The sink locations ξ_j^* are ordered $0 \leq \xi_1^* \leq \ldots \leq \xi_N^* \leq L$, where $j = 1, \ldots, N$ and L is the domain length. The average inter-sink distance is denoted by l, with the inlet and outlet positions being assigned at $\xi_0^* = 0$ and $\xi_{N+1}^* = L$ respectively. Let the upstream boundary condition be a prescribed flux $\hat{q}$ and the downstream be zero diffusive flux, where the downstream condition differs from that used in Russell and Jensen (2020) to minimise its influence on solute concentration, thereby allowing the impact of disorder to be better illustrated. By letting D and U be the diffusion coefficient and advection velocity respectively, the concentration $C^*(x^*)$ can be described using the homogeneous, linear, second-order differential equation

$$UC_{x^*}^* = DC_{x^*x^*}^* - \mathrm{S}_0 C^* \sum_{j=1}^{N} \delta(x^* - \xi_j^*), \tag{2.1.1a}$$

with boundary conditions given by

$$(U - D\partial_{x^*})C^*|_{x^*=0} = \hat{q} \quad \text{and} \quad C_{x^*}^*|_{x^*=L} = 0, \tag{2.1.1b}$$

where $0 \leq x^* \leq L$ and δ represents the Dirac delta function (δ-function). Now define the following non-dimensional parameters: $\varepsilon = l/L = 1/(N+1)$ is the inter-sink density, $\mathrm{Pe}_l = Ul/D$ the Péclet number (which represents the strength of advection to diffusion) and $\mathrm{S} = \mathrm{S}_0/U$ represents the strength of uptake to advection. By introducing the dimensionless variables $x = x^*/l$, $\xi_j = \xi_j/l$ and $C(x) = C^*(x^*)/C_0^*$, where $C_0^* = \hat{q}/U$ is a concentration scale, the non-dimensional form of (2.1.1) is given by

$$C_x = \mathrm{Pe}_l^{-1} C_{xx} - \mathrm{S}\, C \sum_{j=1}^{N} \delta(x - \xi_j), \tag{2.1.2a}$$

$$(C - \mathrm{Pe}_l^{-1} C_x)|_{x=0} = 1, \tag{2.1.2b}$$

$$C_x|_{x=\varepsilon^{-1}} = 0, \tag{2.1.2c}$$

where $0 \leq x \leq \varepsilon^{-1}$. Throughout, we will consider the following sink distributions:

1. Periodic configuration, where $\xi_j = j$ for $j = 1, \ldots, N$.

2. Independently normally perturbed from a periodic configuration, where each ξ_j is an ordered value from the normal distribution $\mathcal{N}(j, \sigma^2)$ for $j = 1, \ldots, N$. Here, the variance σ^2 will remain suitably small to ensure the probability of sinks leaving the domain or trading positions is negligible.

3. Order statistics drawn from a uniform distribution, where each ξ_j is an order statistic from $\mathcal{U}(0, \varepsilon^{-1})$ for $j = 1, \ldots, N$. Note here that sink locations are spatially correlated due to ordering, which is unlike independently-drawn uniform variates.

We will now evaluate (2.1.2) using Monte Carlo simulations (Section 2.2.1), the approach to homogenization presented in Russell and Jensen (2020) (Section 2.2.2) and a reconstructed staircase method (Section 2.2.3). Careful consideration will be paid to the multiple spatial scales in the problem, which consist of the inter-sink length l, the domain length L, the variance σ^2 and a boundary-layer width $1/\operatorname{Pe}_l$. It is now instructive to assemble the possible behaviours of the model in various regions of $(\operatorname{Pe}_l, \mathrm{S})$-parameter space.

2.1.1 Asymptotic regimes in $(\operatorname{Pe}_l, \mathrm{S})$-parameter space

Let us find distinct asymptotic regimes in $(\operatorname{Pe}_l, \mathrm{S})$-parameter space which highlight the dominant effects governing concentration profiles. These regimes will be exposed by balancing terms in (2.1.2) over different lengthscales. Consider a homogenized problem where we replace $\sum_{j=1}^{N} \delta(x - \xi_j)$ with 1, which is the approximate spatial average for large N due the there being N sinks distributed in a domain of length $N + 1$. This essentially smears out the impact of individual point sinks and instead represents a continuous removal process occurring throughout the domain. By letting x be of any lengthscale, we see an advection-diffusion balance exists when $x \sim 1/\operatorname{Pe}_l$, an uptake-diffusion balance exists when $x \sim 1/\sqrt{\operatorname{Pe}_l \, \mathrm{S}}$, an advection-uptake balance exists when $x \sim 1/\mathrm{S}$ and an advection-uptake-diffusion balance exists when $\operatorname{Pe}_l \sim \mathrm{S}$. Table 2.1 summarises this, along with when x varies over the macroscale and microscale, which can be seen by considering x varying over the domain length ($x \sim \varepsilon^{-1}$) and over the inter-sink distance ($x \sim 1$) respectively.

A depiction of the asymptotic regions in $(\operatorname{Pe}_l, \mathrm{S})$-parameter space is shown in Figure 2.1(a). Three distinguished limits (1), (2) and (3) are marked, representing when asymptotic boundaries meet, along with two additional markers showing when an advection-uptake balance exists

	lengthscale	Microscale ($x \sim 1$)	Macroscale ($x \sim \varepsilon^{-1}$)
A-D balance	$x \sim 1/\mathrm{Pe}_l$	$\mathrm{Pe}_l \sim 1$	$\mathrm{Pe}_l \sim \varepsilon$
U-D balance	$x \sim 1/\sqrt{\mathrm{Pe}_l\,\mathrm{S}}$	$\mathrm{Pe}_l\,\mathrm{S} \sim 1$	$\mathrm{Pe}_l\,\mathrm{S} \sim \varepsilon^2$
A-U balance	$x \sim 1/\mathrm{S}$	$\mathrm{S} \sim 1$	$\mathrm{S} \sim \varepsilon$
A-U-D balance	$\mathrm{Pe}_l \sim \mathrm{S}$	$(\mathrm{Pe}_l, \mathrm{S}) \sim (1, 1)$	$(\mathrm{Pe}_l, \mathrm{S}) \sim (\varepsilon, \varepsilon)$

Table 2.1: Table containing the required balances of parameters for different effects to dominate, where A, U and D represent advection, diffusion and uptake respectively.

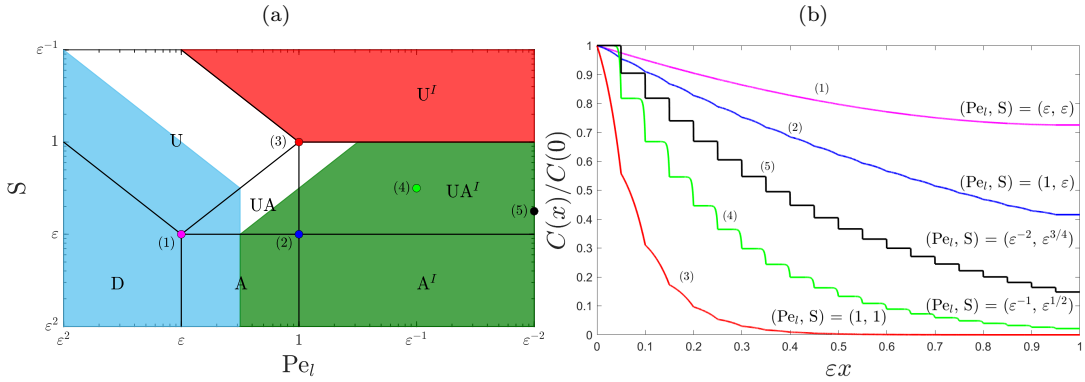

Figure 2.1: (a) Depiction of asymptotic regions in $(\mathrm{Pe}_l, \mathrm{S})$-parameter space, where $\varepsilon \ll 1$. D, A, U and UA represent regions where diffusion, advection, uptake and both advection and uptake dominate over the domain length respectively, with diffusion dominating on the inter-sink length. Alternatively, A^I, U^I and UA^I represent regions where advection, uptake and both advection and uptake dominate on the domain and inter-sink length respectively. The blue region shows the area of parameter space considered in Russell and Jensen (2020). The green region shows the area of parameter space considered in this chapter. The red region shows when the homogenized solution found in Section 2.2.2 is seen to fail (Chernyavsky et al., 2011). (b) Different concentration profiles for varying values of Pe_l and S, which correspond to markers (1) - (5) in figure (a). Each profile is scaled using the concentration at the inlet ($C(0)$) and is calculated using the numerical method outlined in Appendix A.1 with $N = 19$ periodically located point sinks (i.e. $\varepsilon = 0.05$).

on the macroscale, but advection dominates on the microscale (Markers (4) and (5)). Concentration profiles corresponding to each of these markers can be seen in Figure 2.1(b). If $(\mathrm{Pe}_l, \mathrm{S}) \sim (\varepsilon, \varepsilon)$ (Marker (1)), diffusion dominates on the microscale with an advection-diffusion-uptake balance on the macroscale. This regime was studied extensively in Russell and Jensen (2020) and has smoothly varying concentration profiles throughout the domain, as can be seen in Figure 2.1(b).

A distinguished limit exists when $(\mathrm{Pe}_l, \mathrm{S}) \sim (1, \varepsilon)$ (Marker (2)), where an advection-uptake balance exists on the macroscale with an advection-diffusion balance on the microscale, see Table 2.1. When $(\mathrm{Pe}_l, \mathrm{S}) \sim (1, 1)$ (Marker (3)) all effects balance on the microscale, but as

uptake is dominant on the macroscale the concentration falls rapidly from the inlet. In both of these regimes the advection-diffusion balanced on the microscale causes concentration profiles to become non-smooth with a wavy sink-to-sink structure appearing, as shown in Figure 2.1(b).

Two alternate examples are marked in Figure 2.1(a), which are $(\mathrm{Pe}_l, \mathrm{S}) \sim (\varepsilon^{-1}, \varepsilon^{1/2})$ (Marker (4)) and $(\mathrm{Pe}_l, \mathrm{S}) \sim (\varepsilon^{-2}, \varepsilon^{3/4})$ (Marker (5)). Both examples have advection dominating diffusion on the microscale, which causes boundary-layers to form upstream of each sink and results in a sink-to-sink 'staircase' structure appearing, as shown in Figure 2.1(b). At (4) the boundary-layers have finite width due to the impact of diffusion, whereas at (5) there is a jump in concentration at each sink location demonstrating that the impact of diffusion is negligible. One feature of note which is highlighted in Figure 2.1(b) is the multiscale nature of the problem over the $(\mathrm{Pe}_l, \mathrm{S})$-parameter space.

2.2 Methods

Here, an outline of methods used to produce the results in Section 2.3 will be shown. First, a numerical approach to evaluating (2.1.2) will be presented, which can be used to calculate multiple realisations with statistical properties being extracted from resulting data sets. Following this, the non-standard homogenization approach in Russell and Jensen (2020) will be extended by considering the distinguished limit where $(\mathrm{Pe}_l, \mathrm{S}) \sim (1, \varepsilon)$. This approach finds corrections to a homogenized solution using a Green's function, which in turn captures the system's inherent disorder through evaluating the moments of corrections. One advantage to using this homogenization approach over a classical one is the ability to capture boundary-layers that appear in concentration profiles. This is because assumptions of two-scale dependence or unit-cell periodicity are not required. Section 2.3 will later compare results with Monte Carlo simulations (see Appendix A.1) and a classical approach to homogenization (see Appendix A.2) to assess their validity.

We then investigate the region of parameter space where advection dominates diffusion on the microscale. This causes a staircase structure to be exhibited in concentration profiles, meaning moments of the concentration become poor descriptors of disorder due to the non-Gaussian distribution of concentration profiles about the mean. Therefore a reconstructed staircase approach is used, which calculates credible intervals using the cumulative distribution function of sink locations. Throughout Section 2.3 we will compare results with sample moments from Monte Carlo realisations to assess the validity of approximations.

2.2.1 Monte Carlo realisations

To produce concentration profiles numerically, we reduce the governing equations in (2.1.2) to a system of linear algebraic equations. These are solved for a given sink distribution to generate multiple realisations for concentration profiles. Note that (2.1.2a) can be re-written as an advection-diffusion equation when in-between sinks, along with a jump condition at sink locations to account for uptake. So by using the methodology outlined in Appendix A.1, we find the concentration is given by

$$C(x) = A_j e^{\mathrm{Pe}_l\,(x-\xi_j)} + B_j, \tag{2.2.1}$$

where A_j and B_j are constants to be found via solving the linear system given in (A.1.6). One method of solving (A.1.6) is via LU factorisation, as described in Higham (2002), which allows many realisations of concentration profiles to be calculated. Statistical properties extracted from these realisations will be used throughout Chapter 2 to allow for comparison and validation of the analytic approach.

2.2.2 Constructing an expansion

We will now outline an approach for predicting the moments of the concentration when in the critical limit $(\mathrm{Pe}_l, \mathrm{S}) \sim (1, \varepsilon)$. A similar method to Russell and Jensen (2020) will be adopted, where a homogenized solution $C_H(x)$ will first be calculated to describe the leading-order behaviour of the concentration field but will neglect the impact of point sinks. Accordingly, a Green's function $G(x, y)$ will be sought, which describes the impact of introducing a sink to the system at a location $x = y$. This Green's function will allow contributions from multiple lengthscales to be included, which is shown to be of great importance when in the limit $(\mathrm{Pe}_l, \mathrm{S}) \sim (1, \varepsilon)$. Corrections to the homogenized solution are then sought to account for both the system's microscale structure and stochastic variation, which are found by rationally approximating integrals with the appropriate Green's function.

An alternative method of approaching this problem is via a classical homogenization approach, which is given in Appendix A.2 and outlined in Davit et al. (2013). This can be used to calculate the leading-order behaviour of the concentration field in a periodic medium. However, drawbacks exist when using this method due to the assumptions of two-scale dependence and unit-cell periodicity. When a system has multiple lengthscales, such as when boundary-layers are present, it is difficult to reconcile Neumann boundary conditions (Dumontet, 1986) which can result in the classical approach becoming insufficient. Another drawback is the inability to

account for the system's inherent disorder. The stochastic nature of this system can cause large variation in concentration profiles, as shown in Figure 2.5 below, which motivates the need for an alternate approach.

Homogenized solution

Let $C_H(x)$ satisfy a homogenized analogue of (2.1.2). Define linear and boundary operators $\mathcal{L} = \mathrm{Pe}_l^{-1}\,\partial_{xx} - \partial_x - \mathrm{S}$ and $\mathcal{B} = \{(1 - \mathrm{Pe}_l^{-1}\,\partial_x)(\cdot)|_{x=0}, \partial_x(\cdot)|_{x=\varepsilon^{-1}}\}$ respectively. Then the homogenized problem can be stated as

$$\mathcal{L}C_H = 0 \quad \text{and} \quad \mathcal{B}C_H = \{1, 0\}, \tag{2.2.2}$$

where $0 \leq x \leq \varepsilon^{-1}$. The exact solution of (2.2.2) is given by

$$C_H(x) = \frac{\mathrm{Pe}_l}{W(\varepsilon^{-1})} e^{\frac{1}{2}\,\mathrm{Pe}_l\,x} \left((2\phi - \mathrm{Pe}_l) e^{\phi\left(x-\varepsilon^{-1}\right)} + (2\phi + \mathrm{Pe}_l) e^{-\phi\left(x-\varepsilon^{-1}\right)} \right), \tag{2.2.3}$$

where $\phi = \sqrt{\mathrm{Pe}_l^2\,/4 + \mathrm{Pe}_l\,\mathrm{S}}$ and $W(x)$ is given by

$$W(x) = (2\,\mathrm{Pe}_l\,\phi + \mathrm{Pe}_l^2 + 2\,\mathrm{Pe}_l\,\mathrm{S}) e^{\phi x} + (2\,\mathrm{Pe}_l\,\phi - \mathrm{Pe}_l^2 - 2\,\mathrm{Pe}_l\,\mathrm{S}) e^{-\phi x}. \tag{2.2.4}$$

Consider when there exists an advection-diffusion balance on the microscale and an advection-uptake balance on the macroscale, i.e. when $(\mathrm{Pe}_l, \mathrm{S}) \sim (1, \varepsilon)$. Within this limit, we will aim to capture the leading-order behaviour of the homogenized solution as ε becomes asymptotically small. Insight is sought into how the solution varies as x and ε vary, along with preventing any round-off errors appearing within the system due to exponentially large terms.

A composite asymptotic expansion of the homogenized solution is given in Appendix A.3, which uses the scaling $x = \mathcal{O}(\varepsilon^{-1})$, $\mathrm{Pe}_l = \mathcal{O}(1)$ and $\mathrm{S} = \mathcal{O}(\varepsilon)$. This proves to be a non-trivial process as careful analysis is required to ensure effects from all lengthscales are considered, which is essential to ensure a boundary-layer at the outlet is accommodated. The results in Appendix A.3 approximates the homogenized solution to be

$$C_H(x) \approx \left(1 + \frac{\mathrm{S}}{\mathrm{Pe}_l} \left(\mathrm{S}x - 1 + f_2\left(x - \varepsilon^{-1}\right) \right) \right) f_1(-x), \tag{2.2.5}$$

where $\mathcal{O}(\varepsilon^2)$ terms are neglected and

$$f_1(x) = \exp\left(\mathrm{S}x\right) \quad \text{and} \quad f_2(x) = \exp\left((\mathrm{Pe}_l + 2\mathrm{S})\, x \right), \tag{2.2.6}$$

with strict asymptotic limits not being distinguished from approximations within this chapter. This expression is uniformly valid throughout the domain, including at the outlet where a diffusive boundary-layer of thickness $1/\,\mathrm{Pe}_l$ exists. This can be seen by considering $x \to \varepsilon^{-1}$ in

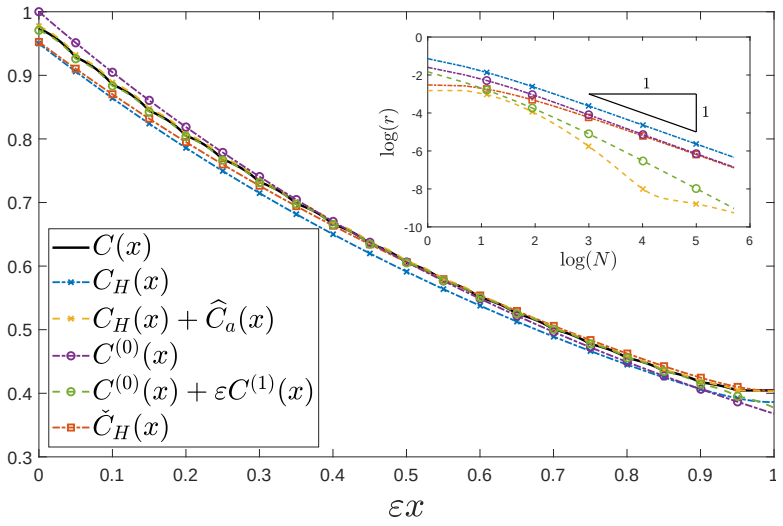

Figure 2.2: Comparison between the numerical solution of (2.1.2) [$C(x)$, solid black], the asymptotic approximation of the homogenized solution [$C_H(x)$, given in (2.2.5), dot-dashed blue], the use of a correction term which accounts for a periodic sink distribution [$C_H(x) + \widehat{C}_a(x)$, given in (2.2.5) and (2.3.1), dashed yellow], the leading-order solution using a classical approach to homogenization [$C^{(0)}(x)$, given in (A.2.6), dot-dashed purple], the second-order solution using a classical approach to homogenization [$C^{(0)}(x)+\varepsilon C^{(1)}(x)$, given in (A.2.6) and (A.2.13), dashed green] and the homogenized solution calculated by replacing $\sum_{j=1}^{N} \delta(x-\xi_j)$ with the exact spatial average $N/(N+1)$ [$\check{C}_H$, calculated by replacing S with $(N/(N+1))$S in 2.2.5, dot-dashed red]. Here, $N = 19$ periodic point sinks are used (i.e. $\varepsilon = 0.05$) and $(\mathrm{Pe}_l, \mathrm{S}) = (1, \varepsilon)$. Depicted in the inset is the relative error between each approximation and the numerical solution using (2.2.7), where $N \in \{1, \ldots, 300\}$.

the $f_2(x - \varepsilon^{-1})$ term, which results from the downstream boundary condition. It is here worth noting that $f_i(a)f_i(b) = f_i(a+b)$ for $i = 1, 2$, a property which is exploited throughout when performing simplifications.

A comparison of the homogenized solution given in (2.2.5) to a numerical approximation of the concentration found using (A.1.5) for $N = 19$ periodic sink locations can be seen in Figure 2.2, where $(\mathrm{Pe}_l, \mathrm{S}) = (1, \varepsilon)$ is used. In this regime we see concentration boundary-layers forming upstream of each sink, which causes a wavy sink-to-sink structure to form. However, this is not captured in the homogenized solution as an averaged sink strength is used. Despite this, the peripheral boundary-layer at $x = \varepsilon^{-1}$ is captured, which is present due to the zero diffusive flux boundary condition at the outlet. This is in contrast to the leading-order solution found when using a classical approach to homogenization ($C^{(0)}(x)$, given in (A.2.6)), which does not capture the boundary-layer at the outlet.

To numerically validate each approximation of the solute concentration, consider the point-wise

relative error r when comparing two vectors $\mathbf{a}$ and $\mathbf{b}$, with r being given by

$$r(\mathbf{a}, \mathbf{b}) = \frac{|\mathbf{a} - \mathbf{b}|}{|\mathbf{a}|}. \tag{2.2.7}$$

The inset of Figure 2.2 shows the relative errors of each approximation to the numerical solution of (2.1.2), which are calculated using the vector positions of each approximation with $N \in \{1, \dots, 300\}$ sink locations. All errors are shown to decrease on a logarithmic scale as N increases (i.e. ε decreases), demonstrating each approach converging to the numerical solution. When using the leading-order approximations $C_H(x)$ (given in (2.2.5)) and $C^{(0)}(x)$ (given in (A.2.6)) this convergence is seen to be linear on the logarithmic scale. Although both solutions converge to the numerical solution at the same rate, the classical approach is seen to have a smaller relative error, despite not capturing the boundary-layer seen at the outlet (which can be seen in Figure 2.2). This is due to the homogenized solution over-predicting the uptake strength when replacing the sink function $\sum_{j=1}^{N} \delta(x-\xi_j)$ with an approximate spatial average of 1. When replacing the sink function with the exact spatial average $N/(N+1)$, as represented by $\check{C}_H$, the error for the homogenized solution is seen to be smaller than that of the classical approach. Here, $\check{C}_H$ is calculated by replacing S with $(N/(N+1))$S in (2.2.5). Using $\check{C}_H$ as opposed to $C^{(0)}$ has a greater difference for small N, which is due to the downstream boundary-layer having a greater impact when the domain size $\varepsilon^{-1} = N+1$ is smaller. Despite the homogenized solution given in (2.2.5) using an approximate spatial average, the effects caused by the sink function are still captured in the approximation $\widehat{C}_a$, which is calculated later. This is seen by the relative error $r(C, C_H + \widehat{C}_a)$, which is smaller in comparison to the second-order classical solution given by $r(C, C^{(0)} + \varepsilon C^{(1)})$ and is discussed further in Section 2.3.2.

We will now seek to find a Green's function $G(x, y)$ which will describe the impact of introducing a single point sink to the system at a location $x = y$. The resulting function will later be used to invert linear operators and allow corrections to the homogenized solution to be found, which will account for both periodic and disordered sink locations.

Green's function

Let $G(x, y)$ be a Green's function associated with the linear operator $\mathcal{L}$ under homogeneous boundary conditions such that

$$\mathcal{L}G = \delta(x - y) \quad \text{and} \quad \mathcal{B}G = \{0, 0\}, \tag{2.2.8}$$

where δ is the Dirac-delta function. The Green's function is piecewise smooth, continuous and satisfies the jump condition $[G_x]_{y^-}^{y^+} = 1/\operatorname{Pe}_l$, which accounts for a point sink being located at

$x = y$. This jump condition can be seen by integrating (2.2.8) inside a vanishing region about $x = y$ and using the fact that $G(x, y)$ is continuous. Define $G^-(x, y)$ and $G^+(x, y)$ such that

$$G(x,y) = \begin{cases} G^-(x,y) & \text{if } 0 \le x \le y \le \varepsilon^{-1}, \\ G^+(x,y) & \text{if } 0 \le y \le x \le \varepsilon^{-1}. \end{cases} \tag{2.2.9}$$

Then by solving (2.2.8), we see that the two pieces of the Green's function are given by

$$G^-(x,y) = -\frac{\mathrm{Pe}_l}{4\phi W(\varepsilon^{-1})} e^{\frac{1}{2}\mathrm{Pe}_l(x-y)} \Bigg((2\phi + \mathrm{Pe}_l)^2 e^{\phi(x-y+\varepsilon^{-1})} + (2\phi - \mathrm{Pe}_l)^2 e^{-\phi(x-y+\varepsilon^{-1})} + 4\,\mathrm{Pe}_l\,\mathrm{S}\left(e^{\phi(x+y-\varepsilon^{-1})} + e^{-\phi(x+y-\varepsilon^{-1})}\right)\Bigg), \tag{2.2.10a}$$

$$G^+(x,y) = -\frac{\mathrm{Pe}_l}{4\phi W(\varepsilon^{-1})} e^{\frac{1}{2}\mathrm{Pe}_l(x-y)} \Bigg((2\phi + \mathrm{Pe}_l)^2 e^{\phi(y-x+\varepsilon^{-1})} + (2\phi - \mathrm{Pe}_l)^2 e^{-\phi(y-x+\varepsilon^{-1})} + 4\,\mathrm{Pe}_l\,\mathrm{S}\left(e^{\phi(x+y-\varepsilon^{-1})} + e^{-\phi(x+y-\varepsilon^{-1})}\right)\Bigg), \tag{2.2.10b}$$

where the function W is given in (2.2.4). In a similar fashion to the homogenized solution, a leading-order asymptotic approximation to the Green's function in the limit where $\mathrm{Pe}_l = \mathcal{O}(1)$ and $\mathrm{S} = \mathcal{O}(\varepsilon)$ can be found. This is done in Appendix A.3, which gives a uniformly valid composite asymptotic expansion of the Green's function using the scaling $x = \mathcal{O}(\varepsilon^{-1})$, $y = \mathcal{O}(\varepsilon^{-1})$, $\mathrm{Pe}_l = \mathcal{O}(1)$ and $\mathrm{S} = \mathcal{O}(\varepsilon)$. Careful consideration is again used to ensure contributions from all lengthscales are included, giving the two pieces of the Green's function as

$$G^-(x,y) \approx \left(-1 + \frac{\mathrm{S}}{\mathrm{Pe}_l}\left(2 + \mathrm{S}(x-y) - f_2(-x) - f_2(y-\varepsilon^{-1})\right)\right) f_1(y-x) f_2(x-y), \tag{2.2.11a}$$

$$G^+(x,y) \approx \left(-1 + \frac{\mathrm{S}}{\mathrm{Pe}_l}\left(2 + \mathrm{S}(y-x) - f_2(-x) - f_2\left(x-\varepsilon^{-1}\right)\right)\right) f_1(y-x), \tag{2.2.11b}$$

where $\mathcal{O}(\varepsilon^2)$ terms have been neglected and the functions f_1 and f_2 are given in (2.2.6). It can be seen that (2.2.11) preserves the symmetry from the exact Green's function by remaining invariant under reflection in the line $x + y = \varepsilon^{-1}$.

Figure 2.3 depicts a contour plot of the piecewise Green's function using (2.2.11). This demonstrates the two peripheral boundary-layers located at $x = \varepsilon^{-1}$ and $y = 0$, as well as an internal boundary-layer located at $x = y$, which are given in (2.2.11) by the terms $f_2\left(x - \varepsilon^{-1}\right)$, $f_2(y)$ and $f_2(x-y)$ respectively. It can be seen that the introduction of a point sink at $x = y$ has little effect upstream of the internal boundary-layer, but the influence of the boundary-layer is swept downstream to the outlet. The inherent non-uniformity of the problem is demonstrated here,

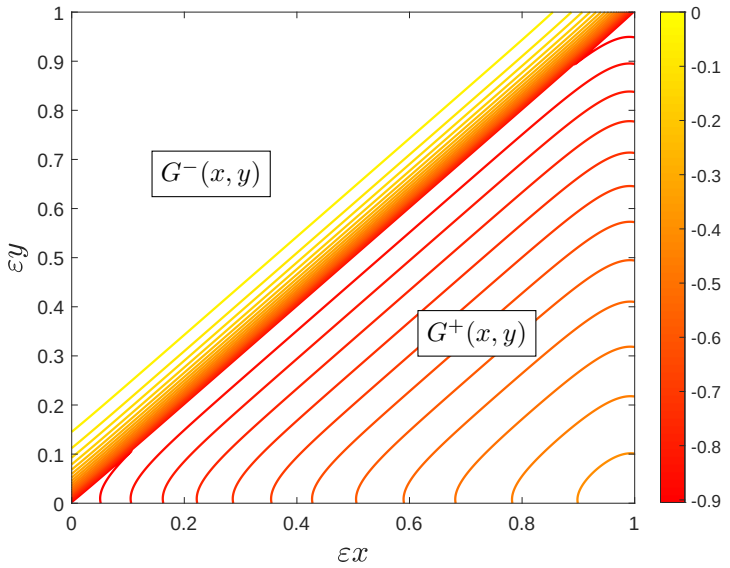

Figure 2.3: A contour plot of the Green's function $[G(x,y)]$ using the leading-order approximation given in (2.2.11), where $(\mathrm{Pe}_l, \mathrm{S}) = (1, \varepsilon)$ and $\varepsilon = 0.05$ are used.

as there exists a discontinuity at $x = y$ which causes the function to be non-smooth, as well as internal and peripheral boundary-layers appearing within the domain. The leading-order expressions of $G^-(x,y)$ and $G^+(x,y)$ can now be used to find a perturbation correction to the homogenized solution, which will account for both periodic and disordered sink locations.

Corrections to the homogenized solution

We pose an expansion of the concentration by writing

$$C(x) = C_H(x) + \widehat{C}(x), \tag{2.2.12}$$

where $C_H(x)$ is the homogenized solution and $\widehat{C}(x)$ contains a series of correction terms. This correction term can account for both periodic and disordered sink locations by being expressed as

$$\begin{aligned}\mathcal{L}\widehat{C}(x) = \mathrm{S}\Bigg(& C_H(x)\left(\sum_{j=1}^{N}\delta(x-j)-1\right) + C_H(x)\sum_{j=1}^{N}\left(\delta(x-\xi_j)-\delta(x-j)\right) \\ & +\widehat{C}(x)\left(\sum_{j=1}^{N}\delta(x-j)-1\right) + \widehat{C}(x)\sum_{j=1}^{N}\left(\delta(x-\xi_j)-\delta(x-j)\right)\Bigg)\end{aligned} \tag{2.2.13}$$

(Russell and Jensen, 2020), where $\mathcal{L}$ is the linear operator given earlier. As (2.2.13) is linear we can consider the solution of each sub-problem associated with the right-hand side of (2.2.13)

independently. Let the first sub-problem be given by

$$\mathcal{L}\widehat{C}_a(x) = \mathrm{S}C_H(x)\left(\sum_{j=1}^{N}\delta(x-j)-1\right), \quad \mathcal{B}\widehat{C}_a = \{0,0\}, \tag{2.2.14}$$

where $\mathcal{B}$ is the boundary operator given earlier. This transport problem models the difference between a periodic sink arrangement and a smooth sink distribution, with strengths modulated by $C_H(x)$. By use of the Green's function the solution can be written as

$$\widehat{C}_a(x) = \mathrm{S}\int_0^{\varepsilon^{-1}} G(x,y)C_H(y)\left(\sum_{j=1}^{N}\delta(y-j)-1\right)\mathrm{d}y, \tag{2.2.15}$$

which gives the leading-order dominant correction of the homogenized solution due to discrete periodic sink effects.

Consider now the sub-problem given by

$$\mathcal{L}\widehat{C}_b(x) = \mathrm{S}C_H(x)\sum_{j=1}^{N}(\delta(x-\xi_j)-\delta(x-j)), \quad \mathcal{B}\widehat{C}_b = \{0,0\}. \tag{2.2.16}$$

This represents the effect of displacing sinks from periodic locations to a disordered arrangement, with strengths again given by $C_H(x)$. By exploiting the Green's function, the solution can be written as

$$\widehat{C}_b(x) = \mathrm{S}\int_0^{\varepsilon^{-1}} G(x,y)C_H(y)\sum_{j=1}^{N}(\delta(y-\xi_j)-\delta(y-j))\,\mathrm{d}y. \tag{2.2.17}$$

Then using $\int_a^c f(x,y)\delta(y-b)\,\mathrm{d}y = f(x,b)$, which holds for some continuous function $f(x,y)$ where $a \le b \le c$, we obtain

$$\widehat{C}_b(x) = \mathrm{S}\sum_{j=1}^{N}\left(G(x,\xi_j)C_H(\xi_j) - G(x,j)C_H(j)\right). \tag{2.2.18}$$

This gives the leading-order dominant correction of the homogenized solution due to discrete disordered sink effects.

We will now recursively carry out this argument to obtain

$$C(x) = C_H(x) + (\widehat{C}_a + \widehat{C}_b) + (\widehat{C}_{aa} + \widehat{C}_{ab} + \widehat{C}_{ba} + \widehat{C}_{bb}) + \ldots, \tag{2.2.19}$$

where the second-order corrections to the homogenized solution are given by the sub problems

$$\mathcal{L}\widehat{C}_{aa}(x) = \mathrm{S}\widehat{C}_a(x)\left(\sum_{j=1}^{N}\delta(x-j)-1\right), \quad \mathcal{L}\widehat{C}_{ab}(x) = \mathrm{S}\widehat{C}_a(x)\sum_{j=1}^{N}(\delta(x-\xi_j)-\delta(x-j)),$$

$$\mathcal{L}\widehat{C}_{ba}(x) = \mathrm{S}\widehat{C}_b(x)\left(\sum_{j=1}^{N}\delta(x-j)-1\right), \quad \mathcal{L}\widehat{C}_{bb}(x) = \mathrm{S}\widehat{C}_b(x)\sum_{j=1}^{N}(\delta(x-\xi_j)-\delta(x-j)),$$

with $\mathcal{B}\widehat{C}_{\alpha,\beta} = \{0,0\}$ for $\alpha,\beta \in \{a,b\}$. Results illustrating the use of the correction $\widehat{C}_a$ for periodically located point sinks will be shown in Section 2.3.2. Following this, the correction $\widehat{C}_b$ will be calculated for two examples of sink distributions; normally perturbed from a periodic configuration and order statistics from a uniform distribution.

2.2.3 Advection-dominated solute transport

Consider when the Péclet number becomes asymptotically large, causing advection to dominate diffusion on the microscale. This occurs when $\mathrm{Pe}_l \gg 1$ (see Figure 2.1(a)) and leads to a staircase structure appearing in concentration profiles due to the boundary-layer thickness $1/\mathrm{Pe}_l$ becoming asymptotically small (see Figure 2.1(b)). Prescribe the concentration upstream and downstream of the sink ξ_j to be C_{j-1} and C_j respectively, as depicted in Figure 2.4. Note that, when away from sink locations (i.e. $x \neq \xi_j$), (2.1.2a) gives $C_{xx} - \mathrm{Pe}_l\, C_x = 0$. Therefore the concentration in the region of a sink ξ_j is given by

$$C(x) = \begin{cases} A_{j-1} + B_{j-1} e^{\mathrm{Pe}_l (x-\xi_j)} & \text{for } x \leq \xi_j, \\ A_j + B_j e^{\mathrm{Pe}_l (x-\xi_j)} & \text{for } x \geq \xi_j, \end{cases} \tag{2.2.20}$$

where $j = 1,\ldots,N$ and A_i and B_i are constants from integration for $i = 0,\ldots,N$. We will now consider the governing equations in (2.1.2) to obtain a jump condition for each sink ξ_j. Integrating (2.1.2a) inside a vanishing region about ξ_j and using the prescribed concentration obtains the jump condition as $[\![C_x]\!]_{x=\xi_j} = \mathrm{Pe}_l\, \mathrm{S}\, C(\xi_j)$. Note that $C \to C_{j-1}$ and $C \to C_j$ for $x \ll \xi_j$ and $x \gg \xi_j$ respectively, which gives $A_{j-1} = C_{j-1}$, $A_j = C_j$ and $B_j = 0$. Then as the concentration is continuous at $x = \xi_j$ we obtain $B_{j-1} = C_j - C_{j-1}$. Therefore, by using the jump condition $[\![C_x]\!]_{x=\xi_j} = \mathrm{Pe}_l\, \mathrm{S}\, C(\xi_j)$, we obtain the height of each jump from C_{j-1} to C_j to be of the size $C_j - C_{j-1} = -\mathrm{S}C_j$. This gives the relationship $C_j = (1+\mathrm{S})^{-1} C_{j-1}$, which can be applied recursively to give $C_j = (1+\mathrm{S})^{-j} C_0$. So using (2.2.20) we obtain the concentration in the region of a sink ξ_j as

$$C(x) = \begin{cases} C_0 (1+\mathrm{S})^{-j} \left(1 + \mathrm{S} - \mathrm{S} e^{\mathrm{Pe}_l (x-\xi_j)}\right) & \text{for } x \leq \xi_j, \\ C_0 (1+\mathrm{S})^{-j} & \text{for } x \geq \xi_j, \end{cases}$$

where the boundary-layer is contained in the exponential term and can be seen to have a thickness $1/\mathrm{Pe}_l$. This can be used to express the concentration globally as

$$\begin{aligned} C(x) =& C_0 \sum_{j=1}^{N} (1+\mathrm{S})^{-j} \left(1 + \mathrm{S} - \mathrm{S} e^{\mathrm{Pe}_l (x-\xi_j)}\right) \left(H(x-\xi_{j-1}) - H(x-\xi_j)\right) \\ &+ C_0 (1+\mathrm{S})^{-N} H(x-\xi_N), \end{aligned}$$

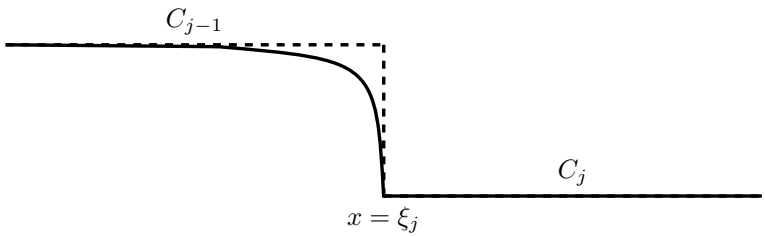

Figure 2.4: Depiction of a concentration profile in the vicinity of one point sink $x = \xi_j$, where the concentration upstream and downstream of the sink are given by C_{j-1} and C_j respectively. The solid line represents when diffusion is still present, whereas the dashed line represents when diffusion is negligible, causing the boundary-layer thickness to become infinitesimally small.

where $H(x - \xi_j)$ represents the Heaviside function such that $H(x - \xi_j) = 0$ for $x < \xi_j$ and $H(x-\xi_j) = 1$ for $x \geq \xi_j$. By gathering terms of $H(x-\xi_j)$ which do not contain the exponential term, this can be rearranged to give

$$C(x) = C_0 - C_0 \mathrm{S} \sum_{j=1}^{N} (1 + \mathrm{S})^{-j} \left(H(x - \xi_j) + e^{\mathrm{Pe}_l (x-\xi_j)} (H(x - \xi_{j-1}) - H(x - \xi_j)) \right). \quad (2.2.21)$$

When there is zero diffusion the boundary-layer thickness becomes infinitesimally small due to the Péclet number becoming infinitely large. This limit is represented by the dotted line in Figure 2.4, with (2.2.21) giving the global concentration as

$$C(x) = C_0 - C_0 \mathrm{S} \sum_{j=1}^{N} (1 + \mathrm{S})^{-j} H(x - \xi_j). \quad (2.2.22)$$

This shows a jump in concentration at each sink location, represented as a Heaviside function. We will now consider two ways to quantify the effects of sink disorder on the solute concentration (2.2.22); a standard mean and variance (moments-based) approach for when there is zero diffusion and an alternative cdf credible-interval approach.

Calculating moments in the absence of diffusion

The mean and variance of the concentration when there is zero diffusion can be calculated by considering the probability of being at a particular discrete concentration $C_j = (1 + \mathrm{S})^{-j} C_0$. For a sink distribution with a cumulative distribution function (cdf) $F_{\xi_j}(x) = \mathbb{P}(\xi_j \leq x)$, the

probability of being at a given concentration for some given x is

$$\begin{aligned}
\mathbb{P}(C_0; x) &= \mathbb{P}(\xi_1 > x) = 1 - F_{\xi_1}(x), \\
\mathbb{P}(C_1; x) &= \mathbb{P}(\xi_1 < x < \xi_2) = F_{\xi_1}(x) - F_{\xi_2}(x), \\
&\vdots \\
\mathbb{P}(C_{N-1}; x) &= \mathbb{P}(\xi_{N-1} < x < \xi_N) = F_{\xi_{N-1}}(x) - F_{\xi_N}(x), \\
\mathbb{P}(C_N; x) &= \mathbb{P}(\xi_N < x) = F_{\xi_N}(x).
\end{aligned}$$

Therefore the expectation can be calculated using $\mathbb{E}[C(x)] = C_0\mathbb{P}(C_0; x) + \cdots + C_N\mathbb{P}(C_N; x)$ to give

$$\mathbb{E}[C(x)] = C_0(1 - F_{\xi_1}(x)) + \sum_{j=1}^{N-1} C_j(F_{\xi_j}(x) - F_{\xi_{j-1}}(x)) + C_N F_{\xi_N}(x),$$

which can be rearranged to obtain

$$\mathbb{E}[C(x)] = C_0 + \sum_{j=1}^{N}(C_j - C_{j-1})F_{\xi_j}(x). \tag{2.2.23}$$

We can calculate the variance in a similar fashion by using $\mathrm{Var}[C(x)] = (C_0)^2\mathbb{P}(C_0; x) + \cdots + (C_N)^2\mathbb{P}(C_N; x) - (C_0\mathbb{P}(C_0; x) + \cdots + C_N\mathbb{P}(C_N; x))^2$, which gives

$$\mathrm{Var}[C(x)] = (C_0)^2 + \sum_{j=1}^{N}((C_j)^2 - (C_{j-1})^2)F_{\xi_j}(x) - (C_0 + \sum_{j=1}^{N}(C_j - C_{j-1})F_{\xi_j}(x))^2,$$

which can be simplified to give

$$\mathrm{Var}[C(x)] = \sum_{j=1}^{N}\left(C_j + C_{j-1} - 2C_0 - \sum_{i=1}^{N}(C_i - C_{i-1})F_{\xi_i}(x)\right)(C_j - C_{j-1})F_{\xi_j}(x). \tag{2.2.24}$$

These will later be evaluated in Section 2.3.3 for the two previously described examples; when sinks are normally perturbed from a periodic configuration and when their locations represent order statistics taken from a uniform distribution. However, it is later shown that moments offer a poor prediction of disorder when solute concentrations are distributed in a non-Gaussian manner about the mean. We will therefore next consider calculating credible intervals based on the cdf of the concentration when there is zero diffusion.

Calculating credible intervals in the absence of diffusion

The cdf credible intervals for the concentration give a region where a fixed percentage of concentration profiles lie. This can be advantageous over a direct approach of calculating Gaussian-based credible intervals (involving the mean and standard deviation) as it captures non-Gaussian behaviour within concentration profiles. To calculate cdf credible intervals when there is zero

diffusion, we must first calculate the cdf of a concentration C_j, which is given by

$$F_{C_j}(C) = \mathbb{P}(C_j \leq C(x); x) = \mathbb{P}(\xi_j > x) = 1 - F_{\xi_j}(x) \tag{2.2.25}$$

for $j = 1, \ldots, N$. Let the cdf of C_j take a value $F_{C_j}(C) = r$, then (2.2.25) can be inverted to give the corresponding sink locations as

$$\breve{\xi}_j = F_{\xi_j}^{-1}(1 - r), \tag{2.2.26}$$

where $F_{\xi_j}^{-1}$ denotes the inverse of the cdf. We can therefore use the concentration expression given in (2.2.22) to find the cdf credible intervals as

$$CI(x; r) = C_0 - C_0 \mathrm{S} \sum_{j=1}^{N} (1 + \mathrm{S})^{-j} H\left(x - F_{\xi_j}^{-1}(1 - r)\right). \tag{2.2.27}$$

To produce a credible interval which ensures 95% of concentration profiles are contained between the two bounds, we can consider when $r = 0.025$ and $r = 0.975$ in (2.2.27), where using $r = 0.5$ in (2.2.27) will produce the median concentration. Both the median and cdf credible intervals can now be evaluated for any distribution of point sinks. For comparison, Section 2.3.3 will compare using moments given in (2.2.23) and (2.2.24) with using cdf credible intervals given in (2.2.27). This will be done for the two previously described examples of sink distributions (normally perturbed from a periodic configuration and order statistics taken from a uniform distribution).

We will next outline an approach that finds cdf confidence intervals in the presence of diffusion. This will be done by replacing the jumps in concentration at sink locations with boundary-layers of finite width.

Calculating credible intervals with non-zero diffusion

Consider now calculating cdf credible intervals for advection-dominated solute transport in the presence of diffusion. Here, a boundary-layer exists upstream from each sink location and the concentration is given globally by (2.2.21). To calculate the intervals we will consider the local concentration when $\xi_{j-1} \leq x \leq \xi_j$, which is given by (2.2.20) as

$$C(x) = C_{j-1} + (C_j - C_{j-1}) e^{\mathrm{Pe}_l (x - \xi_j)} \tag{2.2.28}$$

for $j = 1, \ldots, N$. This can be rearranged to give

$$x = \xi_j + \frac{1}{\mathrm{Pe}_l} \ln \left| \frac{C(x) - C_{j-1}}{C_j - C_{j-1}} \right|. \tag{2.2.29}$$

So for some $x = \hat{x}$ and corresponding concentration $C(\hat{x}) = \hat{C}$ we obtain

$$F_{\hat{C}}(C) = \mathbb{P}(x \leq \hat{x}) = \mathbb{P}\left(x \leq \xi_j + \frac{1}{\mathrm{Pe}_l} \ln\left|\frac{\hat{C} - C_{j-1}}{C_j - C_{j-1}}\right|\right)$$
$$= 1 - F_{\xi_j}\left(x - \frac{1}{\mathrm{Pe}_l} \ln\left|\frac{\hat{C} - C_{j-1}}{C_j - C_{j-1}}\right|\right).$$

As before, let us consider some value of $F_{\hat{C}}(C)$ given by r. Then the sink location which obtains the confidence interval corresponding to r is given by

$$\breve{\xi}_j = F_{\xi_j}^{-1}(1 - r) + \frac{1}{\mathrm{Pe}_l} \ln\left|\frac{\hat{C} - C_{j-1}}{C_j - C_{j-1}}\right|. \tag{2.2.30}$$

These sink locations can then be used with the expression for the concentration given in (2.2.21). This gives the cdf credible intervals corresponding to each r value as

$$CI(x; r) = C_0 - C_0 \mathrm{S} \sum_{j=1}^{N} (1 + \mathrm{S})^{-j} \Big(H(x - \breve{\xi}_j) + e^{\mathrm{Pe}_l (x - \breve{\xi}_j)} (H(x - \breve{\xi}_{j-1}) - H(x - \breve{\xi}_j)) \Big). \tag{2.2.31}$$

As for the zero diffusion example, both the median and cdf 95% credible intervals can be found using (2.2.31) with $r = 0.5$ and $r = 0.5 \pm 0.475$ respectively. These are later calculated for two examples of sink distributions; normally perturbed from a periodic configuration and order statistics from a uniform distribution. Comparison between the cdf credible intervals and sample Gaussian-based credible intervals are made using the sample mean and variance from Monte Carlo simulations.

We now use all methodology outlined in Section 2.2 to produce results, which aim to quantify the effect of disorder on the solute concentration. This will be separated into three sections: using Monte Carlo simulations, using the correction to a homogenized solution when $(\mathrm{Pe}_l, \mathrm{S}) = (1, \varepsilon)$ and considering when advection dominates diffusion on both the microscale and macroscale.

2.3 Results

We begin with results from 10^4 Monte Carlo simulations of multiple concentration profiles. These are illustrated using a cloud plot, where the sample mean, sample median, sample Gaussian-based 95% credible intervals and sample 95% credible-intervals of the concentration are also shown.

Following this, the use of a correction to the homogenized solution in the critical limit $(\mathrm{Pe}_l, \mathrm{S}) \sim (1, \varepsilon)$ will be considered. Asymptotic expressions of corrections will be found, allowing the

impact of different sink distributions to be quantified via the evaluation of the concentration's moments. Three ways in which sinks can be distributed will be considered; periodic, normally perturbed from a periodic configuration and order statistics from a uniform distribution.

Finally, a reconstructed staircase approach will be used when solute transport is advection dominated, where disorder in the concentration will be quantified using both moments and credible intervals, with results from Gaussian-based and cdf credible intervals being compared. Two different examples of advection-dominated solute transport will be considered; when there is zero diffusion and when advection dominates diffusion on both the microscale and macroscale. Results will be verified throughout the section by comparing with sample statistics taken from Monte Carlo realisations.

2.3.1 Monte Carlo realisations

Realisations of the concentration for different sink distributions are calculated using the numerical method outlined in Section 2.2.1. Figure 2.5 shows 10^4 concentration profiles for both a normally-perturbed and uniformly-random sink distribution, with the sample mean, sample median, sample Gaussian-based 95% credible intervals and sample 95% credible intervals being denoted by $\hat{\mu}$, $\hat{\mu}_{0.5}$, $\hat{\mu} \pm 1.96\hat{\sigma}$, and $\hat{\mu}_{0.5\pm0.475}$ respectively. Also shown in Figure 2.5 are the resulting sample covariances for each sink distribution, given by $\hat{K}[x, y]$, which quantifies the impact of disordered sinks locations on the resulting concentration. All plots use $N = 19$ point sinks with $(\mathrm{Pe}_l, \mathrm{S}) = (1, \varepsilon)$, which admits an advection-uptake balance over the domain length with an advection-diffusion balance on inter-sink lengthscale. This scenario leads to a 'wavy' sink-to-sink structure appearing across the domain.

Figures 2.5(a) and 2.5(b) shows when sinks are normally perturbed from a periodic configuration such that $\xi_j \sim \mathcal{N}(j, \sigma^2)$ with $\sigma = 0.194$. Here, σ is chosen for illustrative purposes and ensures a 99% confidence level that each sink ξ_j will remain within the unit-cell $(j-1/2, j+1/2)$, therefore avoiding sinks trading places or exiting the domain. Figure 2.5(a) shows good agreement between the sample Gaussian-based 95% credible intervals and the sample 95% credible intervals, with the distribution of profiles about the mean being predominantly Gaussian. Figure 2.5(b) shows how the sample covariance is zero except where spikes are exhibited, which are periodically located on the diagonal and decrease in size through the domain. These spikes represent how fluctuations due to point sinks have a strong local influence on concentration profiles, but negligible long-range impact.

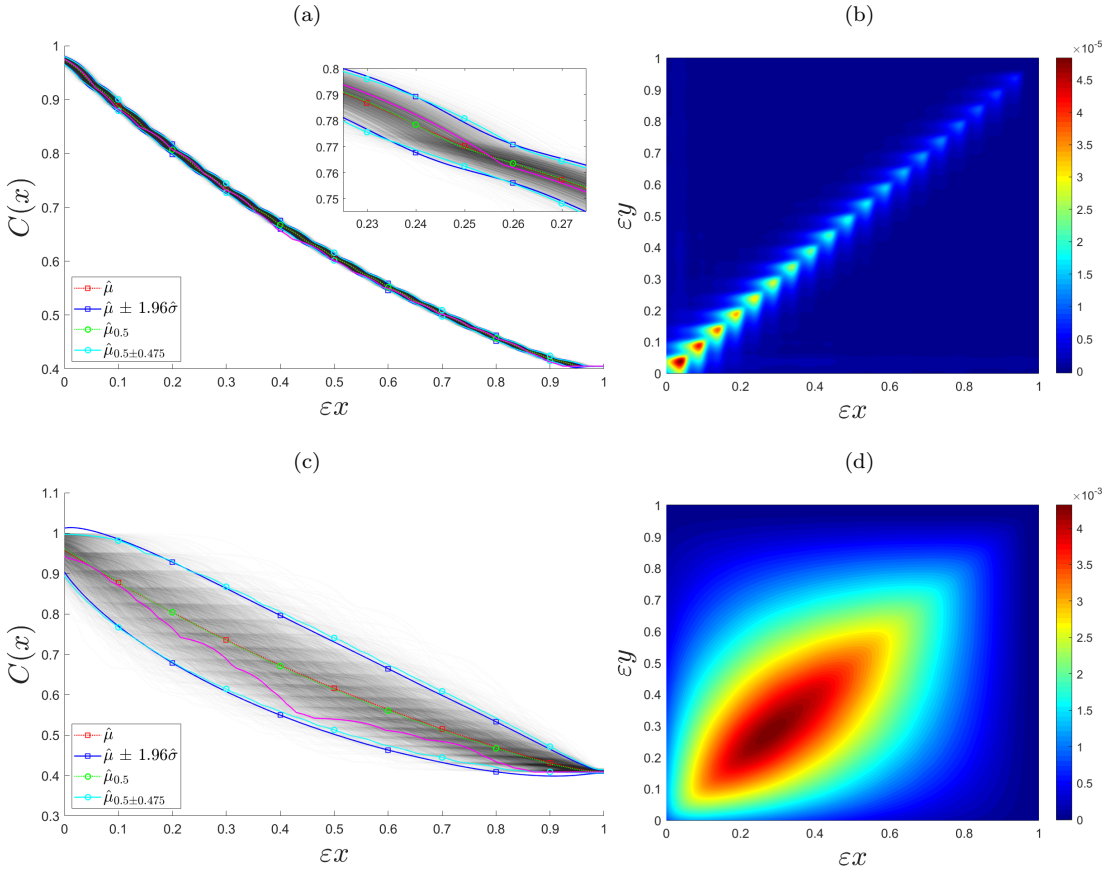

Figure 2.5: (a) & (c) Multiple realisations of concentration profiles [grey] with the sample mean [$\hat{\mu}$, dashed red], sample Gaussian-based 95% credible intervals [$\hat{\mu} \pm 1.96\hat{\sigma}$ (where $\hat{\sigma}$ represents the sample standard deviation), solid blue], sample median [$\hat{\mu}_{0.5}$, dashed green], the sample 95% credible intervals [$\hat{\mu}_{0.5\pm0.475}$, solid cyan] and a single realisation [solid magenta]. (b) & (d) Depiction of the sample covariances [$\hat{K}[x, y]$]. Figures (a) and (b) use a normally-perturbed sink distribution with $\xi_j \sim \mathcal{N}(j, \sigma^2)$, where $\sigma = 0.194$. Figures (c) and (d) use order statistics from a uniform distribution $\mathcal{U}(0, \varepsilon^{-1})$ as the sink locations. All figures use 10^4 Monte Carlo simulation for $N = 19$ point sinks (i.e. $\varepsilon = 0.05$), where $(\mathrm{Pe}_l, \mathrm{S}) = (1, \varepsilon)$.

Alternatively, Figures 2.5(c) and 2.5(d) have sink locations prescribed using order statistics from a uniform distribution $\mathcal{U}(0, \varepsilon^{-1})$. Here, despite each profile independently exhibiting a wavy sink-to-sink structure with inherently non-smooth properties, the mean concentration and covariance are represented by smooth functions. This shows that small perturbations which occur on the inter-sink lengthscale become lost when only considering the macroscale problem and neglecting the microscale structure. In Figure 2.5(d) we see the covariance for uniformly-random sink locations is considerably larger when away from the diagonal when compared to using normally-perturbed sink locations, showing how fluctuations cause a strong long-range impact on the concentration. Figure 2.5(c) largely shows good agreement between the sample

Gaussian-based 95% credible intervals and sample 95% credible intervals, with the distribution of profiles about the mean again being predominantly Gaussian. However, differences between the two can be seen due to the non-smooth properties of the concentration profiles, which individually exhibit a wavy sink-to-sink structure.

Producing Figure 2.5 is computationally expensive due to requiring many realisations. It also offers little explanation for the uncertainty caused to the concentration due to disordered sink locations, with no insight as to how the parameters Pe_l, S and ε influence disorder. Therefore we seek an alternate approach using the expansion given in Section 2.2.2, where corrections to a homogenized solution are found. These corrections aid in quantifying the uncertainty due to a disordered domain and can be validated *a posteriori* through comparison to the Monte Carlo simulations.

2.3.2 Corrections to the homogenized solution

We now consider calculating corrections to the homogenized solution for either periodic or disordered sink locations, which is done using the expansion in (2.2.12). When sinks are periodically located we will calculate a correction $\widehat{C}_a(x)$ using (2.2.15), which will give the leading-order correction to the homogenized solution which accounts for sink locations. Alternatively, when sinks are disordered we will calculate the moments of the correction $\widehat{C}_b(x)$ given in (2.2.18) to quantify the impact of disorder.

Correction for periodic sink locations

Let us consider sub-problem (2.2.15) in the distinguished limit where $(\mathrm{Pe}_l, \mathrm{S}) \sim (1, \varepsilon)$. Solving for the correction $\widehat{C}_a$ requires an alternative approach to that taken in Russell and Jensen (2020) as the Green's function is non-smooth with a boundary-layer present, meaning the integral cannot be converted into a Riemann sum. Instead, let us decompose the integral so that

$$\widehat{C}_a(x) = \mathrm{S}(I_1(x) - I_2(x)), \tag{2.3.1}$$

where I_1 and I_2 are given by

$$I_1(x) = \int_0^{\varepsilon^{-1}} (GC_H)|_{x,y} \sum_{j=1}^{N} \delta(y-j)\,\mathrm{d}y \quad \text{and} \quad I_2(x) = \int_0^{\varepsilon^{-1}} (GC_H)|_{x,y}\,\mathrm{d}y \tag{2.3.2}$$

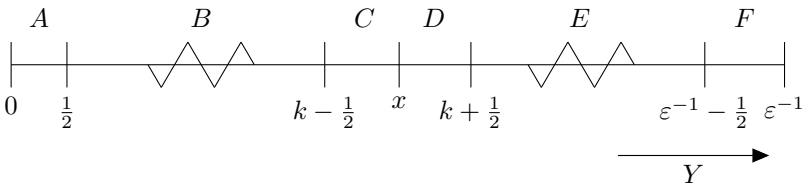

Figure 2.6: Depiction of the Y-domain separation, where A, B, C, D, E and F represent the domains $[0, \frac{1}{2}]$, $[\frac{1}{2}, k-\frac{1}{2}]$, $[k-\frac{1}{2}, x]$, $[x, k+\frac{1}{2}]$, $[k+\frac{1}{2}, \varepsilon^{-1}-\frac{1}{2}]$ and $[\varepsilon^{-1}-\frac{1}{2}, \varepsilon^{-1}]$ respectively.

respectively. We will now evaluate each integral independently. First, consider the composite term $(GC_H)|_{x,y}$, which by Appendix A.3 has the piecewise leading-order expression

$$\begin{aligned}(G^- C_H)|_{x,y} &= \left(-1 + \frac{\mathrm{S}}{\mathrm{Pe}_l}\left(3 + \mathrm{S}\,(x-2y) - f_2(-x) - 2f_2(y-\varepsilon^{-1})\right)\right) f_1(-x) f_2(x-y),\\ (G^+ C_H)|_{x,y} &= \left(-1 + \frac{\mathrm{S}}{\mathrm{Pe}_l}\left(3 - \mathrm{S}\,x - f_2(-y) - f_2\left(x-\varepsilon^{-1}\right) - f_2(y-\varepsilon^{-1})\right)\right) f_1(-x),\end{aligned} \tag{2.3.3}$$

with $\mathcal{O}(\varepsilon^2)$ terms neglected. In order to evaluate I_2 we can used the explicit integral values of these expressions given in (A.3.7) to give

$$\begin{aligned}\int_0^y (G^- C_H)|_{x,y}\,\mathrm{d}y &= \frac{1}{\mathrm{Pe}_l}\left(1 - 2\,\mathrm{S}\,y f_2(y-\varepsilon^{-1})\right) f_1(-x) f_2(x-y),\\ \int_0^y (G^+ C_H)|_{x,y}\,\mathrm{d}y &= \left(-1 + \frac{\mathrm{S}}{\mathrm{Pe}_l}\left(3 - \mathrm{S}\,x - f_2\left(x-\varepsilon^{-1}\right)\right)\right) y f_1(-x),\end{aligned} \tag{2.3.4}$$

where $\mathcal{O}(\varepsilon^2)$ terms are neglected. We can use these approximations with (2.3.4) to obtain

$$\begin{aligned}I_2(x) &= \int_x^{\varepsilon^{-1}} (G^- C_H)|_{x,y}\,\mathrm{d}y + \int_0^x (G^+ C_H)|_{x,y}\,\mathrm{d}y\\ &\approx -\left(x + \frac{1}{\mathrm{Pe}_l}\left(1 - 3\mathrm{S}\,x + \mathrm{S}^2\,x^2 - (1 + \mathrm{S}(x - 2\varepsilon^{-1}))f_2\left(x-\varepsilon^{-1}\right)\right)\right) f_1(-x).\end{aligned} \tag{2.3.5}$$

To evaluate $I_1(x)$, let the y-domain be split into N unit-cells $(j-\frac{1}{2}, j+\frac{1}{2})$ for $j = 1, \ldots, N$, with two half cells $(0, 1/2)$ and $(\varepsilon^{-1}-\frac{1}{2}, \varepsilon^{-1})$ at either end. Now let $x \in (k-\frac{1}{2}, k+\frac{1}{2})$ for some $k \in \mathbb{Z}$, i.e. $k = \lfloor x + \frac{1}{2} \rfloor$, then the y-domain $[0, \varepsilon^{-1}]$ can be separated into sections A, B, C, D, E and F, as shown in Figure 2.6. Here, the k^{th} unit-cell is separated into $[k-\frac{1}{2}, x]$ and $[x, k+\frac{1}{2}]$ to allow for careful handling of any discontinuities at $y = x$. We can now consider the contributions from each section of the domain independently to obtain

$$I_1(x) = \sum_{j<k} (G^+ C_H)|_{x,j} + H(x-k)(G^+ C_H)|_{x,k} + H(k-x)(G^- C_H)|_{x,k} + \sum_{j>k} (G^- C_H)|_{x,j}. \tag{2.3.6}$$

In Russell and Jensen (2020), $I_1(x)$ was evaluated by converting the summations into a Riemann integral, therefore creating a smooth function. However, this cannot be done in the distinguished

limit $(\mathrm{Pe}_l, \mathrm{S}) \sim (1, \varepsilon)$ due to the internal and peripheral boundary-layers within $(GC_H)|_{x,y}$. Instead, the summations are evaluated directly using (2.3.3) to obtain an expression for $I_1(x)$, which in turn gives the correction due to periodic sink locations given by (2.3.1).

Figure 2.2 shows the correction being used with the homogenized solution for $N = 19$ periodic sink locations. Both the classical approach to homogenization and the correction $\widehat{C}_a$ are shown to capture the microscale perturbations on the inter-sink scale for periodic sink locations, which is demonstrated by the wavy sink-to-sink structure. However, one drawback for the classical approach stems from being based on an ad-hoc assumption of two-scale dependence, which prevents the multiscale structure associated with the downstream diffusive boundary-layer from being included in the approximation. This is in contrast to the integral approach, where the homogenized solution and the sequential correction can include effects from multiple length-scales. As a result, when comparing each approach to a numerical solution there is a smaller relative error when using the integral approach, which is shown to be true for $N \in \{1, \dots 300\}$, despite the convergence to the numeric solution as N increases (ε decreases) being irregular.

Arguably the greatest advantage to using the integral approach is the ability for corrections to quantify the impact of disordered sink locations, which cannot be done when using the classical approach. This will now be demonstrated by calculating the correction $\widehat{C}_b$ for two different sink distributions; normally perturbed from a periodic configuration and order statistics taken from a uniform distribution.

Moments of a correction for normally-perturbed sink locations

Consider when sinks are weakly perturbed from a periodic sink arrangement by a normally-perturbed random variable. Let the sink locations be given by $\xi_j = j + \sigma\widehat{\xi}_j$, where $\sigma \ll 1$, $\widehat{\xi}_j \sim \mathcal{N}(0,1)$ and $j = 1, \dots, N$. When the standard deviation is significantly smaller than the boundary-layer, i.e. $\sigma \ll 1/\mathrm{Pe}_l$, we can Taylor expand about the periodic sink arrangement $\xi_j = j$ and use (2.2.18) to give

$$\widehat{C}_b(x) = \mathrm{S}\left(\sum_{j\neq k}\left(\sigma\widehat{\xi}_j(GC_H)_y|_{x,j} + \frac{1}{2}\sigma^2\widehat{\xi}_j^2(GC_H)_{yy}|_{x,j} + \dots\right) + \left[(GC_H)|_{x,y}\right]_{y=k}^{k+\sigma\widehat{\xi}_k}\right), \quad (2.3.7)$$

where the k^{th} cell is again treated separately to avoid expanding non-smooth functions, with $k = \lfloor x + \frac{1}{2}\rfloor$. So for a sufficiently small standard deviation we obtain, to leading-order,

$$\widehat{C}_b(x) = \mathrm{S}\left(\sum_{j\neq k}\sigma\widehat{\xi}_j(GC_H)_y|_{x,j} + \left[(GC_H)|_{x,y}\right]_{y=k}^{k+\sigma\widehat{\xi}_k}\right) + \mathcal{O}(\sigma^2). \quad (2.3.8)$$

Let us now calculate the covariance of the correction. When the variance is sufficiently small we can assume sink locations are independently and identically distributed (i.i.d) as sinks do not trade places. Therefore Appendix A.4 can be used to give the covariance of the corrections $\widehat{C}_b(x_1)$ and $\widehat{C}_b(x_2)$ as

$$\mathcal{K}[\widehat{C}_b(x_1),\widehat{C}_b(x_2)] = \begin{cases} \mathrm{S}^2\Bigg(\sigma^2 \displaystyle\sum_{j\notin\{k_1,k_2\}} (GC_H)_y|_{x_1,j}(GC_H)_y|_{x_2,j} \\ +\sigma(GC_H)_y|_{x_1,k_2}\mathbb{E}\left[\widehat{\xi}_{k_2}[(GC_H)|_{x_2,y}]_{y=k_2}^{k_2+\sigma\widehat{\xi}_{k_2}}\right] \\ +\sigma(GC_H)_y|_{x_2,k_1}\mathbb{E}\left[\widehat{\xi}_{k_1}[(GC_H)|_{x_1,y}]_{y=k_1}^{k_1+\sigma\widehat{\xi}_{k_1}}\right]\Bigg) & \text{if } k_1\neq k_2, \\ \mathrm{S}^2\Bigg(\sigma^2\displaystyle\sum_{j\neq k}(GC_H)_y|_{x_1,j}(GC_H)_y|_{x_2,j} \\ +\mathbb{E}\left[[(GC_H)|_{x_1,y}]_{y=k}^{k+\sigma\widehat{\xi}_k}[(GC_H)|_{x_2,y}]_{y=k}^{k+\sigma\widehat{\xi}_k}\right] \\ -\mathbb{E}\left[[(GC_H)|_{x_1,y}]_{y=k}^{k+\sigma\widehat{\xi}_k}\right]\mathbb{E}\left[[(GC_H)|_{x_2,y}]_{y=k}^{k+\sigma\widehat{\xi}_k}\right]\Bigg) & \text{if } k\equiv k_1=k_2. \end{cases} \tag{2.3.9}$$

This gives the variance of the correction $\widehat{C}_b(x)$ as

$$\begin{aligned}\mathrm{Var}[\widehat{C}_b(x)] = \mathrm{S}^2\Bigg(\sigma^2\sum_{j\neq k}\left((GC_H)_y|_{x,j}\right)^2 + \mathbb{E}\left[\left([(GC_H)|_{x,y}]_{y=k}^{k+\sigma\widehat{\xi}_k}\right)^2\right] \\ -\left(\mathbb{E}\left[[(GC_H)|_{x,y}]_{y=k}^{k+\sigma\widehat{\xi}_k}\right]\right)^2\Bigg),\end{aligned} \tag{2.3.10}$$

where we have used the relation $\mathrm{Var}(\widehat{C}_b(x)) = \mathcal{K}[\widehat{C}_b(x),\widehat{C}_b(x)]$. So for a sufficiently small σ, a Taylor expansion about $k+\sigma\widehat{\xi}_k = k$ gives

$$\begin{aligned}\mathrm{Var}[\widehat{C}_b(x)] =& \mathrm{S}^2\Bigg(\sigma^2\sum_{j\neq k}\left((GC_H)_y|_{x,j}\right)^2 + \mathbb{E}\left[\left(\sigma\widehat{\xi}_k(GC_H)_y|_{x,k} + (\sigma\widehat{\xi}_k)^2(GC_H)_{yy}|_{x,k}\right)^2\right] \\ &-\left(\mathbb{E}\left[\sigma\widehat{\xi}_k(GC_H)_y|_{x,k} + (\sigma\widehat{\xi}_k)^2(GC_H)_{yy}|_{x,k}\right]\right)^2\Bigg) \\ =& \mathrm{S}^2\Bigg(\sigma^2\sum_{j\neq k}\left((GC_H)_y|_{x,j}\right)^2 + \sigma^2\left((GC_H)_y|_{x,j}\right)^2\mathbb{E}\left[\widehat{\xi}_k^2\right] \\ &-\sigma^2\left((GC_H)_y|_{x,j}\right)^2\mathbb{E}\left[\widehat{\xi}_k\right]^2\Bigg),\end{aligned}$$

where $\mathcal{O}(\sigma^3)$ terms are neglected throughout. So using $\mathbb{E}[\widehat{\xi}_k] = 0$ and $\mathbb{E}[\widehat{\xi}_k^2] = 1$ we obtain

$$\mathrm{Var}[\widehat{C}_b(x)] = \mathrm{S}^2\sigma^2\sum_j\left((GC_H)_y|_{x,j}\right)^2 + \mathcal{O}(\sigma^3). \tag{2.3.11}$$

We now evaluate (2.3.11) directly using the composite asymptotic expansions of $C_H(x)$ and $G(x,y)$ given in (2.2.5) and (2.2.11). First, note that the differential of $(GC_H)|_{x,y}$ is given in

Appendix A.3 as

$$\begin{aligned}(G^{-}C_H)_y|_{x,y} &= (\mathrm{Pe}_l - \mathrm{S}\,(1 + \mathrm{S}(x-2y) - f_2(-x)))\, f_1(-x) f_2(x-y),\\ (G^{+}C_H)_y|_{x,y} &= \mathrm{S}\left(f_2(-Y) - f_2(y-\varepsilon^{-1})\right) f_1(-x),\end{aligned} \tag{2.3.12}$$

where $\mathcal{O}(\varepsilon^2)$ terms are neglected. This can be used to evaluate (2.3.11), which in turn gives the variance of the correction $\widehat{C}_b(x)$.

Figure 2.7(a) compares the sample variance found when performing 10^5 Monte Carlo simulations with the variance of $\widehat{C}_b(x)$ given in (2.3.11). It demonstrates the sharp, spiky structure of the variance, where the sharpness of each spike is dependent upon the sink variance σ. By (2.3.11) we can see the height of each spike is of order $\mathcal{O}(\mathrm{Pe}_l^2\,\mathrm{S}^2\sigma^2)$, with the width of each spike being dependent on the boundary-layer width $1/\,\mathrm{Pe}_l$. This spiky structure can also be seen by examining the diagonal of the covariance matrix in Figure 2.5(b). The sample variance for $(\mathrm{Pe}_l, \mathrm{S}) = (1, \varepsilon)$ was calculated in Russell and Jensen (2020), but when comparing to analytic results for the variance of $\widehat{C}_b$ there was poor agreement. This is due to the non-smooth properties of the Green's function being disregarded, which arise when advection is dominant on the macroscale. However, the analysis performed here captures the spiky structure of the variance.

We will next consider when strong disorder exists in the system, with sink locations being given by order statistics from a uniform distribution. Russell and Jensen (2020) previously evaluated the sample variance in the distinguished limit $(\mathrm{Pe}_l, \mathrm{S}) = (1, \varepsilon)$, but the structure for when advection is dominant on the macroscale was again not considered.

Moments of a correction for uniformly-random sink locations

Let $(U_1, U_2, \ldots, U_N)$ be N random variables taken from a uniform distribution $U \sim \mathcal{U}(0, \varepsilon^{-1})$ with a given pdf $\pi_U(x) = \varepsilon$ for $x \in [0, \varepsilon^{-1}]$ and zero otherwise. The random variables U_j will have corresponding order statistics $U_{j:N}$ when arranged into ascending order, such that $U_{1:N} \leq U_{2:N} \leq \cdots \leq U_{N:N}$. Let each sink location be given by an order statistic such that $\xi_j = U_{j:N}$. By properties of order statistics (Arnold et al., 1992) each sink location will follow a Beta distribution such that $\varepsilon\xi_j \sim \beta(j, N-j+1)$, where $j = 1, \ldots, N$. A plot of the probability density functions for each ξ_j can be seen in Figure 2.8(a).

We now note the following properties of order statistics, which will be used to calculate the covariance of the correction $\widehat{C}_b$. Firstly, summing over the N order statistics $U_{j:N}$ is equivalent to summing over the N underlying random variables U_j. Secondly, by Chunsheng (1992) and

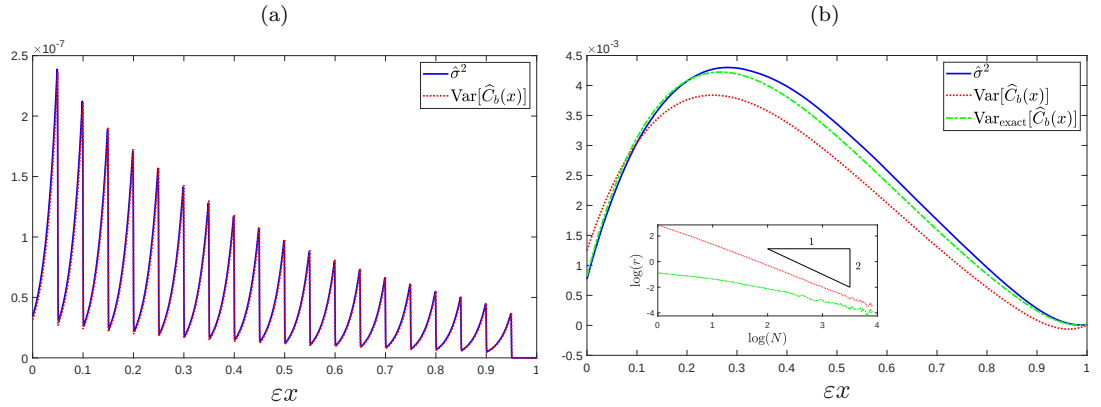

Figure 2.7: Comparison between the sample variance for 10^5 Monte Carlo simulations [$\hat{\sigma}^2$, solid blue] and the expression for the variance of the correction [$\mathrm{Var}[\widehat{C}_b(x)]$, dashed red]. Here, $N = 19$ point sinks (i.e. $\varepsilon = 0.05$) and $(\mathrm{Pe}_l, \mathrm{S}) = (1, \varepsilon)$. (a) Variance of solute concentration when sinks are normally perturbed from a periodic arrangement with $\sigma = 0.01$, where the variance of $\widehat{C}_b(x)$ is given in (2.3.11). (b) Variance of solute concentration when sinks are given by order statistics from a uniform distribution, where the variance of $\widehat{C}_b(x)$ is given in (2.3.19). Also shown is the variance calculated using the exact values of $C_H(x)$ and $G(x, y)$ given in (2.2.3) and (2.2.10) respectively. These are used to solve for $\mathcal{K}[\widehat{C}_b(x), \widehat{C}_b(x)]$ given in (2.3.14) [$\mathrm{Var}_{\mathrm{exact}}[\widehat{C}_b(x)]$, dot-dashed green], where the integral solver given in Shampine (2008) is used. The convergence of both $\mathrm{Var}[\widehat{C}_b(x)]$ and $\mathrm{Var}_{\mathrm{exact}}[\widehat{C}_b(x)]$ to the sample variance can be seen in the inset for $N \in \{0, \ldots, 50\}$.

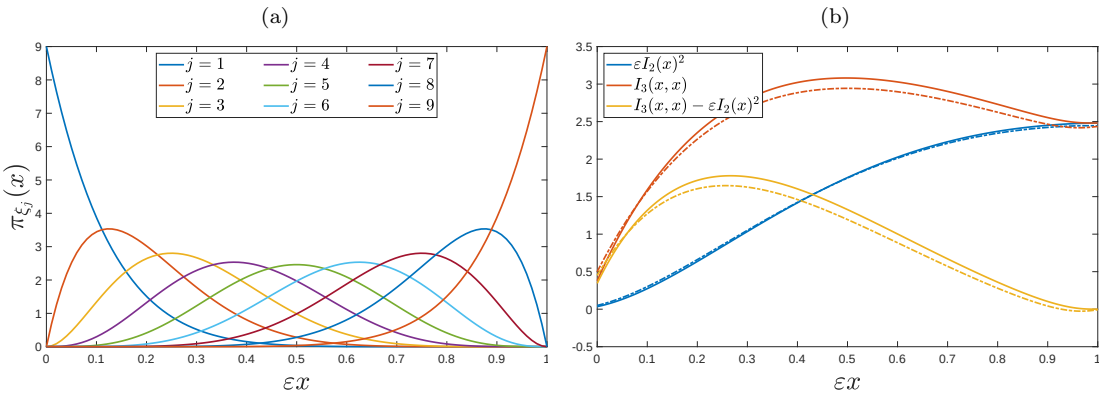

Figure 2.8: (a) Depiction of the probability density functions $\pi_{\xi_j}(x)$ when sink locations are prescribed as order statistics taken from a uniform distribution. Here, $j = 1, \ldots, N$ and $N = 9$ (i.e. $\varepsilon = 0.1$) are used. (b) Shown are the functions $\varepsilon I_2(x)^2$ [blue], $I_3(x, x)$ [red] and $I_3(x, x) - \varepsilon I_2(x)^2$ [yellow], where I_2 and I_3 are defined in (2.3.5) and (2.3.15) respectively. Solid lines are calculated using the integral solver given in Shampine (2008) with the exact values of the homogenized solution and Green's function given in (2.2.3) and (2.2.10) respectively. Dashed lines use the approximations of $I_3(x, x)$ and $I_2(x)^2$ given in (2.3.17) and (2.3.18) respectively. Here, $N = 19$ ($\varepsilon = 0.05$) and $(\mathrm{Pe}_l, \mathrm{S}) = (1, \varepsilon)$ are used.

David and Nagaraja (2004), for any random variable X with a corresponding N order statistics $X_{j:N}$, we know that

$$\sum_{\substack{j=1\\j\neq k}}^{N}\sum_{k=1}^{N}\mathcal{K}[g(X_{j:N}),h(X_{k:N})]=\sum_{j=1}^{N}\left(\langle g(X_{j:N})\rangle\langle h(X_{j:N})\rangle-\langle g(X)\rangle\langle h(X)\rangle\right) \tag{2.3.13}$$

where K is the covariance function, $\langle\,\cdot\,\rangle$ the mean and g,h are real valued functions such that $\mathrm{Var}(g(X))<\infty$ and $\mathrm{Var}(h(X))<\infty$. These can be used with (2.2.18) to give the covariance of the correction $\widehat{C}_b(x)$ as

$$\begin{aligned}\mathcal{K}[\widehat{C}_b(x_1),\widehat{C}_b(x_2)]&=\mathrm{S}^2\sum_{j=1}^{N}\sum_{k=1}^{N}\mathcal{K}[(GC_H)|_{x_1,\xi_j},(GC_H)|_{x_2,\xi_k}]\\&=\mathrm{S}^2\sum_{\substack{j=1\\j\neq k}}^{N}\sum_{k=1}^{N}\mathcal{K}[(GC_H)|_{x_1,\xi_j},(GC_H)|_{x_2,\xi_k}]+\sum_{j=1}^{N}\mathcal{K}[(GC_H)|_{x_1,\xi_j},(GC_H)|_{x_2,\xi_j}]\\&=N\mathrm{S}^2\left(\langle(GC_H)|_{x_1,U}(GC_H)|_{x_2,U}\rangle-\langle(GC_H)|_{x_1,U}\rangle\langle(GC_H)|_{x_2,U}\rangle\right).\end{aligned}$$

Here, we used (2.3.13) to transform averages over the order statistics into averages over the uniform variable in a similar fashion to Russell and Jensen (2020). Therefore the covariance of the corrections $\widehat{C}_b(x_1)$ and $\widehat{C}_b(x_2)$ is given by

$$\mathcal{K}[\widehat{C}_b(x_1),\widehat{C}_b(x_2)]=\mathrm{S}^2\left(1-\varepsilon\right)\left(I_3(x_1,x_2)-\varepsilon I_2(x_1)I_2(x_2)\right), \tag{2.3.14}$$

where

$$I_3(x_1,x_2)=\int_0^{\varepsilon^{-1}}(GC_H)|_{x_1,y}(GC_H)|_{x_2,y}\,\mathrm{d}y \tag{2.3.15}$$

and $I_2(x)$ is given in (2.3.5). First, note that (A.3.10) gives

$$\begin{aligned}\int_0^y(G^-C_H)^2|_{x,y}\,\mathrm{d}y&=-\frac{1}{2\,\mathrm{Pe}_l}f_1(-2x)f_2(2(x-y)),\\\int_0^y(G^+C_H)^2|_{x,y}\,\mathrm{d}y&=\left(1-\frac{2\mathrm{S}}{\mathrm{Pe}_l}\left(3-\mathrm{S}x-f_2\left(x-\varepsilon^{-1}\right)\right)\right)yf_1(-2x),\end{aligned} \tag{2.3.16}$$

where $\mathcal{O}(\varepsilon)$ corrections have been neglected. So when calculating the variance of the correction $\widehat{C}_b(x)$, which is given by $\mathrm{Var}[\widehat{C}_b(x)]=\mathcal{K}[\widehat{C}_b(x),\widehat{C}_b(x)]$, we can use this with (2.3.5) to give

$$I_3(x,x)=\left(x+\frac{1}{2\,\mathrm{Pe}_l}\left(1-12\mathrm{S}x+4\mathrm{S}^2x^2+4\mathrm{S}xf_2\left(x-\varepsilon^{-1}\right)-f_2\left(2\left(x-\varepsilon^{-1}\right)\right)\right)\right)f_1(-2x) \tag{2.3.17}$$

$$I_2(x)^2=\left(x^2+\frac{2}{\mathrm{Pe}_l}x\left(1-3\mathrm{S}x+\mathrm{S}^2x^2-\left(1+\mathrm{S}(x-2\varepsilon^{-1})\right)f_2\left(x-\varepsilon^{-1}\right)\right)\right)f_1(-2x) \tag{2.3.18}$$

where $I_3(x,x)$ and $I_2(x)^2$ neglect $\mathcal{O}(\varepsilon)$ and $\mathcal{O}(1)$ terms respectively. Each of these expressions along with their sum are shown in Figure 2.8(b). There is seen to be good agreement between the

expansions given in (2.3.17) and (2.3.18) when comparing to using an integral solver (Shampine, 2008) with the exact values of the homogenized solution and Green's function given in (2.2.3) and (2.2.10) respectively. These two expressions can then be combined using (2.3.14) to obtain the variance of $\widehat{C}_b(x)$ to second-order as

$$\begin{aligned}\mathrm{Var}[\widehat{C}_b(x)] = \varepsilon \mathrm{S}^2 \Bigg(&- (1-\varepsilon)x\left(x-\varepsilon^{-1}\right) + \frac{1}{2\,\mathrm{Pe}_l}\Bigg(\varepsilon^{-1} - 4x + 12\mathrm{S}x\left(x-\varepsilon^{-1}\right) \\ &- 4\mathrm{S}^2x^2\left(x-\varepsilon^{-1}\right) - f_2\left(2\left(x-\varepsilon^{-1}\right)\right) + 4x(1+\mathrm{S}\left(x-\varepsilon^{-1}\right))f_2\left(x-\varepsilon^{-1}\right)\Bigg)\Bigg) f_1(-2x).\end{aligned} \tag{2.3.19}$$

Note we can calculate the value of x ($x_{\max}$) which corresponds to the maximum value of the variance ($\mathrm{Var}_{\max}$) by setting the differential of (2.3.19) to zero, which gives

$$x_{\max} = \frac{\mathrm{S}+\varepsilon-\sqrt{\mathrm{S}^2+\varepsilon^2}}{2\varepsilon\mathrm{S}} \quad \text{and} \quad \mathrm{Var}_{\max} = \frac{1}{2}\left(\sqrt{\mathrm{S}^2+\varepsilon^2}-\varepsilon\right) f_1(-2x_{\max}) \tag{2.3.20}$$

to leading-order. Therefore in the critical limit $(\mathrm{Pe}_l, \mathrm{S}) = (1, \varepsilon)$, where $\varepsilon \ll 1$, the magnitude of the variance is of order $\mathcal{O}(\varepsilon)$. This is larger in comparison to the magnitude of the variance for normally-perturbed sink locations, which is given in Section 2.3.2 as $\mathcal{O}(\mathrm{Pe}_l^2\,\mathrm{S}^2\sigma^2) = \mathcal{O}(\varepsilon^2\sigma^2)$, where $\sigma \ll \varepsilon \ll 1$.

Figure 2.7(b) compares the sample variance ($\hat{\sigma}^2$) for 10^5 Monte Carlo simulations against (2.3.19). When comparing Figures 2.7(a) and 2.7(b) we notice that moving from normally-perturbed to uniformly-random sink locations causes the variance to become smooth. This is due to the effect from each point sink being smeared out when considering the macroscale problem due to strong disorder. It should be noted that the variance given in (2.3.19) is only calculated to second-order, which results in a discrepancy when comparing to the sample variance in Figure 2.7(b). Calculating the variance of the correction using the exact expressions for the homogenized solution and Green's function produces a better approximation of the sample variance for $N = 19$ point sinks, given by $\mathrm{Var}_{\mathrm{exact}}[\widehat{C}_b(x)]$ in Figure 2.7(b). The inset of Figure 2.7(b) shows the relative errors $r(\hat{\sigma}^2, \mathrm{Var}[\widehat{C}_b(x)])$ and $r(\hat{\sigma}^2, \mathrm{Var}_{\mathrm{exact}}[\widehat{C}_b(x)])$ calculated using (2.2.7). It is here seen that both $\mathrm{Var}[\widehat{C}_b(x)]$ and $\mathrm{Var}_{\mathrm{exact}}[\widehat{C}_b(x)]$ converge quadratically on a logarithmic scale to the sample variance as N increases (ε decreases), with the latter having a smaller relative error than the former.

Next, we will consider when the Péclet number becomes asymptotically large, which causes advection to dominate diffusion on all lengthscales. This causes the boundary-layer width ($1/\,\mathrm{Pe}_l$) to become asymptotically small, leading to a staircase structure forming, as demonstrated in

regimes (4) and (5) from Figure 2.1(b). Therefore we use a reconstructed staircase approach, as previously outlined in Section 2.2.3. Two regimes for when solute transport is advection dominated are considered: when there is zero diffusion, causing the boundary-layer width to be infinitesimally small, meaning a jump in concentration occurs at each sink location; and when the boundary-layer width $1/\operatorname{Pe}_l$ is small but finite, leading to a boundary-layer forming upstream of each sink.

2.3.3 Advection-dominated solute transport

We will now consider when advection dominates diffusion on both the microscale and macroscale. To calculate both moments and cdf credible-intervals of the concentration, we will first calculate the cumulative distribution function (cdf) of the sink function. This will be done for the usual two examples of sink distributions; normally perturbed from a periodic configuration and order statistics from a uniform distribution.

Following this we will consider when the Péclet number becomes infinitely large, i.e. the transport problem given in (2.1.2) has zero diffusion. This causes a jump in concentration at each sink location, as is shown by the Heaviside function in (2.2.22). Here, examples are broken into two sections based on the sink distributions, where the effect of disordered sink locations on the solute concentration will be considered using two methods, a direct evaluation of the mean and variance and a cdf credible-interval approach, both of which are outlined in Section 2.2.3.

Finally, cdf credible intervals for the concentration will be calculated in the presence of diffusion, but where advection still dominates on both the microscale and macroscale. This causes the jump in concentration at sink locations to be replaced with boundary-layers of finite width forming upstream of each sink. Results will here be compared to using sample Gaussian-based credible intervals, which are calculated using the sample mean and variance.

Cumulative distribution function for sink locations

First, let us consider when sink locations are normally perturbed from a periodic array. Allow each sink location to be given by $\xi_j = j + \sigma\widehat{\xi}_j$, where $\widehat{\xi}_j \sim \mathcal{N}(0,1)$ for $j = 1, \ldots, N$ and σ is suitably small such that sinks cannot trade positions. Let x be contained inside the unit-cell $(k-1/2, k+1/2)$ for some $k = 1, \ldots, N$. Then each sink location has a cdf within the unit-cell

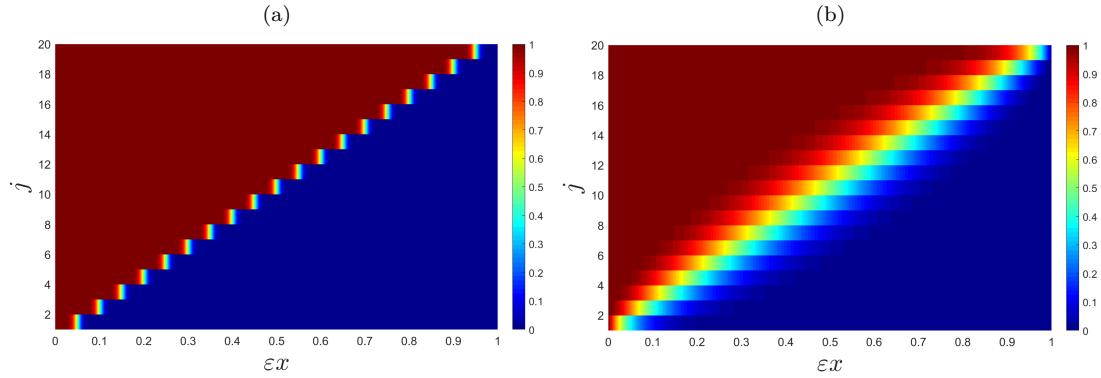

Figure 2.9: Cumulative distribution functions for $N = 19$ sink locations. (a) normally-perturbed sink locations with a standard deviation $\sigma = 0.194$, with the cdf given in (2.3.21). (b) uniformly-random sink locations, with the cdf given in (2.3.22).

given by

$$F_{\xi_j}(x) = \begin{cases} 0 & \text{for } j < k \\ \Phi_{\xi_k}(x) = \dfrac{1}{2}\left(1 + \operatorname{erf}\left(\dfrac{x-k}{\sqrt{2}\sigma}\right)\right) & \text{for } j = k, \\ 1 & \text{for } j > k, \end{cases} \tag{2.3.21}$$

where $\operatorname{erf}(x) = (2/\sqrt{\pi}) \int_0^x e^{-t^2}\, \mathrm{d}t$ represents the error function and the notation $\Phi_{\xi_k}(x)$ is introduced to conform with previous literature on the cdf of a normal distribution. This is plotted for $j = 1, \ldots, 19$ in Figure 2.9(a).

Secondly, let the sink locations ξ_j be given by the N order statistics $U_{j:N}$ taken from a uniform distribution $U \sim \mathcal{U}(0, \varepsilon^{-1})$, where the pdf of the underlying uniform variables are given by $\pi_U(x) = \varepsilon$ for $0 \leq x \leq \varepsilon^{-1}$ and zero otherwise. We know from Arnold et al. (1992) that each sink location will follow a Beta distribution such that $\varepsilon\xi_j \sim \beta(j, N-j+1)$, where $j = 1, \ldots, N$. As the beta distribution is defined such that $\beta(x, y) = t^{x-1}(1-t)^{y-1}/\mathrm{B}(x, y)$, where $\mathrm{B}(x, y) = \Gamma(x)\Gamma(y)/\Gamma(x+y)$ is the beta function, the cdf is given by the regularised incomplete beta function

$$F_{\xi_j}(x) = I_{\varepsilon x}(j, N-j+1) = \frac{\int_0^{\varepsilon x} t^{j-1}(1-t)^{N-j}\mathrm{d}t}{\mathrm{B}(j, N-j+1)}, \tag{2.3.22}$$

which is shown in Figure 2.9(b) for different values of $j = 1, \ldots, 19$.

The cdf for both sink functions, given in (2.3.21) and (2.3.22), will now be used to calculate both moments and cdf credible-intervals of the concentration. First, the example where there is zero diffusive transport will be considered, which results in concentration profiles becoming

discontinuous.

Moments and cdf credible-intervals of the concentration for normally-perturbed sink locations with zero diffusion

Let us begin by using the cdf of normally-perturbed sink locations given in (2.3.21), which can be used with (2.2.24) to give the variance as

$$\begin{aligned}\mathrm{Var}[C(x)] = &\sum_{j<k}\left((C_j)^2-(C_{j-1})^2-2C_0(C_j-C_{j-1})\right)\\ &+((C_k)^2-(C_{k-1})^2-2C_0(C_k-C_{k-1}))\Phi_{\xi_j}(x)\\ &-\sum_{i<k}\sum_{j<k}(C_i-C_{i-1})(C_j-C_{j-1})-2(C_k-C_{k-1})\Phi_{\xi_k}(x)\sum_{j<k}(C_j-C_{j-1})\\ &-(C_k-C_{k-1})^2\Phi_{\xi_k}(x)^2.\end{aligned}$$

So by expanding out each summation using

$$\sum_{j<k}(C_j-C_{j-1})=C_{k-1}-C_0 \quad \text{and} \quad \sum_{j<k}((C_j)^2-(C_{j-1})^2)=(C_{k-1})^2-(C_0)^2,$$

we obtain

$$\mathrm{Var}[C(x)]=(C_k-C_{k-1})^2(1-\Phi_{\xi_k}(x))\Phi_{\xi_k}(x) \quad \text{for } x\in(k-1/2,k+1/2).$$

Therefore the global variance can be obtained by summing over all N unit-cells to give

$$\mathrm{Var}[C(x)]=\sum_{k=1}^{N}(C_k-C_{k-1})^2(1-\Phi_{\xi_k}(x))\Phi_{\xi_k}(x). \tag{2.3.23}$$

So by using (2.2.22) with (2.2.23) and (2.3.23) we obtain the expectation and variance as

$$\mathbb{E}[C(x)]=1-\frac{\mathrm{S}}{2}\sum_{j=1}^{N}(1+\mathrm{S})^{-j}\left(1+\mathrm{erf}\left(\frac{x-j}{\sqrt{2}\sigma}\right)\right) \tag{2.3.24}$$

and

$$\mathrm{Var}[C(x)]=\frac{\mathrm{S}^2}{4}\sum_{j=1}^{N}(1+\mathrm{S})^{-2j}\left(1-\mathrm{erf}^{\,2}\left(\frac{x-j}{\sqrt{2}\sigma}\right)\right) \tag{2.3.25}$$

respectively. Figure 2.10(a) compares the sample mean and variance of 10^5 Monte Carlo simulations using (2.2.22) with the expectation and variance given in (2.3.24) and (2.3.25) respectively. Note here that, as we no longer require $\sigma \ll 1/\mathrm{Pe}_l$, the standard deviation is chosen to be $\sigma = 0.194$ (larger than that used in Figure 2.7(a)). This gives a 99% probability that the location of a sink ξ_k will remain inside the unit-cell $(k-1/2, k+1/2)$ for $k = 1,\ldots,N$. By examining (2.3.25) we see that the width and height of each spike are proportional to σ and

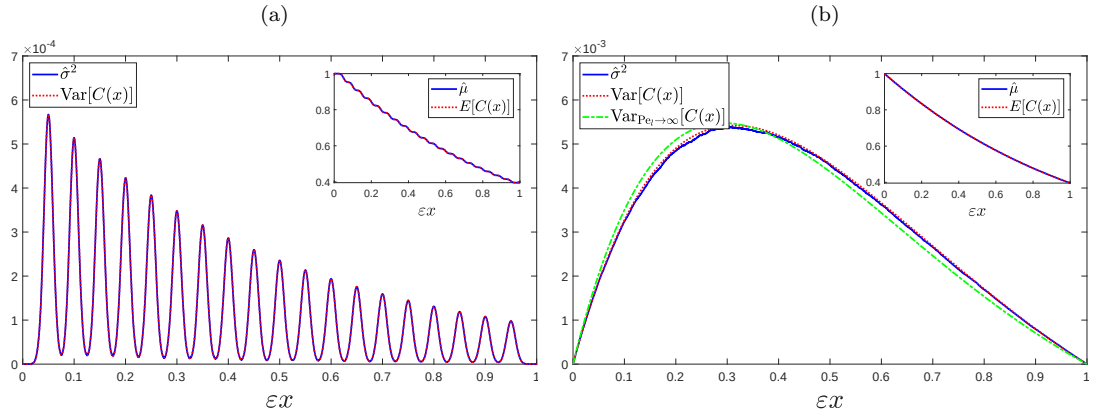

Figure 2.10: Comparison between the sample variance [$\hat{\sigma}^2$, solid blue] and the expression for the variance found using (2.2.24) [Var$[C(x)]$, dashed red]. Insets show a comparison between the sample mean [$\hat{\mu}$, solid blue] and the expectation found using (2.2.23) [$\mathbb{E}[C(x)]$, dashed red]. Here, 10^5 Monte Carlo simulations with (2.2.22) are used, where $N = 19$ (i.e. $\varepsilon = 0.05$) and $\mathrm{S} = \varepsilon$ in the limit of infinite Pe_l. (a) normally-perturbed sink locations with $\sigma = 0.194$, where the expectation and variance are given in (2.3.24) and (2.3.25) respectively. (b) uniformly-random sink locations with the expectation and variance given in (2.3.29) and (2.3.30) respectively. Also plotted is the variance given in (2.3.19) in the limit where $\mathrm{Pe}_l \to \infty$ [$\mathrm{Var}_{\mathrm{Pe}_l\to\infty}[C(x)]$, dot-dashed green].

S^2 respectively. When comparing this with (2.3.11) it is evident that the removal of diffusion causes the width and height of each spike to lose their dependence on the boundary-layer width and sink variance respectively. The smoothness of each spike is still dependent solely on σ, where choosing a larger σ for Figure 2.10(a) causes each spike to exhibit a smoother tip.

Let us now calculate the cdf credible interval using (2.2.27) to compare the two methods of quantifying disorder in the solute concentration. By (2.2.25) we have the cdf of a concentration C_j and its inverse are given by

$$F_{C_j}(C) = (1 + \mathrm{erf}((x-j)/(\sqrt{2}\sigma)))/2 \quad \text{and} \quad F^{-1}_{C_j}(C) = j + \sqrt{2}\sigma\,\mathrm{erf}^{-1}(2x-1) \tag{2.3.26}$$

respectively. So by using these with (2.2.26) we obtain

$$\breve{\xi}_j = j + \sqrt{2}\sigma\,\mathrm{erf}^{-1}(1-2r), \tag{2.3.27}$$

for $j = 1, \ldots, N$. Therefore using (2.2.27) gives the cdf credible intervals for a given r value as

$$CI(x;r) = C_0 - \mathrm{S}C_0 \sum_{j=1}^{N} (1+\mathrm{S})^{-j} H(x - j - \sqrt{2}\sigma\,\mathrm{erf}^{-1}(1-2r)). \tag{2.3.28}$$

This shows that the height of each jump is still dependent on S, but the width of the confidence interval is now dependent only on σ and r. Figure 2.11(a) shows the expectation, median

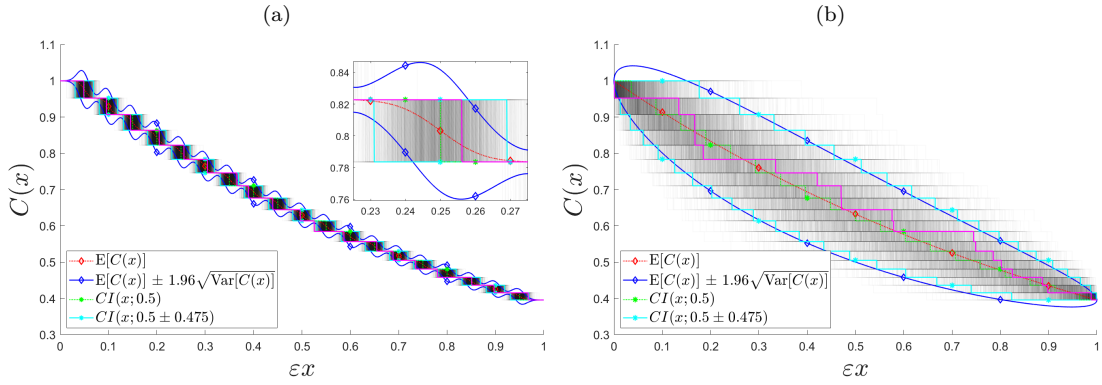

Figure 2.11: Depiction of 10^4 concentration profiles [grey] using (2.2.22), the expectation [$\mathbb{E}[C(x)]$, dashed red], Gaussian-based 95% credible intervals [$\mathbb{E}[C(x)] \pm 1.96\sqrt{\mathrm{Var}[C(x)]}$, solid blue], median [$CI(x;0.5)$, dashed green], cdf 95% credible intervals [$CI(x;0.5 \pm 0.475)$, solid cyan] and a single realisation [solid magenta]. Here, there are $N = 19$ point sinks (i.e. $\varepsilon = 0.05$) and $\mathrm{S} = \varepsilon$ in the limit of infinite Pe_l. (a) Sink locations are normally-perturbed with a standard deviation $\sigma = 0.194$, where (2.3.24) and (2.3.25) give the expectation and variance respectively and (2.3.28) gives the median and cdf 95% credible interval. The inset shows a magnification of one unit-cell. (b) Sink locations are uniformly random, where (2.3.29) and (2.3.30) give the expectation and variance respectively and (2.3.33) gives the median and cdf 95% credible interval.

($CI(x;0.5)$), Gaussian-based 95% credible intervals (calculated using 1.96 standard deviations on either side of the mean) and cdf 95% credible intervals ($CI(x;0.5 \pm 0.475)$), which are found using (2.3.24), (2.3.25) and (2.3.28). It is seen that both the expectation and Gaussian-based 95% credible intervals are represented by smooth functions, whereas the median and cdf 95% credible intervals are represented by discontinuous functions. These discontinuities are due to Heaviside function being present in (2.3.28), which result in the median and cdf 95% credible intervals preserving the jumps seen in concentration profiles, a structure which is lost when using moments. Figure 2.11(a) also shows large portions of concentration profiles lying outside (and empty spaces existing inside) the Gaussian-based 95% credible intervals, which is due to concentration profiles being distributed in a non-Gaussian manner about the mean. In contrast, we see the cdf 95% credible intervals preserving this non-Gaussian behaviour, thereby offering a better description of the system's disorder.

Let us now consider when sink locations are given by order statistics from a uniform distribution in the absence of diffusion. As for normally-perturbed sink locations, we calculate and compare the moments and cdf credible-intervals of the solute concentration.

Moments and cdf credible-intervals of the concentration for uniformly-random sink locations with zero diffusion

We will now consider the example where sink locations are prescribed as order statistics from a uniform distribution. In this example, by using the cdf given in (2.3.22) with (2.2.23) and (2.2.24), we obtain the expectation and variance as

$$\mathbb{E}[C(x)] = 1 - \mathrm{S}\sum_{j=1}^{N} (1+\mathrm{S})^{-j}\, I_{\varepsilon x}(j, N-j+1) \tag{2.3.29}$$

and

$$\begin{aligned}\mathrm{Var}[C(x)] = \mathrm{S}\sum_{j=1}^{N} \left(2 - (2+\mathrm{S})(1+\mathrm{S})^{-j} - \mathrm{S}\sum_{i=1}^{N}(1+\mathrm{S})^{-i} I_{\varepsilon x}(i, N-i+1)\right) \\ \times (1+\mathrm{S})^{-j} I_{\varepsilon x}(j, N-j+1)\end{aligned} \tag{2.3.30}$$

respectively. Figure 2.10(b) compares the sample mean and variance from 10^5 Monte Carlo simulations using (2.2.22), with the expectation and variance given in (2.3.29) and (2.3.30) respectively. The figure demonstrates a close match between moments of the concentration calculated using Monte Carlo simulations and ones calculated using the analytic expressions derived from (2.2.22). Also shown is the leading-order expression for the variance obtained by taking the limit $\mathrm{Pe}_l \to \infty$ in (2.3.19), which again shows a close fit to the sample variance. This demonstrates that the variance obtains the same maximum to leading-order as when diffusion is present, with $\mathrm{Var}_{\max}$ given in (2.3.20). When comparing the impact of diffusion on disorder, as can be seen by comparing Figures 2.7(b) and 2.10(b), both resulting variances exhibit a similar quadratic structure. However, differences can be seen when comparing the variance's structure near the outlet, as well as a difference in the variance's magnitude due to the use of different parameters.

Consider now using (2.2.26) to calculate credible-intervals of the concentration. By (2.2.25) we find the cdf of a concentration C_j and its inverse are

$$F_{C_j}(C) = 1 - I_{\varepsilon x}(j, N-j+1) \quad \text{and} \quad F^{-1}_{C_j}(C) = \varepsilon^{-1} I^{-1}_{1-x}(j, N-j+1) \tag{2.3.31}$$

respectively. So by using (2.2.26), we see the sink location for some cdf value r is given by

$$\breve{\xi}_j = \varepsilon^{-1} I_r^{-1}(j, N-j+1) \tag{2.3.32}$$

where $j = 1, \ldots, N$. So by using (2.2.27) the credible intervals for a given r value are given by

$$CI(x; r) = C_0 - \mathrm{S}C_0 \sum_{j=1}^{N} (1+\mathrm{S})^{-j} H(x - \varepsilon^{-1} I_r^{-1}(j, N-j+1)). \tag{2.3.33}$$

As for normally-perturbed sink locations we again find that the height of each jump is dependent only on S, but the width of each interval is now dependent on r and ε (which in turn shows a dependency on the number of sinks N). Figure 2.11(b) shows the expectation, median ($CI(x;0.5)$), Gaussian-based 95% credible intervals (calculated using 1.96 standard deviations on either side of the mean) and cdf 95% credible intervals ($CI(x;0.5\pm0.475)$, which are found using (2.3.29), (2.3.30) and (2.3.33). As for normally-perturbed sink locations we find both the expectation and Gaussian-based 95% credible intervals are given by smooth functions, whereas the median and cdf 95% credible intervals are given by discontinuous functions due to the Heaviside function in (2.3.28). As a result, both the median and cdf 95% credible intervals preserve jumps seen at sink locations in the concentration profiles. Also shown is how the Gaussian-based 95% credible intervals have empty spaces above (below) the maximum (minimum) concentrations near the inlet (outlet), showing that concentration profiles are distributed in a non-Gaussian manner about the mean. As the cdf 95% credible intervals are capable of preserving this non-Gaussian behaviour, we see a better description of the system's disorder when using (2.3.33).

Let us now consider using the cdf credible intervals for the solute concentration when diffusion is present in advection-dominated solute transport. This leads to concentration boundary-layers forming upstream of each sink, which replace the jumps in concentration seen when diffusion is zero.

Credible intervals for advection-dominated solute transport with non-zero diffusion

Consider now calculating cdf credible intervals when solute transport is advection dominated with a non-zero diffusive term. For this example we see a concentration boundary-layer form upstream of each sink location, with the concentration being given globally by (2.2.21). Let us use the cdf of sink locations given in (2.3.21) and (2.3.22) with the cdf confidence intervals given in (2.2.31). Firstly, when (2.2.30) uses normally-perturbed sink locations the confidence interval corresponding to r is given by

$$\breve{\xi}_j = j + \sqrt{2}\sigma\,\mathrm{erf}^{-1}(1-2r) + \frac{1}{\mathrm{Pe}_l}\ln\left|\frac{\hat{C}-C_{j-1}}{C_j-C_{j-1}}\right|. \tag{2.3.34}$$

Similarly, when sinks are given by order statistics from a uniform distribution then (2.2.30) gives the sink locations which obtain confidence intervals as

$$\breve{\xi}_j = I^{-1}_{1-r}(j, N-j+1) + \frac{1}{\mathrm{Pe}_l}\ln\left|\frac{\hat{C}-C_{j-1}}{C_j-C_{j-1}}\right|. \tag{2.3.35}$$

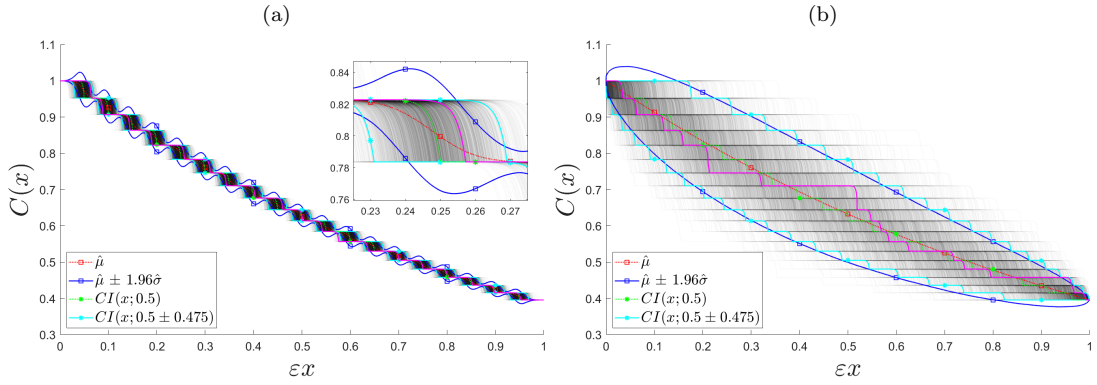

Figure 2.12: Depiction of 10^4 concentration profiles [grey] using (2.2.21), the sample mean [$\hat{\mu}$, dashed red], sample Gaussian-based 95% credible intervals [$\hat{\mu} \pm 1.96\hat{\sigma}$ (where $\hat{\sigma}$ represents the sample standard deviation), solid blue], median [$CI(x;0.5)$, dashed green], cdf 95% credible intervals [$CI(x;0.5 \pm 0.475)$, solid cyan] and a single realisation [solid magenta]. Here, there are $N = 19$ point sinks (i.e. $\varepsilon = 0.05$) with $\mathrm{Pe}_l = \varepsilon^{-1}$ and $\mathrm{S} = \varepsilon$. (a) Sink locations are normally-perturbed with a variance $\sigma = 0.194$, where the median and cdf 95% credible interval are calculated using (2.3.28). The inset shows a magnification of one unit-cell. (b) Sink locations are uniformly random, with the median and cdf 95% credible interval are calculated using (2.3.33).

Both (2.3.34) and (2.3.35) can then be used with (2.2.31) to calculate the cdf credible-intervals of the concentration. Figures 2.12(a) and 2.12(b) shows the sample mean and median ($CI(x;0.5)$) for normally-perturbed and uniformly-random sink locations respectively. Both figures show the median preserving the staircase structure of concentration profiles, which is lost when considering the sample mean. Also shown are the sample Gaussian-based 95% credible intervals and the cdf 95% credible intervals ($CI(x;0.5 \pm 0.475)$) calculated using (2.2.31). It is again shown that cdf credible intervals allow for the concentration profiles' staircase structure to be preserved as well as the non-Gaussian distribution of profiles about the mean to be captured, whereas Gaussian-based credible intervals do not.

2.4 Discussion

A one-dimensional advection-diffusion-uptake equation is used to model solute transport past a disordered array of point sinks with first-order uptake kinetics. Three different sink distributions are considered; periodic, normally perturbed from periodic locations and order statistics from a uniform distribution. To quantify the impact of sink locations on the solute concentration we use Monte Carlo simulations, a non-standard approach to homogenizing transport through a disordered system and the calculation of credible intervals. The homogenization approach, originally presented in Russell and Jensen (2020), initially calculates a deterministic

homogenized solution to the problem. Corrections which account for the impact of individual sink locations are subsequently calculated using an appropriate Green's function.

When there exists an advection-uptake balance on the macroscale with an advection-diffusion balance on the microscale a peripheral boundary-layer appears within concentration profiles at the outlet, see Figure 2.1(b). Consequently an alternative approach to classical homogenization is required due to using an ad-hoc assumption of two-scale dependence, where instead multiple lengthscales are present, an issue previously noted in Pavliotis and Stuart (2008). An integral approach is adopted to find a non-smooth correction $\widehat{C}_a(x)$ to the homogenized solution. This correction accounts for the periodic sink locations and the peripheral boundary-layer at the outlet, as shown in Figure 2.2. The integral approach is shown to converge to the numerical solution as the number of sinks (N) increases, with this approach having a smaller relative error than the classical approach given in Appendix A.2 for $N = 1, \ldots, 300$, as shown by the inset of Figure 2.2.

Disordered sink locations are then considered by normally-perturbing sinks away from a periodic configuration. The sink locations are given by $\xi_j = j + \sigma\widehat{\xi}_j$ for some standard deviation σ, where $\widehat{\xi}_j \sim \mathcal{N}(0,1)$ and $j = 1, \ldots, N$. Weak disorder is assumed by using $\sigma \ll 1$, which makes the probability of sinks trading places asymptotically small, therefore sink locations are independent of each other. To quantify how disordered sink locations influence the resulting solute concentration we again use the integral approach to find a correction to the homogenized solution, given by $\widehat{C}_b(x)$. The variance of this correction is seen to provide a close fit to the variance found when performing Monte Carlo simulations, which has a structure exhibiting sharp spikes in concentration at each sink location, see Figure 2.7(a). The structure of each spike is found to be dependent on various lengthscales, with the sharpness, magnitude and width of each spike being dependent on σ, $\mathrm{Pe}_l^2\,\mathrm{S}^2\sigma^2$ and $1/\mathrm{Pe}_l$ respectively, see Section 2.3.2. The sample covariance is given in Figure 2.5(b) and shows sinks having a strong local influence but weak far-field impact on the concentration.

Following this sink locations ξ_j are prescribed according to order statistics $U_{j:N}$ taken from the uniform distribution $\mathcal{U}(0, \varepsilon^{-1})$, where $U_{1:N} \leq U_{2:N} \leq \cdots \leq U_{N:N}$. Due to properties of order statistics each sink location depends on a Beta distribution such that $\varepsilon\xi_j \sim \mathrm{Beta}(j, N - j + 1)$ (Arnold et al., 1992), where the pdf for each ξ_j can be seen in Figure 2.8(a). Moments of the correction to the homogenized solution, given by $\widehat{C}_b(x)$, are calculated. In Figure 2.7(b) the concentration's variance is shown to be smooth, despite each concentration profile independently

exhibiting a 'wavy' sink-to-sink structure, with the magnitude being of order $\mathcal{O}(\mathrm{S}^2/\varepsilon)$. This is due to stronger disorder within the system causing microscale effects from individual point sinks to be smeared out. When away from the diagonal the sample covariance in Figure 2.5(d) is considerably larger when compared to using normally-perturbed sink locations, demonstrating how fluctuations in the sink locations can cause a strong long-range impact on the concentration.

A summary of the conditions for validity can be seen in Table 2.2, which are calculated using $\sqrt{\mathrm{Var}[C(x)]} \ll \mathbb{E}[C(x)]$. This requirement results in the correction due to disorder being asymptotically smaller than the mean. Both the mean and standard deviation have an order of magnitude in the limit $(\mathrm{Pe}_l, \mathrm{S}) \sim (1, \varepsilon)$ given by $\mathcal{O}\big(C_H(x)\big)$ and $\mathcal{O}\left(\sqrt{\mathrm{Var}[C(x)]}\right)$ respectively, where the variance for normally-perturbed and uniformly-random sink locations are given in (2.3.11) and (2.3.19) respectively. When considering solute transport being advection dominated with normally-perturbed and uniformly-random sink locations the mean is given in (2.3.24) and (2.3.29) and the variance is given in (2.3.25) and (2.3.30) respectively. The requirements show that uptake strength relative to advection must be suitably small to prevent disorder of sink locations causing too much variation from the mean concentration.

	Regime	$\mathcal{O}\big(\mathbb{E}[C(x)]\big)$	$\mathcal{O}\left(\sqrt{\mathrm{Var}[C(x)]}\right)$	Condition for validity
NP	$(\mathrm{Pe}_l, \mathrm{S}) \sim (1, \varepsilon)$, $\sigma \ll 1$	1	$\mathrm{Pe}_l\,\mathrm{S}\sigma$	$\mathrm{Pe}_l\,\mathrm{S}\sigma \ll 1$
UR	$(\mathrm{Pe}_l, \mathrm{S}) \sim (1, \varepsilon)$	1	$\sqrt{\sqrt{\mathrm{S}^2+\varepsilon^2}-\varepsilon}$	$\max(\mathrm{S}, \varepsilon) \ll 1$
NP	$\mathrm{Pe}_l \gg 1$, $\mathrm{S} \sim \varepsilon$, $\sigma \ll 1$	1	S	$\mathrm{S} \ll 1$
UR	$\mathrm{Pe}_l \gg 1$, $\mathrm{S} \sim \varepsilon$	1	$\sqrt{\sqrt{\mathrm{S}^2+\varepsilon^2}-\varepsilon}$	$\max(\mathrm{S}, \varepsilon) \ll 1$

Table 2.2: Table showing the conditions of validity for different regimes when sinks are normally perturbed from a periodic configuration (NP) and order statistics from a uniform distribution (UR).

We then consider when the Péclet number becomes asymptotically large, which causes a staircase structure to be exhibited in concentration profiles due to the boundary-layer width becoming asymptotically small. First, the mean and variance of the concentration is calculated when there is zero diffusion in the transport problem. Due to jumps in the solute concentration at each sink location results are found by considering the probability of being at a particular concentration. Despite jumps being present in each concentration profile at each sink location, the mean and variance are smooth functions depending on the cumulative distribution function (cdf) of sink locations, as shown in Figure 2.10. When sinks have normally-perturbed locations the magnitude of the variance is seen to lose dependency on the standard deviation as the impact of diffusion becomes negligible, where the magnitude instead only depends on the size

of each jump. Conversely, uniformly-random sink locations have no difference in the magnitude of the variance to leading-order, irrespective of the presence of diffusion. The conditions of validity for this example, which ensure disorder remains an order of magnitude smaller than the sample mean, are again given in Table 2.2.

An alternate method that preserved the staircase structure is then considered, which uses the inverse of the fixed concentration's cdf to calculate the expected location of each jump in concentration. This method allows comparison between Gaussian-based (which are given by 1.96 standard deviations either side of the mean) and cdf credible intervals. In Figure 2.11 we see the cdf credible intervals ($CI(x;r)$) are advantageous due to capturing the non-Gaussian distribution of concentration profiles about the sample mean, as well as preserving the jumps in concentration. For normally-perturbed sink locations the distance of each cdf credible interval from the median in the x-direction is seen to depend on σ and r, whereas for uniformly-random sink locations this dependency was on r and ε. One could consider tracking the cdf of the concentration, as done for an advection-uptake equation with a generic sink covariance function in Appendix A.5. However, solving the full partial differential equation derived (which is given in (A.5.16)) is beyond the scope of this research and so is not considered further.

The example where diffusion is present in the transport problem but advection dominates on both the microscale and macroscale is then considered. This results in the jumps in concentration at sink locations being replaced by boundary-layers forming upstream of each sink. The cdf credible intervals are calculated using (2.2.31) and are again found to preserve the structure of concentration profiles and capture the non-Gaussian distribution of concentration profiles about the mean, which is not found for the Gaussian-based approach.

Although the alternate approach to homogenization considered in this chapter demonstrates the importance of quantifying errors due to disordered sink locations, many other challenges still exist when considering its practical applications. Issues could arise due to variable sink strengths being introduced, a concept previously discussed in Russell et al. (2016). When considering the example of solute transport through the placenta, uptake strengths are likely to vary due to the complexity of uptake sites (Erlich et al., 2019a). Other extensions could consider having non-linear uptake kinetics (where zeroth-order kinetics have previously been studied (Chernyavsky et al., 2011)), using an unsteady or stochastic flow field (which have been observed in disordered media (Jin et al., 2016; Alim et al., 2017)) or describing uptake using a Gaussian process (which is later considered in Chapter 4).

Using a Green's function when homogenizing has proved a useful tool for this one-dimensional problem throughout parameter space (Russell and Jensen, 2020). As a result, an appropriate Green's function will be used in Chapter 3 for developing a generalised moments-based approach to homogenization that quantifies the impact of a disordered uptake function on solute concentration. This approach is applied in one, two and three spatial dimensions, where sink locations are regularised to prevent point sinks from introducing singularities in the solute concentration in higher dimensions. The present approach should aid the investigation of transport occurring over multiple lengthscales through disordered media.

Chapter 3

A moments-based approach to characterise uncertainty for solute transport past a discrete sink distribution

In this chapter, a more direct approach for quantifying the effect of a disordered sink distribution on the concentration of a solute will be considered. A direct mapping between the first two moments of the sink distributions and the first two moments of the solute concentration will be found, which allows discrete sink distributions, as were used in Chapter 2, as well as continuous sink distributions, which will be considered in Chapter 4 for Gaussian processes, to be used. This 'moments-based approach' is found to recover the one-dimensional corrections used in both Chapter 2 and Russell and Jensen (2020) and offer an extension into higher dimensions.

A three-dimensional solute transport model where advection is assumed to be unidirectional is presented in Section 3.1. Uptake occurs according to a distributed sink function $\hat{g}$, which contains isolated sinks with locally Gaussian structures of finite width ς. To approximate the solute concentration we seek non-local corrections to a deterministic homogenized solution that quantify the impact of a disordered uptake function in Section 3.2. These corrections are found by

successively inverting linear operators using an appropriate Green's function, as done in Chapter 2. To calculate moments of corrections to the homogenized solution we first find moments of the sink function $\hat{g}$ in Section 3.3. This is followed by calculating an appropriate free-space Green's function applying when advection and uptake dominate diffusion on the microscale in Section 3.4. By inverting the free-space Green's function we find a region of influence, wherein any sinks can influence the concentration at some given point. Throughout, analogous one- and two-dimensional results are also calculated, which allow any three-dimensional results to be generalised into n dimensions.

In one dimension, Panasenko and Volpert (2016) showed both the existence and convergence of the homogenized solution for an infinitesimally small sink width, a result which was implicitly used in Chapter 2 for point sink locations. However, Mahiout et al. (2020) found that, in three- (two-) dimensions having small volumes (areas) of sinks, the homogenized solution may become insufficient. These findings are reflected by the properties of the n-dimensional free-space Green's function $\mathcal{G}_n(\mathbf{x}-\mathbf{x}')$ (see Section 3.4), which at $\mathbf{x}=\mathbf{x}'$ has no singularity, a singularity of logarithmic scale ($\log|\mathbf{x}-\mathbf{x}'|$) and a singularity of reciprocal scale ($1/|\mathbf{x}-\mathbf{x}'|$) in one, two and three dimensions respectively. A key question addressed in this chapter is how well the homogenization approximations of disordered point sinks perform as the sink width ς tends to zero.

Deterministic corrections to the homogenized solution are found for periodic sink locations in Section 3.5.1. We find that, in the limit of an asymptotically small sink width, the correction scales with the logarithm and reciprocal of the sink width in two and three dimensions respectively. Following this, we use a direct mapping between moments of the sink function and moments of corrections to quantify the impact of a disordered uptake field on the solute concentration. In Section 3.5.2 we consider perturbing sinks from periodic locations using a normal distribution with mean zero and variance σ^2. In the limit $\varsigma, \sigma \ll 1$ we find that the leading-order mean correction in two and three dimensions scales with the logarithm and reciprocal of $\sqrt{\varsigma^2+\sigma^2}$ respectively. In Section 3.5.3 sink locations are prescribed according to a uniform distribution, where due to the expected sink location being constant in space we find the leading-order mean correction is zero. Therefore we calculate the second-order mean correction, which is found to become dependent only on the advective direction when sufficiently far from lateral boundaries. By again taking the limit of an asymptotically small sink width we find the second-order correction scales with the logarithm and reciprocal of the sink width in two and three dimensions respectively. For disordered sink locations in Sections 3.5.2 and 3.5.3

we will find an upper bound for the variance of the leading-order correction, which is calculated by approximating the regularised sink function for an asymptotically small sink width with a δ-function.

3.1 Model

We will here present a three-dimensional model, but analogous one- and two-dimensional models will later be adopted when required. Let $\mathcal{D}_3$ be a three-dimensional domain with position vector $\mathbf{x}^* = (x_1^*, x_2^*, x_3^*) \in \mathcal{D}_3$ such that $x_1^* \in [0, L]$ and $x_2^*, x_3^* \in \mathbb{R}$ for some domain length L. Allow $C^*(\mathbf{x}^*; \omega), U, D$ and S_1 to represent the solute concentration field, constant advective velocity in the x_1^* direction, constant diffusion coefficient and constant uptake rate respectively. Note that S_1 has dimensions 1/time, as opposed to S_0 in Chapter 2 which had dimensions length/time (i.e. $S_1 = lS_0$ where l is the inter-sink distance used in Chapter 2). We represent uptake using a distributed sink function $\hat{g}^*(\mathbf{x}^*; \omega)$, which describes discrete, isolated sink locations of finite width and satisfies $1 + \hat{g}^*(\mathbf{x}^*; \omega) \geq 0$. Here, ω denotes that $\hat{g}^*(\mathbf{x}^*; \omega)$ is a realisation drawn from a prescribed distribution, which in turn makes $C^*(\mathbf{x}^*; \omega)$ a random variable. Note that $\hat{g}^*(\mathbf{x}^*; \omega)$ could also be used to describe a continuous random field with non-uniform sink strengths, which is later considered in Chapter 4 for the example of a Gaussian process.

We prescribe a flux q on the plane $x_1 = 0$, zero diffusive flux on $x_1 = 1$ and allow the diffusive flux to approach zero as $x_2, x_3 \to \pm\infty$. By assuming that the sink function has zero impact on the flow field, the solute concentration $C^*(\mathbf{x}^*; \omega)$ can be described using a three-dimensional advection-diffusion-uptake equation given by

$$D\nabla_{3D}^{*2} C^* - UC_{x_1^*}^* - S_1 C^*(1 + \hat{g}^*(\mathbf{x}^*; \omega)) = 0, \tag{3.1.1}$$

with boundary conditions

$$(U - D\partial_{x_1^*})C^*|_{x_1^*=0} = q, \quad C_{x_1^*}^*|_{x_1^*=L} = 0, \quad C_{x_2^*}|_{x_2^* \to \pm\infty} \to 0, \quad \text{and} \quad C_{x_3^*}|_{x_3^* \to \pm\infty} \to 0,$$

where $\nabla_{3D}^{*2} = \partial_{x_1^{*2}} + \partial_{x_2^{*2}} + \partial_{x_3^{*2}}$. The boundary conditions are chosen to minimise their influence on the solute concentration, allowing the influence of the sink function $\hat{g}^*$ to be illustrated. We introduce the following non-dimensional parameters: $\mathrm{Pe}_L = UL/D$ is the Péclet number (which represents the strength of advection to diffusion), $\mathrm{Da} = S_1 L^2/D$ is the Damköhler number (which relates the rate of uptake to diffusion), $\mathbf{x} = \mathbf{x}^*/L$, $\hat{g}(\mathbf{x}; \omega) = \hat{g}^*(\mathbf{x}^*; \omega)$ and $C(\mathbf{x}; \omega) = C^*(\mathbf{x}^*; \omega)/C_0$ where $C_0 = q/U$ is a concentration scale. Variables are non-dimensionalized using the domain length L as opposed to the inter-sink distance l used in Chapter 2, where the variables in each chapter can be related by $\mathrm{Pe}_L = \varepsilon\,\mathrm{Pe}_L$ and $\mathrm{Da} = \varepsilon\,\mathrm{Pe}_L\,\mathrm{S}$

for $\varepsilon = l/L$ (as in Chapter 2). These non-dimensional parameters give the non-dimensional form of (3.1.1) as

$$\nabla^2_{3D} C - \mathrm{Pe}_L \, C_{x_1} - \mathrm{Da}\, C(1 + \hat{g}(\mathbf{x};\omega)) = 0, \tag{3.1.2a}$$

with boundary conditions

$$(1 - \mathrm{Pe}_L^{-1}\, \partial_{x_1}) C|_{x_1=0} = 1, \quad C_{x_1}|_{x_1=1} = 0, \quad C_{x_2}|_{x_2 \to \pm\infty} \to 0 \quad \text{and} \quad C_{x_3}|_{x_3 \to \pm\infty} \to 0, \tag{3.1.2b}$$

where $x_1 \in [0,1]$, $x_2, x_3 \in \mathbb{R}$ and $\nabla^2_{3D} = \partial_{x_1^2} + \partial_{x_2^2} + \partial_{x_3^2}$.

Consider a discrete sink function with regularised sink locations of finite size occupying a cuboid $\mathcal{D}_3^s$, where for all $\mathbf{x} \in \mathcal{D}_3^s$ then $x_1 \in [0,1]$ and $x_2, x_3 \in [-L_s, L_s]$. Allow $\lambda = 1/N$ to be the average inter-sink distance in the x_1-, x_2- and x_3-directions and set $L_s = (2k-1)\lambda/2$ for any $k \in \mathbb{Z}^+$, where $N \in \mathbb{Z}^+$ represents the number of sinks per unit length. Let the midpoint of sink locations be represented by $\boldsymbol{\xi}_{\mathbf{i}_3} = (\xi_i, \xi_j, \xi_k)$, where $\mathbf{i}_3 \in \{i,j,k\}$, $i = 1, \ldots, N$ and $j,k = -M, \ldots, M$ with $M = \lfloor L_s N \rfloor \in \mathbb{Z}$. This causes there to be $(2M+1)^2/\lambda$ sinks in the domain $\mathcal{D}_3^s$ with an average density per unit volume given by λ^{-3}. We will now define the sink function $\hat{g}(\mathbf{x};\omega)$ to be

$$\hat{g}(\mathbf{x};\omega) = \lambda^3 \sum_{\mathbf{i}_3} F^3_\varsigma(\mathbf{x} - \boldsymbol{\xi}_{\mathbf{i}_3}) - 1, \tag{3.1.3}$$

where $\sum_{\mathbf{i}_3} \equiv \sum_{i=1}^{N} \sum_{j=-M}^{M} \sum_{k=-M}^{M}$ and $F^3_\varsigma(\mathbf{x} - \boldsymbol{\xi}_{\mathbf{i}_3})$ is a regularised uptake function with width $\varsigma \ll 1$ such that

$$\int_{\mathcal{D}_3^s} F^3_\varsigma(\mathbf{x} - \boldsymbol{\xi}_{\mathbf{i}_3}) \, \mathrm{d}\boldsymbol{\xi}_{\mathbf{i}_3} = 1. \tag{3.1.4}$$

Here, the choice of F^3_ς ensures $\hat{g}(\mathbf{x};\omega)$ has a spatially averaged sink density of zero within the domain $\mathcal{D}_3^s$. Throughout, three different sink distributions will be considered, with sink locations being prescribed according to the following distributions:

1. Periodic, where $\boldsymbol{\xi}_{\mathbf{i}_3} = \mathbf{e}_{\mathbf{i}_3} = \lambda((2i-1)/2, j, k)$ for $\mathbf{i}_3 \in \{i,j,k\}$, $i = 1, \ldots, N$ and $j,k = -M, \ldots, M$.

2. Normally-perturbed from a periodic configuration, where $\boldsymbol{\xi}_{\mathbf{i}_3} \sim \mathcal{N}(\mathbf{e}_{\mathbf{i}_3}, \sigma^2 I)$ for $\mathbf{i}_3 \in \{i,j,k\}$, $i = 1, \ldots, N$ and $j,k = -M, \ldots, M$. Here, I represents the identity matrix and $\mathbf{e}_{\mathbf{i}_3} = \lambda((2i-1)/2, j, k)$ are the mean sink locations. It will be assumed that σ remains sufficiently small, thereby ensuring sinks remain within the domain and do not trade positions, resulting in the sink locations being independent and identically distributed.

3. Multivariate uniform distribution, where $\boldsymbol{\xi}_{\mathbf{i}_3} = (\xi_i, \xi_j, \xi_k)$ for $\mathbf{i}_3 \in \{i, j, k\}$, $i = 1, \ldots, N$ and $j, k = -M, \ldots, M$ such that $\xi_i \sim \mathcal{U}[0, 1]$ and $\xi_j, \xi_k \sim \mathcal{U}[-L_s, L_s]$.

Similar definitions of the sink function can be made for a one- [two-] dimensional domain $\mathcal{D}_1$ [$\mathcal{D}_2$], where F_ς^3 is replaced by F_ς^1 [F_ς^2], volumes (λ^3) are replaced by distances (λ) [areas (λ^2)] and triple-sums over $\mathbf{i}_3 \in \{i, j, k\}$ are replaced by single- [double-] sums over $\mathbf{i}_1 = i$ [$\mathbf{i}_2 \in \{i, j\}$]. When taking the limit $\varsigma \to 0$ in n dimensions we see the function F_ς^n converges to an n-dimensional δ-function with the correct weight.

When the sink function has a Gaussian structure we define the n-dimensional sink function F_ς^n as

$$F_\varsigma^n(\mathbf{x} - \mathbf{x}_{\mathbf{i}_n}) = \frac{1}{(2\pi\varsigma^2)^{n/2}} \exp\left(-\frac{1}{2\varsigma^2}|\mathbf{x} - \mathbf{x}_{\mathbf{i}_n}|^2\right), \tag{3.1.5}$$

where ς must remain suitably small to satisfy (3.1.4) and prevent sinks influencing the concentration outside the domain $\mathcal{D}_n^s$.

Figures 3.1(a), 3.1(b) and 3.1(c) show realisations of the solute concentration in two dimensions for 25 periodic, normally-perturbed and uniformly-random sink locations respectively. Sinks are contained inside the domain $\mathcal{D}_2^s = [0, 1] \times [-0.5, 0.5]$ and have an average inter-sink distance $\lambda = 0.2$. Each realisation is calculated numerically using the finite-difference solver outlined in Appendix B.2. Sample moments of the solute concentration are calculated by averaging over 10^4 Monte Carlo realisations and are shown in Figure 3.1 (d)-(g). Each realisation produced uses a step-size $h = 0.004$ with sample moments requiring approximately 1 day of 8-core parallel computation. The convergence of each solution has been verified.

Figures 3.1(d) and 3.1(e) show the sample expectation of the concentration when sinks take normally-perturbed and uniformly-random locations respectively. When sinks are normally-perturbed the expectation is shown to preserve the row structure which is exhibited in each realisation, with an ellipsoidal shape forming about the mean sink locations. However, when sink locations are given by a uniform distribution the mean sink location becomes uniform across $\mathcal{D}_2^s$. As a result, any behaviour exhibited by individual sink locations is smeared out when averaging over many realisations.

Figures 3.1(f) and 3.1(g) show the sample variance of the concentration. Figure 3.1(f) uses normally-perturbed sink locations with a standard deviation $\sigma = 0.02$. This causes the variance from each row of sinks to become small when reaching the boundary of a neighbouring row,

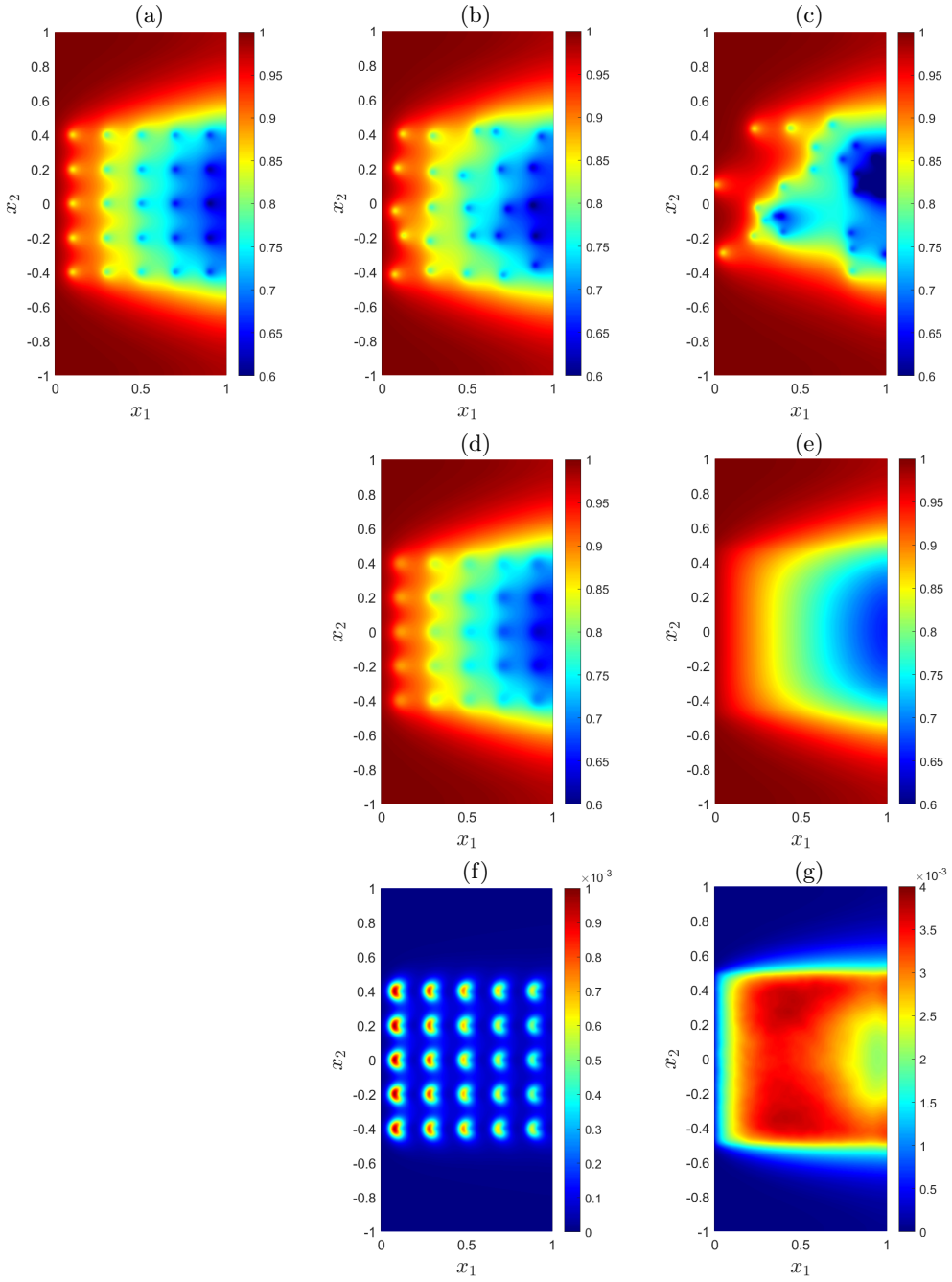

Figure 3.1: Two-dimensional solute concentration, where (a)-(c) show realisations with sinks appearing as spots, (d)-(e) show sample expectations and (f)-(g) show sample variances. Panel (a), panels (b), (d), (f) and panels (c), (e), (g) represent periodic, normally-perturbed according to a standard deviation $\sigma = 0.02$ and uniformly-random sink locations respectively. Realisations are found using (3.1.2) with Appendix B.2 and sample moments are calculated using 10^4 realisations. All figures use $\mathcal{D}_2^s = [0,1] \times [-0.5, 0.5]$, $\lambda = 0.2$, $(\mathrm{Pe}_L, \mathrm{Da}) = (20, 10)$ and $\varsigma = 0.01$.

demonstrating the influence of sink locations being independent and identically distributed. Therefore individual sinks have a strong short-range impact but a weak long-range impact. This is in contrast with Figure 3.1(g) which uses uniformly-random sink locations. As the probability of a sink being at a given $\mathbf{x}$ location is uniform within $\mathcal{D}_2^s$, we see the variance is a smooth, x_2-independent function with a single peak when suitably far from boundaries. This reflects how the impact from individual sinks is smeared out when averaging over many realisations.

To further illustrate the two-dimensional uniformly-random case, consider when L_s becomes asymptotically large compared to the average inter-sink distance λ. Figures 3.2(a), 3.2(b) and 3.2(c) use $L_s = 2.5$ and $\lambda = 0.2$ in two dimensions to show one realisation, the sample expectation and the sample variance respectively, where sample statistics are calculated using 10^4 Monte Carlo realisations. We again use Appendix B.2 with a step-size $h = 0.004$ and verify convergence, with sample moments requiring approximately 2 days of 8-core parallel computation. Figures 3.2(b) and 3.2(c) show the expectation and variance becoming independent of x_2 when suitably far from the boundaries of $\mathcal{D}_2^s$ respectively. This is again due to smearing the impact of individual sinks, as well as the influences from x_2-boundaries being negligible for large portions of the domain $\mathcal{D}_2^s$ due to L_s being suitably large. We will seek to approximate these smooth one-dimensional functions in terms of the sink density λ and width ς.

A moments-based approach will now be developed, which is used to approximate the moments of the concentration found in Figures 3.1 and 3.2. The approach finds iterative corrections to a homogenized solution by exploiting an appropriate Green's function when inverting linear operators. This will allow the impact of a disordered sink function on the solute concentration field to be quantified, which is done using a direct mapping between the first two moments of the sink function and the first two moments of the concentration field.

3.2 Developing a moments-based approach for characterising uncertainty

Define a three-dimensional linear and boundary operator as

$$\mathcal{L}_3 = \nabla_{3D}^2 - \mathrm{Pe}_L\, \partial_{x_1} - \mathrm{Da} \quad \text{and}$$

$$\mathcal{B}_3 = \{(1 - (1/\mathrm{Pe}_L)\partial_{x_1})\,(\cdot)|_{x_1=0},\, \partial_{x_1}(\cdot)|_{x_1=1},\, \partial_{x_2}(\cdot)|_{x_2\to-\infty}, \partial_{x_2}(\cdot)|_{x_2\to\infty},\, \partial_{x_3}(\cdot)|_{x_3\to-\infty},\, \partial_{x_3}(\cdot)|_{x_3\to\infty}\}$$

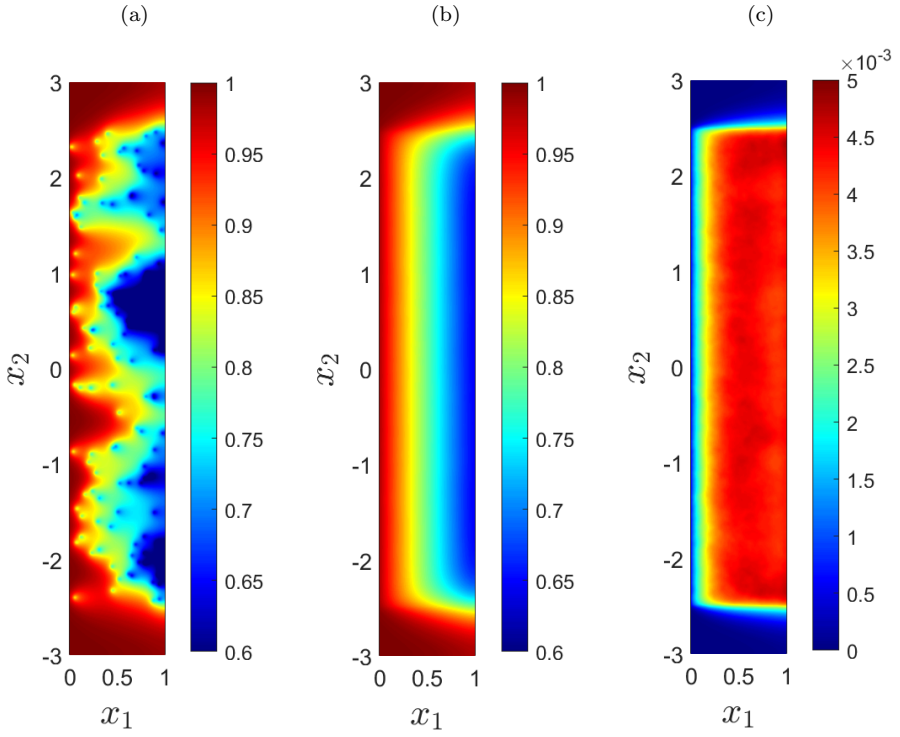

Figure 3.2: Two-dimensional solute concentration for uniformly-random sinks located in a domain $\mathcal{D}_2^s = [0,1] \times [-2.5, 2.5]$. Here, (a) shows a single realisation, (b) shows the sample expectation and (c) shows the sample variance. Realisations are found using (3.1.2) with Appendix B.2 and sample moments are calculated using 10^4 realisations. All figures use $\lambda = 0.2$, $(\mathrm{Pe}_L, \mathrm{Da}) = (20, 10)$ and $\varsigma = 0.01$.

respectively. Then a homogenized solution $C_H(\mathbf{x})$ associated with (3.1.2) can be found by solving

$$\mathcal{L}_3 C_H(\mathbf{x}) = 0, \quad \mathcal{B}_3 C_H(\mathbf{x}) = \{1, 0, 0, 0, 0, 0\}. \tag{3.2.1}$$

Using separation of variables we see that $C_H(\mathbf{x})$ depends only on x_1, therefore (3.2.1) can be solved using an identical approach to that used in Chapter 2 to give

$$C_H(\mathbf{x}) = C_H(x_1) = \frac{\mathrm{Pe}_L}{\psi(1)}\Big((2\phi - \mathrm{Pe}_L)e^{\phi(x_1-1)} + (2\phi + \mathrm{Pe}_L)e^{\phi(1-x_1)}\Big)e^{(\mathrm{Pe}_L/2)x_1}, \tag{3.2.2}$$

where $\phi = \sqrt{\mathrm{Pe}_L^2/4 + \mathrm{Da}}$ and $\psi(x_1) = (2\,\mathrm{Pe}_L\,\phi + \mathrm{Pe}_L^2 + 2\,\mathrm{Da})e^{\phi x_1} + (2\,\mathrm{Pe}_L\,\phi - \mathrm{Pe}_L^2 - 2\,\mathrm{Da})e^{-\phi x_1}$. As done in Russell and Jensen (2020) and Chapter 2, we will now pose that the concentration can be written

$$C(\mathbf{x};\omega) = C_H(x_1) + \widehat{C}(\mathbf{x};\omega), \tag{3.2.3}$$

where $\widehat{C}(\mathbf{x};\omega)$ is some correction accounting for the disordered sink function. To calculate this correction an integral approach which exploits the associated Green's function will be used,

similar to that presented in Dagan (1984). This approach is a modification of that given in Russell and Jensen (2020) and Chapter 2, where it is later shown to recover the approach for a discrete sink function. Let the correction to the homogenized solution be given by

$$\widehat{C}(\mathbf{x};\omega) = \mathrm{Da}\,\widehat{C}_1(\mathbf{x};\omega) + \mathrm{Da}^2\,\widehat{C}_2(\mathbf{x};\omega) + \dots \tag{3.2.4}$$

where we assume $\mathrm{Da}\,\widehat{C}_1(\mathbf{x};\omega) \ll \mathrm{Da}^2\,\widehat{C}_2(\mathbf{x};\omega) \ll \dots$, then (3.1.2) gives

$$\mathcal{L}_3\left(\widehat{C}_1(\mathbf{x};\omega) + \mathrm{Da}\,\widehat{C}_2(\mathbf{x};\omega) + \dots\right) = \hat{g}(\mathbf{x};\omega)\left(C_H(x_1) + \mathrm{Da}\,\widehat{C}_1(\mathbf{x};\omega) + \mathrm{Da}^2\,\widehat{C}_2(\mathbf{x};\omega) + \dots\right).$$

So a solution, which is validated *a posteriori*, can be constructed using the ansatz

$$\mathcal{L}_3\widehat{C}_1(\mathbf{x};\omega) = \hat{g}(\mathbf{x};\omega)C_H(x_1), \quad \mathcal{B}_3\widehat{C}_1(\mathbf{x};\omega) = \{0,\dots,0\}, \tag{3.2.5a}$$

$$\mathcal{L}_3\widehat{C}_2(\mathbf{x};\omega) = \hat{g}(\mathbf{x};\omega)\widehat{C}_1(\mathbf{x};\omega), \quad \mathcal{B}_3\widehat{C}_2(\mathbf{x};\omega) = \{0,\dots,0\}, \tag{3.2.5b}$$

$$\vdots$$

As in Chapter 2 we will take a constructive approach, without seeking to prove formal convergence of the series given in (3.2.4). To invert the linear operators in (3.2.5), define $G_3(\mathbf{x},\mathbf{x}')$ to be the associated three-dimensional Green's function such that

$$\mathcal{L}_3G_3(\mathbf{x},\mathbf{x}') = \delta(\mathbf{x}-\mathbf{x}'), \quad \text{where} \quad \mathcal{B}_3G_3(\mathbf{x},\mathbf{x}') = \{0,\dots,0\}. \tag{3.2.6}$$

Note that applying homogeneous boundary conditions in the x_2- and x_3-directions is appropriate as the source term is compact. The Green's function can then be used to give the corrections $\widehat{C}_1(\mathbf{x};\omega), \widehat{C}_2(\mathbf{x};\omega), \dots$ as

$$\widehat{C}_1(\mathbf{x};\omega) = \int_{\mathcal{D}_3} G_3(\mathbf{x},\mathbf{x}')C_H(x_1')\hat{g}(\mathbf{x}';\omega)\,\mathrm{d}\mathbf{x}', \tag{3.2.7}$$

$$\widehat{C}_2(\mathbf{x};\omega) = \int_{\mathcal{D}_3}\int_{\mathcal{D}_3} G_3(\mathbf{x},\mathbf{x}')G_3(\mathbf{x}',\mathbf{x}'')C_H(x_1'')\hat{g}(\mathbf{x}';\omega)\hat{g}(\mathbf{x}'';\omega)\,\mathrm{d}\mathbf{x}'\,\mathrm{d}\mathbf{x}'', \tag{3.2.8}$$

$$\vdots$$

We will now characterise the corrections in terms of their moments evaluated over realisations, specifically

$$\mathbb{E}\left[\widehat{C}_1(\mathbf{x};\omega)\right] = \int_{\mathcal{D}_3} G_3(\mathbf{x},\mathbf{x}')C_H(x_1')\mathbb{E}[\hat{g}(\mathbf{x}';\omega)]\,\mathrm{d}\mathbf{x}', \tag{3.2.9}$$

$$\mathcal{K}_{\widehat{C}_1}[\mathbf{x},\mathbf{y}] = \int_{\mathcal{D}_3}\int_{\mathcal{D}_3} G_3(\mathbf{x},\mathbf{x}')C_H(x_1')\mathcal{K}_{\hat{g}}[\mathbf{x}',\mathbf{y}']G_3(\mathbf{y},\mathbf{y}')C_H(y_1')\,\mathrm{d}\mathbf{x}'\,\mathrm{d}\mathbf{y}' \tag{3.2.10}$$

and

$$\mathbb{E}\left[\widehat{C}_2(\mathbf{x};\omega)\right] = \int_{\mathcal{D}_3}\int_{\mathcal{D}_3} G_3(\mathbf{x},\mathbf{x}')G_3(\mathbf{x}',\mathbf{x}'')C_H(x_1'')\mathbb{E}\left[\hat{g}(\mathbf{x}';\omega)\hat{g}(\mathbf{x}'';\omega)\right]\,\mathrm{d}\mathbf{x}'\,\mathrm{d}\mathbf{x}'', \tag{3.2.11}$$

where $\mathcal{K}_f[\mathbf{x},\mathbf{y}] \equiv \mathcal{K}[f(\mathbf{x};\omega), f(\mathbf{y};\omega)]$ and $\mathcal{K}$ represents the covariance function. This approach can be extended into n dimensions using identical calculations and replacing $\mathcal{D}_3$ and $G_3(\mathbf{x},\mathbf{x}')$ with $\mathcal{D}_n$ and $G_n(\mathbf{x},\mathbf{x}')$ respectively. When $\hat{g}$ represents point sink locations in one dimension, the corrections recover those found in Russell and Jensen (2020) and Chapter 2. This is done by comparing the sum of $\widehat{C}_a$ and $\widehat{C}_b$ (found in (2.2.15) and (2.2.17) respectively) with using $\hat{g}(x_1) = \sum_{j=1}^{N} \delta(x_1 - \xi_j) - 1$ in (3.2.7), with S being replaced by Da due a change in non-dimensional parameters.

From (3.2.9)-(3.2.11) we see that when finding corrections to the homogenized solution, we first must characterise sink distributions in terms of their first two statistical moments. This will be done in Section 3.3 for normally-perturbed and uniformly-random sink locations, where the sink function with Gaussian structure given in (3.1.5) is used. For both examples, the moments are calculated for three spatial dimensions, with analogous n-dimensional results being stated.

3.3 Moments of the sink function

3.3.1 Normally-perturbed sink locations

Let sink locations be normally-perturbed from a periodic configuration such that

$$\boldsymbol{\xi}_{\mathbf{i}_3} = \mathbf{e}_{\mathbf{i}_3} + \sigma\hat{\boldsymbol{\xi}}_{\mathbf{i}_3}, \qquad \text{where} \qquad \hat{\boldsymbol{\xi}}_{\mathbf{i}_3} \sim \mathcal{N}(\mathbf{0}, I) \tag{3.3.1}$$

with I representing the identity matrix and $\mathbf{e}_{\mathbf{i}_3}$ some mean sink location. Thus, each sink location $\boldsymbol{\xi}_{\mathbf{i}_3}$ has a normally distributed probability density function (pdf)

$$\pi_{\boldsymbol{\xi}_{\mathbf{i}_3}}(\mathbf{x}) = \frac{1}{(2\pi\sigma^2)^{(3/2)}} \exp\left(-\frac{1}{2\sigma^2}|\mathbf{x} - \mathbf{e}_{\mathbf{i}_3}|^2\right).$$

When σ is sufficiently small, the sink locations $\boldsymbol{\xi}_{\mathbf{i}_3}$ are independently distributed, therefore the joint pdf of sink locations becomes

$$\pi_{\boldsymbol{\xi}_1,\boldsymbol{\xi}_2,\ldots}(\mathbf{x_1},\mathbf{x_2},\ldots) = \prod_{\mathbf{i}_3} \pi_{\boldsymbol{\xi}_{\mathbf{i}_3}}(\mathbf{x}_{\mathbf{i}_3}). \tag{3.3.2}$$

This gives the expectation of the sink function $\hat{g}(\mathbf{x};\omega)$ as

$$\begin{aligned}\mathbb{E}\left[\hat{g}(\mathbf{x};\omega)\right] &= \int_{\mathcal{D}_3}\int_{\mathcal{D}_3} \ldots \left(\lambda^3 \sum_{\mathbf{i}_3} F_\varsigma^3(\mathbf{x} - \mathbf{x}_{\mathbf{i}_3}) - 1\right) \prod_{\mathbf{j}_3} \pi_{\boldsymbol{\xi}_{\mathbf{j}_3}}(\mathbf{x}_{\mathbf{j}_3})\, \mathrm{d}\mathbf{x_1}\mathrm{d}\mathbf{x_2}\ldots \\ &= \lambda^3 \sum_{\mathbf{i}_3} \mathbb{E}[F_\varsigma^3(\mathbf{x} - \mathbf{x}_{\mathbf{i}_3})] - 1. \end{aligned} \tag{3.3.3}$$

In a similar fashion we can calculate $\mathbb{E}[\hat{g}(\mathbf{x};\omega)\hat{g}(\mathbf{y};\omega)]$ to be

$$\mathbb{E}\left[\hat{g}(\mathbf{x};\omega)\hat{g}(\mathbf{y};\omega)\right] = \lambda^6 \sum_{\substack{\mathbf{i}_3 \\ \mathbf{i}_3 \neq \mathbf{j}_3}} \sum_{\mathbf{j}_3} \mathbb{E}[F_\varsigma^3(\mathbf{x}-\mathbf{x}_{\mathbf{i}_3})]\mathbb{E}[F_\varsigma^3(\mathbf{y}-\mathbf{x}_{\mathbf{j}_3})] + \lambda^6 \sum_{\mathbf{i}_3} \mathbb{E}[F_\varsigma^3(\mathbf{x}-\mathbf{x}_{\mathbf{i}_3})F_\varsigma^3(\mathbf{y}-\mathbf{x}_{\mathbf{i}_3})]$$
$$-\lambda^3 \sum_{\mathbf{i}_3} \mathbb{E}[F_\varsigma^3(\mathbf{x}-\mathbf{x}_{\mathbf{i}_3})] - \lambda^3 \sum_{\mathbf{j}_3} \mathbb{E}[F_\varsigma^3(\mathbf{y}-\mathbf{x}_{\mathbf{j}_3})] + 1, \tag{3.3.4}$$

which can be used with (3.3.3) to give the covariance of the correction $\hat{g}$ as

$$\begin{aligned}\mathcal{K}_{\hat{g}}[\mathbf{x},\mathbf{y}] &= \lambda^6 \sum_{\mathbf{i}_3} \left(\mathbb{E}[F_\varsigma^3(\mathbf{x}-\mathbf{x}_{\mathbf{i}_3})F_\varsigma^3(\mathbf{y}-\mathbf{x}_{\mathbf{i}_3})] - \mathbb{E}[F_\varsigma^3(\mathbf{x}-\mathbf{x}_{\mathbf{i}_3})]\mathbb{E}[F_\varsigma^3(\mathbf{y}-\mathbf{x}_{\mathbf{i}_3})]\right) \\ &= \lambda^6 \sum_{\mathbf{i}_3} \mathcal{K}_{F_\varsigma^3}[\mathbf{x}-\mathbf{x}_{\mathbf{i}_3}, \mathbf{y}-\mathbf{x}_{\mathbf{i}_3}],\end{aligned} \tag{3.3.5}$$

where for some function f we let $\mathcal{K}_f$ represent the covariance function of f, notation previously used in Section 3.1. The moments of $\hat{g}(\mathbf{x};\omega)$ can then be used with (3.2.9)-(3.2.11) to find the moments of the corrections $\widehat{C}_1(\mathbf{x};\omega), \widehat{C}_2(\mathbf{x};\omega), \ldots$, which quantify the effect of disordered sink locations on the solute concentration.

We will now consider when the function F_ς^3 has a Gaussian structure given in (3.1.5), which gives $\pi_{\boldsymbol{\xi}_{\mathbf{j}_3}}(\mathbf{x}_{\mathbf{j}_3}) = F_\sigma^3(\mathbf{x}-\mathbf{e}_{\mathbf{j}_3})$. For this example we have

$$\mathbb{E}[F_\varsigma^3(\mathbf{x}-\mathbf{x}_{\mathbf{i}_3})] = I_2(x_1,e_1;\varsigma,\sigma)I_2(x_2,e_2;\varsigma,\sigma)I_2(x_3,e_3;\varsigma,\sigma) \tag{3.3.6}$$

and

$$\mathbb{E}[F_\varsigma^3(\mathbf{x}-\mathbf{x}_{\mathbf{i}_3})F_\varsigma^3(\mathbf{y}-\mathbf{x}_{\mathbf{i}_3})] = I_3(x_1,y_1,e_1;\varsigma,\varsigma,\sigma)I_3(x_2,y_2,e_2;\varsigma,\varsigma,\sigma)I_3(x_3,y_3,e_3;\varsigma,\varsigma,\sigma), \tag{3.3.7}$$

where

$$I_2(x,y;\sigma_x,\sigma_y) \equiv \frac{1}{2\pi\sigma_x\sigma_y}\int_{-\infty}^{\infty} \exp\left(-\frac{1}{2\sigma_x^2}(\hat{x}-x)^2 - \frac{1}{2\sigma_y^2}(\hat{x}-y)^2\right) \mathrm{d}\hat{x} \tag{3.3.8}$$

and

$$I_3(x,y,z;\sigma_x,\sigma_y,\sigma_z) \equiv \frac{1}{(2\pi)^{3/2}\sigma_x\sigma_y\sigma_z}\int_{-\infty}^{\infty} \exp\left(-\frac{1}{2\sigma_x^2}(\hat{x}-x)^2 - \frac{1}{2\sigma_y^2}(\hat{x}-y)^2 - \frac{1}{2\sigma_z^2}(\hat{x}-z)^2\right) \mathrm{d}\hat{x}. \tag{3.3.9}$$

By the definition of a Gaussian integral we have

$$\int_{-\infty}^{\infty} e^{-a(x+b)^2}\,\mathrm{d}x_1 = \sqrt{\frac{\pi}{a}},$$

which gives

$$\mathbb{E}[F_\varsigma^3(\mathbf{x}-\mathbf{x}_{\mathbf{i}_3})] = \frac{1}{(2\pi(\varsigma^2+\sigma^2))^{3/2}} \exp\left(-\frac{1}{2(\varsigma^2+\sigma^2)}|\mathbf{x}-\mathbf{e}_{\mathbf{i}_3}|^2\right) = F^3_{\sqrt{\varsigma^2+\sigma^2}}(\mathbf{x}-\mathbf{e}_{\mathbf{i}_3}) \tag{3.3.10}$$

and

$$\begin{aligned}
&\mathbb{E}[F_\varsigma^3(\mathbf{x}-\mathbf{x}_{\mathbf{i}_3})F_\varsigma^3(\mathbf{y}-\mathbf{x}_{\mathbf{i}_3})] \\
&\quad= \left(\frac{1}{(2\pi\varsigma)^3(\varsigma^2+2\sigma^2)^{3/2}}\right)\exp\left(-\frac{1}{2(\varsigma^2+2\sigma^2)}\left(\frac{\sigma^2}{\varsigma^2}|\mathbf{x}-\mathbf{y}|^2+|\mathbf{x}-\mathbf{e}_{\mathbf{i}_3}|^2+|\mathbf{y}-\mathbf{e}_{\mathbf{i}_3}|^2\right)\right) \\
&\quad= F^3_{\sqrt{2}\varsigma}\left(\sqrt{\frac{2\sigma^2}{2\sigma^2+\varsigma^2}}(\mathbf{x}-\mathbf{y})\right)\sqrt{F^3_{\sqrt{\sigma^2+\varsigma^2/2}}(\mathbf{x}-\mathbf{e}_{\mathbf{i}_3})F^3_{\sqrt{\sigma^2+\varsigma^2/2}}(\mathbf{y}-\mathbf{e}_{\mathbf{i}_3})}.
\end{aligned} \tag{3.3.11}$$

Therefore (3.3.10) and (3.3.11) can be used in (3.3.3)-(3.3.5) to give the moments of $\hat{g}(\mathbf{x};\omega)$. These results can be extended to n dimensions via similar calculations to obtain the moments of F_ς^n as

$$\mathbb{E}[F_\varsigma^n(\mathbf{x}-\mathbf{x}_{\mathbf{i}_n})] = F^n_{\sqrt{\varsigma^2+\sigma^2}}(\mathbf{x}-\mathbf{e}_{\mathbf{i}_n}) \tag{3.3.12}$$

and

$$\begin{aligned}
&\mathbb{E}[F_\varsigma^n(\mathbf{x}-\mathbf{x}_{\mathbf{i}_n})F_\varsigma^n(\mathbf{y}-\mathbf{x}_{\mathbf{i}_n})] \\
&\qquad= F^n_{\sqrt{2}\varsigma}\left(\sqrt{\frac{2\sigma^2}{2\sigma^2+\varsigma^2}}(\mathbf{x}-\mathbf{y})\right)\sqrt{F^n_{\sqrt{\sigma^2+\varsigma^2/2}}(\mathbf{x}-\mathbf{e}_{\mathbf{i}_n})F^n_{\sqrt{\sigma^2+\varsigma^2/2}}(\mathbf{y}-\mathbf{e}_{\mathbf{i}_n})}.
\end{aligned} \tag{3.3.13}$$

So when normally perturbing sink locations for a Gaussian-shaped sink function we find the width ς is replaced by an effective width $\sqrt{\varsigma^2+\sigma^2}$. These expectations allows the moments of the sink function to be calculated using (3.3.3)-(3.3.5), which in turn allows moments of corrections to be calculated using (3.2.9)-(3.2.11). Figure 3.3(a) shows the covariance of the sink function in one space dimension. This is zero, positive and negative when away, on and near to the diagonal, which represents sinks being independently distributed, correlated and anti-correlated respectively.

3.3.2 Uniformly-random sink locations

Let sink locations be prescribed by a multivariate uniform distribution, with position vectors given by $\boldsymbol{\xi}_{\mathbf{i}_3} = (\xi_i, \xi_j, \xi_k)$ such that $\xi_i \sim \mathcal{U}[0,1]$ and $\xi_j, \xi_k \sim \mathcal{U}[-L_s, L_s]$ for $i = 1,\ldots,N$ and $j,k = -M,\ldots,M$. Therefore each continuous uniformly-random variable $\boldsymbol{\xi}_{\mathbf{i}_3}$ is independently and identically distributed with a pdf given by

$$\pi_{\boldsymbol{\xi}_{\mathbf{i}_3}}(\mathbf{x}_{\mathbf{i}_3}) = \begin{cases} \dfrac{1}{(2L_s)^2} = \dfrac{1}{\lambda^2(2M+1)^2} & \text{for } \mathbf{x}_{\mathbf{i}_3} \in \mathcal{D}_3^s, \\ 0 & \text{otherwise.} \end{cases} \tag{3.3.14}$$

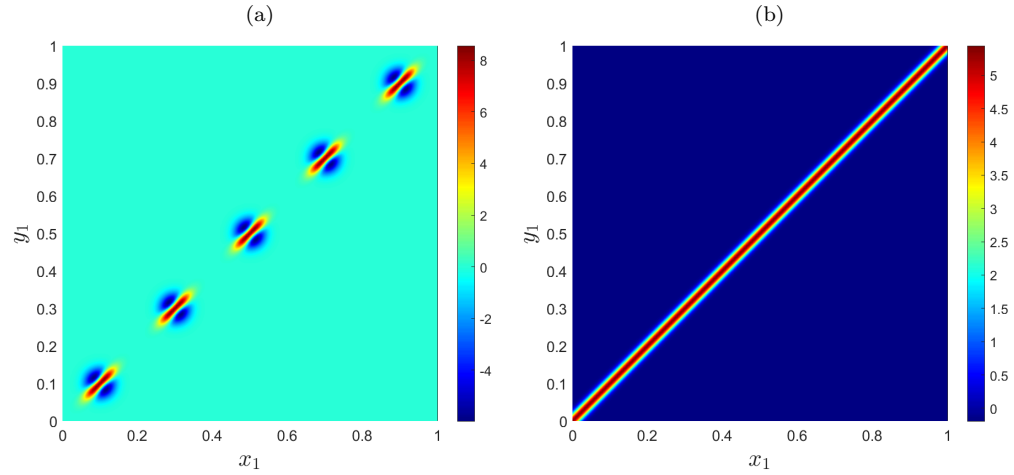

Figure 3.3: Covariance $\mathcal{K}_{\hat{g}}[x_1, y_1]$ of the one-dimensional sink function $\hat{g}$. (a) normally-perturbed sink locations calculated using (3.3.12) and (3.3.13) with (3.3.5). (b) uniformly-random sink locations calculated using (3.3.20). Both figures use $(\mathrm{Pe}_L, \mathrm{Da}) = (20, 10)$, $\lambda = 0.2$ and $\varsigma = 0.01$, with (b) using $e_i = (2i-1)/2N$ as the mean sink locations for $i = 1, \ldots, N$.

So using the definition of the sink function given in (3.1.3) we find the expectation of $\hat{g}(\mathbf{x};\omega)$ is given by

$$\begin{aligned}\mathbb{E}\left[\hat{g}(\mathbf{x};\omega)\right] &= \int_{\mathcal{D}_3}\int_{\mathcal{D}_3} \cdots \left(\lambda^3 \sum_{\mathbf{i}_3} F_\varsigma^3(\mathbf{x}-\mathbf{x}_{\mathbf{i}_3}) - 1\right) \pi_{\boldsymbol{\xi}_\mathbf{1},\boldsymbol{\xi}_\mathbf{2},\ldots}(\mathbf{x_1},\mathbf{x_2},\ldots)\,\mathrm{d}\mathbf{x_1}\mathrm{d}\mathbf{x_2}\ldots \\ &= \lambda^3 \sum_{\mathbf{i}_3} \int_{\mathcal{D}_3} F_\varsigma^3(\mathbf{x}-\mathbf{x}_{\mathbf{i}_3})\pi_{\boldsymbol{\xi}_{\mathbf{i}_3}}(\mathbf{x}_{\mathbf{i}_3})\,\mathrm{d}\mathbf{x}_{\mathbf{i}_3} - 1 = 0. \end{aligned} \tag{3.3.15}$$

The expectation of $\hat{g}(\mathbf{x};\omega)$ being zero results in the expectation of the leading-order correction $\widehat{C}_1(\mathbf{x},\omega)$ being zero. This is a direct result of the mean sink location being uniform throughout $\mathcal{D}_3^s$ and reflects how strong disorder smears out the impact of individual sink locations. This is in contrast to using periodic and normally-perturbed sink locations, where the mean sink location is not constant and the leading-order mean correction to the homogenized solution is non-zero.

To calculate the covariance $\mathcal{K}_{\hat{g}}(\mathbf{x},\mathbf{y}) = \mathbb{E}[\hat{g}(\mathbf{x};\omega)\hat{g}(\mathbf{y};\omega)]$ we can again use the pdf given in (3.3.14) to obtain

$$\begin{aligned}\mathcal{K}_{\hat{g}}(\mathbf{x},\mathbf{y}) =& \lambda^6 \sum_{\substack{\mathbf{i}_3 \\ \mathbf{i}_3\neq\mathbf{j}_3}} \sum_{\mathbf{j}_3} \int_{\mathcal{D}_3}\int_{\mathcal{D}_3} F_\varsigma^3(\mathbf{x}-\mathbf{x}_{\mathbf{i}_3})F_\varsigma^3(\mathbf{y}-\mathbf{x}_{\mathbf{j}_3})\pi_{\boldsymbol{\xi}_{\mathbf{i}_3},\boldsymbol{\xi}_{\mathbf{j}_3}}(\mathbf{x}_{\mathbf{i}_3},\mathbf{x}_{\mathbf{j}_3})\,\mathrm{d}\mathbf{x}_{\mathbf{i}_3}\,\mathrm{d}\mathbf{x}_{\mathbf{j}_3} \\ &+ \lambda^6 \sum_{\mathbf{i}_3} \int_{\mathcal{D}_3} F_\varsigma^3(\mathbf{x}-\mathbf{x}_{\mathbf{i}_3})F_\varsigma^3(\mathbf{y}-\mathbf{x}_{\mathbf{i}_3})\pi_{\boldsymbol{\xi}_{\mathbf{i}_3}}(\mathbf{x}_{\mathbf{i}_3})\,\mathrm{d}\mathbf{x}_{\mathbf{i}_3} \\ &- \lambda^3 \sum_{\mathbf{i}_3} \int_{\mathcal{D}_3} F_\varsigma^3(\mathbf{x}-\mathbf{x}_{\mathbf{i}_3})\pi_{\boldsymbol{\xi}_{\mathbf{i}_3}}(\mathbf{x}_{\mathbf{i}_3})\,\mathrm{d}\mathbf{x}_{\mathbf{i}_3} - \lambda^3 \sum_{\mathbf{j}_3} \int_{\mathcal{D}_3} F_\varsigma^3(\mathbf{y}-\mathbf{x}_{\mathbf{j}_3})\pi_{\boldsymbol{\xi}_{\mathbf{j}_3}}(\mathbf{x}_{\mathbf{j}_3})\,\mathrm{d}\mathbf{x}_{\mathbf{j}_3} + 1\end{aligned}$$

which gives

$$\mathcal{K}_{\hat{g}}(\mathbf{x},\mathbf{y}) = \lambda^3 \int_{\mathcal{D}_3} F_\varsigma^3(\mathbf{x}-\mathbf{x}_{\mathbf{i}_3}) F_\varsigma^3(\mathbf{y}-\mathbf{x}_{\mathbf{i}_3})\,\mathrm{d}\mathbf{x}_{\mathbf{i}_3} - \frac{\lambda}{(2M+1)^2}.$$

Define the function $\mathcal{F}_\varsigma^3$ to measure the overlap of the two functions $F_\varsigma^3(\mathbf{x}-\hat{\mathbf{x}})$ and $F_\varsigma^3(\mathbf{y}-\hat{\mathbf{x}})$, i.e.

$$\mathcal{F}_\varsigma^3(\mathbf{x},\mathbf{y}) = \int_{\mathcal{D}_3} F_\varsigma^3(\mathbf{x}-\hat{\mathbf{x}}) F_\varsigma^3(\mathbf{y}-\hat{\mathbf{x}})\,\mathrm{d}\hat{\mathbf{x}}. \tag{3.3.16}$$

Therefore $\mathcal{F}_\varsigma^3$ is a monotonic function with width ς and is zero when $\mathbf{x}$ is sufficiently far from $\mathbf{y}$. This gives the covariance of $\hat{g}$ as

$$\mathcal{K}_{\hat{g}}(\mathbf{x},\mathbf{y}) = \lambda^3 \mathcal{F}_\varsigma^3(\mathbf{x},\mathbf{y}) - \frac{\lambda}{(2M+1)^2}. \tag{3.3.17}$$

The moments of $\hat{g}(\mathbf{x};\omega)$ given in (3.3.15) and (3.3.17) can then be used with (3.2.9)-(3.2.11) to find the moments of the corrections to the homogenized solution, which approximates the impact of disordered sink locations on the solute concentration.

Consider now when F_ς^3 has a Gaussian structure and is given in (3.1.5). We can again use the definition of a Gaussian integral to give

$$\mathcal{F}_\varsigma^3(\mathbf{x},\mathbf{y}) = I_2(x_1,y_1;\varsigma,\varsigma) I_2(x_2,y_2;\varsigma,\varsigma) I_2(x_3,y_3;\varsigma,\varsigma) = F_{\sqrt{2}\varsigma}^3(\mathbf{x}-\mathbf{y}),$$

where I_2 is defined in (3.3.8). This in turn gives the covariance of $\hat{g}$ as

$$\mathcal{K}_{\hat{g}}[\mathbf{x},\mathbf{y}] = \lambda^3 F_{\sqrt{2}\varsigma}^3(\mathbf{x}-\mathbf{y}) - \frac{\lambda}{(2M+1)^2}. \tag{3.3.18}$$

Via similar calculations we can once again extend these results into n dimensions by replacing λ^3 with λ^n and noting that the number of sinks $(2M+1)^2/\lambda$ becomes $(2M+1)^{n-1}/\lambda$, therefore

$$\mathbb{E}[\hat{g}(\mathbf{x};\omega)] = 0 \tag{3.3.19}$$

and

$$\mathcal{K}_{\hat{g}}[\mathbf{x},\mathbf{y}] = \lambda^n F_{\sqrt{2}\varsigma}^n(\mathbf{x}-\mathbf{y}) - \frac{\lambda}{(2M+1)^{n-1}}. \tag{3.3.20}$$

We see from (3.3.20) that the covariance has a non-local component in one spatial dimension, but when $M \gg N$ we find the non-local contribution is negligible in two and three dimensions. Figure 3.3(b) shows the covariance of the sink function in one spatial dimension, which is seen to be everywhere non-local due to remaining non-zero throughout the domain. This is due to the second term in (3.3.20) causing the covariance to be negative away from the diagonal.

Before calculating the moments of corrections given in (3.2.9)-(3.2.11), we first need to calculate an approximation to the Green's function in n dimensions. This approximation will be a free-space Green's function, which remains valid when suitably far from exterior boundaries. The validity of this approximation across $(\mathrm{Pe}_L, \mathrm{Da})$-parameter space will be tested and regions of influence on the concentration at a given location will be found by inverting the Green's function in one, two and three dimensions.

3.4 Calculating a free-space Green's function

The n-dimensional free-space Green's function $\mathcal{G}_n$ associated with the n-dimensional form of (3.1.2) will satisfy any singularity contained at $\mathbf{x} = \mathbf{x}'$ and the linear operator $\mathcal{L}_n$ such that $\mathcal{L}_n G^n = \delta(\mathbf{x}-\mathbf{x}')$, but will ignore the impact from boundary conditions. Therefore the function will approximate the exact Green's function G^n and remain valid when sufficiently far from all boundaries of $\mathcal{D}_n$. As the free-space Green's function $\mathcal{G}_n$ is stationary it can be expressed as $\mathcal{G}_n = \mathcal{G}_n(\mathbf{x} - \mathbf{x}')$. So by assuming $G^n(\mathbf{x}, \mathbf{x}') = \mathcal{G}_n(\mathbf{x} - \mathbf{x}')$ and seeking a solution of the form

$$\mathcal{G}_n(\mathbf{x}) = e^{\alpha x_1} f(r) \quad \text{where} \quad r = |\mathbf{x}|, \tag{3.4.1}$$

we can use (3.1.2) to obtain

$$\left(f_{rr} + (n - 1 + (2\alpha - \mathrm{Pe}_L)x_1)\frac{f_r}{r} + (\alpha^2 - \mathrm{Pe}_L\,\alpha - \mathrm{Da})f \right) e^{\alpha x_1} = \delta(\mathbf{x}) \tag{3.4.2}$$

in n dimensions. By considering $\alpha = \mathrm{Pe}_L/2$ we can find a single solution of (3.4.2) by solving

$$\left(f_{rr} + (n-1)\frac{f_r}{r} - \phi^2 f \right) \exp\left(\frac{\mathrm{Pe}_L}{2} x_1 \right) = \delta(\mathbf{x}), \tag{3.4.3}$$

where $\phi = \sqrt{\mathrm{Pe}_L^2/4 + \mathrm{Da}}$. By multiplying both sides of (3.4.3) by $\exp(-(\mathrm{Pe}_L/2)x_1)$ and noting that $\exp(-(\mathrm{Pe}_L/2)x_1)\delta(\mathbf{x}) = \delta(\mathbf{x})$ in the sense of distributions, we obtain

$$\left(\nabla^2_{nD,r} - \phi^2 \right) f(r) = \delta(\mathbf{x}) \tag{3.4.4}$$

where $\nabla^2_{nD,r} = \partial_{rr} + ((n-1)/r)\partial_r$ in n dimensions. The left-hand side of (3.4.4) has a known free-space solution, which is given (for example) in Tikhonov and Samarskiĭ (2013) as

$$f(r) = -(2\pi)^{n/2} \left(\frac{\phi}{r} \right)^{n/2-1} K_{n/2-1}(\phi r) \tag{3.4.5}$$

where K_ν represents the modified Bessel function of the second kind. Therefore the free-space Green's function in n dimensions is given by

$$\mathcal{G}_n(\mathbf{x} - \mathbf{x}') = -(2\pi)^{-n/2} \left(\frac{\phi}{|\mathbf{x} - \mathbf{x}'|} \right)^{n/2-1} K_{n/2-1}(\phi|\mathbf{x} - \mathbf{x}'|) \exp\left(\frac{\mathrm{Pe}_L}{2}(x_1 - x_1') \right). \tag{3.4.6}$$

Note that (3.4.6) shows that there is no singularity in the free-space Green's function in one dimension, but in two and three dimensions there exists a singularity at $\mathbf{x} = \mathbf{x}'$ of order $\log(\phi|\mathbf{x} - \mathbf{x}'|)$ and $1/|\mathbf{x} - \mathbf{x}'|$ respectively, as will be discussed later on. Integrating the two- and three-dimensional governing equation for the free-space Green's function gives the relation

$$\int_{-\infty}^{\infty}\int_{-\infty}^{\infty} \mathcal{G}_3(\mathbf{x})\,\mathrm{d}x_2\,\mathrm{d}x_3 = \int_{-\infty}^{\infty} \mathcal{G}_2(\mathbf{x})\,\mathrm{d}x_2 = \mathcal{G}_1(x_1), \tag{3.4.7}$$

a property which will later be used. We now consider the range of validity of the free-space Green's function in one, two and three dimensions.

3.4.1 One-dimensional free-space Green's function

By using Abramowitz and Stegun (1964) we see the modified Bessel function of the second kind $K_{-1/2}(z)$ takes the form

$$K_{-1/2}(z) = K_{1/2}(z) = \sqrt{\frac{\pi}{2z}}\exp(-z). \tag{3.4.8}$$

So (3.4.6) give the free-space Green's function in one dimension to be

$$\mathcal{G}_1(x_1 - x_1') = -\frac{1}{2\phi}\exp\left(\frac{\mathrm{Pe}_L}{2}(x_1 - x_1') - \phi|x_1 - x_1'|\right). \tag{3.4.9}$$

A plot of this free-space Green's function can be seen in Figure 3.4(a) for $(\mathrm{Pe}_L, \mathrm{Da}) = (20, 10)$. To better understand the structure of the Green's function, consider the decay lengthscales of $\mathcal{G}_1$. By (3.4.9) these are given by

$$L_{\mathcal{G}^-_{x_1}} = \left(\phi + \frac{\mathrm{Pe}_L}{2}\right)^{-1} \quad \text{and} \quad L_{\mathcal{G}^+_{x_1}} = \left(\phi - \frac{\mathrm{Pe}_L}{2}\right)^{-1} \tag{3.4.10}$$

for $x_1 < x_1'$ and $x_1 > x_1'$ respectively. When $\mathrm{Pe}_L^2 \gg \mathrm{Da}$ we have

$$\phi = \sqrt{\frac{\mathrm{Pe}_L^2}{4} - \mathrm{Da}} = \frac{\mathrm{Pe}_L}{2}\left(1 + \frac{4\,\mathrm{Da}}{\mathrm{Pe}_L^2}\right)^{1/2} \approx \frac{\mathrm{Pe}_L}{2} + \frac{\mathrm{Da}}{\mathrm{Pe}_L} + \ldots,$$

where we will not be distinguishing between strict asymptotic limits and approximations within this chapter. This gives the decay lengthscales of $\mathcal{G}_1$ as

$$L_{\mathcal{G}^-_{x_1}} \approx \frac{1}{\mathrm{Pe}_L} \quad \text{and} \quad L_{\mathcal{G}^+_{x_1}} \approx \frac{\mathrm{Pe}_L}{\mathrm{Da}} \tag{3.4.11}$$

for $x_1 < x_1'$ and $x_1 > x_1'$ respectively. So for $\mathrm{Pe}_L \gg \max(1, \sqrt{\mathrm{Da}})$ we have $L_{\mathcal{G}^-_{x_1}} \ll 1$, meaning the decay lengthscale $L_{\mathcal{G}^-_{x_1}}$ is much shorter than the domain length in the x_1-direction. As a result, the free-space Green's function offers a good approximation to the exact solutions except when x_1' is within a distance $1/\mathrm{Pe}_L$ from the inlet.

Consider now the range of validity of the free-space Green's function downstream of $x_1 = x_1'$. The order of magnitude of the decay lengthscale $L_{\mathcal{G}^+_{x_1}}$ can become similar to that of the

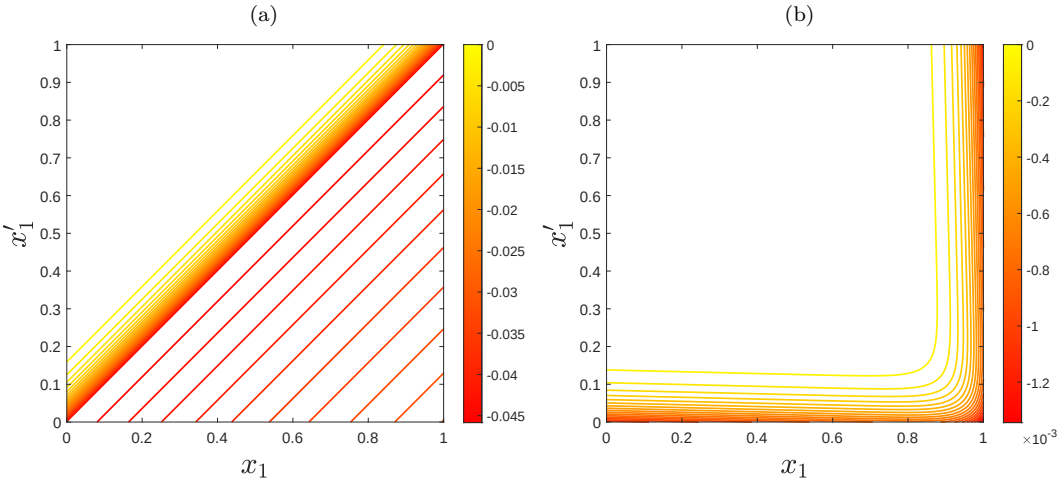

Figure 3.4: (a) Contour plot of the free-space Green's function $\mathcal{G}_1(x_1 - x_1')$ in one dimension. (b) Contour plot showing the difference between the exact and free-space Green's function $(G(x_1, x_1') - \mathcal{G}_1(x_1 - x_1'))$. Here, the free-space and exact Green's function are given in (3.4.9) and (B.1.2) respectively, with both figures using $(\mathrm{Pe}_L, \mathrm{Da}) = (20, 10)$. Note the similarities in structure when compared to Figure 2.3 from Chapter 2, which uses an exact Green's function with different parameter values.

domain length in the x_1-direction. However, the zero diffusive flux boundary condition gives an external boundary layer of width $1/\mathrm{Pe}_L$ in the exact Green's function, see Appendix B.1. A physical interpretation of this is that advection causes any effect from boundary layers to be swept downstream, meaning the impact of any boundary layer is felt more downstream than upstream of its location. As a result of this boundary layer, we again see the free-space Green's function is a good approximation over distances greater than $\mathcal{O}(1/\mathrm{Pe}_L)$ from the downstream boundary. Therefore the free-space Green's function will remain valid almost everywhere so long as $\mathrm{Pe}_L \gg \max(1, \sqrt{\mathrm{Da}})$. However, when this condition doesn't hold then boundary effects influence large regions of the Green's function, resulting in an exact Green's function being required.

A plot comparing the free-space Green's function given in (3.4.9) to the exact solution given in (B.1.2) from Appendix B.1 is shown in Figure 3.4(b). This error is seen to be asymptotically small when a distance of at least $\mathcal{O}(1/\mathrm{Pe}_L)$ from the downstream x_1-boundary due to the outlet boundary condition. There is also an error of width $\mathcal{O}(1/\mathrm{Pe}_L)$ from the $x_1 = 0$ boundary, but this is only notable when a distance $\mathcal{O}(1/\mathrm{Pe}_L)$ from $x_1 = x_1'$ due to the decay lengthscale $L_{\mathcal{G}_{x_1}^-}$. From the symmetry in the Green's function (invariance under reflection in the line $x_1 + x_1' = 1$) we also see the same effects on the x_1' boundaries in the reverse order.

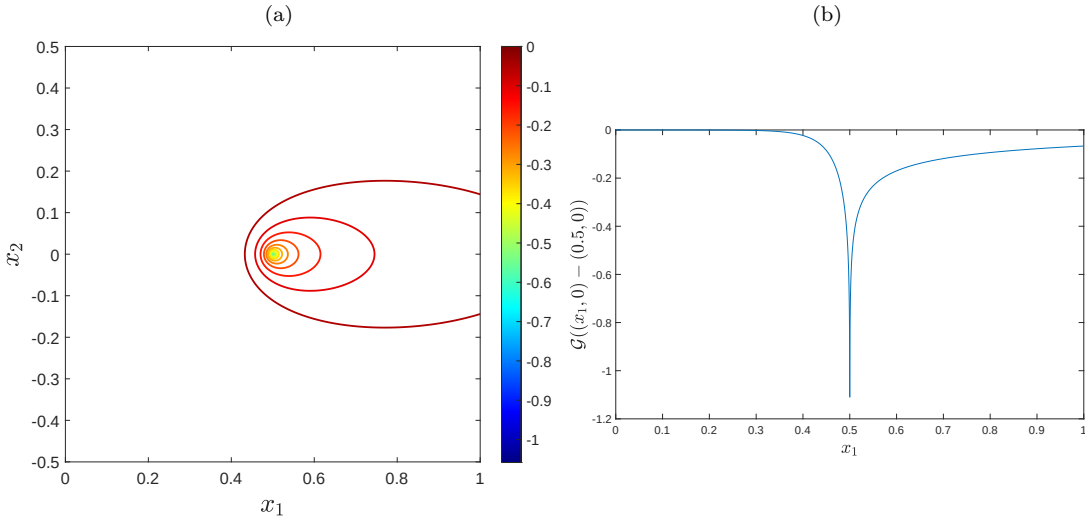

Figure 3.5: (a) Contour plot of the free-space Green's function $\mathcal{G}_2(\mathbf{x}-\mathbf{x}')$ in two dimensions. (b) Plot of the free-space Green's function $\mathcal{G}_2(\mathbf{x}-\mathbf{x}')$ along $x_2 = 0$. Both figures use $(\mathrm{Pe}_L, \mathrm{Da}) = (20, 10)$ and $\mathbf{x}' = (0.5, 0)$.

The one-dimensional free-space Green's function given in (3.4.11) shows how a sink located at $x_1 = x_1'$ influences the solute concentration a distance $L_{\mathcal{G}_{x_1}^-}$ and $L_{\mathcal{G}_{x_1}^+}$ upstream and downstream of x_1' respectively. Therefore when considering some point $x_1 = x_0$ we see the concentration at x_0 can be influenced by a sink $L_{\mathcal{G}_{x_1}^+}$ or $L_{\mathcal{G}_{x_1}^-}$ upstream or downstream of the location respectively. Therefore the parameters $L_{\mathcal{G}_{x_1}^-}$ and $L_{\mathcal{G}_{x_1}^+}$ define the lengthscales of a region of influence about x_0, where any sinks lying within this region will influence the solute concentration at x_0.

3.4.2 Two-dimensional free-space Green's function

In two dimensions, (2.2.10) gives the free-space Green's function as

$$\mathcal{G}_2(\mathbf{x}-\mathbf{x}') = -\frac{1}{2\pi} K_0(\phi|\mathbf{x}-\mathbf{x}'|) \exp\left(\frac{\mathrm{Pe}_L}{2}(x_1 - x_1')\right). \tag{3.4.12}$$

A contour plot of the two-dimensional free-space Green's function given in (3.4.12) can be seen in Figure 3.5, where $\mathbf{x}' = (0.5, 0.5)$ and $(\mathrm{Pe}_L, \mathrm{Da}) = (20, 10)$ are used.

Although the modified Bessel function of the second kind does not here have a simplified expression, Abramowitz and Stegun (1964) state that for $z \to 0$ and $z \to \infty$ then

$$K_0(z) \approx -\log(z) \quad \text{and} \quad K_0(z) \approx \sqrt{\frac{\pi}{2z}}(1 + \mathcal{O}(1/|z|)) \exp(-z) \tag{3.4.13}$$

respectively. Therefore near the sink location $\mathbf{x} = \mathbf{x}'$ we can use (3.4.13) with $\exp((\mathrm{Pe}_L/2)(x_1 -$

$x_1'))\approx 1+\mathcal{O}(x_1-x_1')$ to give the free-space Green's function to leading-order as

$$\mathcal{G}_2(\mathbf{x}-\mathbf{x}')\approx\frac{1}{2\pi}\log(\phi|\mathbf{x}-\mathbf{x}'|). \tag{3.4.14}$$

This allows us to approximate the flux from the source to be

$$F=2\pi r\frac{\partial\mathcal{G}_2(\mathbf{x}-\mathbf{x}')}{\partial r}\approx 1, \tag{3.4.15}$$

where r is defined to be $r=|\mathbf{x}-\mathbf{x}'|$.

Far-field behaviour

Let us now consider the behaviour of the free-space Green's function when far field of the sink location $\mathbf{x}=\mathbf{x}'$. This is done by using $\phi|\mathbf{x}-\mathbf{x}'|\gg 1$, meaning (3.4.13) gives the free-space Green's function to leading-order by

$$\mathcal{G}_2(\mathbf{x}-\mathbf{x}')\approx-\frac{1}{2}\sqrt{\frac{1}{2\pi\phi|\mathbf{x}-\mathbf{x}'|}}\exp\left(\frac{\mathrm{Pe}_L}{2}(x_1-x_1')-\phi|\mathbf{x}-\mathbf{x}'|\right). \tag{3.4.16}$$

We can consider the behaviour in the x_1-direction by considering $x_2=x_2'$ (where $\mathbf{x}=(x_1,x_2)$ and $\mathbf{x_1'}=(x_1',x_2')$). This gives $|\mathbf{x}-\mathbf{x}'|=|x_1-x_1'|$, so by considering $x_1<x_1'$ and $x_1>x_1'$ separately we obtain the decay lengthscales downstream and upstream of the sink as

$$L_{\mathcal{G}^-_{x_1}}=\left(\phi+\frac{\mathrm{Pe}_L}{2}\right)^{-1}\quad\text{for } x_1<x_1'\quad\text{and}\quad L_{\mathcal{G}^+_{x_1}}=\left(\phi-\frac{\mathrm{Pe}_L}{2}\right)^{-1}\quad\text{for } x_1>x_1' \tag{3.4.17}$$

respectively. These are the same lengthscales as found in one spatial dimension in (3.4.10). Along $x_1=x_1'$ the lengthscale over which $\mathcal{G}_2$ decays in the x_2-direction is

$$L_{\mathcal{G}_{x_2}}=\phi^{-1}.$$

These lengthscales can be approximated in the limit $\mathrm{Pe}_L\gg\max(1,\sqrt{\mathrm{Da}})$ to be

$$L_{\mathcal{G}^-_{x_1}}\approx\frac{1}{\mathrm{Pe}_L},\quad L_{\mathcal{G}^+_{x_1}}\approx\frac{\mathrm{Da}}{\mathrm{Pe}_L}\quad\text{and}\quad L_{\mathcal{G}_{x_2}}\approx\frac{1}{\mathrm{Pe}_L},$$

which are depicted in Figure 3.6(a).

Let us now consider the asymptotic shape of the wake in the far field. The lengthscales when downstream of $\mathbf{x}=\mathbf{x}'$ are given by $L_{\mathcal{G}^+_{x_1}}=\mathrm{Pe}_L/\mathrm{Da}$ and $L_{\mathcal{G}_{x_2}}=1/\mathrm{Pe}_L$ in the limit where $\mathrm{Pe}_L\gg\max(1,\sqrt{\mathrm{Da}})$. So by rescaling using $x_1-x_1'=(\mathrm{Pe}_L/\mathrm{Da})X_1$ and $x_2-x_2'=(1/\mathrm{Pe}_L)X_2$ for $X_1,X_2=\mathcal{O}(1)$ we obtain

$$\phi=\frac{\mathrm{Pe}_L}{2}\left(1+\frac{4\,\mathrm{Da}}{\mathrm{Pe}_L^2}\right)^{1/2}\approx\frac{\mathrm{Pe}_L}{2}\left(1+\frac{2\,\mathrm{Da}}{\mathrm{Pe}_L^2}-\frac{2\,\mathrm{Da}^2}{\mathrm{Pe}_L^4}+\dots\right)$$

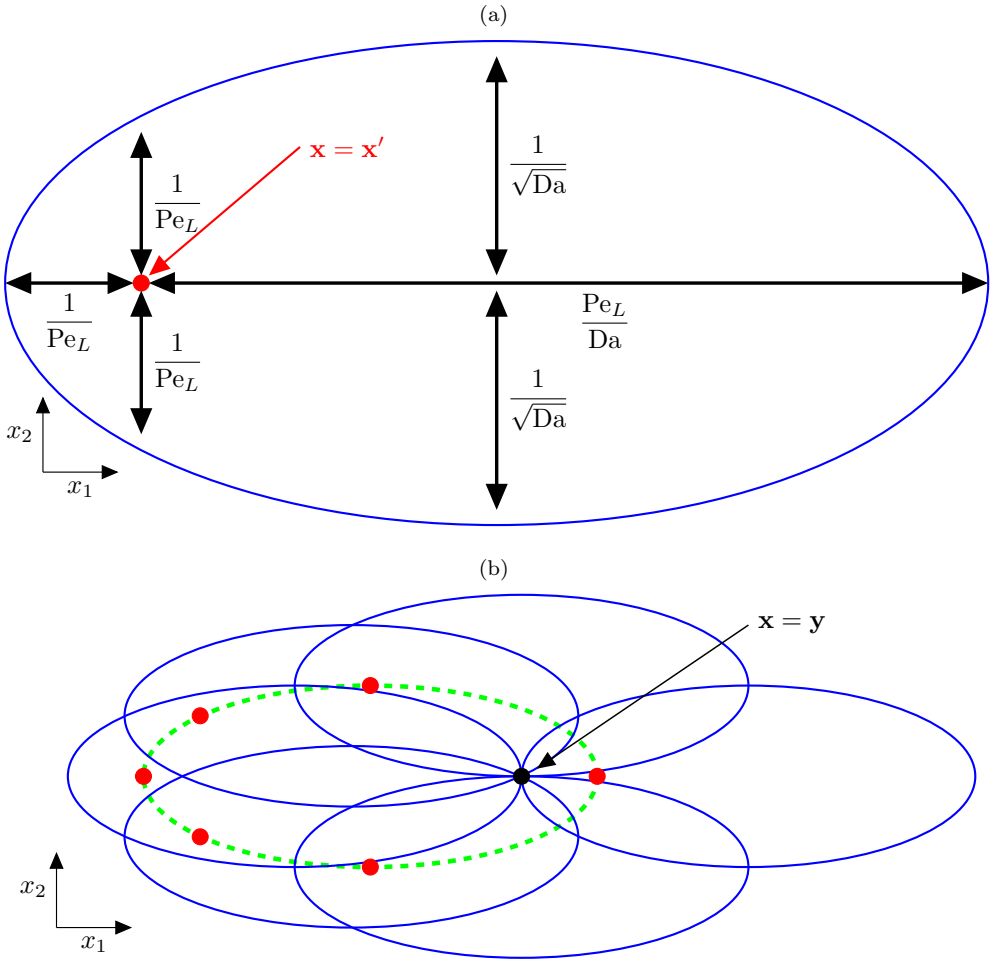

Figure 3.6: (a) Depiction of the lengthscales involved in the Green's function for a sink located at $\mathbf{x} = \mathbf{x}'$ [red dot] and the asymptotic shape of the wake [solid blue], where $\mathrm{Pe}_L \gg \max(1, \sqrt{\mathrm{Da}})$. (b) The region of influence [dashed green] about the point $\mathbf{x} = \mathbf{y}$ [black dot]. Sinks located outside of this region will have weak influence on the concentration at $\mathbf{x} = \mathbf{y}$. Here, red dots represent sink locations $\mathbf{x} = \mathbf{x}'$ and blue ellipses represent the asymptotic shapes of the wake about each sink.

and

$$|\mathbf{x} - \mathbf{x}'| = \frac{\mathrm{Pe}_L}{\mathrm{Da}} X_1 \left(1 + \frac{\mathrm{Da}^2}{\mathrm{Pe}_L^4}\left(\frac{X_2^2}{X_1^2}\right)\right)^{1/2} \approx \frac{\mathrm{Pe}_L}{\mathrm{Da}} X_1 \left(1 + \frac{\mathrm{Da}^2}{2\,\mathrm{Pe}_L^4}\left(\frac{X_2^2}{X_1^2}\right) + \dots\right).$$

Therefore

$$\phi|\mathbf{x} - \mathbf{x}'| \approx \frac{\mathrm{Pe}_L^2}{2\,\mathrm{Da}} X_1 \left(1 + \frac{2\,\mathrm{Da}}{\mathrm{Pe}_L^2} + \frac{\mathrm{Da}^2}{\mathrm{Pe}_L^4}\left(\frac{X_2^2}{2X_1^2} - 2\right) + \dots\right)$$

and

$$\frac{1}{\sqrt{\phi|\mathbf{x} - \mathbf{x}'|}} \approx \frac{1}{\mathrm{Pe}_L}\sqrt{\frac{2\,\mathrm{Da}}{X_1}}\left(1 - \frac{\mathrm{Da}}{\mathrm{Pe}_L^2} + \frac{\mathrm{Da}^2}{\mathrm{Pe}_L^4}\left(4 - \frac{X_2^2}{4X_1^2}\right) + \dots\right),$$

which can be used with (3.4.16) to give

$$\mathcal{G}_2(\mathbf{x} - \mathbf{x}') \approx -\frac{1}{2\,\mathrm{Pe}_L}\sqrt{\frac{\mathrm{Da}}{\pi X_1}} \exp\left(-\left(1 + \frac{\mathrm{Da}}{2\,\mathrm{Pe}_L^2}\left(\frac{X_2^2}{2X_1^2} - 2\right)\right) X_1\right).$$

To consider one contour of the free-space Green's function set $\mathcal{G}_2$ to be constant, which gives $-\log(-2\,\mathrm{Pe}_L\sqrt{\pi/\,\mathrm{Da}}\mathcal{G}_2) = X_0 \geq 0$ where $X_0 \in \mathbb{R}^+$. Therefore

$$X_0 \approx \frac{\log X_1}{2} + X_1 + \frac{\mathrm{Da}}{2\,\mathrm{Pe}_L^2}\left(\frac{X_2^2}{2X_1^2} - 2\right)X_1,$$

so noting that 1 - $\mathrm{Da}\,/\,\mathrm{Pe}_L^2 \approx 1$ in the limit $\mathrm{Pe}_L \gg \max(1, \sqrt{\mathrm{Da}})$ gives

$$\left(X_1 - \frac{X_0}{2}\right)^2 + \frac{X_1 \log X_1}{2} + \frac{\mathrm{Da}}{4\,\mathrm{Pe}_L^2}X_2^2 \approx \left(\frac{X_0}{2}\right)^2. \tag{3.4.18}$$

By setting $X_0 = (2\,\mathrm{Da}\,/\,\mathrm{Pe}_L)x_0$ and converting back to the original variables using $X_1 = (\mathrm{Da}\,/\,\mathrm{Pe}_L)(x_1 - x_1')$ and $X_2 = \mathrm{Pe}_L(x_2 - x_2')$ gives

$$(x_1 - x_1' - x_0)^2 + \frac{\mathrm{Pe}_L}{2\,\mathrm{Da}}(x_1 - x_1')\log\left(\frac{\mathrm{Da}}{\mathrm{Pe}_L}(x_1 - x_1')\right) + \frac{\mathrm{Pe}_L^2}{4\,\mathrm{Da}}(x_2 - x_2')^2 \approx x_0^2.$$

We can consider the asymptotic shape of the wake far downstream from the location $x_1 - x_1'$ for $x_1 - x_1' \approx \mathrm{Pe}_L\,/\,\mathrm{Da}$, which causes the log term to be asymptotically small, resulting in contours taking the shape of an ellipse with centre $(x_1' + x_0, x_2')$, length $2x_0$ and width $(2\sqrt{\mathrm{Da}}/\,\mathrm{Pe}_L)x_0$. So for $x_1 = \mathcal{O}(\mathrm{Pe}_L\,/\,\mathrm{Da})$ we have $x_0 \sim \mathrm{Pe}_L\,/2\,\mathrm{Da}$ which gives the width to be $\mathcal{O}(1/\sqrt{\mathrm{Da}})$, which is given in Figure 3.6(a).

Figure 3.6(b) shows the region of influence about a point $\mathbf{x} = \mathbf{y}$, such that any sinks located inside this region can be seen to impact the concentration at $\mathbf{x} = \mathbf{y}$. This is found by inverting the ellipse seen in the Green's function, causing the lengthscales to also be inverted. The lengthscales for the region of influence will later be used to show the long-range impact of each sink location for discrete sinks.

3.4.3 Three-dimensional free-space Green's function

In three dimensions we can again use (3.4.8) to give the free-space Green's function as

$$\mathcal{G}_3(\mathbf{x} - \mathbf{x}') = -\frac{1}{4\pi|\mathbf{x} - \mathbf{x}'|}\exp\left(\frac{\mathrm{Pe}_L}{2}(x_1 - x_1') - \phi|\mathbf{x} - \mathbf{x}'|\right). \tag{3.4.19}$$

This gives decay lengthscales in the x_1-direction as

$$L_{\mathcal{G}_{x_1}^-} = \left(\phi + \frac{\mathrm{Pe}_L}{2}\right)^{-1} \text{ for } x_1 < x_1' \quad \text{and} \quad L_{\mathcal{G}_{x_1}^+} = \left(\phi - \frac{\mathrm{Pe}_L}{2}\right)^{-1} \text{ for } x_1 > x_1'$$

and in the x_2- and x_3-direction as

$$L_{\mathcal{G}_{x_2}} = \phi^{-1} \quad \text{and} \quad L_{\mathcal{G}_{x_3}} = \phi^{-1}$$

respectively. The decay lengthscales in the x_1-direction are again the same as for one and two dimensions, which are given in (3.4.10) and (3.4.17) respectively. To calculate the leading-order

behaviour of the free-space Green's function near $\mathbf{x} = \mathbf{x}'$, by setting $r = |\mathbf{x} - \mathbf{x}'|$ and noting that $\exp((\mathrm{Pe}_L/2)(x_1 - x_1') - \phi r) \approx 1 + \dots$ we obtain

$$\mathcal{G}_3(\mathbf{x} - \mathbf{x}') \approx -\frac{1}{4\pi r}. \tag{3.4.20}$$

Therefore the flux from the source is given by

$$F = 4\pi r^2 \frac{\partial G}{\partial r} \approx 1, \tag{3.4.21}$$

which is the same as the two-dimensional flux given in (3.4.15).

Far-field behaviour

Let us again consider the far-field behaviour of the free-space Green's function by calculating the asymptotic shape of the wake. The lengthscales when downstream of $\mathbf{x} = \mathbf{x}'$ are given by $L_{\mathcal{G}_{x_1}^+} = \mathrm{Pe}_L / \mathrm{Da}$ and $L_{\mathcal{G}_{x_2}} = 1/\mathrm{Pe}_L$ in the limit where $\mathrm{Pe}_L \gg \max(1, \sqrt{\mathrm{Da}})$. So by rescaling using $x_1 - x_1' = (\mathrm{Pe}_L / \mathrm{Da})X_1$, $x_2 - x_2' = (1/\mathrm{Pe}_L)X_2$ and $x_3 - x_3' = (1/\mathrm{Pe}_L)X_3$ for $X_1, X_2, X_3 = \mathcal{O}(1)$ we obtain

$$\phi = \frac{\mathrm{Pe}_L}{2}\left(1 + \frac{4\,\mathrm{Da}}{\mathrm{Pe}_L^2}\right)^{1/2} \approx \frac{\mathrm{Pe}_L}{2}\left(1 + \frac{2\,\mathrm{Da}}{\mathrm{Pe}_L^2} - \frac{2\,\mathrm{Da}^2}{\mathrm{Pe}_L^4} + \dots\right)$$

and

$$|\mathbf{x} - \mathbf{x}'| = \frac{\mathrm{Pe}_L}{\mathrm{Da}} X_1 \left(1 + \frac{\mathrm{Da}^2}{\mathrm{Pe}_L^4}\left(\frac{X_2^2 + X_3^2}{X_1^2}\right)\right)^{1/2} \approx \frac{\mathrm{Pe}_L}{\mathrm{Da}} X_1 \left(1 + \frac{\mathrm{Da}^2}{2\,\mathrm{Pe}_L^4}\left(\frac{X_2^2 + X_3^2}{X_1^2}\right) + \dots\right).$$

Therefore

$$\phi|\mathbf{x} - \mathbf{x}'| \approx \frac{\mathrm{Pe}_L^2}{2\,\mathrm{Da}} X_1 \left(1 + \frac{2\,\mathrm{Da}}{\mathrm{Pe}_L^2} + \frac{\mathrm{Da}^2}{\mathrm{Pe}_L^4}\left(\frac{X_2^2 + X_3^2}{2X_1^2} - 2\right) + \dots\right)$$

which can be used with (3.4.19) to give

$$\mathcal{G}_3(\mathbf{x} - \mathbf{x}') \approx -\frac{\mathrm{Da}}{4\pi\,\mathrm{Pe}_L\, X_1} \exp\left(-\left(1 + \frac{\mathrm{Da}}{2\,\mathrm{Pe}_L^2}\left(\frac{X_2^2 + X_3^2}{2X_1^2} - 2\right)\right) X_1\right).$$

So by setting $\mathcal{G}_3$ to be constant, which gives $-\log(-2\,\mathrm{Pe}_L \sqrt{\pi/\,\mathrm{Da}}\mathcal{G}_3) = X_0 \geq 0$ where $X_0 \in \mathbb{R}^+$, we obtain the contours of the Green's function to be

$$X_0 \approx \frac{\log X_1}{2} + X_1 + \frac{\mathrm{Da}}{2\,\mathrm{Pe}_L^2}\left(\frac{X_2^2 + X_3^2}{2X_1^2} - 2\right) X_1.$$

By noting that 1 - $\mathrm{Da}\,/\,\mathrm{Pe}_L^2 \approx 1$ in the limit $\mathrm{Pe}_L \gg \max(1, \sqrt{\mathrm{Da}})$ we obtain

$$\left(X_1 - \frac{X_0}{2}\right)^2 + \frac{X_1 \log X_1}{2} + \frac{\mathrm{Da}}{4\,\mathrm{Pe}_L^2} X_2^2 + \frac{\mathrm{Da}}{4\,\mathrm{Pe}_L^2} X_3^2 \approx \left(\frac{X_0}{2}\right)^2. \tag{3.4.22}$$

By setting $X_0 = (2\,\mathrm{Da}\,/\,\mathrm{Pe}_L)x_0$ and converting back to the original variables we see the asymptotic shape of the wake is given by

$$(x_1 - x_1' - x_0)^2 + \frac{\mathrm{Pe}_L}{2\,\mathrm{Da}}(x_1 - x_1')\log\left(\frac{\mathrm{Da}}{\mathrm{Pe}_L}(x_1 - x_1')\right) + \frac{\mathrm{Pe}_L^2}{4\,\mathrm{Da}}(x_2 - x_2')^2 + \frac{\mathrm{Pe}_L^2}{4\,\mathrm{Da}}(x_3 - x_3')^2 \approx x_0^2.$$

We can consider the asymptotic shape of the wake far downstream from the location $x_1 - x_1'$ when $x_1 - x_1' \approx \mathrm{Pe}_L \,/\, \mathrm{Da}$, which causes the log term to be asymptotically small, meaning the contours take the shape of an ellipsoid with centre $(x_1' + x_0, x_2', x_3')$, x_1-direction length as $2x_0$ and x_2-direction width and x_3-direction height as $(2\sqrt{\mathrm{Da}}/\,\mathrm{Pe}_L)x_0$. So for $x_1 = \mathcal{O}(\mathrm{Pe}_L \,/\, \mathrm{Da})$ we have $x_0 \sim \mathrm{Pe}_L \,/ 2\,\mathrm{Da}$, which gives the width and height to be $\mathcal{O}(1/\sqrt{\mathrm{Da}})$. We can again find the region of influence by the inverse of the asymptotic shape of the wake. As a result, Figures 3.6(a) and 3.6(b) remains valid and can be extended into three dimensions by making the dependence in the x_3-direction identical to that in the x_2-direction.

The free-space Green's functions given in (3.4.9), (3.4.12) and (3.4.19) will now be used with the moments of sink functions found in Section 3.3 to find the moments of corrections to the homogenized solution. This is done using (3.2.9) - (3.2.11) for periodic, normally-perturbed from a periodic configuration and uniformly-random sink locations. Approximations of results will be obtained using the regions of influence of the Green's function and its near- and far-field forms.

3.5 Characterising uncertainty using corrections to the homogenized solution

In this section corrections to the homogenized solution will be found, which are used to approximate the solute concentration for both periodic and disordered sink locations. When sinks are periodically located, the corrections given in (3.2.7) and (3.2.8) will be evaluated and compared to solving (3.1.2) using a finite-difference solver. In contrast, when sinks are disordered the moments of the corrections given in (3.2.9)-(3.2.11) will be evaluated and compared with sample moments taken from Monte Carlo simulations in one- and two- dimensions. For both periodic and disordered sink locations the corrections will be considered in the limit where the sink width becomes asymptotically small (i.e. $\varsigma \to 0$). Throughout, the corrections are calculated using the moments of the sink function given in Section 3.3 with n-dimensional free-space Green's functions found in Section 3.4.

3.5.1 Corrections accounting for periodic sink locations

Let sinks be periodically located with their positions given by $\xi_i = e_i = \lambda(2i-1)/2$, $\boldsymbol{\xi}_{\mathbf{i}_2} = \mathbf{e}_{\mathbf{i}_2} = \lambda((2i-1)/2, j)$ and $\boldsymbol{\xi}_{\mathbf{i}_3} = \mathbf{e}_{\mathbf{i}_3} = \lambda((2i-1)/2, j, k)$ in one, two and three dimensions respectively, where $i = 1, \ldots, N$ and $j, k = -M, \ldots, M$. As this results in the sink function $\hat{g}$

being deterministic we in turn find the corrections $\widehat{C}_1(\mathbf{x}), \widehat{C}_2(\mathbf{x}), \dots$ are deterministic, where the ω notation is now dropped. Therefore the leading- and second-order corrections to the homogenized solution in n dimensions are given by (3.2.7) and (3.2.8) as

$$\widehat{C}_1(\mathbf{x}) = \lambda^n \sum_{\mathbf{i}_n} \int_{\mathcal{D}_n} \mathcal{G}_n(\mathbf{x}-\mathbf{x}')C_H(x_1')F_\varsigma^n(\mathbf{x}'-\mathbf{e}_{\mathbf{i}_n})\,\mathrm{d}\mathbf{x}' - \int_{\mathcal{D}_1} \mathcal{G}_1(x_1-x_1')C_H(x_1')\,\mathrm{d}x_1'. \quad (3.5.1)$$

and

$$\begin{aligned}\widehat{C}_2(\mathbf{x}) =& \lambda^{2n} \sum_{\mathbf{i}_n}\sum_{\mathbf{j}_n} \int_{\mathcal{D}_n}\int_{\mathcal{D}_n} \mathcal{G}_n(\mathbf{x}-\mathbf{x}')\mathcal{G}_n(\mathbf{x}'-\mathbf{x}'')C_H(x_1'')F_\varsigma^n(\mathbf{x}'-\mathbf{e}_{\mathbf{i}_n})F_\varsigma^n(\mathbf{x}''-\mathbf{e}_{\mathbf{j}_n})\,\mathrm{d}\mathbf{x}'\,\mathrm{d}\mathbf{x}'' \\ &- \lambda^n \sum_{\mathbf{i}_n} \int_{\mathcal{D}_n}\int_{\mathcal{D}_n} \mathcal{G}_n(\mathbf{x}-\mathbf{x}')\mathcal{G}_n(\mathbf{x}'-\mathbf{x}'')C_H(x_1'')\left(F_\varsigma^n(\mathbf{x}'-\mathbf{e}_{\mathbf{i}_n}) + F_\varsigma^n(\mathbf{x}''-\mathbf{e}_{\mathbf{i}_n})\right)\,\mathrm{d}\mathbf{x}'\,\mathrm{d}\mathbf{x}'' \\ &+ \int_{\mathcal{D}_1}\int_{\mathcal{D}_1} \mathcal{G}_1(x_1-x_1')\mathcal{G}_1(x_1'-x_1'')C_H(x_1'')\,\mathrm{d}x_1'\,\mathrm{d}x_1''\end{aligned} \quad (3.5.2)$$

respectively, where the integrals of $\mathcal{G}_n(\mathbf{x}-\mathbf{x}')$ and $\mathcal{G}_n(\mathbf{x}-\mathbf{x}')C_H(x_1')$ have been reduced to one-dimensional integrals using a change of variables with (3.4.7). Represented in (3.5.1) and (3.5.2) is a classic homogenization problem, which is previously represented in both Russell and Jensen (2020) and Chapter 2 for one-dimensional point sinks by the corrections $\widehat{C}_a(x_1)$ and $\widehat{C}_{aa}(x_1)$ respectively. Both (3.5.1) and (3.5.2) use an n-dimensional free-space Green's function $\mathcal{G}_n$, which causes the expressions to remain valid except when within a distance $1/\mathrm{Pe}_L$ from either x_1-boundary. To evaluate (3.5.1) and (3.5.2) we can use results in Appendix B.5, where the integrals of $\mathcal{G}_1(x_1-x_1')C_H(x_1')$ and $\mathcal{G}_1(x_1-x_1')\mathcal{G}_1(x_1'-x_1'')C_H(x_1'')$ are calculated using the homogenized solution and one-dimensional free-space Green's function given in (3.2.2) and (3.4.9) respectively. Any remaining integrals can then be solved in n dimensions using the integral solver given in Appendix B.3.

Consider approximating the corrections $\widehat{C}_1(\mathbf{x})$ and $\widehat{C}_2(\mathbf{x})$ in the limit $\varsigma \to 0$. Because the sink function F_ς^n recovers an n-dimensional δ-function in the distribution sense, we might consider approximating the integrals in (3.5.1) and (3.5.2) by substituting an n-dimensional δ-function for F_ς^n. By denoting these solutions $\widehat{C}_1^\delta(\mathbf{x})$ and $\widehat{C}_2^\delta(\mathbf{x})$ we obtain

$$\widehat{C}_1^\delta(\mathbf{x}) \approx \lambda^n \sum_{\mathbf{i}_n} \mathcal{G}_n(\mathbf{x}-\mathbf{e}_{\mathbf{i}_n})C_H(e_i) - \int_{\mathcal{D}_1} \mathcal{G}_1(x_1-x_1')C_H(x_1')\,\mathrm{d}x_1' \quad (3.5.3)$$

and

$$\begin{aligned}\widehat{C}_2^{\delta}(\mathbf{x}) \approx & \lambda^{2n} \sum_{\mathbf{i}_n} \sum_{\mathbf{j}_n} \mathcal{G}_n(\mathbf{x}-\mathbf{e}_{\mathbf{i}_n}) \mathcal{G}_n(\mathbf{e}_{\mathbf{i}_n}-\mathbf{e}_{\mathbf{j}_n}) C_H(e_j) \\ & - \lambda^n \sum_{\mathbf{i}_n} \int_{\mathcal{D}_n} \mathcal{G}_n(\mathbf{x}-\mathbf{e}_{\mathbf{i}_n}) \mathcal{G}_n(\mathbf{e}_{\mathbf{i}_n}-\mathbf{x}'') C_H(x_1'') \, \mathrm{d}\mathbf{x}'' \\ & - \lambda^n \sum_{\mathbf{j}_n} \int_{\mathcal{D}_n} \mathcal{G}_n(\mathbf{x}-\mathbf{x}') \mathcal{G}_n(\mathbf{x}'-\mathbf{e}_{\mathbf{j}_n}) C_H(e_j) \, \mathrm{d}\mathbf{x}' \\ & + \int_{\mathcal{D}_1} \int_{\mathcal{D}_1} \mathcal{G}_1(x_1-x_1') \mathcal{G}_1(x_1'-x_1'') C_H(x_1'') \, \mathrm{d}x_1' \, \mathrm{d}x_1''. \end{aligned} \tag{3.5.4}$$

However, a singularity exists in the two- and three-dimensional free-space Green's function. So in the limit $\varsigma \to 0$ we see $\widehat{C}_1^{\delta}(\mathbf{x})$ only offers an appropriate approximation when $\mathbf{x}$ is suitably far from $\mathbf{e}_{\mathbf{i}_n}$, with $\widehat{C}_2^{\delta}(\mathbf{x})$ being everywhere singular. In contrast, as the one dimensional free-space Green's function contains no singularities, both $\widehat{C}_1^{\delta}(x_1)$ and $\widehat{C}_2^{\delta}(x_1)$ offer appropriate approximations of the corrections $\widehat{C}_1(x_1)$ and $\widehat{C}_2(x_1)$ respectively.

In one dimension we can calculate the magnitude of the leading-order correction $\widehat{C}_1(x_1)$ by calculating the order of integrals in (3.5.3). So using Appendix B.5 we find

$$\widehat{C}_1^{\delta}(x_1) = \mathcal{O}\left(\mathrm{Pe}_L^{-1} \max(\mathrm{Pe}_L^{-1}, \lambda)\right). \tag{3.5.5}$$

Figure 3.7(a) shows a comparison between (3.1.2) solved with finite-differences (Appendix B.2) and (3.5.1) and (3.5.2) solved with the quadrature (Appendix B.3) in one spatial dimension. The leading-order correction is seen to account for the staircase structure caused by discrete sink locations, with the second-order correction accounting for an over-prediction of uptake strength by the homogenized solution. Also shown are the δ-function approximations of the corrections given in (3.5.3) and (3.5.4). As the one-dimensional free-space Green's function contains no singularities, we see (3.5.3) and (3.5.4) offer close approximations of the corrections $\widehat{C}_1(x_1)$ and $\widehat{C}_2(x_1)$ respectively. However, discrepancies are seen near sink locations in the leading-order approximation, with an under-prediction of uptake being shown by the second-order correction. The inset of Figure 3.7(a) shows the difference between each prediction and the numerical solution to (3.1.2). This verifies how each correction to the homogenized solution results in an improved prediction of the solute concentration, with solving (3.5.1) and (3.5.2) with an integral solver being advantageous to using the δ-function approximations given in (3.5.3) and (3.5.4) respectively.

In two and three dimensions, due to singularities in the free-space Green's function, which are of order $\log|\mathbf{x}-\mathbf{x}'|$ and $1/|\mathbf{x}-\mathbf{x}'|$ respectively, we in turn find singularities in the δ-function approximation of the leading-order correction $\widehat{C}_1^{\delta}(\mathbf{x})$ (given in (3.5.3)) at sink locations $\mathbf{x} = \mathbf{e}_{\mathbf{i}_n}$.

(a) 1D periodic; concentration (b) 1D normally-perturbed; expectation

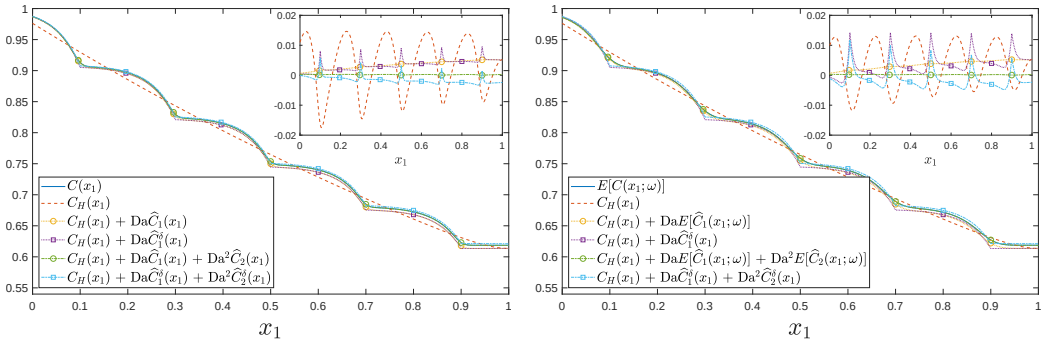

Figure 3.7: Concentration in one dimension, where $\mathbb{E}[C(x_1;\omega)]$ represents the sample expectation from 10^6 Monte Carlo realisations. Insets show the difference between each approximation and the sample expectation. Figure (a) uses periodic sink locations, whereas figure (b) uses normally-perturbed sink locations according to a standard deviation $\sigma = 0.02$. All figures use $\lambda = 0.2$, $(\mathrm{Pe}_L, \mathrm{Da}) = (20, 10)$ and $\varsigma = 0.01$.

Also, from (3.5.4) we find the second-order estimated correction $\widehat{C}_2^{\delta}(\mathbf{x})$ is everywhere singular due to the first term containing a $\mathcal{G}_n(\mathbf{0})$ term when $\mathbf{i}_n = \mathbf{j}_n$. Therefore regularisation of sink distributions is required in two and three dimensions (Mahiout et al., 2020), which will replace singularities in concentration profiles with smooth minima.

Consider the leading-order correction given in (3.5.1) in the limit $\varsigma \ll 1$ for both two and three dimensions. When away from sink locations we can use the δ-function approximation given in (3.5.3) due to no functions being evaluated at singularities. However, when in the vicinity of sink locations the integral given in (3.5.1) must instead be carefully approximated, which can be used to obtain the local minima of $\widehat{C}_1(\mathbf{x})$ which occur at $\mathbf{x} = \mathbf{e}_{\mathbf{i}_n}$. To approximate the correction when $\mathbf{x}$ is in the neighbourhood of $\mathbf{e}_{\mathbf{i}_n}$ we must approximate the integral

$$I_{\varsigma}^{n}(\boldsymbol{x}, \mathbf{e}_{\mathbf{i}_n}) \equiv \int_{\mathcal{D}_n} \mathcal{G}_n(\mathbf{x} - \mathbf{x}') C_H(x_1') F_{\varsigma}^{n}(\mathbf{x}' - \mathbf{e}_{\mathbf{i}_n})\, \mathrm{d}\mathbf{x}' \tag{3.5.6}$$

from (3.5.1). In the limit where $\varsigma \ll 1$ we see that $F_{\varsigma}^{n}(\mathbf{x}' - \mathbf{e}_{\mathbf{i}_n})$ becomes asymptotically small for $\mathbf{x}'$ sufficiently far from $\mathbf{e}_{\mathbf{i}_n}$, so we will consider the integral near $\mathbf{x} = \mathbf{e}_{\mathbf{i}_n}$ by setting

$$\mathbf{x} = \mathbf{e}_{\mathbf{i}_n} + \varsigma\mathbf{u} \quad \text{and} \quad \mathbf{x}' = \mathbf{e}_{\mathbf{i}_n} + \varsigma\mathbf{v}$$

and defining $R_u = |\mathbf{u}|$ and $R_v = |\mathbf{v}|$. By Figure 3.8 we see that

$$|\mathbf{x} - \mathbf{e}_{\mathbf{i}_n}| = \varsigma R_u, \quad |\mathbf{x}' - \mathbf{e}_{\mathbf{i}_n}| = \varsigma R_v \quad \text{and} \quad |\mathbf{x} - \mathbf{x}'| = \varsigma\sqrt{R_u^2 - 2R_uR_v\cos\theta + R_v^2}, \tag{3.5.7}$$

where θ is the angle made by the vectors $\mathbf{u}$ and $\mathbf{v}$. Consider the homogenized solution $C_H(x_1')$ in the neighbourhood of a sink by setting $x_1' = e_i + \varsigma v_1$, where e_i is the first component of $\mathbf{e}_{\mathbf{i}_n}$.

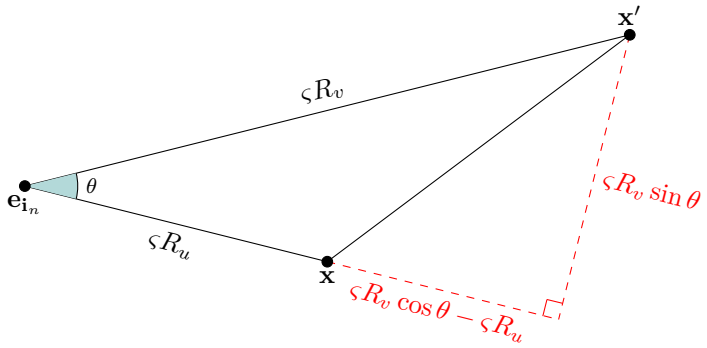

Figure 3.8: Depiction of the relevant angles and lengths created by $\mathbf{x}, \mathbf{x}'$ and $\mathbf{e}_{\mathbf{i}_n}$ in two and three dimensions.

By (3.2.2) we know that $C_H(x_1)$ is a smooth function of order $\mathcal{O}(1)$, therefore the homogenized solution can be approximated by

$$C_H(x_1') \approx C_H(e_i) + \mathcal{O}(\varsigma).$$

This will now be used to calculate an approximation of $\widehat{C}_1(\mathbf{x})$ in two and three dimensions, which will remain valid within a distance of order $\mathcal{O}(\varsigma)$ away from $\mathbf{e}_{\mathbf{i}_3}$ for $\varsigma \ll 1$.

In two dimensions we will approximate the free-space Green's function when $\mathbf{x}$ is in the vicinity of $\mathbf{x}'$ with the near-field free-space Green's function given in (3.4.14). Therefore F_ς^2 and $\mathcal{G}_2$ can be approximated using (3.1.5) and (3.4.14) to be

$$F_\varsigma^2(\mathbf{x}' - \mathbf{e}_{\mathbf{i}_2}) = \frac{1}{2\pi\varsigma^2} e^{-\frac{1}{2}R_v^2} \quad \text{and} \quad \mathcal{G}_2(\mathbf{x} - \mathbf{x}') \approx \frac{1}{2\pi} \log\left(\phi\varsigma\sqrt{R_u^2 - 2R_uR_v\cos\theta + R_v^2}\right)$$

respectively. This gives, using (3.5.6),

$$I_\varsigma^2(\boldsymbol{x}, \mathbf{e}_{\mathbf{i}_2}) \approx \frac{1}{4\pi^2} C_H(e_i) \int_0^{2\pi} \int_0^{\infty} R_v \log\left(\phi\varsigma\sqrt{R_u^2 - 2R_uR_v\cos\theta + R_v^2}\right) e^{-\frac{1}{2}R_v^2} \,\mathrm{d}R_v \,\mathrm{d}\theta$$

for $\varsigma \ll 1$. We can approximate the logarithmic term as $\log\left(\phi\varsigma\sqrt{R_u^2 - 2R_uR_v\cos\theta + R_v^2}\right) \approx \log(\phi\varsigma)$ for $\varsigma \ll 1$ due to both R_u and R_v being of order $\mathcal{O}(1)$ and $\phi\varsigma \ll 1$. Therefore the integral given in (B.4.3) can be approximated by

$$I_\varsigma^2(\boldsymbol{x}, \mathbf{e}_{\mathbf{i}_2}) \approx \frac{1}{2\pi} \log(\phi\varsigma) C_H(e_i)$$

when $\mathbf{x}$ is within a distance of order $\mathcal{O}(\varsigma)$ of $\mathbf{e}_{\mathbf{i}_2}$ as $\varsigma \to 0$. Using this with (3.5.1) we find the leading-order correction $\widehat{C}_1(\mathbf{x})$ when $\mathbf{x}$ is in the vicinity of $\mathbf{e}_{\mathbf{i}_2}$ to be

$$\widehat{C}_1(\mathbf{x}) \approx \frac{\lambda^2}{2\pi} \log(\phi\varsigma) C_H(e_i) \tag{3.5.8}$$

in the limit $\varsigma \to 0$. This gives that the leading-order correction $\widehat{C}_1(\mathbf{x})$ scales as $\log(\phi\varsigma)$ when $\mathbf{x}$ is in the vicinity of $\mathbf{e}_{\mathbf{i}_2}$, which is a direct consequence of the logarithmic singularity in the free-space Green's function $\mathcal{G}_2$.

For three dimensions we will use the near-field form of the free-space Green's function to obtain

$$F^3_\varsigma(\mathbf{x}' - \mathbf{e}_{\mathbf{i}_3}) = \frac{1}{(2\pi)^{3/2}\varsigma^3} e^{-\frac{1}{2}R_v^2} \quad \text{and} \quad \mathcal{G}_3(\mathbf{x} - \mathbf{x}') \approx \frac{-1}{4\pi\varsigma\sqrt{R_u^2 - 2R_uR_v\cos\theta + R_v^2}},$$

which are calculated using (3.1.5) and (3.4.20) respectively. This gives

$$I^3_\varsigma(\boldsymbol{x}, \mathbf{e}_{\mathbf{i}_3}) \approx -\frac{1}{2(2\pi)^{3/2}\varsigma} C_H(e_i) \int_0^\pi \int_0^\infty \frac{1}{\sqrt{R_u^2 - 2R_uR_v\cos\theta + R_v^2}} \exp\left(-\frac{1}{2}R_v^2\right) R_v^2 \sin\theta \, \mathrm{d}R_v \, \mathrm{d}\theta \tag{3.5.9}$$

for $\varsigma \ll 1$. To evaluate the θ integral the substitution $h^2 = R_u^2 - 2R_uR_v\cos\theta + R_v^2$ can be used to give

$$\int_0^\pi \frac{1}{\sqrt{R_u^2 - 2R_uR_v\cos\theta + R_v^2}} \sin\theta \, \mathrm{d}\theta = \int_{|R_u - R_v|}^{R_u + R_v} \frac{1}{R_uR_v} \mathrm{d}h = \begin{cases} 2/R_u & \text{for } R_u > R_v \\ 2/R_v & \text{for } R_u < R_v \end{cases}.$$

So by considering $0 \leq R_v \leq R_u$ and $R_u \leq R_v \leq \infty$ separately in (3.5.9) and using the integrals evaluated in (B.4.3) and (B.4.5) in Appendix B.4 we obtain

$$I^3_\varsigma(\boldsymbol{x}, \mathbf{e}_{\mathbf{i}_3}) \approx -\frac{1}{4\pi\varsigma R_u} \operatorname{erf}\left(\frac{R_u}{\sqrt{2}}\right) C_H(e_i), \tag{3.5.10}$$

which gives the asymptotic shape of the leading-order correction $\widehat{C}_1$ when $\mathbf{x}$ is in the vicinity of $\mathbf{e}_{\mathbf{i}_2}$ for $\varsigma \ll 1$. By Taylor expanding the error function about $R_u = 0$ we find that

$$\operatorname{erf}\left(\frac{R_u}{\sqrt{2}}\right) = \frac{2}{\sqrt{\pi}} \int_0^{R_u/\sqrt{2}} \exp\left(-t^2\right) \mathrm{d}t \approx \frac{2}{\sqrt{\pi}} \int_0^{R_u/\sqrt{2}} \left(1 - t^2 + \dots\right) \mathrm{d}t = \sqrt{\frac{2}{\pi}} \left(R_u - \frac{R_u^3}{6} + \dots\right). \tag{3.5.11}$$

So by using (3.5.1), we see that the leading-order correction $\widehat{C}_1$ when $\boldsymbol{x}$ is in the vicinity of $\mathbf{e}_{\mathbf{i}_3}$ is approximately

$$\widehat{C}_1(\mathbf{x}) \approx -\frac{\lambda^3}{(2\pi)^{3/2}\varsigma} C_H(e_i) \tag{3.5.12}$$

in the limit $\varsigma \to 0$. As for two dimensions, we find the magnitude of the singularity in the free-space Green's function governs the scaling of the leading-order correction $\widehat{C}_1(\mathbf{x})$, where this scaling is given by $1/\varsigma$ when $\mathbf{x}$ is in the vicinity of $\mathbf{e}_{\mathbf{i}_3}$ for $\varsigma \ll 1$. We can therefore find the order of magnitude for the leading-order correction $\widehat{C}_1$ in the vicinity of $\mathbf{x} = \mathbf{e}_{\mathbf{i}_n}$, which is given in one, two and three dimensions for $\mathrm{Pe}_L \gg \max(1, \sqrt{\mathrm{Da}})$ as

$$\mathcal{O}\left(\mathrm{Pe}_L^{-1} \max\left(\lambda, \mathrm{Pe}_L^{-1}\right)\right), \quad \mathcal{O}\left(\lambda^2 \log\left(\mathrm{Pe}_L \varsigma\right)\right) \quad \text{and} \quad \mathcal{O}\left(\lambda^3 \left(\frac{1}{\varsigma}\right)\right) \tag{3.5.13}$$

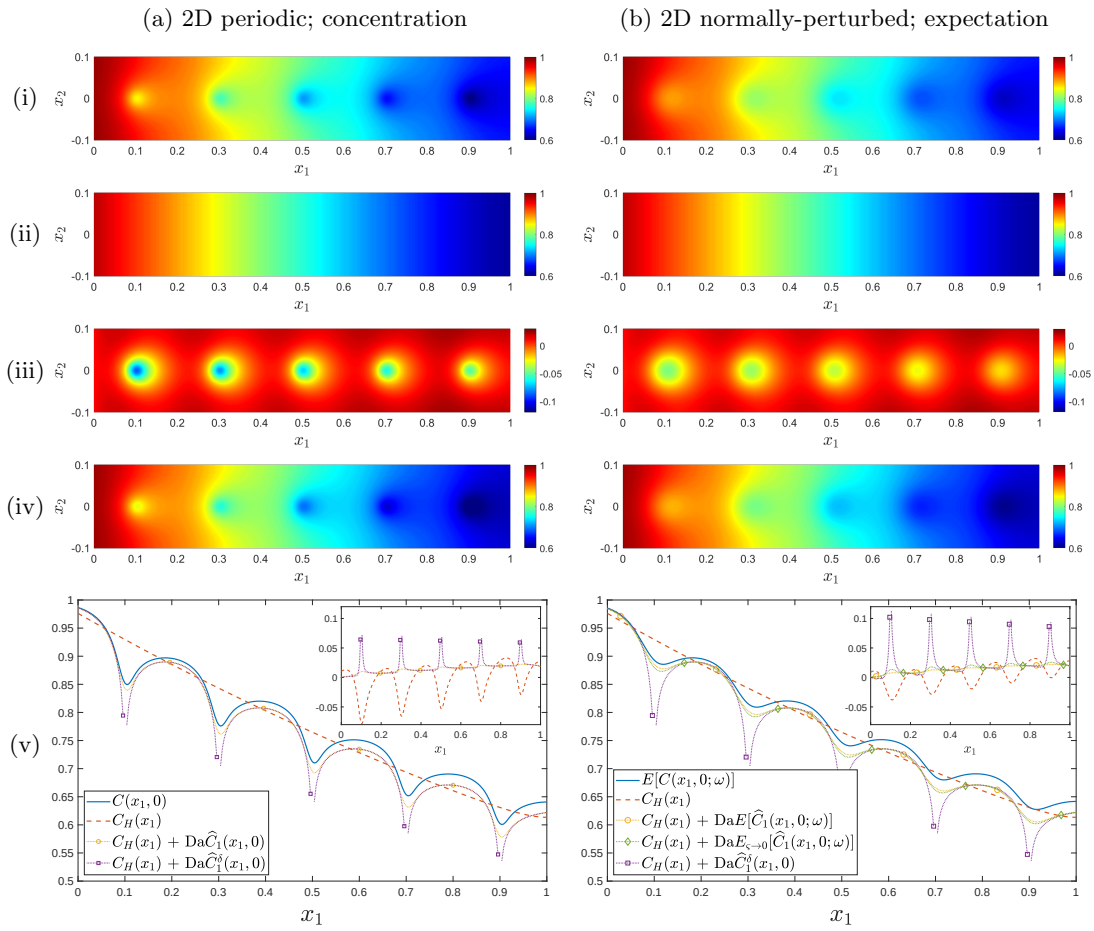

Figure 3.9: Concentration in two dimensions, where figures in column (a) use periodic sinks locations and figures in column (b) use normally-perturbed sink locations with a standard deviation $\sigma = 0.02$. For periodic and normally-perturbed sink locations row (i) shows the numerical concentration $C(\mathbf{x})$ and expected concentration $\mathbb{E}[C(\mathbf{x};\omega)]$ (the central sink-row from Figures 3.1(a) and 3.1(d) respectively), (ii) shows the homogenized solution for both cases, (iii) shows the correction $\widehat{C}_1(\mathbf{x})$ and expected correction $\mathbb{E}[\widehat{C}_1(\mathbf{x};\omega)]$ and (iv) the combination of the homogenized solution with the correction $\widehat{C}_1(\mathbf{x})$ and the expected correction $\mathbb{E}[\widehat{C}_1(\mathbf{x};\omega)]$ respectively in one strip of the domain where $x_2 \in [-0.1, 0.1]$. Row (v) shows the results from (i), (ii), (iv), (3.5.3) and (3.5.19) with $x_2 = 0$, where the inset shows the difference between each approximation and the numerical or expected concentration. All sample expectations are calculated using 10^4 realisations with Appendix B.2. All figures use $\lambda = 0.2$, $\varsigma = 0.01$, $(\mathrm{Pe}_L, \mathrm{Da}) = (20, 10)$ and $\mathcal{D}_2^s = [0,1] \times [-0.5, 0.5]$.

respectively.

Figure 3.9(a) shows two-dimensional results by comparing solutions from a finite-difference solver given in Appendix B.2 with (3.1.2) and the integral solver described in Appendix B.3 with (3.5.1) and (3.5.2). Figure 3.9(a)(i) shows the numerical concentration in the region

$\mathcal{D}^2_{\text{strip}} = [0,1] \times [-\lambda/2, \lambda/2]$ taken from Figure 3.1(a). This is compared to the homogenized solution, the correction $\widehat{C}_1(\mathbf{x})$ and the combination of the two in Figures 3.9(a)(ii), 3.9(a)(iii) and 3.9(a)(iv) respectively. By using the region of influence given in Figure 3.6 we see that the concentration in $\mathcal{D}^2_{\text{strip}}$ is heavily influenced by sinks within the domain $\mathcal{D}^2_{\text{strip}} = [0,1]\times[-2\lambda, 2\lambda]$, with little impact being felt from sinks outside this domain and from the x_2-boundary in $\mathcal{D}^s_2$. Therefore $\widehat{C}_1$ in Figure 3.9(a)(iii) is constructed from sums over sinks from two rows above to two rows below $\mathcal{D}^2_{\text{strip}}$.

Figure 3.9(a) shows how the leading-order correction accounts for a decrease (increase) in concentration when near to (away from) sink locations, with an ellipsoidal structure being exhibited about each sink location. This again reflects a wavy structure within the concentration, as is seen in the one-dimensional form of $\widehat{C}_1(\mathbf{x})$ in Figure 3.7(a). The second-order correction for two spatial dimensions is not evaluated here but is thought to again account for an error in the prediction of uptake strength by the homogenized solution, as found in one dimension. This error is seen to be an over-prediction in the slice taken from the two-dimensional concentration through $x_2 = 0$ shown in Figure 3.9(a)(v). Also shown in Figure 3.9(a)(v) is how the δ-function approximation in (3.5.3) offers a good prediction of the correction away from sink locations, but how the singularities at sink locations results in discrepancies. Figures 3.7(b) and 3.9(b) show the expected concentration when sink locations are normally-perturbed from a periodic configuration and will be discussed in the following section.

3.5.2 Moments of corrections accounting for normally-perturbed sink locations

Let sink locations be normally-perturbed from a periodic configuration, where the mean sink locations are given by $\mathbf{e}_{\mathbf{i}_n}$ and position vectors are given in (3.3.1). Using (3.2.9)-(3.2.11) the first two moments of $\widehat{C}_1(\mathbf{x};\omega)$ and the first moment of $\widehat{C}_2(\mathbf{x};\omega)$ in n dimensions are given by

$$\mathbb{E}\left[\widehat{C}_1(\mathbf{x};\omega)\right] = \int_{\mathcal{D}_n} \mathcal{G}_n(\mathbf{x}-\mathbf{x}')C_H(x_1')\left(\lambda^n \sum_{\mathbf{i}_n} \mathbb{E}[F^n_\varsigma(\mathbf{x}'-\mathbf{x}_{\mathbf{i}_n})] - 1\right) \mathrm{d}\mathbf{x}', \tag{3.5.14}$$

$$\begin{aligned}\mathcal{K}_{\widehat{C}_1}[\mathbf{x},\mathbf{y}] = \lambda^{2n} \sum_{\mathbf{i}_n} \int_{\mathcal{D}_n}\int_{\mathcal{D}_n} \mathcal{G}_n(\mathbf{x}-\mathbf{x}')C_H(x_1') \\ \times \mathcal{K}_{F^n_\varsigma}[\mathbf{x}'-\mathbf{x}_{\mathbf{i}_n}, \mathbf{y}'-\mathbf{x}_{\mathbf{i}_n}]\mathcal{G}_n(\mathbf{y}-\mathbf{y}')C_H(y_1')\,\mathrm{d}\mathbf{x}'\,\mathrm{d}\mathbf{y}'\end{aligned} \tag{3.5.15}$$

and

$$\mathbb{E}\left[\widehat{C}_2(\mathbf{x};\omega)\right] = \int_{\mathcal{D}_n}\int_{\mathcal{D}_n} \mathcal{G}_n(\mathbf{x}-\mathbf{x}')\mathcal{G}_n(\mathbf{x}'-\mathbf{x}'')C_H(x_1'') \times \left(\lambda^{2n}\sum_{\substack{\mathbf{i}_n \\ \mathbf{i}_n\neq\mathbf{j}_n}}\sum_{\mathbf{j}_n}\mathbb{E}[F_\varsigma^n(\mathbf{x}'-\mathbf{x}_{\mathbf{i}_n})]\mathbb{E}[F_\varsigma^n(\mathbf{x}''-\mathbf{x}_{\mathbf{j}_n})] + \lambda^{2n}\sum_{\mathbf{i}_n}\mathbb{E}[F_\varsigma^n(\mathbf{x}'-\mathbf{x}_{\mathbf{i}_n})F_\varsigma^n(\mathbf{x}''-\mathbf{x}_{\mathbf{i}_n})] - \lambda^n\sum_{\mathbf{i}_n}\mathbb{E}[F_\varsigma^n(\mathbf{x}'-\mathbf{x}_{\mathbf{i}_n})] - \lambda^n\sum_{\mathbf{j}_n}\mathbb{E}[F_\varsigma^n(\mathbf{x}''-\mathbf{x}_{\mathbf{j}_n})] + 1\right)\mathrm{d}\mathbf{x}'\,\mathrm{d}\mathbf{x}'' \tag{3.5.16}$$

where $\mathbb{E}[F_\varsigma^n(\mathbf{x}-\mathbf{x}_{\mathbf{i}_n})]$ and $\mathbb{E}[F_\varsigma^n(\mathbf{x}-\mathbf{x}_{\mathbf{i}_n})F_\varsigma^n(\mathbf{y}-\mathbf{x}_{\mathbf{i}_n})]$ are given in (3.3.12) and (3.3.13) respectively. As noted in Section 3.1, when $\hat{g}$ represents point sink locations in one dimension the moments given in (3.5.14)-(3.5.16) relate to the corrections $\widehat{C}_b(x_1)$ and $\widehat{C}_{bb}(x_1)$ from Russell and Jensen (2020) and Chapter 2.

The integrals given in (3.5.14)-(3.5.16) can be solved numerically using the integral solver given in Appendix B.3, but this becomes more computationally expensive as the number of dimensions, order of the correction or domain size increase. We therefore estimate the corrections when the sink width is asymptotically small (i.e. $\varsigma \to 0$). As for periodic sink locations we can replace the sink functions with n-dimensional δ-functions, which can be used in (3.3.12) and (3.3.13) to give

$$\mathbb{E}_{\varsigma\to 0}[F_\varsigma^n(\mathbf{x}-\mathbf{x}_{\mathbf{i}_n})] = F_\sigma^n(\mathbf{x}-\mathbf{e}_{\mathbf{i}_n}) \tag{3.5.17}$$

and

$$\mathbb{E}_{\varsigma\to 0}[F_\varsigma^n(\mathbf{x}-\mathbf{x}_{\mathbf{i}_n})F_\varsigma^n(\mathbf{y}-\mathbf{x}_{\mathbf{i}_n})] = \delta(\mathbf{x}-\mathbf{y})\sqrt{F_\sigma^n(\mathbf{x}-\mathbf{e}_{\mathbf{i}_n})F_\sigma^n(\mathbf{y}-\mathbf{e}_{\mathbf{i}_n})} \tag{3.5.18}$$

respectively, which in turn give the moments of the sink function. Using these in (3.5.14) - (3.5.16) gives

$$\mathbb{E}_{\varsigma\to 0}\left[\widehat{C}_1(\mathbf{x};\omega)\right] = \int_{\mathcal{D}_n}\mathcal{G}_n(\mathbf{x}-\mathbf{x}')C_H(x_1')\left(\lambda^n\sum_{\mathbf{i}_n}F_\sigma^n(\mathbf{x}'-\mathbf{e}_{\mathbf{i}_n}) - 1\right)\mathrm{d}\mathbf{x}', \tag{3.5.19}$$

$$\mathrm{Var}_{\varsigma\to 0}[\widehat{C}_1(\mathbf{x};\omega)] = \lambda^{2n}\sum_{\mathbf{i}_n}\left(\int_{\mathcal{D}_n}\left(\mathcal{G}_n(\mathbf{x}-\mathbf{x}')C_H(x_1')\right)^2 F_\sigma^n(\mathbf{x}'-\mathbf{e}_{\mathbf{i}_n})\,\mathrm{d}\mathbf{x}' - \left(\int_{\mathcal{D}_n}\mathcal{G}_n(\mathbf{x}-\mathbf{x}')C_H(x_1')F_\sigma^n(\mathbf{x}'-\mathbf{e}_{\mathbf{i}_n})\,\mathrm{d}\mathbf{x}'\right)^2\right). \tag{3.5.20}$$

and

$$\mathbb{E}_{\varsigma\to 0}\left[\widehat{C}_2(\mathbf{x};\omega)\right] = \int_{\mathcal{D}_n}\int_{\mathcal{D}_n} \mathcal{G}_n(\mathbf{x}-\mathbf{x}')\mathcal{G}_n(\mathbf{x}'-\mathbf{x}'')C_H(x_1'') \times \left(\lambda^{2n}\sum_{\substack{\mathbf{i}_n\\ \mathbf{i}_n\neq\mathbf{j}_n}}\sum_{\mathbf{j}_n} F_\sigma^n(\mathbf{x}'-\mathbf{e}_{\mathbf{i}_n})F_\sigma^n(\mathbf{x}''-\mathbf{e}_{\mathbf{i}_n}) + \lambda^{2n}\delta\left(\mathbf{x}'-\mathbf{x}''\right)\sum_{\mathbf{i}_n}\sqrt{F_\sigma^n(\mathbf{x}'-\mathbf{e}_{\mathbf{i}_n})F_\sigma^n(\mathbf{x}''-\mathbf{e}_{\mathbf{i}_n})} - \lambda^n\sum_{\mathbf{i}_n} F_\sigma^n(\mathbf{x}'-\mathbf{e}_{\mathbf{i}_n}) - \lambda^n\sum_{\mathbf{j}_n} F_\sigma^n(\mathbf{x}''-\mathbf{e}_{\mathbf{i}_n}) + 1\right)\mathrm{d}\mathbf{x}'\,\mathrm{d}\mathbf{x}'' \tag{3.5.21}$$

respectively. Comparing the expectation given in (3.5.19) with the correction $\widehat{C}_1^\delta(\mathbf{x})$ given in (3.5.3) we see that perturbing sinks results in singularities being smoothed out when taking the expectation. However, the δ-function present in (3.5.21) shows a singularity still exists in the second-order correction when considering two and three dimensions. Note how taking the limit $\varsigma \to 0$ reduces the two $2n$-dimensional integrals in the variance down to two n-dimensional integrals, thereby making it less computationally expensive to compute.

To find an approximation of the expectations given in (3.5.19) and (3.5.21), we can consider the limit $\sigma \to 0$ by replacing the regularised function F_σ^n with an n-dimensional δ-function. This removes disorder from (3.5.19) and (3.5.21) and introduces singularities at mean sink locations in two and three dimensions. When away from $\mathbf{x} = \mathbf{x}'$ in the limit $\varsigma, \sigma \to 0$ we find the expectation of $\widehat{C}_1(\mathbf{x};\omega)$ and $\widehat{C}_2(\mathbf{x};\omega)$ locally converge to the deterministic expressions of $\widehat{C}_1^\delta(\mathbf{x})$ and $\widehat{C}_2^\delta(\mathbf{x})$ given in (3.5.3) and (3.5.4) respectively. So in one dimension we find that the magnitude of the leading-order correction in the limit $\varsigma, \sigma \to 0$ is of the same size as for periodic sink locations, which is given by (3.5.5). We can also find an approximation of the leading-order correction for finite ς and σ in the limit $\varsigma, \sigma \ll 1$ when $\mathbf{x}$ is in the vicinity of $\mathbf{e}_{\mathbf{i}_n}$ in two and three dimensions. This is done by using the periodic results given in (3.5.8) and (3.5.12), where the width ς is now replaced by an effective width $\sqrt{\sigma^2+\varsigma^2}$ due to the expectation of F_ς from (3.3.12). So for two and three dimensions the expectation of $\widehat{C}_1(\mathbf{x};\omega)$ near $\mathbf{x} = \mathbf{e}_{\mathbf{i}_n}$ in the limit $\varsigma, \sigma \ll 1$ is given by

$$\mathbb{E}[\widehat{C}_1(\mathbf{x};\omega)] \approx \frac{\lambda^2}{2\pi}\log\left(\phi\sqrt{\sigma^2+\varsigma^2}\right)C_H(e_i) \tag{3.5.22}$$

and

$$\mathbb{E}[\widehat{C}_1(\mathbf{x};\omega)] \approx -\frac{\lambda^3}{(2\pi)^{3/2}\sqrt{\sigma^2+\varsigma^2}}C_H(e_i) \tag{3.5.23}$$

respectively. Therefore the magnitude of the leading-order correction for $\mathrm{Pe}_L \gg \max(1, \sqrt{\mathrm{Da}})$

in the vicinity of $\mathbf{x} = \mathbf{e}_{\mathbf{i}_n}$ in one, two and three dimensions is given by

$$\mathcal{O}\left(\mathrm{Pe}_L^{-1}\max(\lambda, \mathrm{Pe}_L^{-1})\right), \quad \mathcal{O}\left(\lambda^2 \log\left(\mathrm{Pe}_L\sqrt{\varsigma^2+\sigma^2}\right)\right) \quad \text{and} \quad \mathcal{O}\left(\lambda^3\left(\frac{1}{\sqrt{\varsigma^2+\sigma^2}}\right)\right) \tag{3.5.24}$$

respectively.

Figures 3.7(b) and 3.9(b) compare sample moments of the concentration calculated from Monte Carlo realisations with moments of corrections found using the integral solver described in Appendix B.3 with (3.5.14) and (3.5.16). Figure 3.7(b) shows the contribution from the expectation of $\widehat{C}_1(x_1;\omega)$ and $\widehat{C}_2(x_1;\omega)$ to the homogenized solution in one dimension. As for periodic sink locations, the leading-order correction accounts for the staircase structure caused by discrete sink locations, with the second-order correction accounting for an over-prediction of uptake strength by the homogenized solution. One difference is how the wavy structure is smoothed out when moving from periodic to normally-perturbed sink locations. This is due to the sink function having a width ς for periodic sink locations, but when taking the expectation this width becomes $\sqrt{\varsigma^2+\sigma^2}$ for normally-perturbed sink locations. This also results in the δ-function approximations $\widehat{C}_1^\delta(x_1;\omega)$ and $\widehat{C}_2^\delta(x_1;\omega)$ being poorer estimators of the expectation when compared to their use for periodic sink locations. The inset of Figure 3.7(b) shows the difference between the sample expectation and each approximation, which demonstrates how each correction improves the prediction of the numerical concentration.

Figure 3.9(b) shows the expected concentration in two dimensions within the region $\mathcal{D}^2_{\text{strip}} = [0,1]\times[-\lambda/2,\lambda/2]$ for normally-perturbed sink locations. It was previously shown that the concentration in $\mathcal{D}^2_{\text{strip}}$ is influenced by two rows of sinks above and below the domain, with little impact being felt from the x_2-boundary in $\mathcal{D}^s_2$. Therefore the expectation is found by summing over five rows of sinks, which include the four rows sandwiching $\mathcal{D}^2_{\text{strip}}$. As for periodic sink locations, we find the expectation of the leading-order correction accounts for an increase in uptake near sink locations with a decrease elsewhere, leading to an ellipsoidal shape forming about the mean sink locations. In the limit $\varsigma \to 0$ Figure 3.9(b)(v) shows good agreement between using (3.5.19) and (3.5.14) when $x_2 = 0$. This is partly due to (3.5.19) containing no singularities due to taking expectations smoothing out variation at $\mathbf{x} = \mathbf{e}_{\mathbf{i}_2}$, which is reflected by the σ dependence in (3.5.19). However, when also taking the limit $\sigma \to 0$ we see the deterministic correction $\widehat{C}_1^\delta$ offers a poor description of the expectation when $\mathbf{x}$ is in the vicinity of $\mathbf{e}_{\mathbf{i}_2}$ due to singularities existing in (3.5.3). Figure 3.9(b) does not calculate the second-order corrections for normally-perturbed sink locations in two spatial dimensions due to the computational expense.

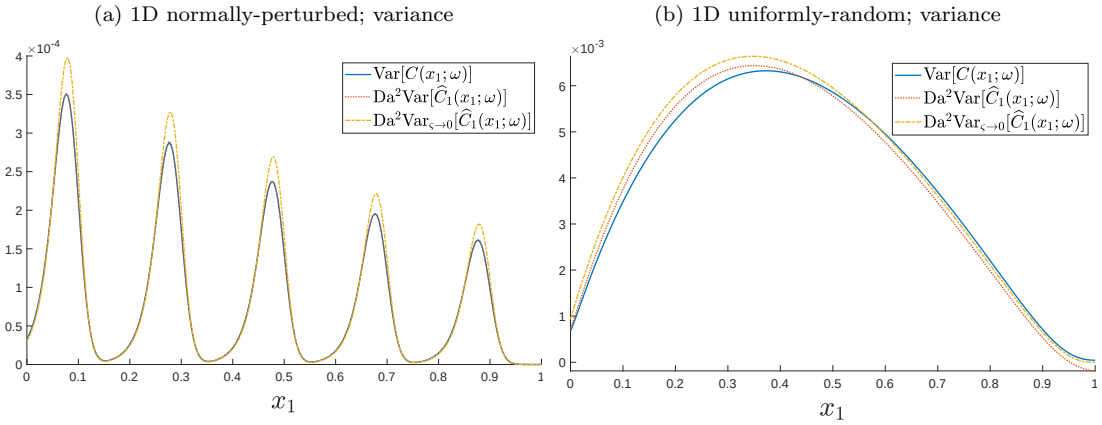

Figure 3.10: Variance of the concentration in one dimension, where (a) uses normally-perturbed sink locations and (b) uses uniformly-random sink locations. Here, $\mathrm{Var}[C(x_1;\omega)]$ represents the sample variance from 10^6 Monte Carlo realisations, $\mathrm{Var}[\widehat{C}(x_1;\omega)]$ is calculated using (3.3.10) and (3.3.11) with (3.3.5) in (3.5.15) for (a) and (3.5.26) for (b) and $\mathrm{Var}_{\varsigma\to 0}[\widehat{C}(x_1;\omega)]$ is calculated using (3.5.20) for (a) and (3.5.38) for (b). All figures use $\lambda = 0.2$, $(\mathrm{Pe}_L, \mathrm{Da}) = (20, 10)$ and $\varsigma = 0.01$, with figure (a) using $\sigma = 0.02$.

Figure 3.10(a) shows the variance of the concentration in one dimension. This is done by comparing 10^6 Monte Carlo realisations of (3.5.15) using the integral solver outlined in Appendix B.3. Good agreement between the sample variance and the variance of the leading-order correction can be seen, with an increase in variation been found about sink locations causing a wavy sink-to-sink structure. Also shown is the variance found when taking the limit $\varsigma \to 0$, as given in (3.5.20). This can be seen to overestimate the variance in one dimension in Figure 3.10(a) when near sink locations, but otherwise has a similar structure to the exact form used to calculate the variance of $\widehat{C}_1(\mathbf{x}, \omega)$.

Figure 3.11(a) shows the variance of the concentration in two dimensions for normally-perturbed sink locations. Figure 3.11(a)(i) calculates the sample variance using 10^4 Monte Carlo realisations, whereas Figure 3.11(a)(ii) uses the variance of the leading-order correction in the limit $\varsigma \to 0$, which is given in (3.5.20). Both figures show the variance decaying and becoming asymptotically small when reaching the x_2 boundaries, which is due to sink locations being independently distributed. However, the crescent shapes shown in the sample variance are not captured and this study cannot explain their appearance. Also, the magnitude of the variance about each sink location has been over-predicted when using the δ-function approximation, with it being approximately double the size at sink locations. This is shown by the sample variance and approximation of the variance of $\widehat{C}_1$ when $\varsigma \to 0$ for $x_2 = 0$ in Figure 3.11(a)(iii).

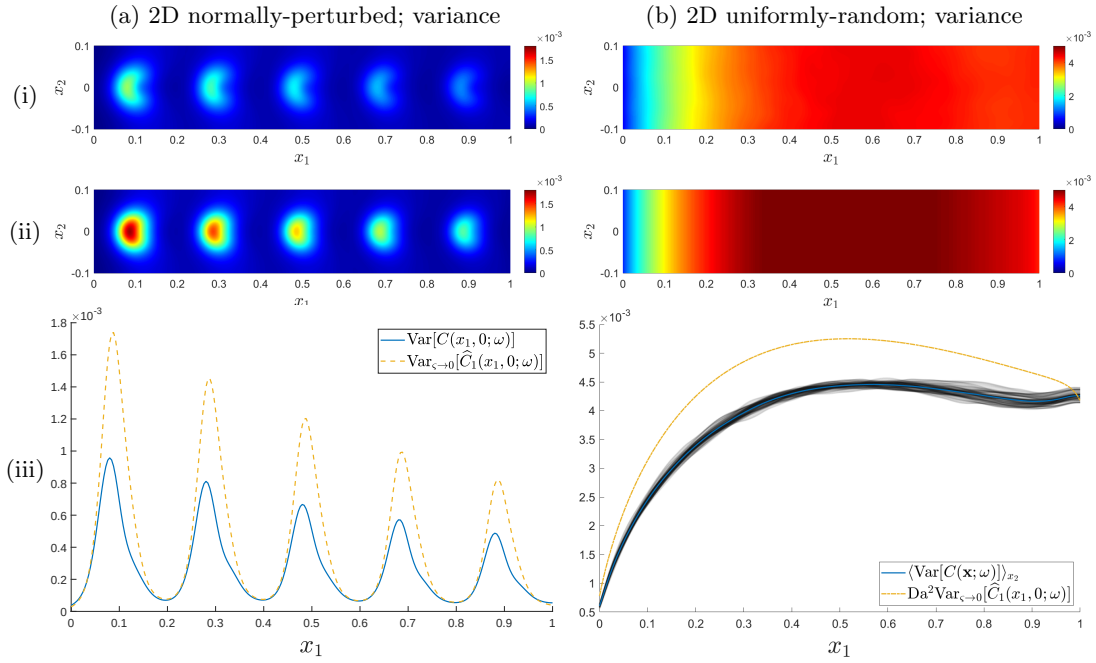

Figure 3.11: Variance of the concentration in two dimension, where columns (a) and (b) use normally-perturbed and uniformly-random sink locations respectively. Figures (i) and (ii) show the sample variance (taken from Figures 3.1(f) and 3.2(c)) $[\mathrm{Var}[C(\mathbf{x};\omega)]]$ and the δ-function approximation of the variance $[\mathrm{Var}_{\varsigma\to 0}[C(\mathbf{x};\omega)]]$ respectively in one strip of the domain where $x_2 \in [-0.1, 0.1]$. To calculate δ-function approximations we uses (3.5.20) and (3.5.38) for normally-perturbed and uniformly-random sink locations respectively. Figure (a)(iii) shows both the sample variance and δ-function approximation with $x_2 = 0$, whereas figure (b)(iii) shows a cloud plot of the sample variance for $x_2 = -2, -1.996, \ldots, 2$ from Figure 3.2(c), the average of these variances over x_2 $[\langle \mathrm{Var}[C(\mathbf{x};\omega)]\rangle_{x_2}]$ and the δ-function approximation of the variance from (3.5.38) $[\mathrm{Var}_{\varsigma\to 0}[\widehat{C}_1(x_1,0;\omega)]]$. All figures use $\lambda = 0.2$, $(\mathrm{Pe}_L, \mathrm{Da}) = (20, 10)$ and $\varsigma = 0.01$ and sample variances are calculated from 10^4 Monte Carlo realisations. Figure (a) uses $\mathcal{D}_2^s = [0,1] \times [-0.5, 0.5]$ and $\sigma = 0.02$ whereas figure (b) uses $\mathcal{D}_2^s = [0,1] \times [-2.5, 2.5]$.

This demonstrates how smearing out the sinks' location reduces the variation in solute concentration. Although this over-prediction is seen in one dimension when taking the limit $\varsigma \to 0$, see Figure 3.10(a), it is thought to be exaggerated in two dimensions due to the singularity in the Green's function.

Both the absence of crescent shapes and over-prediction of the variance could potentially be corrected by using the full expression for the variance of $\widehat{C}_1$ given in (3.5.15). However, difficulties arise when solving (3.5.15) due to being computationally expensive in two and three dimensions. Figures 3.10(b) and 3.11(b) show the variance of the concentration for uniformly-random sink locations, as will be discussed in the following section.

3.5.3 Moments of corrections accounting for uniformly-random sink locations

Let sink locations be prescribed by a multivariate uniform distribution, with the position vector given by $\boldsymbol{\xi}_{\mathbf{i}_3} = (\xi_i, \xi_j, \xi_k)$ such that $\xi_i \sim \mathcal{U}[0,1]$ and $\xi_j, \xi_k \sim \mathcal{U}[-L_s, L_s]$ for $i = 1, \ldots, N$ and $j, k = -M, \ldots, M$. Then (3.2.9)-(3.2.11) can be used with (3.3.19) and (3.3.20) to give the corrections to the homogenized solution in n dimensions as

$$\mathbb{E}\left[\widehat{C}_1(\mathbf{x};\omega)\right] = 0, \tag{3.5.25}$$

$$\begin{aligned}\mathcal{K}_{\widehat{C}_1}[\mathbf{x},\mathbf{y}] = \int_{\mathcal{D}_n}\int_{\mathcal{D}_n} &\mathcal{G}_n(\mathbf{x}-\mathbf{x}')C_H(x_1')\mathcal{G}_n(\mathbf{y}-\mathbf{y}')C_H(y_1') \\ &\times\left(\lambda^n F^n_{\sqrt{2}\varsigma}(\mathbf{x}'-\mathbf{y}') - \frac{\lambda}{(2M+1)^{n-1}}\right)\mathrm{d}\mathbf{x}'\,\mathrm{d}\mathbf{y}'\end{aligned} \tag{3.5.26}$$

and

$$\begin{aligned}\mathbb{E}\left[\widehat{C}_2(\mathbf{x};\omega)\right] = \int_{\mathcal{D}_n}\int_{\mathcal{D}_n} &\mathcal{G}_n(\mathbf{x}-\mathbf{x}')\mathcal{G}_n(\mathbf{x}'-\mathbf{x}'')C_H(x_1'') \\ &\times\left(\lambda^n F^n_{\sqrt{2}\varsigma}(\mathbf{x}'-\mathbf{x}'') - \frac{\lambda}{(2M+1)^{n-1}}\right)\mathrm{d}\mathbf{x}'\,\mathrm{d}\mathbf{x}''.\end{aligned} \tag{3.5.27}$$

In two and three dimensions, consider when L_s becomes asymptotically large in comparison to the average inter-sink distance λ. In this limit, the expectation and variance become independent of x_2 and x_3 when suitably far from boundaries, as is seen in two dimensions in Figures 3.2(b) and 3.2(c) respectively. To calculate $\widehat{C}_2$, which is the leading-order correction to the expectation, we must evaluate the following two integrals

$$I_4(\mathbf{x}) = \int_{\mathcal{D}_n}\mathcal{G}_n(\mathbf{x}-\mathbf{x}')\left(\int_{\mathcal{D}_n}\mathcal{G}_n(\mathbf{x}'-\mathbf{x}'')C_H(x_1'')F^n_{\sqrt{2}\varsigma}(\mathbf{x}'-\mathbf{x}'')\,\mathrm{d}\mathbf{x}''\right)\mathrm{d}\mathbf{x}', \tag{3.5.28a}$$

$$I_5(\mathbf{x}) = \int_{\mathcal{D}_n}\int_{\mathcal{D}_n}\mathcal{G}_n(\mathbf{x}-\mathbf{x}')\mathcal{G}_n(\mathbf{x}'-\mathbf{x}'')C_H(x_1'')\,\mathrm{d}\mathbf{x}'\,\mathrm{d}\mathbf{x}''. \tag{3.5.28b}$$

In n dimensions I_5 can be simplified using a change of variables with (3.4.7) to reduce the two- and three-dimensional problem to one dimension. For I_4, consider when $\varsigma \ll 1$, which results in $F^n_{\sqrt{2}\varsigma}(\mathbf{x}'-\mathbf{x}'')$ becoming asymptotically small when $\mathbf{x}'$ is far from $\mathbf{x}''$. As a result, consider the integral near $\mathbf{x}' = \mathbf{x}''$ by setting $\mathbf{x}'' = \mathbf{x}' + \varsigma\mathbf{u}$ for some vector $\mathbf{u}$. So as $C_H(x_1)$ is a smooth function of order $\mathcal{O}(1)$ we can approximate the homogenized solution as

$$C_H(x_1'') \approx C_H(x_1') + \mathcal{O}(\varsigma).$$

This will now be used to approximate I_4 in one, two and three dimensions.

In one dimension we can use (3.4.9) with $x_1'' = x_1' + \varsigma u$ to give

$$\mathcal{G}_1(x_1'-x_1'') = -\frac{1}{2\phi}\exp\left(\frac{-\mathrm{Pe}_L}{2}\varsigma u - \phi\varsigma|u|\right). \tag{3.5.29}$$

Therefore the x_1'' integral in I_4 is given by

$$\int_{\mathcal{D}_1} \mathcal{G}_1(x_1' - x_1'')C_H(x_1'')F^1_{\sqrt{2}\varsigma}(x_1' - x_1'')\,\mathrm{d}x_1'' \approx \int_{\mathcal{D}_1} \mathcal{G}_1(-\varsigma u)(C_H(x_1') + \dots)F^1_{\sqrt{2}\varsigma}(-\varsigma u)\varsigma\,\mathrm{d}u,$$
$$\approx -\frac{1}{4\sqrt{\pi}\phi}C_H(x_1')\int_{-\infty}^{\infty}\exp\left(-\frac{u^2}{4} - \frac{\mathrm{Pe}_L}{2}\varsigma u - \phi\varsigma|u|\right)\mathrm{d}u.$$

To solve this integral we can consider when $0 \leq u \leq \infty$ and $-\infty \leq u \leq 0$ separately and use Appendix B.4 to obtain

$$\int_{-\infty}^{\infty}\exp\left(-\frac{u^2}{4} - \frac{\mathrm{Pe}_L}{2}\varsigma u - \phi\varsigma|u|\right) \to 2\sqrt{\pi} \quad \text{as } \varsigma \to 0. \tag{3.5.30}$$

Therefore as $\varsigma \to 0$ we obtain

$$I_4(x_1) \approx -\frac{1}{2\phi}\int_{\mathcal{D}_1}\mathcal{G}_1(x_1 - x_1')C_H(x_1')\,\mathrm{d}x',$$

which gives

$$\begin{aligned}\mathbb{E}\left[\widehat{C}_2(x_1;\omega)\right] \approx &-\frac{\lambda}{2\phi}\int_{\mathcal{D}_1}\mathcal{G}_1(x_1 - x_1')C_H(x_1')\,\mathrm{d}x_1' \\ &- \lambda\int_{\mathcal{D}_1}\int_{\mathcal{D}_1}\mathcal{G}_1(x_1 - x_1')\mathcal{G}_1(x_1' - x_1'')C_H(x_1'')\,\mathrm{d}x_1'\,\mathrm{d}x_1''.\end{aligned} \tag{3.5.31}$$

In two dimensions the approximation of the free-space Green's function given in (3.4.14) can be used with $\mathbf{x}'' = \mathbf{x}' + \varsigma\mathbf{u}$ and $\hat{r} = |\mathbf{u}|$ to give

$$\mathcal{G}_2(\mathbf{x}' - \mathbf{x}'') = \mathcal{G}_2(-\varsigma\mathbf{u}) \approx \frac{1}{2\pi}\log(\phi\varsigma\hat{r})$$

when $\varsigma \ll 1/\phi \ll 1$. Therefore the $\mathbf{x}''$ integral in I_4 is given by

$$\int_{\mathcal{D}_2}\mathcal{G}_2(\mathbf{x}' - \mathbf{x}'')C_H(x_1'')F^2_{\sqrt{2}\varsigma}(\mathbf{x}' - \mathbf{x}'')\,\mathrm{d}\mathbf{x}'' \approx \int_{\mathcal{D}_2}\mathcal{G}_2(-\varsigma\mathbf{u})(C_H(x_1') + \dots)F^2_{\sqrt{2}\varsigma}(-\varsigma\mathbf{u})\,\mathrm{d}\mathbf{x}''$$
$$\approx \frac{1}{4\pi}C_H(x_1'')\int_0^{\infty}\hat{r}\log(\phi\varsigma\hat{r})\exp\left(-\frac{\hat{r}^2}{4}\right)\mathrm{d}\hat{r}.$$

Here, the integral gives a constant which can be solved using results in Appendix B.4, resulting in I_4 being given by

$$I_4(\mathbf{x}) \approx -\frac{1}{4\pi}\left(\gamma - 2\log(2\phi\varsigma)\right)\int_{\mathcal{D}_2}\mathcal{G}_2(\mathbf{x} - \mathbf{x}')C_H(x_1')\,\mathrm{d}\mathbf{x}',$$

where $\gamma \approx 0.577216$ is the Euler-Mascheroni constant. This, combined with the reduction of I_5 to a one-dimensional integral, gives the expectation of $\widehat{C}_2(\mathbf{x};\omega)$ as

$$\begin{aligned}\mathbb{E}\left[\widehat{C}_2(\mathbf{x};\omega)\right] \approx &-\frac{\lambda^2}{4\pi}\left(\gamma - 2\log(2\phi\varsigma)\right)\int_{\mathcal{D}_1}\mathcal{G}_1(x_1 - x_1')C_H(x_1')\,\mathrm{d}x_1' \\ &- \frac{\lambda}{2M+1}\int_{\mathcal{D}_1}\int_{\mathcal{D}_1}\mathcal{G}_1(x_1 - x_1')\mathcal{G}_1(x_1' - x_1'')C_H(x_1'')\,\mathrm{d}x_1'\,\mathrm{d}x_1''.\end{aligned} \tag{3.5.32}$$

In three dimensions we can use the approximation of the free-space Green's function given in (3.4.20) with $\mathbf{x}'' = \mathbf{x}' + \varsigma\mathbf{u}$ and $\hat{r} = |\mathbf{u}|$ to give

$$\mathcal{G}_3(\mathbf{x}' - \mathbf{x}'') = \mathcal{G}_3(-\varsigma\mathbf{u}) \approx -\frac{1}{4\pi\varsigma\hat{r}}$$

when $\varsigma \ll 1/\phi \ll 1$. Therefore the $\mathbf{x}''$ integral in I_4 is given by

$$\begin{aligned}\int_{\mathcal{D}_3} \mathcal{G}_3(\mathbf{x}' - \mathbf{x}'')C_H(x_1'')F^3_{\sqrt{2}\varsigma}(\mathbf{x}' - \mathbf{x}'')\,\mathrm{d}\mathbf{x}'' &\approx \int_{\mathcal{D}_3} \mathcal{G}_3(-\varsigma\mathbf{u})(C_H(x_1') + \dots)F^3_{\sqrt{2}\varsigma}(-\varsigma\mathbf{u})\,\mathrm{d}\mathbf{x}'' \\ &\approx -\frac{1}{(4\pi)^{3/2}\varsigma}C_H(x_1'')\int_0^\infty \hat{r}\exp\left(-\frac{\hat{r}^2}{4}\right)\,\mathrm{d}\hat{r}.\end{aligned}$$

As before we obtain a constant from integration, which can be obtained using Appendix B.4 to give

$$I_4(\mathbf{x}) \approx -\frac{1}{4\pi^{3/2}\varsigma}\int_{\mathcal{D}_3} \mathcal{G}_3(\mathbf{x} - \mathbf{x}')C_H(x_1')\,\mathrm{d}\mathbf{x}'.$$

By yet again exploiting (3.4.7) we can reduce the three-dimensional integral into one dimension to give the expectation of $\widehat{C}_2(\mathbf{x};\omega)$ as

$$\begin{aligned}\mathbb{E}\left[\widehat{C}_2(\mathbf{x};\omega)\right] \approx &-\frac{\lambda^3}{4\pi^{3/2}\varsigma}\int_{\mathcal{D}_1} \mathcal{G}_1(x_1 - x_1')C_H(x_1')\,\mathrm{d}x_1' \\ &-\frac{\lambda}{(2M+1)^2}\int_{\mathcal{D}_1}\int_{\mathcal{D}_1} \mathcal{G}_1(x_1 - x_1')\mathcal{G}_1(x_1' - x_1'')C_H(x_1'')\,\mathrm{d}x_1'\,\mathrm{d}x_1''.\end{aligned} \tag{3.5.33}$$

Therefore we can write the expectation of $\widehat{C}_2(\mathbf{x};\omega)$ as $\varsigma \to 0$ in n dimensions in the compact form

$$\begin{aligned}\mathbb{E}\left[\widehat{C}_2(\mathbf{x};\omega)\right] \approx &-\lambda^n\beta_n\int_{\mathcal{D}_1} \mathcal{G}_1(x_1 - x_1')C_H(x_1')\,\mathrm{d}x_1' \\ &-\frac{\lambda}{(2M+1)^{n-1}}\int_{\mathcal{D}_1}\int_{\mathcal{D}_1} \mathcal{G}_1(x_1 - x_1')\mathcal{G}_1(x_1' - x_1'')C_H(x_1'')\,\mathrm{d}x_1'\,\mathrm{d}x_1'',\end{aligned} \tag{3.5.34}$$

where

$$\beta_1 = \frac{1}{2\phi}, \quad \beta_2 = \frac{1}{4\pi}\left(\gamma - 2\log(2\phi\varsigma)\right) \quad \text{and} \quad \beta_3 = \frac{1}{4\pi^{3/2}\varsigma}. \tag{3.5.35}$$

We see here that the correction in one dimension becomes independent of the lengthscale ς as $\varsigma \to 0$ for uniformly-random sink locations. However, in two and three dimensions the correction instead contains a singularity as the sink width (ς) becomes asymptotically small, which scales with $\log\varsigma$ and $1/\varsigma$ respectively. These results are due to the free-space Green's function in one, two and three dimensions at $\mathbf{x} = \mathbf{x}'$ having no singularity, a singularity of order $\log|\mathbf{x} - \mathbf{x}'|$ and a singularity of order $1/|\mathbf{x} - \mathbf{x}'|$ respectively.

To calculate the approximate size of the corrections for $M \gg \lambda$ (i.e. L_s is asymptotically large) we see that the expectation of $\widehat{C}_2(\mathbf{x};\omega)$ to leading-order is given by the first term of (3.5.34) in

two and three dimensions. So using (B.5.4), which gives the order of each integral in the limit $\mathrm{Pe}_L \gg \max(1, \sqrt{\mathrm{Da}})$, we see the expectation of $\widehat{C}_2(\mathbf{x};\omega)$ in the vicinity of $\mathbf{x} = \mathbf{e}_{\mathbf{i}_n}$ in one, two and three dimensions has an order depending on Pe_L, λ and ς given by

$$\mathcal{O}\left(\frac{\lambda}{\mathrm{Pe}_L^2}\right), \quad \mathcal{O}\left(\frac{\lambda^2}{\mathrm{Pe}_L}\log(\mathrm{Pe}_L\,\varsigma)\right) \quad \text{and} \quad \mathcal{O}\left(\frac{\lambda^3}{\mathrm{Pe}_L\,\varsigma}\right) \tag{3.5.36}$$

respectively.

Figure 3.12 uses (3.5.34) with the integrals given in Appendix B.5 to compare the approximate expectation of $\widehat{C}_2(\mathbf{x};\omega)$ to the sample mean in one and two dimensions and the homogenized solution. Figure 3.12(a) shows the expected concentration when sinks take uniformly-random locations in one, two and three dimensions. Although individual concentration profiles exhibit local structures about sink locations, these structures are not present in sample expectations due to a smearing effect when averaging over many realisations with strong disorder. This is reflected in the expectation of the leading-order correction $\widehat{C}_1(x,\omega)$, which is zero in one, two and three dimensions.

The expectation of the second-order correction $\widehat{C}_2(x,\omega)$ is non-zero, smooth and given by (3.5.34). Note that the correction in two (three) dimensions is independent of x_2 (x_2 and x_3). This correction accounts for the homogenized solution over-predicting uptake, as found for normally-perturbed sink locations. For uniformly-random sink locations the correction is seen to scale in n dimensions by the factors β_n from (3.5.35) as $\varsigma \to 0$. In two dimensions this scaling goes like $\log(\varsigma)$, whereas in three dimensions the correction is scaled according to $1/\varsigma$. Summing the expectation of $\widehat{C}_2(x,\omega)$ from (3.5.34) with the homogenized solution is seen to closely predict the sample expectations in one and two dimensions, as is seen by the errors in Figure 3.12(b). Here, sample moments of the concentration couldn't be calculated for three dimensions due to the computational expense, but the expectation of $\widehat{C}_2(x,\omega)$ can be calculated by simply solving the one- and two-dimensional integrals in (3.5.34). In two and three dimensions when taking the limit $M \gg \lambda$ (i.e. L_s is asymptotically large) the expectation of $\widehat{C}_2(\mathbf{x};\omega)$ can be simplified as the second integral becomes asymptotically small. Therefore the computational expense of calculating the correction is further reduced to solving one simple one-dimensional integral.

Let us now consider approximating the (co-)variance of $\widehat{C}_1$ for $L_s \gg \lambda$ in the limit $\varsigma \to 0$. Because the sink function F_ς^n transforms into an n-dimensional δ-function as $\varsigma \to 0$, (3.3.20)

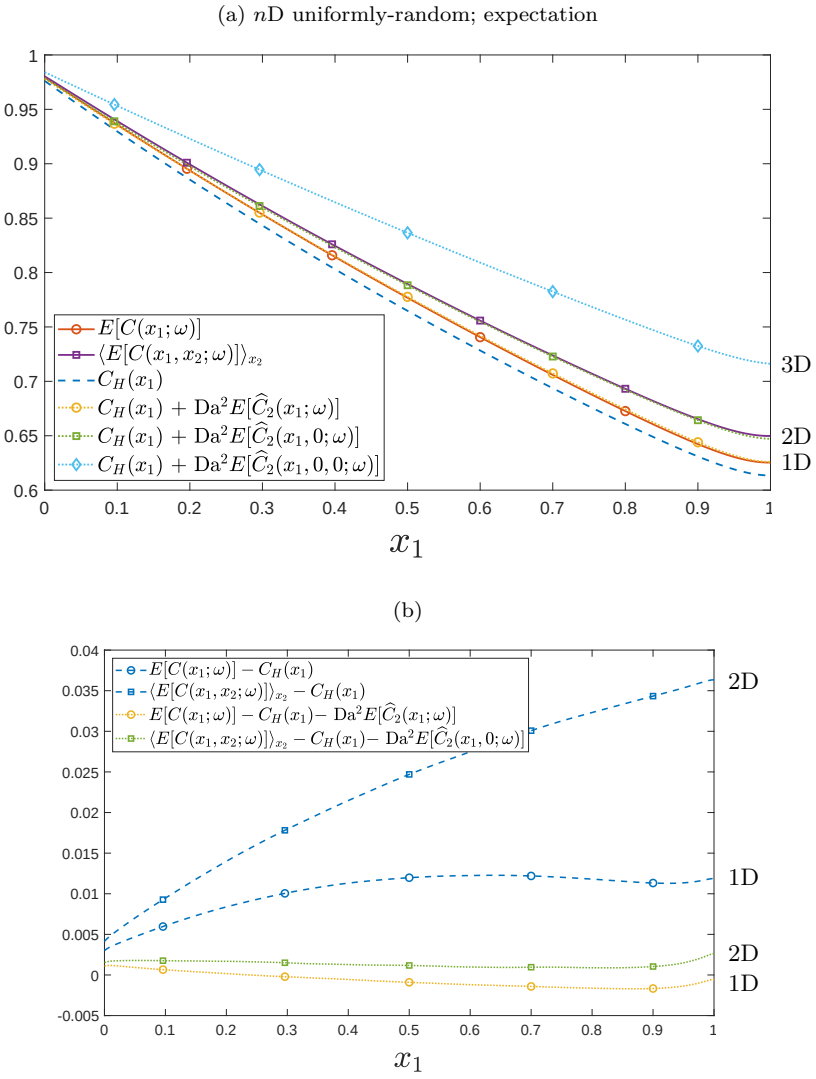

Figure 3.12: Expected concentrations for uniformly-random sink locations, where circles, squares and diamonds represent one-, two- and three-dimensional domains respectively. Figure (a) uses dashed and dot-dashed lines to represent the homogenized solution $[C_H(x_1)]$ and the approximation found using the expected correction $\mathbb{E}[\widehat{C}_2(\boldsymbol{x};\omega)]$. The solid lines represent the sample expectation, where in one dimension we use 10^6 realisations $[\mathbb{E}[\widehat{C}_2(x_1;\omega)]]$ and in two dimensions we use 10^4 realisations with $\mathcal{D}_2^s = [0,1]\times[-2.5,2.5]$ and then take the average over $x_2 = -2, -1.996, \ldots, 2$ $[\langle\mathbb{E}[\widehat{C}_2(x_1,x_2;\omega)]\rangle_{x_2}]$. Figure (b) shows the difference between sample expectations and each correction. Throughout we use $\lambda = 0.2$, $\varsigma = 0.01$ and $(\mathrm{Pe}_L, \mathrm{Da}) = (20,10)$, with the expectation of $\widehat{C}_2(x_1,x_2;\omega)$ being approximated using (3.5.34).

gives

$$\mathcal{K}_{\hat{g}}[\mathbf{x},\mathbf{y}] \to \lambda^n \delta(\mathbf{x}-\mathbf{y}) - \frac{\lambda}{(2M+1)^{n-1}} \tag{3.5.37}$$

as $\varsigma \to 0$. By also noting that the second integral in (3.5.26) can be reduced to one dimension using a change of variables with (3.4.7) we find the variance of the leading-order correction in

the limit $\varsigma \to 0$ can be approximated by

$$\begin{aligned}\mathrm{Var}_{\varsigma\to 0}[\widehat{C}_1(\mathbf{x},\omega)] = \lambda^n \int_{\mathcal{D}_n} (\mathcal{G}_n(\mathbf{x}-\mathbf{x}')C_H(x_1'))^2 \,\mathrm{d}\mathbf{x}' \\ - \frac{\lambda}{(2M+1)^{n-1}} \left(\int_{\mathcal{D}_1} \mathcal{G}_1(x_1 - x_1')C_H(x_1') \,\mathrm{d}x_1' \right)^2 .\end{aligned} \tag{3.5.38}$$

As for normally-perturbed sink locations, we see an advantage to taking the limit $\varsigma \to 0$ is to reduce the order of the integral down, with a $2n$-dimensional integral being reduced to an n-dimensional integral.

Figure 3.10(b) shows the variance of the concentration in one dimension. A sample variance is obtained using 10^6 Monte Carlo realisations with the variance of the leading-order correction $\widehat{C}_1(x,\omega)$ being calculated by solving (3.5.26) with the integral solver outlined in Appendix B.3. Although the expectation of the correction offers a close approximation to sample variance with the correct magnitude, the next order correction is thought to account for any differences seen. Also shown is the variance of the correction in the limit $\varsigma \to 0$, as given in (3.5.38), which appears to be a good description of the variance and is advantageous due to being cheaper to solve computationally.

Figure 3.11(b)(iii) compares the sample variance from 10^4 Monte Carlo realisations (Figure 3.11(b)(i)) with the variance of the correction $\widehat{C}_1(x,\omega)$ in the limit $\varsigma \to 0$ from (3.5.38) (Figure 3.11(b)(ii)) in two dimensions. Here, the cloud plot shows the sample variance for $x_2 = -2, -1.996, \ldots, 2$ from Figure 3.2(c) along with an average from the sample variances. Averaging over the variances is done to reduce the sampling error, where the variance is expected to be independent of x_2 from Figure 3.2(c). The variance of the correction in the limit $\varsigma \to 0$ is seen to be an over-prediction of the sample variance, as seen in one dimension in Figure 3.10(b). As for normally-perturbed sink locations, this demonstrates the impact of smearing out sink locations, which is seen to reduce the magnitude of variation in the concentration.

3.6 Discussion

A moments-based approach to homogenization is presented in this chapter for a one-, two- and three-dimensional advection-diffusion-uptake equation, with uptake being prescribed via first-order kinetics and governed by a discrete sink function $\hat{g}(\mathbf{x},\omega)$. Solute concentration is characterised by a deterministic homogenized solution with sequential corrections which account for sink locations. A direct mapping between the first two moments of the sink function and the first two moments of corrections is derived in (3.2.9)-(3.2.11) using an appropriate Green's

function.

The sink function $\hat{g}(\mathbf{x}, \omega)$ contains an ensemble of discrete sink locations with finite width ς, with sinks being confined to an n-dimensional domain $\mathcal{D}_n^s$ which represents a cuboid, rectangle or line in three, two or one dimensions respectively. An average inter-sink distance in all directions is prescribed to be λ, with $F_\varsigma^n(\mathbf{x} - \boldsymbol{\xi}_{\mathbf{i}_n})$ being a Gaussian-shaped uptake function with width $\varsigma \ll 1$ such that the sink function is ensured to have a spatial averaged sink density of zero within the domain $\mathcal{D}_n^s$. The impact of ordered and disordered sink locations is then considered using three different examples; periodic, normally-perturbed from a periodic configuration and uniformly-random sink locations. Throughout, results from the moments-based approach are verified by comparing to sample moments of the concentration, which are obtained using (3.1.2) with the finite-difference solver given in Appendix B.2 to produce multiple realisations of the solute concentration.

In Section 3.3 the first two moments of the sink function are calculated for disordered sink locations. When sinks are normally-perturbed the covariance is non-local, where it is zero, positive and negative when away, on and near to the diagonal, which represents sinks being independently distributed, correlated and anti-correlated respectively. When sink locations are prescribed by a uniform distribution in one dimension the covariance is everywhere non-local. However, in two and three dimensions as the sink domain size increases the non-local contribution to the covariance becomes negligible, making the covariance local to leading order.

An approximation of the n-dimensional Green's function, which demonstrates the impact of one individual sink location on the solute concentration, is calculated in Section 3.4. This approximation is a free-space Green's function, which captures singularities at sink locations but neglects any impact due to boundary conditions. When a distance greater than $1/\mathrm{Pe}_L$ from either x_1-boundary and in the limit $\mathrm{Pe}_L \gg \max(1, \sqrt{\mathrm{Da}})$, the free-space Green's function is a good approximation of the exact Green's function. In one, two and three dimensions at the sink location there is no singularity, a singularity of logarithmic order and a singularity of reciprocal order respectively. Calculating the asymptotic shape of the wake and lengthscales of the free-space Green's function produces a region of influence in one, two and three dimensions. Any sink located within this region can influence the concentration at some given point $\mathbf{x} = \mathbf{y}$, see Figure 3.6(b) for the two-dimensional case. In two and three dimensions the region is elliptical and ellipsoidal in shape respectively, with advection smearing the impact of a sink on the solute concentration downstream of the sink location.

In Sections 3.5.1, 3.5.2 and 3.5.3 we find the impact of periodic, normally-perturbed and uniformly-random sink locations on the solute concentration respectively. For periodic sinks, as the sink function $\hat{g}$ is non-zero the resulting leading-order correction $\widehat{C}_1$ is also non-zero, which is calculated in one and two dimensions using the integral solver in Appendix B.3 with (3.5.1). The correction accounted for changes in the solute concentration centred about sink locations, as seen in Figure 3.7(a) for one dimension and Figure 3.9(a) for two dimensions. The one-dimensional second-order correction is also found, which is calculated using Appendix B.3 with (3.5.2) and further improves the approximation by accounting for the homogenized solution over-predicting solute uptake.

To calculate approximations of periodic corrections we consider taking the limit of an asymptotically small sink width ς. As $\varsigma \to 0$ the leading-order correction is approximated by replacing sink functions in (3.5.1) with δ-function approximations. Although this is appropriate in one dimension (see Figure 3.7(a)), due to singularities in the Green's function it is not appropriate in two (see Figure 3.9(a)(v)) and three dimensions when near sink locations, as found in Mahiout et al. (2020). A more careful approach for approximating (3.5.1) in two and three dimensions is taken by approximating integrals within the neighbourhood of sink locations, which prevents evaluating the Green's function at a singularity. The magnitude of this leading-order periodic correction near sink locations is calculated for one, two and three dimensions, which can be seen in Table 3.1. We find the correction in two and three dimensions to scale with the logarithm and reciprocal of the sink width respectively, with these being the order of singularities for point sink locations.

	Periodic	Normally-perturbed	Uniformly-random
1D	$\dfrac{\mathrm{Da}}{\mathrm{Pe}_L}\max\left(\lambda, \mathrm{Pe}_L^{-1}\right)$	$\dfrac{\mathrm{Da}}{\mathrm{Pe}_L}\max\left(\lambda, \mathrm{Pe}_L^{-1}\right)$	$\dfrac{\mathrm{Da}^2\,\lambda}{\mathrm{Pe}_L^2}$
2D	$\mathrm{Da}\,\lambda^2\log(\mathrm{Pe}_L\,\varsigma)$	$\mathrm{Da}\,\lambda^2\log\left(\mathrm{Pe}_L\sqrt{\varsigma^2+\sigma^2}\right)$	$\dfrac{\mathrm{Da}^2\,\lambda^2}{\mathrm{Pe}_L}\log(\mathrm{Pe}_L\,\varsigma)$
3D	$\mathrm{Da}\,\lambda^3\left(\dfrac{1}{\varsigma}\right)$	$\mathrm{Da}\,\lambda^3\left(\dfrac{1}{\sqrt{\varsigma^2+\sigma^2}}\right)$	$\dfrac{\mathrm{Da}^2\,\lambda^3}{\mathrm{Pe}_L}\left(\dfrac{1}{\varsigma}\right)$

Table 3.1: Table showing how the (expected) correction to the homogenized solution in the vicinity of $\mathbf{x} = \mathbf{e}_{\mathbf{i}_n}$ depends on $\lambda, \varsigma, \sigma, \mathrm{Pe}_L$ and Da for $\mathrm{Pe}_L \gg \max(1, \sqrt{\mathrm{Da}})$ in the limit $\varsigma \to 0$. These are given for periodic, normally-perturbed and uniformly-random sink locations in (3.5.13), (3.5.24) and (3.5.36) respectively.

In Section 3.5.2 we find that, as the expectation of the sink function is non-zero for normally-perturbed sink locations, the expectation of the leading-order correction $\widehat{C}_1$ is non-zero. This correction is calculated in one and two dimensions using Appendix B.3 with (3.5.14), where it again accounts for changes in the concentration centred about sink locations, see Figure 3.7 and Figure 3.9 respectively. The one-dimensional expected second-order correction is calculated using (3.5.16), which, as for periodic sink locations, accounts for an over-prediction in uptake by the homogenized solution.

When taking the limit of an asymptotically small sink width the disorder in sink locations is seen to smooth out singularities in individual concentration profiles which are present in two and three dimensions. As a result the expected leading-order correction remained non-singular, see (3.5.21). Near sink locations in the limit where both the sink width (ς) and standard deviation of sink locations (σ) are asymptotically small, the leading-order correction scales with the logarithm and reciprocal of $\sqrt{\varsigma^2 + \sigma^2}$ in two and three dimensions respectively, see Table 3.1. Therefore both disorder and sink regularisation can prevent singularities occurring in solute concentration profiles.

In Section 3.5.2 we also use the variance of the leading-order correction to estimate the variance of solute concentration. In one dimension Figure 3.10(a) shows good agreement between the sample variance and the variance of the leading-order correction, where an increase in variation is seen near sink locations causing a wavy sink-to-sink structure. Despite an overestimation near sink locations, close approximations of this variance can be obtained by replacing regularised sink functions with δ-functions in the limit $\varsigma \to 0$, as seen in Figure 3.10(a). Figure 3.11(a) compares the sample variance with the δ-function approximation of the leading-order correction's variance in two dimensions. The approximation fails to capture the correct crescent-shaped structure of the variance, as well as over-predicting the magnitude. This demonstrates that regularising sink locations reduces the amount of variation in the concentration. Although the variance of the second-order correction is not calculated using (3.5.15) due to the computational expense, we would expect it to better capture the shape and magnitude of the numerical variance than the approximation.

The expectation of the sink function for uniformly-random sink locations is zero, meaning in Section 3.5.3 we find the expectation of the leading-order correction to be zero. So although individual concentration profiles can exhibit local structures about sink locations, these structures are not present when taking expectations due to a smearing effect when averaging over

many realisations. The expectation of the second-order correction becomes independent of the x_2- and x_3-directions in two and three dimensions when suitably far from boundaries. A dependency of the second-order correction on the n-dimensional β_n scaling is then calculated, where each β_n is given in (3.5.35) to be

$$\beta_1 = \frac{1}{2\phi}, \quad \beta_2 = \frac{1}{4\pi}\left(\gamma - 2\log(2\phi\varsigma)\right) \quad \text{and} \quad \beta_3 = \frac{1}{4\pi^{3/2}\varsigma}$$

as $\varsigma \to 0$. So for a small sink width in higher dimensions, a correction to the homogenized solution is required, which scales with $\log(\varsigma)$ and $1/\varsigma$ in two and three dimensions respectively. By using these scalings with (3.5.34) in one and two dimensions, Figure 3.12 shows good agreement between the sample expectations and using the second-order correction to the homogenized solution. Here, although the sample moments of the concentration couldn't be calculated for three dimensions due to being computationally expensive, the expectation of the second-order correction can be calculated relatively cheaply by solving the integrals in (3.5.34). Table 3.1 summarises the magnitude of the second-order correction in one, two and three dimensions.

The variance of the leading-order correction when sink locations are uniformly-random in one dimension is shown in Figure 3.10(b). Here, good agreement is seen between the sample variance and that of the correction, with a slight discrepancy in the magnitude which is thought to be accounted for by the next order correction. Also shown in Figure 3.10(b) is the variance of the correction in the limit $\varsigma \to 0$, as given in (3.5.38). This is seen to offer a close prediction of the variance and is advantageous due to being cheaper to solve computationally. The two-dimensional variance is then considered in Figure 3.11(b), where the variance of the correction in the limit $\varsigma \to 0$ again offers a close prediction of the variance. However, it is shown to over-predict the variance which again demonstrates how smearing out sink locations reduces the magnitude of variation in the concentration.

This chapter modifies a simple transport problem by introducing a disordered sink function to the uptake term in one, two and three dimensions. The sink function represents an ensemble of discrete sink locations with a finite sink width. Large corrections to the homogenized solution are found for asymptotically small sink widths, with the magnitude of corrections increasing with the dimension size due to singularities in the free-space Green's function. Although this alternate approach to homogenization quantifies errors due to disordered sink locations, other challenges exist when considering its practical applications. For example, it could be beneficial to quantify the impact of disordered sink strengths (as is considered in Russell et al. (2016) for one-dimension), the impact of a non-linear relation between solute uptake and concentration (as considered in Dalwadi and King (2020) using the classical approach to homogenization with

a relaxed periodicity assumption) or the impact of an unsteady or stochastic flow field (which can be of importance for solute transport through disordered media (Jin et al., 2016; Alim et al., 2017)). One could also modify corrections to account for boundary conditions in the Green's function (Morse and Ingard, 1986). In Chapter 4 we consider applying this moments-based approach for a continuous sink function represented by a Gaussian process in one, two and three dimensions. Throughout, we find the moments-based approach allows the impact of a disordered uptake field on the solute concentration to be quantified when transport occurs over multiple lengthscales.

Chapter 4

Solute transport past sink distributions represented by Gaussian processes

Chapter 3 used a 'moments-based' approach, which offered a connection between the statistical moments of a sink function and the statistical moments of the solute field. We considered a discrete sink function with finite sink widths and two examples of disordered sink locations: normally-perturbed from a periodic array and uniformly-random. For both examples we calculated corrections to a homogenized solution, which were expressed as integrals due to the non-local impact of the disordered uptake function on the solute concentration. This chapter will consider a continuous sink distribution represented by a Gaussian process. The impact of disorder on the solute concentration will be characterised using the moments-based approach from Chapter 3. We also consider the limit when a local approximation is feasible, allowing definitions of an effective uptake parameter $\mathrm{Da}_{\mathrm{eff}}$, which replaces the Damköhler number in the homogenized solution. This is illustrated for both Gaussian processes with asymptotically small correlation lengths and discrete sink functions with uniformly-random sink locations in the limit of asymptotically small sink widths, with the effective uptake parameter offering accurate predictions of the impact of a disordered sink function on the solute concentration.

In Section 4.1 we outline the three-dimensional solute transport model which will be used, where

advection is assumed to be unidirectional and uptake occurs via a continuous sink function represented by a Gaussian process with a correlation length ℓ. Throughout the chapter we consider both a Gaussian and exponential sink covariance function, as defined (for example) in Lord et al. (2014). For both an asymptotically small and large correlation length, we show that the sink covariance functions can be approximated using a δ-function or constant approximation respectively. This allows simplifications when calculating moments and effective parameters of the solute concentration within these limits.

Section 4.2 outlines the two approaches used to characterise uncertainty in the solute concentration. A recap of the moments-based approach used in Chapter 3 is first given. Here, we find expected corrections are simplified for asymptotically large correlation lengths, with the covariance of corrections being simplified for both asymptotically small and large correlation lengths. Following this, we develop an alternative approach which finds local corrections to the mean concentration field using an effective uptake parameter. This is found to be appropriate for Gaussian processes with asymptotically small correlation lengths due to the correction to the mean concentration being local.

One-dimensional results are given in Section 4.3, in which we calculate the first two moments of corrections and an effective uptake parameter for a variety of correlation lengths. Good agreement between each approach and sample moments are shown, where sample moments are calculated using 10^7 Monte Carlo realisations. Following this we calculate expressions for the two- and three-dimensional effective uptake parameters in Section 4.4, with the effective uptake in n dimensions being summarised in Section 4.5. We finish by drawing relations between the sink function's covariance for discrete, uniformly-random sink locations and using a continuous Gaussian process with a Gaussian covariance function in Section 4.6. Here, both in two and three dimensions we find good agreement between using effective uptake parameters and calculating the expectation of corrections for sufficiently many uniformly-random sinks. Results are illustrated for two practical applications: solute transport within maternal blood through the intervillous space of the placenta and oxygen uptake by mitochondria within placental tissue.

4.1 Model

As in Chapter 3, solute transport will be described by a three-dimensional advection-diffusion-reaction equation. This is done using the system of equations given in (3.1.2), namely

$$\nabla_3^2 C - \mathrm{Pe}_L\, C_{x_1} - \mathrm{Da}\, C(1 + \hat{g}(\mathbf{x};\omega)) = 0, \tag{4.1.1a}$$

with boundary conditions

$$(1 - \mathrm{Pe}_L^{-1}\,\partial_{x_1})C|_{x_1=0} = 1, \quad C_{x_1}|_{x_1=1} = 0, \quad C_{x_2}|_{x_2\to\pm\infty} \to 0 \quad \text{and} \quad C_{x_3}|_{x_3\to\pm\infty} \to 0, \tag{4.1.1b}$$

where $\nabla_3^2 = \partial_{x_1^2} + \partial_{x_2^2} + \partial_{x_3^2}$ and $\mathbf{x} = (x_1, x_2, x_3) \in \mathcal{D}_3$ is such that $x_1 \in [0, 1]$ and $x_2, x_3 \in \mathbb{R}$. Here, non-dimensionalization occurred over the domain length and there is a prescribed flux on the $x_1 = 0$ boundary, zero diffusive flux on the $x_1 = 1$ boundary and the diffusive flux approaches zero as $x_2, x_3 \to \pm\infty$. As before, $\hat{g}(\mathbf{x};\omega)$ represents a sink function and the non-dimensional parameters Pe_L and Da represent the Péclet (ratio of advection to diffusion) and Damköhler (ratio of uptake to diffusion) numbers respectively. Note that the ω notation has been kept to denote $\hat{g}(\mathbf{x};\omega)$ being a realisation drawn from a prescribed distribution, which in turn makes the solute concentration field $C(\mathbf{x};\omega)$ a random variable.

The situation when the uptake function $\hat{g}(\mathbf{x};\omega)$ from Chapter 3 represents a Gaussian process with zero mean and covariance $\mathcal{K}_{\hat{g}}(\mathbf{x}, \mathbf{x}';\sigma,\ell)$ will be considered. Here, σ and ℓ represent a variance and non-dimensional correlation length respectively, where ℓ is non-dimensionalized using the domain length. The continuous sink function $\hat{g}(\mathbf{x};\omega)$ will occupy a domain $\mathcal{D}_3^s$, where for all $\mathbf{x} \in \mathcal{D}_3^s$ then $x_1 \in [0, 1]$ and $x_2, x_3 \in [-L_s, L_s]$. Both a Gaussian and exponential covariance function will be considered, as defined (for example) in Lord et al. (2014) to be

$$\mathcal{K}_{\hat{g}}^G(\mathbf{x}, \mathbf{y};\sigma,\ell) = \sigma^2 \exp\left(-\frac{|\mathbf{x}-\mathbf{y}|^2}{\ell^2}\right) \tag{4.1.2}$$

and

$$\mathcal{K}_{\hat{g}}^E(\mathbf{x}, \mathbf{y};\sigma,\ell) = \sigma^2 \exp\left(-\frac{|\mathbf{x}-\mathbf{y}|}{\ell}\right) \tag{4.1.3}$$

respectively. As done previously, analogous definitions will be used to extend results to one and two dimensions. Figure 4.1 illustrates using a Gaussian and exponential covariance function to produce two-dimensional realisations of the sink function $\hat{g}(\mathbf{x};\omega)$. Here, functions are evaluated using the eigenvalue decomposition described in Appendix B.6 and we use $\sigma = 0.2$ and $\ell = [0.01, 0.1, 1]$. We consider examples throughout using $\sigma = 0.2$, which is chosen to allow notable fluctuations in the sink function whilst keeping the probability of solute being added to the domain as negligible.

It is here beneficial to consider the behaviour of an n-dimensional covariance function for two limiting cases: an asymptotically small ($\ell \to 0$) and asymptotically large ($\ell \to \infty$) correlation length. In order to evaluate the covariance function for an asymptotically small correlation length we first note that the δ-function $\delta(\mathbf{x} - \mathbf{y})$ in n dimensions can be represented in the

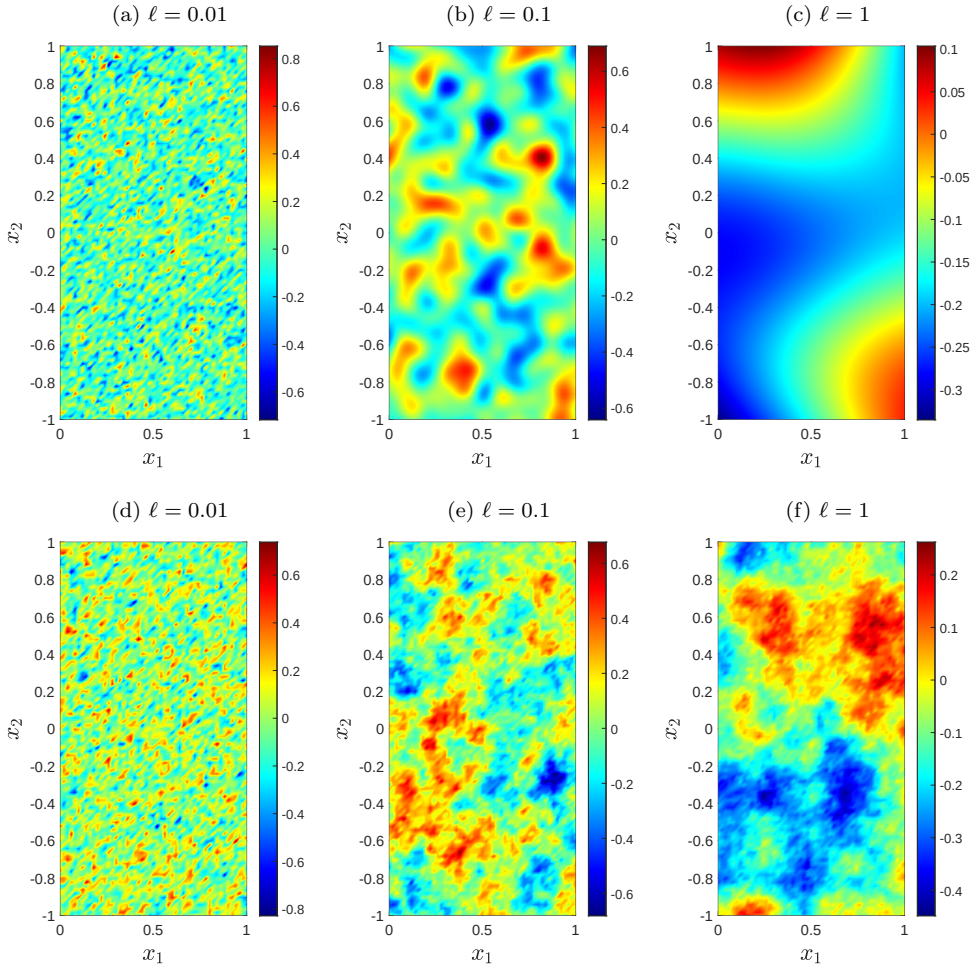

Figure 4.1: Two-dimensional realisations of the sink function $\hat{g}(\mathbf{x};\omega)$ using a Gaussian [(a), (b), (c)] and exponential [(d), (e), (f)] covariance function from (4.1.2) and (4.1.3) respectively. Here, (a) & (d), (b) & (e) and (c) & (f) use $\ell = 0.01$, $\ell = 0.1$ and $\ell = 1$ respectively, with all realisations using $\sigma = 0.2$ and eigenvalue decomposition from Appendix B.6.

distribution sense using

$$\left(\pi t^2\right)^{-n/2} \exp\left(\frac{-|\mathbf{x}-\mathbf{y}|^2}{t^2}\right) \quad \text{or} \quad \left(\pi t^2\right)^{-n/2} \exp\left(\frac{-|\mathbf{x}-\mathbf{y}|}{t}\right) \quad \text{as } t \to 0. \tag{4.1.4}$$

So the covariance function in n dimensions is given by

$$\mathcal{K}_{\hat{g}}(\mathbf{x},\mathbf{y}) \to \sigma^2 \left(\pi\ell^2\right)^{n/2} \delta(\mathbf{x}-\mathbf{y}) \quad \text{as } \ell \to 0 \tag{4.1.5}$$

in the sense of a distribution for both a Gaussian and exponential covariance function. Alternatively, when the correlation length is asymptotically large we see from both (4.1.2) and (4.1.3) that the covariance function becomes constant, giving

$$\mathcal{K}_{\hat{g}}(\mathbf{x},\mathbf{y}) \to \sigma^2 \quad \text{as } \ell \to \infty \tag{4.1.6}$$

for both a Gaussian and exponential covariance function. Both (4.1.5) and (4.1.6) will prove useful in later sections of this chapter.

We will now outline three methods for characterising uncertainty in the uptake term. First, we calculate sample moments of the concentration using eigenvalue decomposition to produce realisations of the sink function. Following this, we revisit the moments-based approach developed in Chapter 3 and calculate an effective uptake term for the concentration in the limit of an asymptotically small correlation length.

4.2 Methods

Sample moments of the solute concentration can be calculated by producing realisations of the sink function using an eigenvalue decomposition, as described in Appendix B.6. This is followed by solving (4.1.1) with the finite-difference solver given in Appendix B.2, which in turn produces multiple realisations of the concentration field. However, this process is computationally expensive and so sample moments of the concentration are only found in one dimension, where 10^7 realisations take approximately 12 hours. As a result we outline two different methods which quantify the effect of disorder on the solute concentration. The first method is using the moments-based approach from Chapter 3 to quantify disorder in terms of the moments of corrections to a homogenized solution. The second considers finding an effective uptake parameter to replace the sink function in (4.1.1), which offers an improvement when compared to using a homogenized solution.

For both approaches we first define $\mathcal{L}_3$ and $\mathcal{B}_3$ to be three-dimensional linear and boundary operator respectively such that

$$\mathcal{L}_3 = \nabla^2_{3D} - \mathrm{Pe}_L\,\partial_{x_1} - \mathrm{Da} \quad \text{and}$$
$$\mathcal{B}_3 = \{(1-(1/\mathrm{Pe}_L)\partial_{x_1})(\cdot)|_{x_1=0},\, \partial_{x_1}(\cdot)|_{x_1=1},\, \partial_{x_2}(\cdot)|_{x_2\to-\infty}, \partial_{x_2}(\cdot)|_{x_2\to\infty},$$
$$\partial_{x_3}(\cdot)|_{x_3\to-\infty},\, \partial_{x_3}(\cdot)|_{x_3\to\infty}\}$$

We can then calculate a homogenized solution ($C_H(\mathbf{x})$) associated with (4.1.1) by solving

$$\mathcal{L}_3 C_H(\mathbf{x}) = 0, \quad \mathcal{B}_3 C_H(\mathbf{x}) = \{1,0,0,0,0,0\}, \tag{4.2.1}$$

which is seen to be the same as in (3.2.2) and given by

$$C_H(\mathbf{x}) = C_H(x_1) = \frac{\mathrm{Pe}_L}{\psi(1)}\Big((2\phi-\mathrm{Pe}_L)e^{\phi(x_1-1)} + (2\phi+\mathrm{Pe}_L)e^{\phi(1-x_1)}\Big)e^{(\mathrm{Pe}_L/2)x_1}, \tag{4.2.2}$$

where $\phi = \sqrt{\mathrm{Pe}_L^2/4 + \mathrm{Da}}$ and $\psi(x_1) = (2\,\mathrm{Pe}_L\,\phi + \mathrm{Pe}_L^2 + 2\,\mathrm{Da})e^{\phi x_1} + (2\,\mathrm{Pe}_L\,\phi - \mathrm{Pe}_L^2 - 2\,\mathrm{Da})e^{-\phi x_1}$. The associated free-space Green's function $\mathcal{G}_3(\mathbf{x}-\mathbf{x}')$ to (4.1.1) can also be calculated by solving

$$\mathcal{L}_3\mathcal{G}_3(\mathbf{x}-\mathbf{x}') = \delta(\mathbf{x}-\mathbf{x}'), \tag{4.2.3}$$

where no influence from boundary conditions is considered. This is solved in n dimensions in Chapter 3, where (3.4.6) gives

$$\mathcal{G}_n(\mathbf{x}-\mathbf{x}') = -(2\pi)^{-n/2}\left(\frac{\phi}{|\mathbf{x}-\mathbf{x}'|}\right)^{n/2-1} K_{n/2-1}(\phi|\mathbf{x}-\mathbf{x}'|)\exp\left(\frac{\mathrm{Pe}_L}{2}(x_1-x_1')\right), \tag{4.2.4}$$

with a singularity existing at $\mathbf{x} = \mathbf{x}'$ of order $\log(\phi|\mathbf{x}-\mathbf{x}'|)$ and $1/|\mathbf{x}-\mathbf{x}'|$ in two and three dimensions respectively. By using the free-space Green's function $\mathcal{G}_n$ we are assuming $\mathbf{x}$ and $\mathbf{x}'$ are sufficiently far from boundaries and the decay lengthscales of the free-space Green's function (which will be denoted $L_{\mathcal{G}_n}$ from now on) are sufficiently small.

In Section 3.4 we found the free-space Green's function to offer a close approximation of the exact Green's function in the limit $\mathrm{Pe}_L \gg \max(1, \sqrt{\mathrm{Da}})$ for one, two and three spatial dimensions. We also noted that integrating the two- and three-dimensional governing equation for the free-space Green's function gives the relation

$$\int_{-\infty}^{\infty}\int_{-\infty}^{\infty}\mathcal{G}_3(\mathbf{x})\,\mathrm{d}x_2\,\mathrm{d}x_3 = \int_{-\infty}^{\infty}\mathcal{G}_2(\mathbf{x})\,\mathrm{d}x_2 = \mathcal{G}_1(x_1), \tag{4.2.5}$$

a property which will later be used. We will now consider two different approaches for quantifying the impact of disorder in the sink function on the solute concentration.

4.2.1 The moments-based approach

As in Chapter 3, we consider using a correction $\widehat{C}(\mathbf{x};\omega)$ to the homogenized solution which accounts for the disordered sink function, i.e.

$$C(\mathbf{x};\omega) = C_H(x_1) + \widehat{C}(\mathbf{x};\omega). \tag{4.2.6}$$

So by writing the correction as the expansion

$$\widehat{C}(\mathbf{x};\omega) = \mathrm{Da}\,\widehat{C}_1(\mathbf{x};\omega) + \mathrm{Da}^2\,\widehat{C}_2(\mathbf{x};\omega) + \ldots, \tag{4.2.7}$$

where we assume $\mathrm{Da}\,\widehat{C}_1(\mathbf{x};\omega) \ll \mathrm{Da}^2\,\widehat{C}_2(\mathbf{x};\omega) \ll \ldots$, then (4.1.1) can be used to construct a solution (to be validated *a posteriori*) using the ansatz

$$\mathcal{L}_3\widehat{C}_1(\mathbf{x};\omega) = \hat{g}(\mathbf{x};\omega)C_H(x_1), \quad \mathcal{B}_3\widehat{C}_1(\mathbf{x};\omega) = \{0,\ldots,0\}, \tag{4.2.8a}$$

$$\mathcal{L}_3\widehat{C}_2(\mathbf{x};\omega) = \hat{g}(\mathbf{x};\omega)\widehat{C}_1(\mathbf{x};\omega), \quad \mathcal{B}_3\widehat{C}_2(\mathbf{x};\omega) = \{0,\ldots,0\}, \tag{4.2.8b}$$

$$\vdots$$

By inverting the linear operators in (4.2.8) using the free-space Green's function given in (4.2.4) we obtain

$$\widehat{C}_1(\mathbf{x};\omega) = \int_{\mathcal{D}_3} \mathcal{G}_3(\mathbf{x}-\mathbf{x}')C_H(x_1')\hat{g}(\mathbf{x}';\omega)\,\mathrm{d}\mathbf{x}', \tag{4.2.9}$$

$$\widehat{C}_2(\mathbf{x};\omega) = \int_{\mathcal{D}_3}\int_{\mathcal{D}_3} \mathcal{G}_3(\mathbf{x}-\mathbf{x}')\mathcal{G}_3(\mathbf{x}'-\mathbf{x}'')C_H(x_1'')\hat{g}(\mathbf{x}';\omega)\hat{g}(\mathbf{x}'';\omega)\,\mathrm{d}\mathbf{x}'\,\mathrm{d}\mathbf{x}'', \tag{4.2.10}$$

$$\vdots$$

These corrections can then be characterised in terms of their moments, specifically

$$\mathbb{E}\left[\widehat{C}_1(\mathbf{x};\omega)\right] = \int_{\mathcal{D}_3} \mathcal{G}_3(\mathbf{x}-\mathbf{x}')C_H(x_1')\mathbb{E}[\hat{g}(\mathbf{x}';\omega)]\,\mathrm{d}\mathbf{x}', \tag{4.2.11}$$

$$\mathcal{K}_{\widehat{C}_1}[\mathbf{x},\mathbf{y}] = \int_{\mathcal{D}_3}\int_{\mathcal{D}_3} \mathcal{G}_3(\mathbf{x}-\mathbf{x}')C_H(x_1')\mathcal{K}_{\hat{g}}[\mathbf{x}',\mathbf{y}']\mathcal{G}_3(\mathbf{y}-\mathbf{y}')C_H(y_1')\,\mathrm{d}\mathbf{x}'\,\mathrm{d}\mathbf{y}' \tag{4.2.12}$$

and

$$\mathbb{E}\left[\widehat{C}_2(\mathbf{x};\omega)\right] = \int_{\mathcal{D}_3}\int_{\mathcal{D}_3} \mathcal{G}_3(\mathbf{x}-\mathbf{x}')\mathcal{G}_3(\mathbf{x}'-\mathbf{x}'')C_H(x_1'')\mathbb{E}\left[\hat{g}(\mathbf{x}';\omega)\hat{g}(\mathbf{x}'';\omega)\right]\,\mathrm{d}\mathbf{x}'\,\mathrm{d}\mathbf{x}'', \tag{4.2.13}$$

where $\mathcal{K}_f[\mathbf{x},\mathbf{y}] \equiv \mathcal{K}[f(\mathbf{x};\omega), f(\mathbf{y};\omega)]$ and $\mathcal{K}$ represents the covariance function. As the sink function $\hat{g}(\mathbf{x};\omega)$ has zero mean, the expectations can be simplified to

$$\mathbb{E}\left[\widehat{C}_1(\mathbf{x};\omega)\right] = 0 \tag{4.2.14}$$

and

$$\mathbb{E}\left[\widehat{C}_2(\mathbf{x};\omega)\right] = \int_{\mathcal{D}_3}\int_{\mathcal{D}_3} \mathcal{G}_3(\mathbf{x}-\mathbf{x}')\mathcal{G}_3(\mathbf{x}'-\mathbf{x}'')C_H(x_1'')\mathcal{K}_{\hat{g}}[\mathbf{x}',\mathbf{x}'']\,\mathrm{d}\mathbf{x}'\,\mathrm{d}\mathbf{x}'' \tag{4.2.15}$$

respectively. This gives a direct mapping between the first two moments of the sink function and the first two moments of the solute concentration.

In the limit of an asymptotically large correlation length we can simplify (4.2.15) due to the covariance of the sink function being uniform for a Gaussian and exponential covariance function, see (4.1.6). So using (4.2.15) with the relation given in (4.2.5) we obtain the expectation of the second-order correction in the limit $\ell \to \infty$ to be

$$\mathbb{E}^{\ell\to\infty}\left[\widehat{C}_2(\mathbf{x};\omega)\right] \to \sigma^2 \int_{\mathcal{D}_1}\int_{\mathcal{D}_1} \mathcal{G}_3(x_1-x_1')\mathcal{G}_3(x_1'-x_1'')C_H(x_1'')\,\mathrm{d}x_1'\,\mathrm{d}x_1''. \tag{4.2.16}$$

The double integral given in (4.2.16) is solved in Appendix B.4 and approximated for $\mathrm{Pe}_L \gg \max(1,\sqrt{\mathrm{Da}})$. which gives

$$\begin{aligned}\mathbb{E}^{\ell\to\infty}\left[\widehat{C}_2(\mathbf{x};\omega)\right] \to \frac{\sigma^2\,\mathrm{Pe}_L}{8\phi^4\hat{\psi}(1)} e^{\frac{\mathrm{Pe}_L}{2}x_1}\Bigg(&(2\phi+\mathrm{Pe}_L)\,(1+\phi x_1)^2 e^{\phi(1-x_1)} \\ &+\left(-\frac{5\,\mathrm{Pe}_L}{2}-\phi(1+\mathrm{Pe}_L+2\phi)\right)e^{\phi(x_1-1)}\Bigg)\end{aligned} \tag{4.2.17}$$

in the limit $\mathrm{Pe}_L \gg \max(1, \sqrt{\mathrm{Da}})$ and $\ell \to \infty$. Therefore the expected second-order correction for an asymptotically large correlation length in one, two and three dimensions is identical for Gaussian and exponential covariance functions. Similarly we can approximate the covariance using $\mathcal{K}_{\hat{g}}[\mathbf{x}, \mathbf{y}] \to \sigma^2$ with (4.2.12) to give

$$\mathcal{K}^{\ell\to\infty}_{\widehat{C}_1}[\mathbf{x}, \mathbf{y}] \to \sigma^2 \int_{\mathcal{D}_1} \mathcal{G}_3(x_1 - x_1') C_H(x_1')\, \mathrm{d}x_1' \int_{\mathcal{D}_1} \mathcal{G}_3(y_1 - y_1') C_H(y_1')\, \mathrm{d}y_1'. \tag{4.2.18}$$

So using the integrals in Appendix B.4 we obtain

$$\begin{aligned}\mathcal{K}^{\ell\to\infty}_{\widehat{C}_1}[\mathbf{x}, \mathbf{y}] \to \sigma^2 \frac{\mathrm{Pe}_L^2}{16\phi^4 \hat{\psi}(1)^2} e^{\frac{\mathrm{Pe}_L}{2}(x_1+y_1)} \Bigg(& 4\,\mathrm{Pe}_L^2\, e^{\phi(x_1+y_1-2)} \\ & - 2\,\mathrm{Pe}_L\,(2\phi + \mathrm{Pe}_L) \left((1+2\phi x_1)\, e^{\phi(y_1-x_1)} + (1+2\phi y_1)\, e^{\phi(x_1-y_1)} \right) \\ & + (2\phi + \mathrm{Pe}_L)^2\, (1+2\phi x_1)\,(1+2\phi y_1)\, e^{\phi(2-x_1-y_1)} \Bigg)\end{aligned} \tag{4.2.19}$$

where $\hat{\psi}$ is an approximation of ψ near $x_1 = 1$, which is given by $\hat{\psi}(x_1) = (2\,\mathrm{Pe}_L\,\phi + \mathrm{Pe}_L^2 + 2\,\mathrm{Da}) e^{\phi x_1}$. Therefore, as for the expectation of the second-order correction, the variance of the first-order correction for $\ell \to \infty$ in one, two and three dimensions is identical for Gaussian and exponential covariance functions.

For the limit of an asymptotically small correlation length we can approximate the covariance of $\widehat{C}_1(\mathbf{x}; \omega)$ by using the δ-function approximation of the covariance from (4.1.5) to give

$$\mathcal{K}^{\ell\to 0}_{\widehat{C}_1}[\mathbf{x}, \mathbf{y}] \to \sigma^2 \left(\pi \ell^2\right)^{3/2} \int_{\mathcal{D}_3} \int_{\mathcal{D}_3} \mathcal{G}_3(\mathbf{x} - \mathbf{x}') \mathcal{G}_3(\mathbf{y} - \mathbf{x}') C_H(x_1')^2\, \mathrm{d}\mathbf{x}', \tag{4.2.20}$$

for both a Gaussian and exponential covariance function. However, we cannot simply use the δ-function approximation of the covariance when finding the expectation of $\widehat{C}_2(\mathbf{x}; \omega)$ with (4.2.15) due to evaluating singularities in the Green's function in two and three dimensions. Instead, we will now consider calculating an effective uptake term to replace the sink function in the governing equations to account for corrections in the mean concentration field.

4.2.2 Calculating an effective uptake term

Here, a method to calculate a constant effective uptake parameter $\mathrm{Da}_{\mathrm{eff}}$ for a sufficiently small correlation length will be proposed, where $\mathrm{Da}_{\mathrm{eff}}$ will replace $\mathrm{Da}(1 + \hat{g}(\mathbf{x}; \omega))$ in (4.1.1). Using the effective uptake parameter will allow for a better approximation of the mean concentration compared to the homogenized solution and be computationally less expensive than evaluating the moments of corrections using the moments-based approach.

Let us seek a constant $\mathrm{Da}_{\mathrm{eff}}$ such that the solution of

$$\nabla^2_{3D} C - \mathrm{Pe}_L\, C_{x_1} - \mathrm{Da}_{\mathrm{eff}}\, C = 0, \tag{4.2.21}$$

subject to $\mathcal{B}_3 C = \{1,0,0,0,0,0\}$ approximates $\mathbb{E}[C(\mathbf{x};\omega)]$ to a suitable degree of accuracy. The exact solution of (4.2.21) is identical to the homogenized solution given in (4.2.2) but with Da replaced with $\mathrm{Da}_{\mathrm{eff}}$. By denoting this solution C_H^{eff} we obtain

$$C_H^{\mathrm{eff}}(\mathbf{x}) = C_H^{\mathrm{eff}}(x_1) = \frac{\mathrm{Pe}_L}{\Psi(1)}\Big((2\Phi - \mathrm{Pe}_L)e^{\Phi(x_1-1)} + (2\Phi + \mathrm{Pe}_L)e^{\Phi(1-x_1)}\Big)e^{(\mathrm{Pe}_L/2)x_1}, \tag{4.2.22}$$

where Φ and Ψ are given by $\Phi = \sqrt{\mathrm{Pe}_L^2/4 + \mathrm{Da}_{\mathrm{eff}}}$ and $\Psi(x_1) = (2\,\mathrm{Pe}_L\,\Phi + \mathrm{Pe}_L^2 + 2\,\mathrm{Da}_{\mathrm{eff}})e^{\Phi x_1} + (2\,\mathrm{Pe}_L\,\Phi - \mathrm{Pe}_L^2 - 2\,\mathrm{Da}_{\mathrm{eff}})e^{-\Phi x_1}$ respectively.

To calculate an effective uptake term we approximate the concentration using the homogenized solution from (4.2.2) plus a correction $\widehat{C}(\mathbf{x};\omega)$, i.e.

$$C(\mathbf{x};\omega) = C_H(x_1) + \widehat{C}(\mathbf{x};\omega). \tag{4.2.23}$$

Then (4.2.21) can be rearranged using (4.2.1) to be

$$\mathcal{L}_3\widehat{C}(\mathbf{x};\omega) = (\mathrm{Da}_{\mathrm{eff}} - \mathrm{Da})(C_H(x_1) + \widehat{C}(\mathbf{x};\omega)). \tag{4.2.24}$$

If we now assume the correction $\widehat{C}(\mathbf{x};\omega)$ is small compared to the homogenized solution then the linear operator can be inverted to give

$$\widehat{C}(\mathbf{x}) = (\mathrm{Da}_{\mathrm{eff}} - \mathrm{Da})\int_{\mathcal{D}_3} \mathcal{G}_3(\mathbf{x}-\mathbf{x}')C_H(x_1')\,\mathrm{d}\mathbf{x}' + \ldots, \tag{4.2.25}$$

where the ω notation is dropped as the leading-order correction is deterministic to leading-order, which in turn gives the concentration given in (4.2.6) to be deterministic to leading-order.

To calculate $\mathrm{Da}_{\mathrm{eff}}$ given in (4.2.25), consider using the expected values of $\widehat{C}_1(\mathbf{x};\omega)$ and $\widehat{C}_2(\mathbf{x};\omega)$ given in (4.2.14) and (4.2.15) respectively. As the expectation of $\widehat{C}_1(\mathbf{x};\omega)$ is zero we obtain the expectation of the correction to the homogenized solution using the moments-based approach to be

$$\mathbb{E}\left[\widehat{C}(\mathbf{x};\omega)\right] = \mathrm{Da}^2\int_{\mathcal{D}_3}\int_{\mathcal{D}_3} \mathcal{G}_3(\mathbf{x}-\mathbf{x}')\mathcal{G}_3(\mathbf{x}'-\mathbf{x}'')\mathcal{K}_{\hat{g}}(\mathbf{x}',\mathbf{x}'')C_H(x_1'')\,\mathrm{d}\mathbf{x}'\,\mathrm{d}\mathbf{x}'' + \ldots \tag{4.2.26}$$

Comparing this with (4.2.25) gives the relation

$$\begin{aligned}(\mathrm{Da}_{\mathrm{eff}} - \mathrm{Da})\int_{\mathcal{D}_3} \mathcal{G}_3(\mathbf{x}-\mathbf{x}')C_H(x_1')\,\mathrm{d}\mathbf{x}' \\ \approx \mathrm{Da}^2\int_{\mathcal{D}_3}\int_{\mathcal{D}_3} \mathcal{G}_3(\mathbf{x}-\mathbf{x}')\mathcal{G}_3(\mathbf{x}'-\mathbf{x}'')\mathcal{K}_{\hat{g}}(\mathbf{x}',\mathbf{x}'')C_H(x_1'')\,\mathrm{d}\mathbf{x}'\,\mathrm{d}\mathbf{x}'',\end{aligned} \tag{4.2.27}$$

where we will not distinguish between strict asymptotic limits and approximations within this chapter. We can simplify (4.2.27) by assuming the covariance is stationary, so can be expressed as $\mathcal{K}_{\hat{g}}(\mathbf{x}, \mathbf{x}') = \widehat{\mathcal{K}}_{\hat{g}}(\mathbf{x} - \mathbf{x}')$ for some function $\widehat{\mathcal{K}}_{\hat{g}}$. This is appropriate for both a Gaussian and exponential covariance function, as can be seen by (4.1.2) and (4.1.3) respectively. Therefore (4.2.27) gives

$$(\mathrm{Da}_{\mathrm{eff}} - \mathrm{Da}) \int_{\mathbb{R}^3} \mathcal{G}_3(\mathbf{x} - \mathbf{x}') C_H(x_1') \, \mathrm{d}\mathbf{x}' \approx \mathrm{Da}^2 \int_{\mathbb{R}^3} \int_{\mathbb{R}^3} \mathcal{G}_3(\mathbf{x} - \mathbf{x}') \mathcal{G}_3 \widehat{\mathcal{K}}_{\hat{g}}(\mathbf{x}' - \mathbf{x}'') C_H(x_1'') \, \mathrm{d}\mathbf{x}' \, \mathrm{d}\mathbf{x}'', \tag{4.2.28}$$

where $\mathcal{G}_3 \widehat{\mathcal{K}}_{\hat{g}}(\mathbf{x}' - \mathbf{x}'') \equiv \mathcal{G}_3(\mathbf{x}' - \mathbf{x}'') \widehat{\mathcal{K}}_{\hat{g}}(\mathbf{x}' - \mathbf{x}'')$. For (4.2.28) we have expanded the domain $\mathcal{D}_3$ to $\mathbb{R}^3$, an assumption which can be made when sufficiently far from boundaries and the decay lengthscale of $\mathcal{G}_3 \widehat{\mathcal{K}}_{\hat{g}}$ is sufficiently short, which holds for $\ell \ll 1$ and $L_{\mathcal{G}_3} \ll 1$.

We can rewrite (4.2.28) in terms of convolutions as

$$(\mathrm{Da}_{\mathrm{eff}} - \mathrm{Da}) \mathcal{G}_3 * C_H \approx \mathrm{Da}^2 \, \mathcal{G}_3 * (\mathcal{G}_3 \widehat{\mathcal{K}}_{\hat{g}}) * C_H, \tag{4.2.29}$$

where $*$ denotes the convolution of functions. If $\ell \ll L_{\mathcal{G}_3}$, i.e. the decay lengthscale in $\widehat{\mathcal{K}}_{\hat{g}}$ is sufficiently shorter than the decay lengthscale in $\mathcal{G}_3$, then $\mathcal{G}_3 \widehat{\mathcal{K}}_{\hat{g}}$ resembles a δ-function with the appropriate weight and is given by (Noetinger et al., 2018)

$$\mathcal{G}_3 \widehat{\mathcal{K}}_{\hat{g}}(\mathbf{y}) \approx \delta(\mathbf{y}) \int_{\mathbb{R}^3} \mathcal{G}_3 \widehat{\mathcal{K}}_{\hat{g}}(\mathbf{x}) \, \mathrm{d}\mathbf{x}. \tag{4.2.30}$$

So by using (4.2.29) we obtain the effective uptake for an asymptotically small correlation length to be

$$\mathrm{Da}_{\mathrm{eff}} \approx \mathrm{Da} \left(1 + \mathrm{Da} \int_{\mathbb{R}^3} \mathcal{G}_3 \widehat{\mathcal{K}}_{\hat{g}}(\mathbf{x}) \, \mathrm{d}\mathbf{x} \right). \tag{4.2.31}$$

As the Green's function and covariance function are always negative and positive respectively, (4.2.31) gives that the effective uptake parameter remains smaller than the Damköhler number, which reflects disordered sink functions reducing the uptake of a solute. As the correlation length becomes larger we see a non-local response in the correction to the homogenized solution, meaning a constant effective uptake parameter becomes less appropriate. It is therefore recommended to evaluate the expectation of $\widehat{C}_2$ directly using (4.2.15). By generalising the three-dimensional methods in Section 4.2.1 and 4.2.2 we will now quantify the effect of disorder on the solute concentration in one, two and three dimensions.

4.3 One-dimensional results

Define a one-dimensional domain $\mathcal{D}_1 = [0, 1]$, a position vector $x_1 \in \mathcal{D}_1$ and a boundary operator $\mathcal{B}_1 = \{(1 - \mathrm{Pe}_L^{-1} \, \partial_{x_1}) \cdot |_{x_1=0}, \partial_{x_1}(\cdot)|_{x_1=1}\}$ where $\mathcal{B}_1 C = \{1, 0\}$. This does not affect

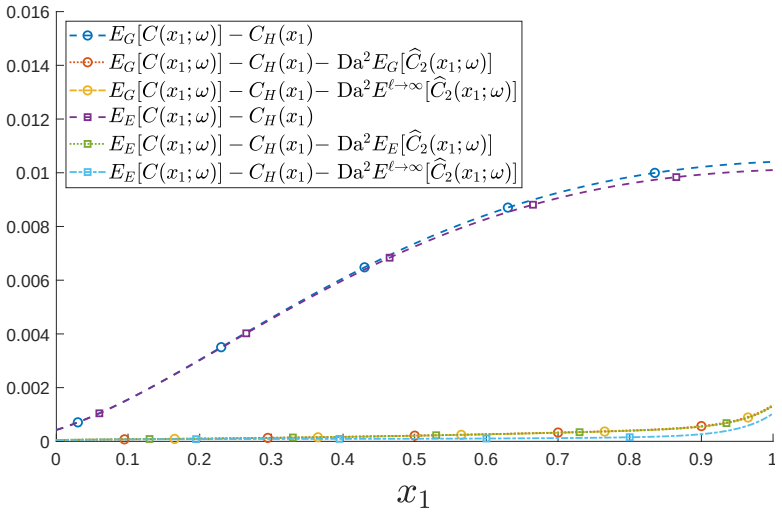

Figure 4.2: Difference between the sample mean $[\mathbb{E}_{\{G,E\}}[C(x_1;\omega)]]$ and the homogenized solution from (4.2.2) $[C_H(x_1)]$, the expected second-order correction from (4.2.15) $[\mathbb{E}_{\{G,E\}}[\widehat{C}_2(x_1;\omega)]]$ and using the approximation given in (4.2.17) $[\mathbb{E}^{\ell\to\infty}[\widehat{C}_2(x_1;\omega)]]$. Here, $(\mathrm{Pe}_L, \mathrm{Da}) = (20, 40)$, $\ell = 10$ and $\sigma = 0.2$ are used, the subscript G and E notation represents using a Gaussian and exponential covariance function respectively and the sample means are calculated using 10^7 realisations.

the homogenized solution given in (4.2.2), with the free-space Green's function being given in (4.2.4). For both a Gaussian and exponential covariance function, which are given in (4.1.2) and (4.1.3) respectively, we will estimate the moments of the solute concentration using moments of corrections and an effective uptake term from Section 4.2.

4.3.1 Expectation of corrections and using an effective uptake parameter

First, consider when the correlation length is asymptotically large. From (4.2.17) we know the expectation of the correction $\widehat{C}_2(x_1;\omega)$ converges to the same approximation for both a Gaussian and exponential covariance function due to the covariance function becoming constant. We can test the approximation given in (4.2.17) against the sample mean and using the full expression for the expectation of $\widehat{C}_2(x_1;\omega)$ given in (4.2.15) for $\ell = 10$. This is done in Figure 4.2, where good agreement between the sample mean and using both (4.2.15) and (4.2.15) are found.

Let us now consider finding an effective uptake parameter when using a Gaussian covariance function. From (4.1.2) we see the one-dimensional covariance function is given by

$$\widehat{\mathcal{K}}_{\hat{g}}^{G}(x_1) = \sigma^2 \exp\left(-\frac{x_1^2}{\ell^2}\right).$$

This can be used with the analogous one-dimensional version of (4.2.30) to obtain

$$\mathcal{G}_1\widehat{\mathcal{K}}(0) = -\frac{\sigma^2}{2\phi}\left(\int_{-\infty}^{0} \exp\left(\left(\frac{\mathrm{Pe}_L}{2} + \phi \right) x_1 - \frac{x_1^2}{\ell^2} \right) \mathrm{d}x + \int_{0}^{\infty} \exp\left(\left(\frac{\mathrm{Pe}_L}{2} - \phi \right) x_1 - \frac{x_1^2}{\ell^2} \right) \mathrm{d}x \right).$$

These integrals are solved in Appendix B.4 and give

$$\mathcal{G}_1\widehat{\mathcal{K}}(0) = -\frac{\sigma^2\ell\sqrt{\pi}}{4\phi}\left(\exp\left(\frac{\ell^2}{4}\left(\frac{\mathrm{Pe}_L}{2} + \phi \right)^2 \right)\left(1 + \operatorname{erf}\left(\frac{\ell}{2}\left(\frac{\mathrm{Pe}_L}{2} + \phi \right) \right) \right) + \exp\left(\frac{\ell^2}{4}\left(\frac{\mathrm{Pe}_L}{2} - \phi \right)^2 \right)\left(1 - \operatorname{erf}\left(\frac{\ell}{2}\left(\frac{\mathrm{Pe}_L}{2} - \phi \right) \right) \right) \right).$$

So by taking the limit $\ell \to 0$ we obtain $\mathcal{G}_1\widehat{\mathcal{K}}(0) \to -\sigma^2\ell\sqrt{\pi}/2\phi$, which can be used with (4.2.31) to give the effective uptake parameter for a Gaussian covariance function as

$$\mathrm{Da}_{\mathrm{eff}}^{G} \to \mathrm{Da}\left(1 - \frac{\sqrt{\pi}\,\mathrm{Da}\,\sigma^2\ell}{2\phi} \right) \tag{4.3.1}$$

for $\ell \ll 1$. As the effective uptake parameter is smaller than the Damköhler number we see that disorder in the sink function reduces the effective uptake of solute.

When using $\mathrm{Da}_{\mathrm{eff}}^{G}$ we will denote the solution $C_H^{\mathrm{eff}}(x_1)$ given in (4.2.22) as $C_H^{G}(x_1)$. Figure 4.3 shows a comparison between using the homogenized solution from (4.2.2) and $C_H^{G}(x_1)$ when $\ell = 0.01$. By replacing Da with $\mathrm{Da}_{\mathrm{eff}}$ we see an improvement in our approximation of the mean concentration due to $\mathrm{Da}_{\mathrm{eff}}$ accounting for the disordered uptake function $\hat{g}(x_1;\omega)$. For comparison Figure 4.3 also shows the expectation of the second-order correction $\widehat{C}_2(x_1;\omega)$, which has a similar response to using an effective uptake term but is computationally more expensive to calculate.

When using the exponential covariance function given in (4.1.3) a similar method can be used with the integrals given in Appendix B.4 to obtain

$$\mathcal{G}_1\widehat{\mathcal{K}}(0) = -\frac{\sigma^2\ell}{\phi}\left(\frac{1 + \phi\ell}{(1+\phi\ell)^2 - \ell^2\,\mathrm{Pe}_L^2\,/4} \right).$$

So by taking the limit $\ell \to 0$ we find $\mathcal{G}_1\widehat{\mathcal{K}}(0) \to -\sigma^2\ell/\phi$, meaning (4.2.31) gives the effective uptake parameter as

$$\mathrm{Da}_{\mathrm{eff}}^{E} \to \mathrm{Da}\left(1 - \frac{\mathrm{Da}\,\sigma^2\ell}{\phi} \right) \tag{4.3.2}$$

for $\ell \ll 1$. From (4.3.2) we again see that disorder reduces the effective uptake of solute, with the term for an exponential covariance function being nearly identical to that for a Gaussian covariance function; (4.3.1) and (4.3.2) differ by a single constant π which is replaced with

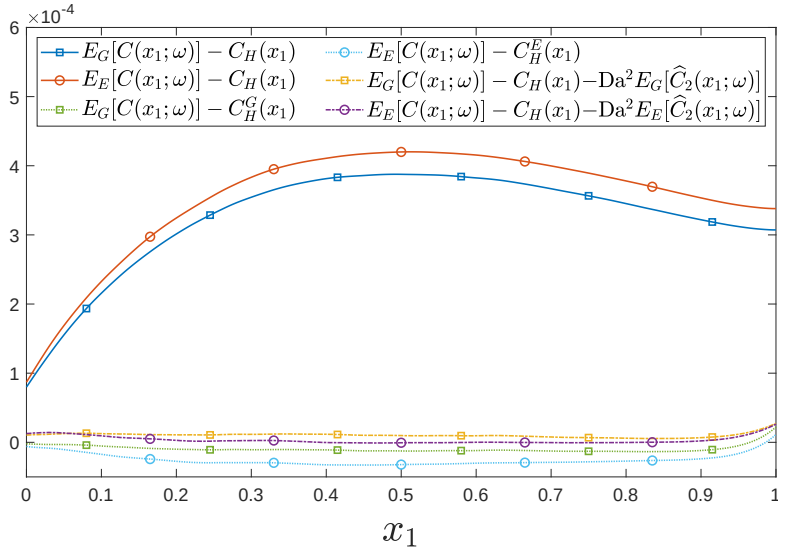

Figure 4.3: Difference between the sample mean $[\mathbb{E}_{\{G,E\}}[C(x_1;\omega)]]$ and the homogenized solution $C_H(x_1)$ from (4.2.2), using the expected correction $\widehat{C}_2(x_1;\omega)$ from (4.2.15) $[C_H(x_1) + \mathrm{Da}^2\,\mathbb{E}_{\{G,E\}}[\widehat{C}_2(x_1;\omega)]]$ and using the effective uptake parameters $\mathrm{Da}^G_{\mathrm{eff}}$ and $\mathrm{Da}^E_{\mathrm{eff}}$ from (4.3.1) and (4.3.2) respectively in (4.2.21) $[C_H^{\{G,E\}}(x_1)]$. Here, $(\mathrm{Pe}_L, \mathrm{Da}) = (20, 40)$, $\ell = 0.01$ and $\sigma = 0.2$ are used throughout, the subscript (and superscript) G and E notation represents using a Gaussian and exponential covariance function respectively and 10^7 realisations are used to calculate sample expectations.

a 4. Denoting the solution of (4.2.22) for $\mathrm{Da}^E_{\mathrm{eff}}$ as $C_H^E(x_1)$, Figure 4.3 shows that using the effective uptake term again better approximates the mean concentration than the homogenized solution given in (4.2.2). It also shows that, despite being computationally cheaper to calculate, the effective uptake term offers a similar response to using the expectation of the second-order correction $\widehat{C}_2(x_1;\omega)$.

4.3.2 Using the (co)variance of the leading-order concentration

We can approximate the concentration covariance using the covariance of the leading-order correction given in (4.2.12), which gives

$$\begin{aligned}\mathcal{K}_C(x_1,x_2) &\approx \mathrm{Da}^2\,\mathcal{K}_{\widehat{C}_1}(x_1,x_2)\\ &= \mathrm{Da}^2 \int_{\mathcal{D}_1}\int_{\mathcal{D}_1} G(x_1,x_1')C_H(x_1')\mathcal{K}_{\hat{g}}[x_1',x_2']G(x_2,x_2')C_H(x_2')\,\mathrm{d}x_1'\,\mathrm{d}x_2'.\end{aligned} \tag{4.3.3}$$

Equation (4.3.3) offers a direct mapping from the covariance of $\hat{g}(x_1;\omega)$ to the covariance of the concentration $C(x_1;\omega)$ in one dimension. By numerically evaluating the integral using the integral solver given in Appendix B.3, Figures 4.4 and 4.5 show the covariance of the sink function and concentration using the Gaussian and exponential covariance function given in (4.1.2) and (4.1.3) respectively. This is done for the range of correlation lengths $\ell = [0.01, 0.1, 1, 10]$,

where a comparison of the concentration's variance (i.e. the diagonals from the covariances given in Figures 4.4 and 4.5) is given in Figure 4.6. As ℓ increases the magnitude of the variance monotonically increases, meaning for an asymptotically large (small) correlation length the variance approaches its maximum (minimum). This allows bounds on the variance to be found by considering the asymptotes for small and large ℓ.

To calculate these asymptotes, consider first when ℓ becomes asymptotically small. So using (4.2.20) with $x_1 = x_2$ we obtain the asymptote of the variance for small ℓ to be

$$\mathrm{Var}_{\ell\to 0}[\widehat{C}_1(x_1;\omega)] = \sigma^2\sqrt{\pi}\ell \int_{\mathcal{D}_1} G(x_1, x_1')^2 C_H(x_1')^2 \,\mathrm{d}x_1' \tag{4.3.4}$$

as $\ell \to 0$. Using the homogenized solution and free-space Green's function given in (4.2.2) and (4.2.4) respectively, Appendix B.5 evaluates this integral to obtain

$$\begin{aligned}\mathrm{Var}_{\ell\to 0}[\widehat{C}_1(x_1;\omega)] = \sqrt{\pi}\ell \left(\frac{\sigma\,\mathrm{Pe}_L}{2\phi^2\psi(1)}\right)^2 \phi e^{\mathrm{Pe}_L\, x_1}\Bigg(\left(\phi + \frac{\mathrm{Pe}_L}{2}\right)^2 (4\phi x_1 + 1)e^{2\phi(1-x_1)} \\ + \left(4\phi^2 - \mathrm{Pe}_L^2\right)\left(2 - e^{-2\phi x_1}\right) + \left(\phi(2\phi - \mathrm{Pe}_L)^2(1-x_1) + \mathrm{Pe}_L^2 - 2\phi\,\mathrm{Pe}_L - 4\phi^2\right) e^{2\phi(x_1-1)}\Bigg).\end{aligned} \tag{4.3.5}$$

This is shown in Figure 4.6 by the dashed red line with circles for $\ell = 0.01$ and is seen to closely match solving (4.3.3) numerically. In (4.3.5) we have a leading-order asymptote for the variance when the correlation length is asymptotically small.

If we now consider when ℓ is asymptotically large using (4.2.19) with $x_1 = x_2$ we obtain the asymptote for large ℓ as

$$\begin{aligned}\mathrm{Var}_{\ell\to\infty}[\widehat{C}_1(x_1;\omega)] \approx \left(\frac{\sigma\,\mathrm{Pe}_L}{2\phi^2\psi(1)}\right)^2 e^{\mathrm{Pe}_L\, x_1}\Bigg((2\phi + \mathrm{Pe}_L)\,(2\phi x_1 + 1)\,(\phi(2\phi - \mathrm{Pe}_L)(1-x_1) - \mathrm{Pe}_L) \\ + (\phi(2\phi - \mathrm{Pe}_L)(1-x_1) - \mathrm{Pe}_L)^2\, e^{2\phi(x_1-1)} + \left(\phi + \frac{\mathrm{Pe}_L}{2}\right)^2 (2\phi x_1 + 1)^2 e^{2\phi(1-x_1)}\Bigg).\end{aligned} \tag{4.3.6}$$

The expression in (4.3.6) gives the leading-order asymptote, plotted in Figure 4.6 using a dashed red line with squares. This is seen to closely match the variance obtained by solving (4.3.3) with an integral solver for $\ell = 10$ for both a Gaussian and exponential covariance function.

Next, we will consider finding an effective uptake parameter for solute transport in two dimensions. Here, despite calculating the expected correction using (4.2.15) being too computationally expensive, the expected correction can be found analytically for a small correlation length.

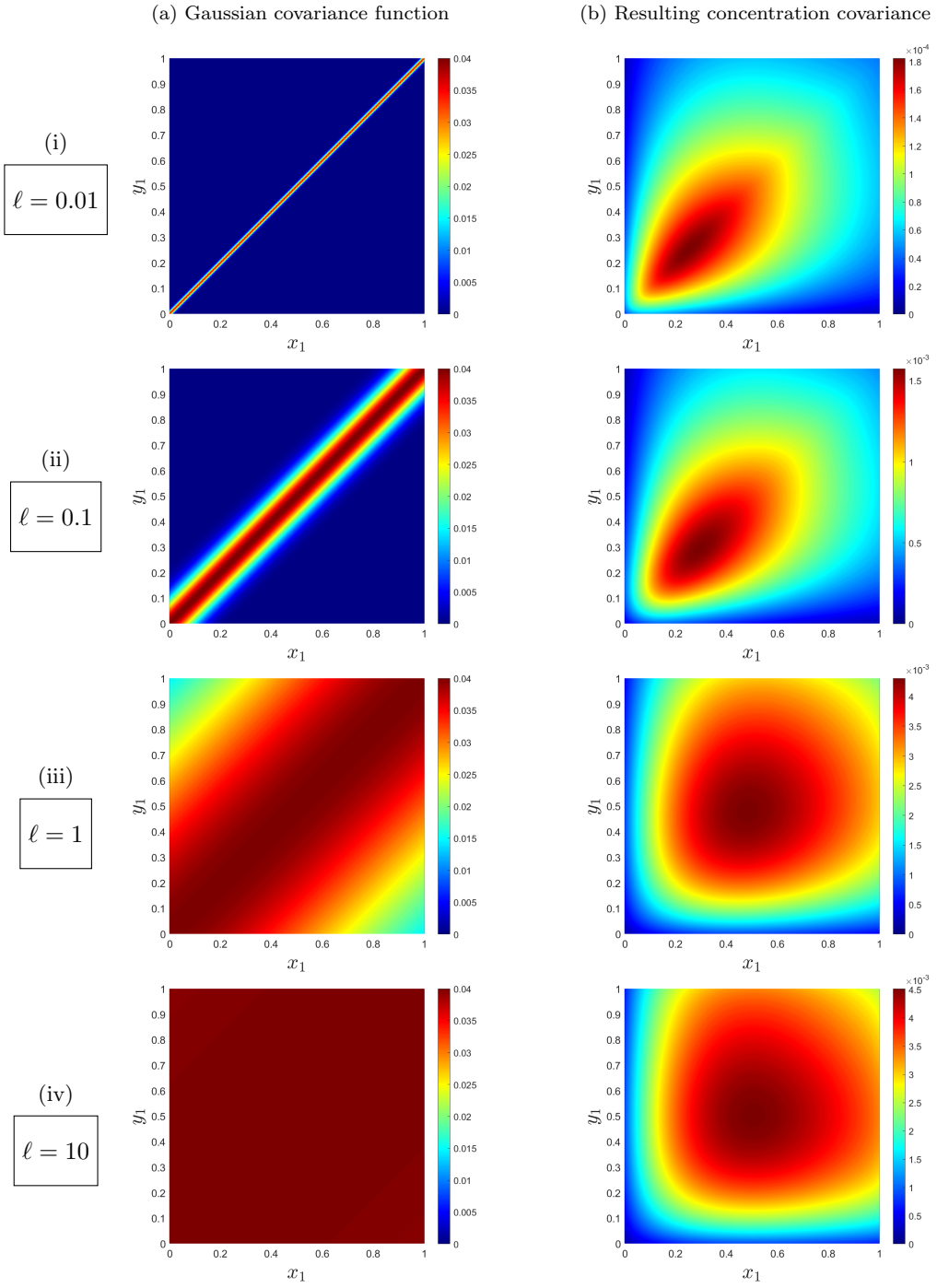

Figure 4.4: Column (a) depicts the sink covariance function $\mathcal{K}^G_{\hat{g}}(x_1, x_2)$ from (4.1.2) whereas column (b) depicts the solute covariance in terms of the correction $\mathcal{K}^G_{\widehat{C}_1}[x_1, x_2]$ from (4.2.12). Here, $\ell = 0.01, 0.1, 1, 10$ is used in rows (i), (ii), (iii) and (iv) respectively. The correction $\mathcal{K}^G_{\widehat{C}_1}[x_1, x_2]$ is calculated using (4.2.12) with the integral solver described in Appendix B.3, with $(\mathrm{Pe}_L, \mathrm{Da}) = (20, 40)$, $\sigma = 0.2$ being used throughout.

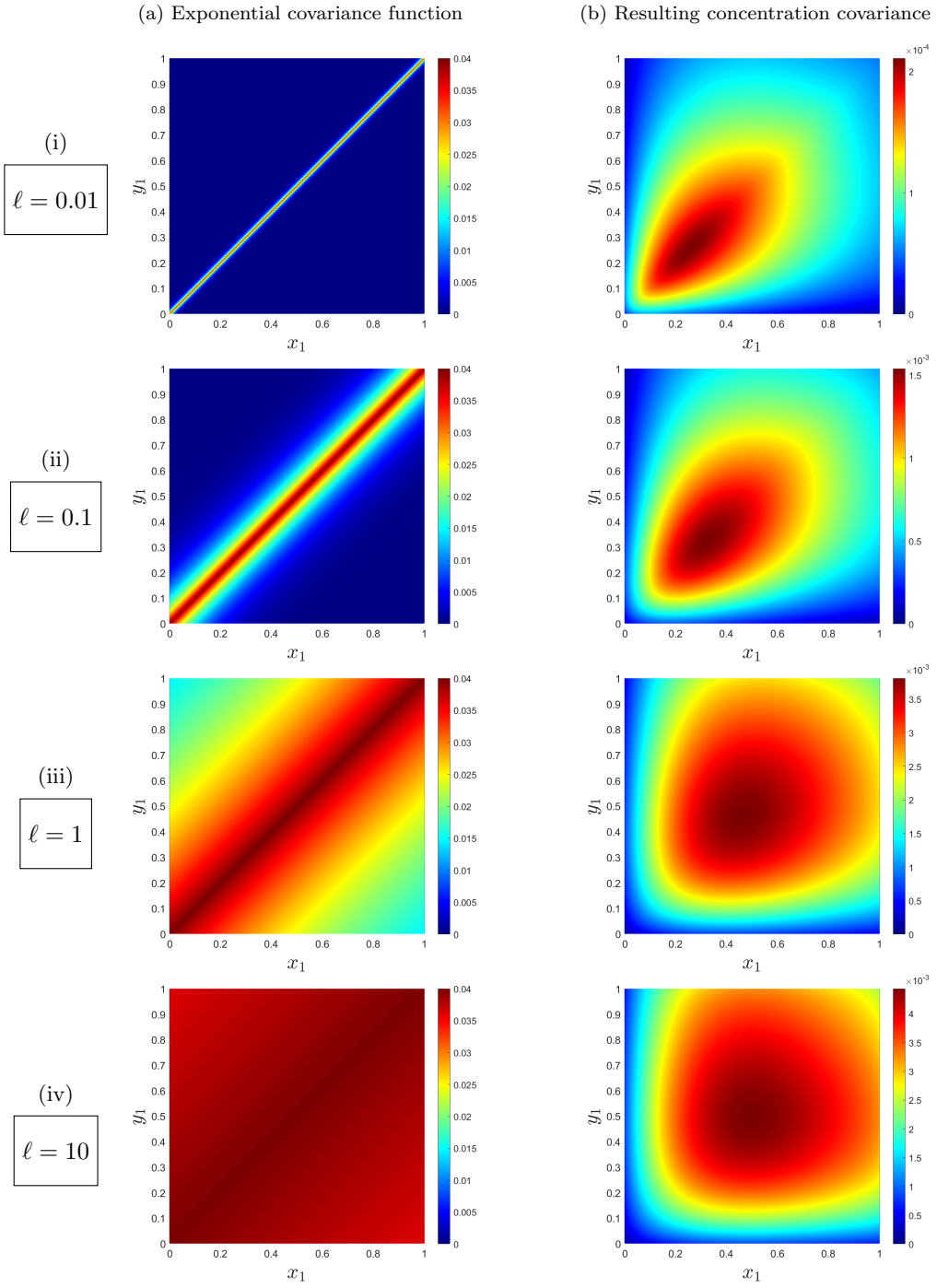

Figure 4.5: Column (a) depicts the sink covariance function $\mathcal{K}^E_{\hat{g}}(x_1, x_2)$ from (4.1.3) whereas column (b) depicts the solute covariance in terms of the correction $\mathcal{K}^E_{\widehat{C}_1}[x_1, x_2]$ from (4.2.12). Here, $\ell = 0.01, 0.1, 1, 10$ is used in rows (i), (ii), (iii) and (iv) respectively. The correction $\mathcal{K}^E_{\widehat{C}_1}[x_1, x_2]$ is calculated using (4.2.12) with the integral solver described in Appendix B.3, with $(\mathrm{Pe}_L, \mathrm{Da}) = (20, 40)$, $\sigma = 0.2$ being used throughout.

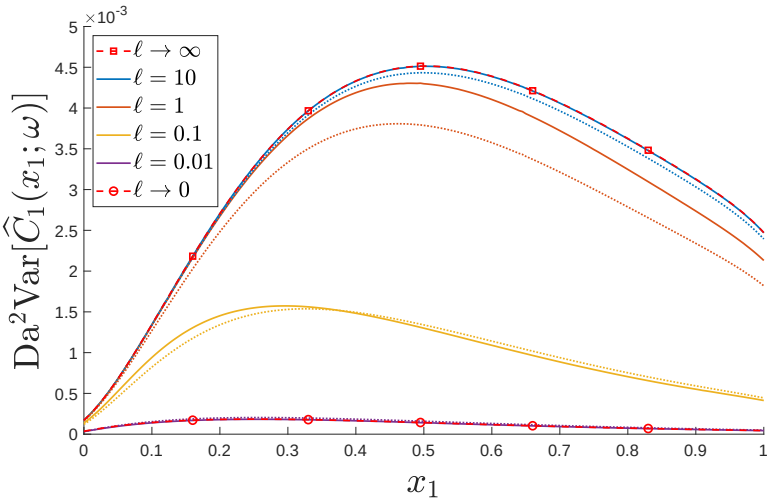

Figure 4.6: A plot showing the variances calculated using (4.3.6), (4.2.12) and (4.3.5) for $\ell \to \infty$, $\ell = [10, 1, 0.1, 0.01]$ and $\ell \to 0$ respectively. Here, solid and dotted lines are used to represent a Gaussian and exponential covariance function respectively. The asymptotes for small and large ℓ are represented by red dashed lines with squares and circles respectively, where the asymptote for $\ell \to 0$ is calculated using $\ell = 0.01$. This figures uses $(\mathrm{Pe}_L, \mathrm{Da}) = (20, 40)$, $\sigma = 0.2$. A second-order Simpson rule is used to evaluate (4.2.12).

4.4 Calculating an effective uptake parameter in two and three dimensions

4.4.1 Two-dimensional effective uptake parameter

Define a two-dimensional domain $\mathcal{D}_2$ such that for all $\mathbf{x} = (x_1, x_2) \in \mathcal{D}_2$ then $x_1 \in [0, 1]$ and $x_2 \in \mathbb{R}$. We also define the boundary operator

$$\mathcal{B}_2 = \{\cdot|_{x_1=0},\, \partial_{x_1}(\cdot)|_{x_1=1},\, \partial_{x_2}(\cdot)|_{x_2\to-\infty},\, \partial_{x_2}(\cdot)|_{x_2\to\infty}\},$$

where $\mathcal{B}_2 C = \{1, 0, 0, 0\}$. Then by using a separation of variables we again find the homogenized solution is given in (4.2.2) and the free-space Green's function is given by (4.2.4). Although the modified Bessel function of the second kind does not have a simplified expression, we can approximate the function for $z \to 0$ and $z \to \infty$ to be (Abramowitz and Stegun, 1964)

$$K_0(z) \approx -\log(z) \quad \text{and} \quad K_0(z) \approx \sqrt{\frac{\pi}{2z}}(1 + \mathcal{O}(1/|z|))\exp(-z). \tag{4.4.1}$$

Let us now calculate an effective uptake parameter $\mathrm{Da}_{\mathrm{eff}}$ using (4.2.31).

Consider using the Gaussian covariance function given in (4.1.2), which gives

$$\widehat{\mathcal{K}}^G_{\hat{g}}(\mathbf{x}) = \sigma^2 \exp\left(-\frac{|\mathbf{x}|^2}{\ell^2}\right).$$

Then (4.2.30) gives

$$\mathcal{G}_2\widehat{\mathcal{K}}(\mathbf{0}) \approx -\frac{\sigma^2}{2\pi}\int_{\mathbb{R}^2}\exp\left(\frac{\mathrm{Pe}_L}{2}x_1 - \frac{|\mathbf{x}|^2}{\ell^2}\right)K_0(\phi|\mathbf{x}|)\,\mathrm{d}\mathbf{x}.$$

By converting to polar coordinates where $x_1 = r\cos\theta$ and $x_2 = r\sin\theta$ we obtain

$$\mathcal{G}_2\widehat{\mathcal{K}}(\mathbf{0}) \approx -\frac{\sigma^2}{2\pi}\int_0^{2\pi}\int_0^{\infty}\exp\left(\frac{\mathrm{Pe}_L}{2}r\cos\theta - \frac{r^2}{\ell^2}\right)K_0(\phi r)r\,\mathrm{d}r\,\mathrm{d}\theta. \tag{4.4.2}$$

We can first solve the θ integral by using

$$I_\nu(z) = \frac{1}{\pi}\int_0^{\pi}\exp\left(z\cos\hat{\theta}\right)\cos(\nu\hat{\theta})\,\mathrm{d}\hat{\theta},$$

where I_ν is a modified Bessel function of the first kind (Abramowitz and Stegun, 1964). So as $\exp(z\cos\theta)$ is symmetric about $\theta = \pi$ we obtain

$$\int_0^{2\pi}\exp\left(z\cos\theta\right)\,\mathrm{d}\theta = 2\int_0^{\pi}\exp\left(z\cos\theta\right)\,\mathrm{d}\theta = 2\pi I_0(z), \tag{4.4.3}$$

which can be used in (4.4.2) to give

$$\mathcal{G}_2\widehat{\mathcal{K}}(\mathbf{0}) \approx -\sigma^2\int_0^{\infty}\exp\left(-\frac{r^2}{\ell^2}\right)I_0\left(\frac{\mathrm{Pe}_L}{2}r\right)K_0(\phi r)r\,\mathrm{d}r.$$

For small correlation lengths we have $\mathcal{G}_2\widehat{\mathcal{K}}(\mathbf{0})$ is only non-zero in the vicinity of $r = 0$ due to the exponential term $\exp\left(-r^2/\ell^2\right)$ decaying rapidly. So by setting $r = \ell R$ we can approximate the modified Bessel functions using Abramowitz and Stegun (1964) to be

$$I_0\left((\mathrm{Pe}_L/2)\ell R\right) \approx 1 + \mathcal{O}(l^2\,\mathrm{Pe}_L^2\,R^2) \quad \text{and} \quad K_0(\phi\ell R) \approx -\log(\phi\ell R) = -\log(\phi\ell) - \log(R), \tag{4.4.4}$$

which gives

$$\mathcal{G}_2\widehat{\mathcal{K}}(\mathbf{0}) \approx \sigma^2\ell^2\left(\log(\phi\ell)\int_0^{\infty}R\exp\left(-R^2\right)\,\mathrm{d}R + \int_0^{\infty}R\log R\exp\left(-R^2\right)\,\mathrm{d}R\right)$$

for suitably small ℓ. Both of these integrals are solved in Appendix B.4 and give

$$\mathcal{G}_2\widehat{\mathcal{K}}(\mathbf{0}) \approx -\frac{\sigma^2\ell^2}{4}\left(\gamma - 2\log(\phi\ell)\right), \tag{4.4.5}$$

where $\gamma \approx 0.577216$ is the Euler-Mascheroni constant. This can then be used with (4.2.31) to obtain the effective uptake as

$$\mathrm{Da}_{\mathrm{eff}}^{G} \approx \mathrm{Da}\left(1 - \frac{1}{4}\,\mathrm{Da}\,\sigma^2\ell^2\left(\gamma - 2\log\left(\phi\ell\right)\right)\right) \tag{4.4.6}$$

for small ℓ. Therefore we find the logarithmic singularity from the free-space Green's function appearing in the effective uptake parameter. By (4.4.6) we see $\mathrm{Da}_{\mathrm{eff}}^{G}$ is smaller than the Damköhler number, meaning disorder in the uptake function reduces the effective uptake of solute.

Let us now consider an exponential covariance function given in (4.1.3). In a similar fashion to using a Gaussian covariance function we can use (4.2.30) to give

$$\mathcal{G}_2\widehat{\mathcal{K}}(\mathbf{0}) \approx \sigma^2\ell^2\left(\log(\phi\ell)\int_0^\infty R\exp\left(-R\right)\,\mathrm{d}r + \int_0^\infty R\log R\exp\left(-R\right)\,\mathrm{d}R\right)$$

where $R = r/\ell$ and $r = |\mathbf{x}-\mathbf{x}'|$. The second integral can be solved and is given in Appendix B.4. We can then use (4.2.31) to find the effective uptake for asymptotically small ℓ as

$$\mathrm{Da}^E_{\mathrm{eff}} \approx \mathrm{Da}\left(1 - \frac{1}{4}\,\mathrm{Da}\,\sigma^2\ell^2\left(\gamma - 1 - \log\left(\phi\ell\right)\right)\right), \tag{4.4.7}$$

which again contains a logarithmic singularity and demonstrates a disordered sink distribution reducing the effective uptake of solute. In Section 4.5 below we will summarise and compare the different expressions of the effective uptake constant for different covariance functions across one-, two- and three dimensions.

4.4.2 Three-dimensional effective uptake parameter

In three dimensions the homogenized solution and free-space Green's function are as found in (4.2.2) and (4.2.4) respectively. Consider using the Gaussian covariance function given in (4.1.2). To calculate an effective uptake parameter $\mathrm{Da}^G_{\mathrm{eff}}$ we can use (4.1.2) with (4.2.4), then by converting into polar coordinates with $x_1 = r\sin\theta\cos\varphi$, $x_2 = r\sin\theta\sin\varphi$ and $x_3 = r\cos\theta$ we obtain

$$\mathcal{G}_3\widehat{\mathcal{K}}(\mathbf{0}) \approx -\frac{\sigma^2}{4\pi}\int_0^{2\pi}\int_0^{\pi}\int_0^{\infty}\exp\left(\frac{\mathrm{Pe}_L}{2}r\sin\theta\cos\varphi - \phi r - \frac{r^2}{\ell^2}\right)r\sin\theta\,\mathrm{d}r\,\mathrm{d}\theta\,\mathrm{d}\varphi.$$

As in two dimensions we can use the relation given in (4.4.3) to evaluate the φ integral and obtain

$$\mathcal{G}_3\widehat{\mathcal{K}}(\mathbf{0}) \approx -\frac{\sigma^2}{2}\int_0^{\pi}\int_0^{\infty}\exp\left(-\phi r - \frac{r^2}{\ell^2}\right)I_0\left(\frac{\mathrm{Pe}_L}{2}r\sin\theta\right)r\sin\theta\,\mathrm{d}r\,\mathrm{d}\theta.$$

As in two dimensions for small ℓ we see $\mathcal{G}_3\widehat{\mathcal{K}}(\mathbf{0})$ is only non-zero in the vicinity of $r = 0$ due to the exponentially decaying term. So by using the approximations of the modified Bessel functions given in (4.4.4) and evaluating the θ integral we obtain

$$\mathcal{G}_3\widehat{\mathcal{K}}(\mathbf{0}) \approx -\sigma^2\int_0^\infty r\exp\left(-\phi r - \frac{r^2}{\ell^2}\right)\mathrm{d}r = -\sigma^2\exp\left(\frac{\phi^2\ell^2}{4}\right)\int_0^\infty r\exp\left(-\ell^{-2}\left(r + \frac{\ell^2\phi}{2}\right)^2\right)\mathrm{d}r.$$

Let us use the substitution $u = \ell^{-1}(r + \ell^2\phi/2)$ to obtain

$$\mathcal{G}_3\widehat{\mathcal{K}}(\mathbf{0}) \approx -\frac{\sigma^2\ell}{2}\exp\left(\frac{\phi^2\ell^2}{4}\right)\left(2\int_{\phi\ell/2}^\infty u\exp\left(-u^2\right)\,\mathrm{d}u - \phi\ell\int_{\phi\ell/2}^\infty\exp\left(-u^2\right)\,\mathrm{d}u\right).$$

So by noting

$$\frac{\mathrm{d}}{\mathrm{d}u}\exp\left(-u^2\right) = -2u\exp\left(-u^2\right) \quad \text{and} \quad \int_0^u\exp\left(-u^2\right)\,\mathrm{d}u = \frac{\sqrt{\pi}}{2}\,\mathrm{erf}(u)$$

we obtain

$$\mathcal{G}_3\widehat{\mathcal{K}}(\mathbf{0}) \approx -\frac{\sigma^2\ell^2}{2}\left(1-\frac{\sqrt{\pi}\phi\ell}{2}\exp\left(\frac{\phi^2\ell^2}{4}\right)\left(1-\operatorname{erf}\left(\frac{\phi\ell}{2}\right)\right)\right).$$

For small ℓ we know $\exp\left(\phi^2\ell^2/4\right) \approx 1+\mathcal{O}(\ell^2)$ and $\operatorname{erf}\left(\phi\ell/2\right) = \mathcal{O}(\ell)$, which gives

$$\mathcal{G}_3\widehat{\mathcal{K}}(\mathbf{0}) \approx -\frac{\sigma^2\ell^2}{2}\left(1-\frac{\sqrt{\pi}\phi\ell}{2}\right). \tag{4.4.8}$$

So by taking the leading-order of (4.4.8) and using (4.2.31) we obtain the effective uptake term to be

$$\mathrm{Da}_{\mathrm{eff}}^{G} \approx \mathrm{Da}\left(1-\frac{1}{2}\,\mathrm{Da}\,\sigma^2\ell^2\right) \tag{4.4.9}$$

in the limit of asymptotically small ℓ. Once again we find disorder in the sink function causes a reduction in overall uptake.

Consider using the exponential covariance function for $\hat{g}$ given in (4.1.3). By using this with (4.2.4) and converting into polar coordinates using $x_1 = r\sin\theta\cos\varphi$, $x_2 = r\sin\theta\sin\varphi$ and $x_3 = r\cos\theta$, with the φ integral being evaluated as for a Gaussian covariance function, we obtain

$$\mathcal{G}_3\widehat{\mathcal{K}}(\mathbf{0}) \approx -\frac{\sigma^2}{2}\int_0^{\pi}\int_0^{\infty}\exp\left(-\phi r-\frac{r}{\ell}\right)I_0\left(\frac{\mathrm{Pe}_L}{2}r\sin\theta\right)r\sin\theta\,\mathrm{d}r\,\mathrm{d}\theta.$$

Note again how $\mathcal{G}_3\widehat{\mathcal{K}}(\mathbf{0})$ is only non-zero in the vicinity of $r=0$ due to the exponentially decaying term in the asymptotic limit $\ell\to 0$. So by again using the approximations given in (4.4.4) and evaluating the θ and r integral we obtain

$$\mathcal{G}_3\widehat{\mathcal{K}}(\mathbf{0}) \approx -\sigma^2\int_0^{\infty}\exp\left(-\phi r-\frac{r}{\ell}\right)r\,\mathrm{d}r = -\frac{\sigma^2\ell^2}{(1+\phi\ell)^2} \approx \sigma^2\ell^2\left(1-2\phi\ell\right)$$

in the limit of asymptotically small ℓ. Therefore by taking the leading-order term and using (4.2.31) the effective uptake is given by

$$\mathrm{Da}_{\mathrm{eff}}^{E} \approx \mathrm{Da}\left(1-\mathrm{Da}\,\sigma^2\ell^2\right) \tag{4.4.10}$$

in the limit $\ell\to 0$, where again we see disorder reducing the effective uptake parameter. These expressions for $\mathrm{Da}_{\mathrm{eff}}^{G}$ and $\mathrm{Da}_{\mathrm{eff}}^{E}$ in three dimensions are compared in Section 4.5 for different parameters and against the results obtained in one- and two dimensions.

4.5 Summary of effective uptake parameters in n dimensions

We can now compare the different effective uptake parameters in one, two and three dimensions, where the values of $\mathrm{Da}_{\mathrm{eff}}$ are given in Table 4.1 for the limit $\ell\to 0$. It can be seen that $\mathrm{Da}_{\mathrm{eff}}$

depends on four variables, Pe_L, Da, σ and ℓ. For both a Gaussian and exponential covariance function in one, two and three spatial dimensions we find the correction to the uptake term is of order ℓ, ℓ^2 and ℓ^3 modified by the factors 1, $\log \ell$ and $1/\ell$ respectively, where these factors are a result of the free-space Green's function present in (4.2.31). As a result, the difference between Da and $\mathrm{Da}_{\mathrm{eff}}$ decreases as the dimension size increases, as shown in Figures 4.7(a)-(d). It can also be seen that in one and two dimensions the correction is of order $\mathcal{O}(1/\phi)$ and $\mathcal{O}(\log(\phi))$ respectively, where $\phi = \sqrt{\mathrm{Pe}_L^2/4 + \mathrm{Da}}$, whereas in three dimensions ϕ does not appears in the correction. This demonstrates how the impact of advection on the effective uptake decreases as the dimension size increases. For all cases we find disorder in the sink function reduces the effective uptake of solute in the transport problem.

$\mathrm{Da}_{\mathrm{eff}}$	Gaussian Covariance	Exponential Covariance
1D	$\mathrm{Da}\left(1 - \dfrac{\sqrt{\pi}\,\mathrm{Da}\,\sigma^2\ell}{2\phi}\right)$	$\mathrm{Da}\left(1 - \dfrac{\mathrm{Da}\,\sigma^2\ell}{\phi}\right)$
2D	$\mathrm{Da}\left(1 - \dfrac{1}{4}\mathrm{Da}\,\sigma^2\ell^2\left(\gamma - 2\log\left(\phi\ell\right)\right)\right)$	$\mathrm{Da}\left(1 - \dfrac{1}{4}\mathrm{Da}\,\sigma^2\ell^2\left(\gamma - 1 - \log\left(\phi\ell\right)\right)\right)$
3D	$\mathrm{Da}\left(1 - \dfrac{1}{2}\mathrm{Da}\,\sigma^2\ell^2\right)$	$\mathrm{Da}\left(1 - \mathrm{Da}\,\sigma^2\ell^2\right)$

Table 4.1: Table showing the different values of $\mathrm{Da}_{\mathrm{eff}}$ in the limit $\ell \to 0$ when using a Gaussian and exponential covariance function. Results are obtained by taking the limit $\ell \to 0$ for Gaussian [exponential] covariance functions in one, two and three dimensions in (4.3.1) [(4.3.2)], (4.4.6) [(4.4.7)] and (4.4.9) [(4.4.10)] respectively.

Figures 4.7(a)-(d) demonstrates how the effective uptake term depends on each variable Pe_L, Da, σ and ℓ in one, two and three dimensions. Throughout, we find an exponential covariance function requires a greater difference between the Damköhler number and the effective uptake parameter when compared to using a Gaussian covariance function. As Pe_L decreases and Da, σ and ℓ increase then there is a greater difference between Da and $\mathrm{Da}_{\mathrm{eff}}$. So as advection becomes stronger (Pe_L increases) the correction to Da required to account for disorder decreases exponentially, whereas as uptake becomes stronger (Da increases) this correction increases exponentially, as shown in Figures 4.7(a) and 4.7(b) respectively. It can also be seen that as the variance and correlation length of the Gaussian process increases (σ and ℓ increase) the correction increases exponentially and linearly respectively. This can be seen in Figures 4.7(c) and 4.7(d). Note that the correlation length remains small compared to the lengthscales in the Green's function throughout to ensure (4.2.30) remains valid.

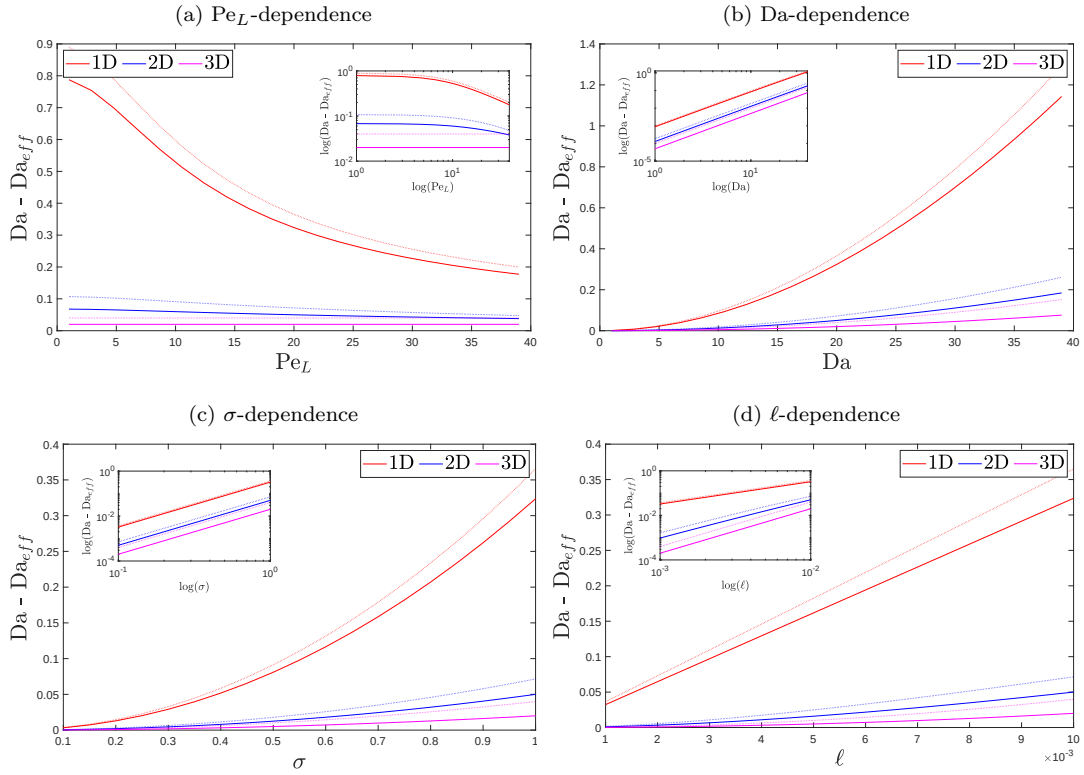

Figure 4.7: Difference between Da and Da_{eff} as the parameters Pe_L, Da, σ and ℓ change, as shown by figures (a), (b), (c) and (d) respectively, with insets showing log-log plots. Here, the difference is shown in one dimension (1D), two dimensions (2D) and three dimensions (3D) with solid and dashed lines representing a Gaussian and Exponential covariance function respectively. Figures (b), (c) and (d) use $\text{Pe}_L = 20$, Figures (a), (c) and (d) use $\text{Da} = 20$, Figures (a), (b) and (d) use $\sigma = 1$ and Figures (a), (b) and (c) use $\ell = 0.01$. Effective uptake parameters for Gaussian [exponential] covariance functions are given in one, two and three dimensions in (4.3.1) [(4.3.2)], (4.4.6) [(4.4.7)] and (4.4.9) [(4.4.10)] respectively.

We will now demonstrate using the effective uptake parameters for a discrete sink function with uniformly-random sink locations. This is seen to be appropriate for asymptotically small sink widths in suitably large domains as corrections to the solute concentration become local.

4.6 Calculating an effective uptake parameter for a discrete uptake function with uniformly-random sink locations

Consider an n-dimensional discrete sink function with regularised sink locations of finite size which occupy a domain $\mathcal{D}_n^s$, where for all $\mathbf{x} \in \mathcal{D}_3^s$ then $x_1 \in [0,1]$ and $x_2, x_3 \in [-L_s, L_s]$ (with analogous definitions in one and two dimensions). Allow $\lambda = 1/N$ to be the average inter-sink distance and $L_s = (2k-1)\lambda/2$ for any $k \in \mathbb{Z}^+$, where $N \in \mathbb{Z}^+$ represents the number of sinks

per unit length. Then the n-dimensional sink function can be given by (3.1.3) and (3.1.5) from Chapter 3 as

$$\hat{g}(\mathbf{x};\omega) = \lambda^n \sum_{\mathbf{i}_n} \frac{1}{(2\pi\varsigma^2)^{n/2}} \exp\left(-\frac{1}{2\varsigma^2}|\mathbf{x} - \boldsymbol{\xi}_{\mathbf{i}_n}|^2\right) - 1, \tag{4.6.1}$$

where $\mathbf{i}_3 \in \{i,j,k\}$, $\mathbf{i}_2 \in \{i,j\}$ and $\mathbf{i}_1 = i$ for $i = 1,\dots,N$ and $j,k = -M,\dots,M$ with $M = \lfloor L_s N \rfloor \in \mathbb{Z}$. Let sink locations be prescribed by a multivariate uniform distribution, with position vectors given by $\boldsymbol{\xi}_{\mathbf{i}_3} = (\xi_i,\xi_j,\xi_k)$, $\boldsymbol{\xi}_{\mathbf{i}_2} = (\xi_i,\xi_j)$ and $\boldsymbol{\xi}_{\mathbf{i}_1} = \xi_i$ such that $\xi_i \sim \mathcal{U}[0,1]$ and $\xi_j,\xi_k \sim \mathcal{U}[-L_s,L_s]$ for $i = 1,\dots,N$ and $j,k = -M,\dots,M$. Then the covariance of the sink function is given by (3.3.20) to be

$$\mathcal{K}_{\hat{g}}[\mathbf{x},\mathbf{y}] = \left(\frac{\lambda}{2\sqrt{\pi}\varsigma}\right)^n \exp\left(-\frac{1}{4\varsigma^2}|\mathbf{x}-\mathbf{y}|^2\right) - \frac{\lambda}{(2M+1)^{n-1}}. \tag{4.6.2}$$

In two and three dimensions by letting $L_s \to \infty$ we find the covariance of the sink function becomes local, with

$$\mathcal{K}_{\hat{g}}[\mathbf{x},\mathbf{y}] \to \mathcal{K}^G_{\hat{g}}\left(\mathbf{x},\mathbf{y};\sigma = \left(\frac{\lambda}{2\sqrt{\pi}\varsigma}\right)^{n/2},\, \ell = 2\varsigma\right). \tag{4.6.3}$$

Therefore the effective uptake parameter $\mathrm{Da}^{UR}_{\mathrm{eff}}$ can be found in two and three dimensions using (4.4.6) and (4.4.9) to give

$$\mathrm{Da}^{UR}_{\mathrm{eff}} \approx \mathrm{Da}\left(1 - \frac{\lambda^2\,\mathrm{Da}}{4\pi}\left(\gamma - 2\log\left(2\phi\varsigma\right)\right)\right) \tag{4.6.4}$$

and

$$\mathrm{Da}^{UR}_{\mathrm{eff}} \approx \mathrm{Da}\left(1 - \frac{\lambda^3\,\mathrm{Da}}{4\pi^{3/2}\varsigma}\right) \tag{4.6.5}$$

respectively. These parameters can be used to find the effective solute concentration for uniformly-random sink locations by substituting each parameter into (4.2.22), where this solution will be denoted $C_H^{UR}(x_1)$. As for a Gaussian process, (4.6.4) and (4.6.5) show that a disordered sink function reduces the effective uptake of a solute when considering the transport problem given in (4.1.1), in a manner that depends on the linear sink density λ and the sink width ς.

Let us compare using effective uptake parameters in (4.6.4) and (4.6.5) to finding the expectation of the correction $\widehat{C}_2(\mathbf{x};\omega)$, which is given in equation (3.5.34) from Chapter 3. The effective uptake parameters give the two- and three-dimensional corrections for an asymptotically small sink width to be dependent on the logarithm and reciprocal of ς respectively. This is consistent with the results for the expectation of the second-order correction in Chapter 3. Figure 4.8 shows a comparison between using both approximations. In two dimensions, both approaches

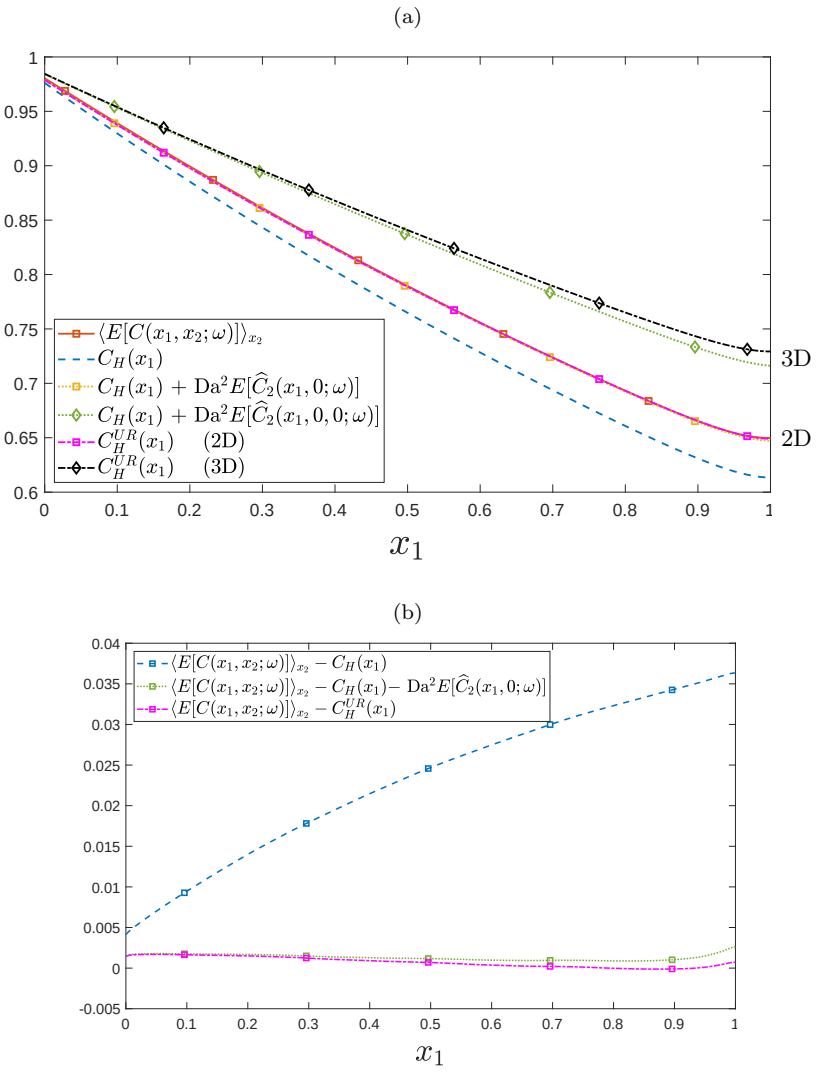

Figure 4.8: (a) Approximations of the expected concentration for uniformly-random sink locations in two and three dimensions, as given in Figure 3.12(a). Added are the two- and three-dimensional effective uptake approximations in magenta and black respectively. (b) Difference between sample expectations and each correction in two dimensions. Throughout we use $\lambda = 0.2$, $\varsigma = 0.01$ and $(\mathrm{Pe}_L, \mathrm{Da}) = (20, 10)$ with squares and diamonds representing two- and three-dimensional domains respectively. Effective concentrations are calculated using (4.6.3) with Table 4.1 and (4.2.22).

improve the approximation of solute concentration when compared to using the homogenized solution from (4.2.2) (Figure 4.8(b)). In three dimensions (Figure 4.8(a)) we see close agreement between both approaches, although sample expectations could not be calculated due to the computational expense.

4.7 Discussion

In this chapter we consider a continuous sink function represented by a Gaussian process with the same transport problem presented in Chapter 3. We consider both a Gaussian and exponential covariance function ($\mathcal{K}_{\hat{g}}$), which are defined in (4.1.2) and (4.1.3) and have a prescribed mean, variance and correlation length as zero, σ^2 and ℓ respectively. Both covariance functions simplified in the limit of an asymptotically large and small correlation length to a constant or δ-function approximation respectively, with both the Gaussian and exponential covariance function converging to the same asymptotes. We use two approaches to characterise the impact a continuous sink distribution has on the solute concentration: a moments-based approach and an effective uptake parameter, both of which are summarised in Section 4.2.

As in Chapter 3, the moments-based approach involves finding a deterministic homogenized solution with sequential non-local corrections. Here, corrections account for disorder by offering a direct mapping between the first two moments of the sink function and the first two moments of the corrections via a Green's function. For an asymptotically large correlation length integrals are simplified when calculating both expectations and (co)variances. For both a Gaussian and exponential covariance function, the moments of the correction are seen to be identical and the (co)variance of corrections become independent of the spatial dimension. For an asymptotically small correlation length, only the (co)variance of corrections can be simplified, which again become independent of the spatial dimension. The expectation of corrections can not be evaluated by using a δ-function approximation of the sink covariance in two and three dimensions due to singularities in the Green's function. As corrections become local in this limit an effective uptake parameter is instead considered.

In Section 4.2.2 the alternate approach of calculating constant effective uptake parameters to replace the Damköhler number in the homogenized solution is considered. This is done for a stationary sink covariance function and free-space Green's function as they can be expressed as $\widehat{\mathcal{K}}_{\hat{g}}(\mathbf{x}-\mathbf{x}')$ and $\mathcal{G}(\mathbf{x}-\mathbf{x}')$ respectively, an assumption which may fail near boundaries. When the decay lengthscale in $\widehat{\mathcal{K}}_{\hat{g}}$ is sufficiently shorter than the decay lengthscale in $\mathcal{G}$, i.e. the correlation length is sufficiently short, we find the product $\mathcal{G}\widehat{\mathcal{K}}_{\hat{g}}$ resembles a δ-function with the appropriate weight (Noetinger et al., 2018) and so the effective uptake parameter is given by (4.2.31). This approach allows computationally cheap evaluation of the expected solute concentration when compared to evaluating moments of corrections.

In one dimension we compare results from both methods to sample moments of the concentration, which are obtained by producing realisations of the sink function using the eigenvalue decomposition described in Appendix B.6. Following this, (4.1.1) is used with the finite-difference solver given in Appendix B.2 to produce multiple realisations of the solute concentration. Note that sample moments of the concentration are only calculated in one dimension due to finding realisations of the sink function being too computationally expensive in higher dimensions.

In Sections 4.3 the first two moments of corrections and an effective uptake parameter are used in one dimension for a range of correlation lengths. When considering an asymptotically large correlation length, Figure 4.2 shows good agreement between the sample mean and asymptote for the expectation of the correction. This asymptote can be found in (4.2.17) and is identical for both Gaussian and exponential covariance functions due to the covariance functions becoming constant. For an asymptotically small correlation length Figure 4.3 shows good agreement between the sample mean, the expectation of the correction and using an effective uptake parameter. This is due to the mean correction having a local influence, where $C_H^{\text{eff}}(x_1)$ is seen to improve the prediction of solute concentration when compared to using the homogenized solution $C_H(x_1)$. Here, the effective uptake parameter varies between a Gaussian and exponential covariance function by a constant factor, see Table 4.1.

When considering the one-dimensional concentration's variance asymptotically small and large correlation lengths cause the variance to converge to the same asymptote for both Gaussian and exponential covariance functions. As Figure 4.6 shows, the magnitude of the variance monotonically increases as ℓ increases. Therefore we find an asymptotically large (small) correlation length causes the variance to approach its maximum (minimum) and so the two limiting expressions for the variance act as bounds.

The effective uptake parameter which accounts for local corrections in two and three dimensions is found in Section 4.4. Results for the effective parameters are summarised in Section 4.5, with Figure 4.7 showing the dependence of Da_{eff} on Pe_L, Da, σ and ℓ in n dimensions. We find the effective uptake parameter remains smaller than the Damköhler number throughout parameter space, representing how a disordered sink function reduces the uptake of a solute. Figure 4.7(a) shows that increased advection causes the required correction to the Damköhler number to decreases exponentially, whereas for increased uptake Figure 4.7(b) shows this correction to increase exponentially. Alternatively, Figures 4.2.31(c) and 4.2.31(d) show that for an increased variance and correlation length of the Gaussian process the correction required

increases exponentially and linearly respectively.

The two- and three-dimensional effective uptake parameters are used in Section 4.6 for a discrete sink function with uniformly-random sink locations. This is done by finding a relation between the covariance of sink locations and the Gaussian covariance function, which holds for a suitably large domain due to the covariance becoming local. Note that this approach was not used in one dimension due to corrections to the solute concentration being non-local. Figure 4.8 shows a comparison between using the expectation of corrections and effective uptake parameters in the limit of an asymptotically small sink width ς. In two dimensions both approaches offer similar predictions for the expected solute concentration, which better describes the sample expectation when compared to using the homogenized solution. In three dimensions we find close agreement between both approaches, which are seen to capture the over-prediction of solute uptake by the homogenized solution. However, sample expectations could not be calculated for comparison due to being too computationally expensive.

Let us consider the application of effective uptake parameters to some practical examples, where we assume sinks have finite size and are distributed uniformly randomly. Define the approximate sink volume, domain volume, volume fraction and dimensional average inter-sink distance to be

$$U_0 = (\varsigma^*)^3, \quad V_0 = L_{x_1} L_{x_2} L_{x_3}, \quad \phi = \frac{N_{\text{total}} U_0}{V_0} \quad \text{and} \quad \lambda^* = \frac{\varsigma^*}{\phi^{1/3}} \tag{4.7.1}$$

respectively, where ς^* and N_{total} are the dimensional average sink width and total number of sinks in the domain respectively and L_{x_1}, L_{x_2} and L_{x_3} are the approximate x_1, x_2 and x_3 domain lengths respectively. One could consider solute transport through the intervillous space (IVS), which is a disordered porous medium and shown in Figure 1.3(a). The magnitude of parameters are given in Tun et al. (2021) to be $\phi \sim 0.5$, $\varsigma^* \sim 10^2\,\mu$m and $L_{x_1} \sim 10^3\,\mu$m, which are the IVS volume fraction, median villous diameter and x_1 length respectively. So by non-dimensionalizing (which is done using L_{x_1}) we obtain the non-dimensional average inter-sink distance as $\lambda \sim 0.1$. Therefore the three-dimensional effective uptake parameter from (4.6.5) gives

$$\frac{\text{Da}_{\text{eff}}}{\text{Da}} \sim 1 - 10^{-2}\,\text{Da}\,. \tag{4.7.2}$$

A range of Damköhler numbers can be expected within maternal circulation due to solutes having different physico-chemical properties (Erlich et al., 2019b). For oxygen, the solute consumption rate (S_1) and diffusivity in blood plasma (D) have been estimated to be $1\,\text{min}^{-1}$ (Chernyavsky et al., 2010) and $10^{-3}\,\text{cm}^2/\text{min}$ (Banerjee et al., 2008) respectively. This would

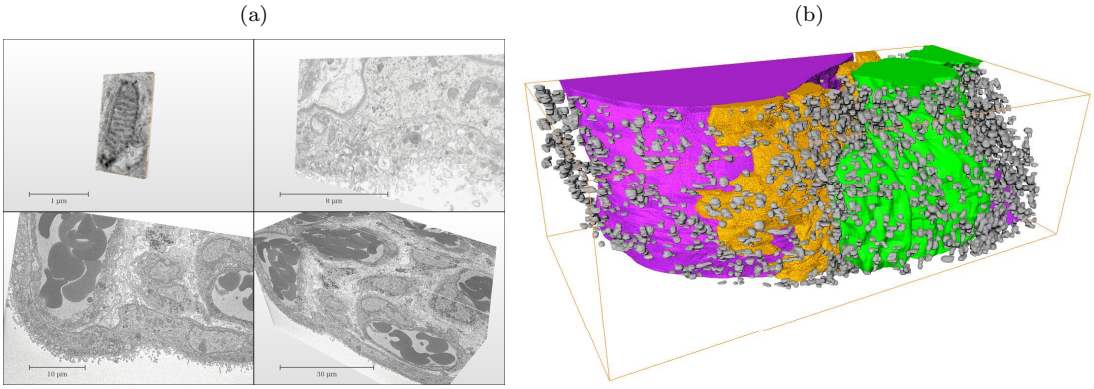

Figure 4.9: (a) Images of fetal tissue obtained using electron microscopy, where the top left image shows a single mitochondria. Images are courtesy of Michelle Desforges [unpublished]. (b) Distribution of mitochondria (grey) in the vasculosyncytial membrane, where the figure includes epithelium and capillaries (magenta), cytotrophoblast (orange) and the nuclei of syncytiotrophoblast (green). The outlining orange cuboid has dimensions $147\,\mu\text{m} \times 305\,\mu\text{m} \times 100\,\mu\text{m}$ and the figure is courtesy of Tomass Vaivods [unpublished] using data from Michelle Desforges [unpublished].

give a Damköhler number of approximately 10, meaning the effective uptake parameter is approximately 90% of this value.

One could also consider oxygen transport through the vasculosyncytial membrane, which separates fetal and maternal blood (see Figure 4.9). Here, oxygen uptake occurs at random mitochondria locations within the syncytiotrophoblast layer. Although solute transport is governed by diffusion with the absence of advection, therefore invalidating the free-space Green's function used due to assuming a suitably large Péclet number, we can obtain an ad-hoc estimation of the effective uptake parameter using (4.6.5). We use the approximate values $\varsigma^* \sim 1\,\mu\text{m}$, $L_{x_1} \sim 10\,\mu\text{m}$ and $N \sim 1 - 10$, which represent the mitochondria width, cell thickness and the average number of mitochondria per cell respectively and are obtained from imaging data courtesy of Tomass Vaivods and Michelle Desforges [unpublished]. So by assuming the distribution of sinks is uniform and isotropic, i.e. the average inter-sink distance is the same in all directions, we obtain $\lambda \geq 0.1$. Therefore the three-dimensional effective uptake parameter given in (4.6.5) gives the relation

$$\frac{\text{Da}_{\text{eff}}}{\text{Da}} \leq 1 - 10^{-2}\,\text{Da}\,. \tag{4.7.3}$$

From both examples we see disordered sink locations result in a notable difference between the naive and effective uptake parameter for sufficiently large Damköhler numbers, which emphasises the need to quantify the influence of a disordered uptake field on solute concentration.

In this chapter we consider using the moments-based approach from Chapter 3 for a continuous sink function described by a Gaussian process. When using Gaussian and exponential covariance functions the moments of corrections are simplified for asymptotically small and large correlation lengths. For an asymptotically small correlation length we use a δ-function approximation for local corrections to calculate effective uptake parameters, which characterises the impact of a disordered sink function on the mean concentration. These effective parameters are illustrated for a discrete sink function with suitably many uniformly-random sink locations in the limit of an asymptotically small sink width. One way to further this study would be to test results for Gaussian processes in higher dimensions by calculating sample moments of the concentration. This could not be done due to the computational expense of eigenvalue decomposition when producing sink function realisations, but it may be possible to overcome this by swapping to the stochastic Galerkin method, as described (for example) in Lord et al. (2014). An alternate approach is to verify effective parameters by evaluating the moments of corrections in higher dimensions using the full expressions given in (4.2.11)-(4.2.13) using an integral solver.

Both approaches are seen to quantify the impact of a disordered sink function on the solute concentration. One alternative is to consider the impact of a disordered flow field, which is an active area of interest in porous media (Jin et al., 2016; Alim et al., 2017). This could be done by randomly perturbing the velocity field and again using a moments-based approach to find corrections to a homogenized solution. Another approach would be to use a log-normal Gaussian process, as discussed for one dimension in Appendix B.7. Here, the distribution of realisations is seen to be non-Gaussian about the mean, causing confidence intervals to offer better descriptions of the impact disorder has on the solute field than calculating statistical moments. Therefore a similar approach to that used in Section 2.3.3 is recommended, which calculates confidence intervals using the cdf of sink locations.

Chapter 5

Conclusions

5.1 Summary

A variety of examples exist where solute transport occurs over multiple lengthscales through inherently random structures. As a result, direct approaches to mathematical modelling are often infeasible, meaning spatial averaging techniques are commonly employed. This thesis has developed multiple methods to characterise the impact of a disordered uptake function on solute transport occurring over multiple lengthscales.

We first considered one-dimensional solute transport past a disordered array of point sinks with first-order uptake kinetics in Chapter 2. When an advection-diffusion balance existed on the microscale, we used a similar approach to Russell and Jensen (2020) for finding corrections to a deterministic homogenized solution by inverting linear operators using a Green's function. The leading-order correction for periodic point sink locations accounted for discrete-to-continuous effects, where it captured a wavy sink-to-sink structure and an external boundary layer at the outlet, see Figure 2.2. For comparison, we used the classical approach to homogenization, which failed to capture the boundary layer due to being based on a two-scale dependence assumption. We then considered the leading-order correction to the homogenized solution for disordered sink locations by calculating the correction's variance. When sinks were normally-perturbed from periodic locations the variance of the correction exhibited sharp spikes about sink locations, which demonstrated individual point sinks have strong local influence but weak far-field impact, see Figure 2.7(a). When sink locations were uniformly random the variance

of the concentration was represented by a smooth function, despite each concentration profile independently exhibiting a wavy sink-to-sink structure, see Figure 2.7(a). This was due to calculating moments in the presence of strong disorder smearing out the impact of individual point sinks on the microscale.

We also considered when advection dominates diffusion on the microscale in Chapter 2, which lead to a staircase structure appearing in concentration profiles due to boundary layers forming upstream of sink locations. This caused moments to be poor predictors of disorder due to concentration profiles being non-Gaussian. As a result we calculated the median and credible-intervals of the solute concentration by inverting the cumulative distribution function (cdf) of the concentration to find the expected location of each jump in concentration. By comparing Gaussian-based (which were given by 1.96 standard deviations on either side of the mean) and cdf credible intervals we found that the cdf credible intervals could capture the non-Gaussian behaviour and preserve the staircase structure exhibited by individual concentration profiles.

In Chapter 3 we considered a more direct 'moments-based' approach for quantifying the impact of disordered sink locations on the solute concentration in one, two and three spatial dimensions. Sinks were again prescribed first-order uptake kinetics but now had a finite width ς. The moments-based approach offered a direct mapping between the first two moments of the sink distribution and the first two moments of the solute field. Therefore we calculated the moments of the sink distribution, which were shown in two dimensions in Figure 3.3. The sink function for normally-perturbed sink locations had a non-local covariance which was zero, positive and negative when away, on and near to the diagonal, which represented sinks being independently distributed, correlated and anti-correlated respectively. The sink function for uniformly-random sink locations also had a non-local covariance but became more local in two and three dimensions as the size of the sink domain increased. We then calculated a region of influence by inverting an associated free-space Green's function, wherein any sinks can influence the concentration at some given point. This was done for one, two and three spatial dimensions, with Figure 3.6 showing a two-dimensional depiction. Non-local corrections to the deterministic homogenized solution were then found by successively inverting linear operators using the calculated free-space Green's function. For periodic sink locations we found deterministic corrections, wherein the limit of an asymptotically small sink width the leading-order periodic correction scaled with the logarithm and reciprocal of the sink width ς in two and three dimensions respectively. This reflected the order of singularities found when using point sink locations in higher dimensions. For normally-perturbed sink locations, we found disorder

smoothed out singularities when taking the expectation of the leading-order correction. In the limit $\varsigma, \sigma \ll 1$ (where σ is the standard deviation of the perturbing variable) we found the leading-order mean correction in two and three dimensions scaled with the logarithm and reciprocal of $\sqrt{\varsigma^2 + \sigma^2}$ respectively. For uniformly-random sink locations we found the mean correction varied only in the advective direction when sufficiently far from boundaries, with the impact of individual sink locations being smeared out. By again taking the limit of an asymptotically small sink width we found the second-order correction scaled with the logarithm and reciprocal of the sink width ς in two and three dimensions respectively. For both normally-perturbed and uniformly-random sink locations, approximating the regularised sink function with a δ-function for an asymptotically small sink width over-predicted the variance of solute concentration. This allowed an upper bound for the variance to be calculated and reflects how regularising sink locations reduces the variation in solute concentration.

In Chapter 4 we considered replacing the discrete sink function from Chapter 3 with a continuous sink function represented by a Gaussian process. Two covariance functions were considered: Gaussian and exponential; where the mean, variance and correlation length were given by zero, σ^2 and ℓ respectively. We found both covariance functions simplify for asymptotically large and small correlation lengths to a constant and δ-function approximation respectively. For asymptotically large correlation lengths we simplified integrals when calculating the first two moments of corrections and found them to be identical for both Gaussian and exponential covariance functions. The resulting (co)variance of corrections became independent of the spatial dimension and is demonstrated in Figure 4.6 for the one-dimensional variance. For an asymptotically small correlation length, the (co)variance of corrections simplified using a δ-function approximation but did not become independent of the spatial dimension. This simplification is used in Figure 4.6 for the one-dimensional variance. To approximate the expectation of corrections for an asymptotically small sink width we could not simply replace the sink covariance function with a δ-function approximation due to evaluating Green's functions at singularities in two and three dimensions. We instead calculated effective uptake parameters, where despite the free-space Green's function in (4.2.31) accounting for non-local contributions, the resulting correction to the homogenized solution is local. These parameters were calculated for both Gaussian and exponential covariance functions in one, two and three dimensions, which were appropriate as corrections to the mean solute field became local. Results were used in one dimension and compared to sample expectations in Figure 4.3, which showed the effective uptake parameter being an improvement in comparison to the homogenized approximation. By finding a relationship between the Gaussian covariance function and the covariance of a

uniformly-random sink function, we illustrated results in two and three dimensions for a discrete sink distribution with uniformly-random sink locations in the limit of asymptotically small sink widths. As for Chapter 3 we found the effective uptake parameter scaled with the logarithm and reciprocal of the sink width ς in two and three dimensions respectively, which again reflected the singularities found when using point sink locations in higher dimensions. Results for uniformly-random sink locations were used to illustrate effective uptake parameters for two practical applications: solute transport within the intervillous space of the placenta and oxygen uptake by mitochondria within placental tissue. Both examples illustrate the non-negligible impact of the micro-statistics of the disordered uptake field on homogenized transport parameters.

5.2 Further work

We will here summarise possible extensions to the work undertaken in this thesis, most of which have been discussed in the final section of each chapter.

Alternate approaches to homogenization are developed throughout, which account for the impact of disordered sink functions on the solute field. When considering discrete sink locations one could consider varying the sink strength (as opposed to the sink size and location or using a continuous Gaussian process), which is a concept previously considered in Russell et al. (2016) for one spatial dimension. One could also consider using non-linear uptake kinetics, as done in Dalwadi and King (2020) and Chernyavsky et al. (2011, 2012), where the latter primarily focused on zeroth-order uptake kinetics.

When considering a continuous sink function one could consider using an alternate distribution to a Gaussian process, such as the log-normal Gaussian process discussed in Appendix B.7, which finds the distribution of concentration realisations to be non-Gaussian for a sufficiently large variance. Therefore credible intervals offer better descriptions of the impact disorder has on the solute field when compared to calculating statistical moments, see Figure B.1. These credible intervals could be found using a similar approach to that used in Chapter 2, which found cdf credible intervals using the cdf of the solute concentration.

Other extensions can come from considering the influence of disordered domains on the flow field, which is an active area of interest in porous media (Dagan, 1984; Jin et al., 2016; Alim et al., 2017). The influence of impenetrable sink locations on two- and three-dimensional fluid flow has been studied extensively for periodic structures, see Deo (2004) and Vasin and Filippov

(2009) for example. Russell (2017) considered strong disorder of impenetrable sink locations in two dimensions, which resulted in rapid-flow channels appearing within the domain. Accounting for disorder in the flow field could be achieved by randomly perturbing the velocity field and using a moments-based approach to find corrections to a homogenized solution. However, difficulty in calculating an appropriate Green's function, finding sample moments using Monte Carlo realisations and coupling the disordered advection and uptake terms are anticipated.

The impact of transient effects is another natural extension to the work undertaken. When considering linear uptake kinetics one could use Laplace transforms with respect to time, which may allow a similar methodology to the moments-based approach developed in Chapter 3 to be used, see the Lagrangian approach in Chapter 10 from Rubin (2003). An alternative approach would be to measure the leading edge of the resulting concentration spread when turning on a flux of solute at a time $t = 0$. By sampling the concentration at a fixed point downstream one could model breakthrough curves, which track the quantity of solute over time, see Shackelford and Redmond (1995) and Pedretti et al. (2013) for example. One anticipated problem is the impact of anomalous transport, as found in Bolster and Dentz (2012) for the transport of a chemical in the presence of weak disorder. This is often addressed by using an individual-based model with a continuous-time random walk (CTRW), as discussed in Section 1.2.2 and used in Berkowitz et al. (2006).

One may want to use the methods developed in this thesis for specific applications. The example of solute transport in maternal blood through the intervillous space of the placenta is considered by treating terminal villi locations as uptake sites in Chapter 4. The approach could be modified to consider the complexity of terminal villi uptake sites, where a wide range of parameter values can be observed for different solutes (Erlich et al., 2019a). Chapter 4 also considered the inter-cellular transport of oxygen through the vasculosyncytial membrane into fetal tissue. This could be furthered by considering Michaelis–Menten kinetics, which accounts for the non-linearity of oxygen uptake by mitochondria, as done in Erlich et al. (2019a) among others.

This thesis considered alternate approaches of homogenization that quantify the impact a disordered uptake function has on the concentration of a solute. These approaches predicted moments of the solute concentration, which can be used to capture fluctuations about the mean. In the limit where advection dominates diffusion, we found moments to be poor descriptors of the influence disorder has on the solute field, so an alternate approach was developed

to find non-Gaussian credible intervals. All approaches considered in this thesis should aid the research of solute transport occurring over multiple lengthscales within disordered media.

Appendix A

Chapter 2 appendices

A.1 Numerical method for solving the governing equations

In this section we describe the methodology used to solve (2.1.2a) numerically, which can be applied for different sink distributions. This will be done by replacing the uptake term in (2.1.2a) with a jump condition at sink locations, allowing the resulting algebraic linear system to be solved numerically.

First, note that when located in-between sinks (i.e. $x \neq \xi_j$) then (2.1.2a) gives

$$\mathrm{Pe}^{-1} C_{xx} - C_x = 0, \tag{A.1.1}$$

where $0 < x < \varepsilon^{-1}$. To find the jump condition to account for sink locations, integrate inside a vanishing region about a sink j, along with using prescribed concentration. This gives the jump condition at a sink j as $[\![C_x]\!]_{x=\xi_j} = \mathrm{S}\, C(\xi_j)$, where $j = 1, \ldots, N$. By imposing that the concentration is continuous across each sink, so $[\![C]\!]_{x=\xi_j} = 0$, and using the boundary conditions

given in (2.1.2b) and (2.1.2c), then the governing equations are given by

$$\mathrm{Pe}^{-1}\, C_{xx} - C_x = 0, \quad \text{where } x \neq \xi_j \text{ for } j = 1, \ldots, N, \tag{A.1.2a}$$

$$(C - \mathrm{Pe}^{-1}\, C_x)|_{x=0} = 1, \tag{A.1.2b}$$

$$[\![C_x]\!]_{x=\xi_j} = \mathrm{Pe}\ \mathrm{S}\, C(\xi_j), \quad \text{where } j = 1, \ldots, N, \tag{A.1.2c}$$

$$[\![C]\!]_{x=\xi_j} = 0, \quad \text{where } j = 1, \ldots, N, \tag{A.1.2d}$$

$$C_x|_{x=\varepsilon^{-1}} = 0. \tag{A.1.2e}$$

The general solution to (A.1.2a) is given by

$$C(x) = A_j e^{\mathrm{Pe}\,(x-\xi_j)} + B_j, \tag{A.1.3}$$

where $\xi_j \leq x \leq \xi_{j+1}$ for $j = 0, \ldots, N$ and A_j, B_j are constants. By using (A.1.2b-A.1.2e), it follows that

$$B_0 = 1, \tag{A.1.4a}$$

$$A_{j-1} e^{\mathrm{Pe}\,(\xi_j - \xi_{j-1})} - A_j + B_{j-1} - B_j = 0, \quad j = 1, \ldots, N, \tag{A.1.4b}$$

$$A_{j-1} e^{\mathrm{Pe}\,(\xi_j - \xi_{j-1})} + (\mathrm{S} - 1) A_j + \mathrm{S} B_j = 0, \quad j = 1, \ldots, N, \tag{A.1.4c}$$

$$A_N = 0. \tag{A.1.4d}$$

Now by eliminating A_{j-1} from (A.1.4b) via (A.1.4c), the system is reduced to the following sparse linear system of $2(N+1)$ algebraic equations for the constants A_j and B_j,

$$B_0 = 1, \tag{A.1.5a}$$

$$\mathrm{S} A_j - B_{j-1} + (1 + \mathrm{S}) B_j = 0, \quad j = 1, \ldots, N, \tag{A.1.5b}$$

$$A_{j-1} e^{\mathrm{Pe}\,(\xi_j - \xi_{j-1})} + (\mathrm{S} - 1) A_j + \mathrm{S} B_j = 0, \quad j = 1, \ldots, N, \tag{A.1.5c}$$

$$A_N = 0. \tag{A.1.5d}$$

Let (A.1.5) be represented by a sparse matrix M, an unknown vector v and a know vector b, such that

$$Mv = b, \tag{A.1.6}$$

where

$$A = \left(\begin{array}{c|c} P & Q \\ \hline R & T \end{array}\right), \quad v = \left(\begin{array}{c} A_0 \\ \vdots \\ A_N \\ \hline B_0 \\ \vdots \\ B_N \end{array}\right), \quad b = \begin{pmatrix} 1 \\ 0 \\ \vdots \\ 0 \end{pmatrix}, \tag{A.1.7}$$

with

$$P = \begin{pmatrix} 0 & & & \\ & \mathrm{S} & & \\ & & \ddots & \\ & & & \mathrm{S} \end{pmatrix}, Q = \begin{pmatrix} 1 & & & \\ -1 & (1+\mathrm{S}) & & \\ & \ddots & \ddots & \\ & & -1 & (1+\mathrm{S}) \end{pmatrix},$$

$$R = \begin{pmatrix} e^{\mathrm{Pe}(\xi_1-\xi_0)} & (\mathrm{S}-1) & & \\ & \ddots & \ddots & \\ & & e^{\mathrm{Pe}(\xi_N-\xi_{N-1})} & (\mathrm{S}-1) \\ & & & 1 \end{pmatrix}, T = \begin{pmatrix} 0 & \mathrm{S} & & \\ & \ddots & \ddots & \\ & & & \mathrm{S} \\ & & & 0 \end{pmatrix}$$

and blank spaces represent zero entries. Many methods exist for solving (A.1.6), lots of which can exploit the system's sparsity (Higham, 2002). This allows the coefficients A_j and B_j to be found, so when used with (A.1.3) we obtain concentration profiles which are uniformly valid throughout the domain. Chapter 2 will use LU factorisation to produce any figures which involve using the numerics outlined in Appendix A.1.

A.2 Classical approach to homogenization

A classical homogenization approach can be used to investigate the periodic sink problem, which is compared to using a correction to the homogenized solution in Figure 2.2. The approach presented will involve a two-scale separation of a short and long lengthscale, as seen in Bensoussan et al. (1978) and Davit et al. (2013). Let us investigate the distinguished limit where $\mathrm{Pe}_l = p$ and $\mathrm{S} = \varepsilon q$ such that $p, q = \mathcal{O}(1)$ for $\varepsilon \to 0$. Then using $\xi_j = j$ in (2.1.2) gives the governing equations as

$$C_x = (1/p)C_{xx} - \varepsilon q \hat{f}(x) C, \tag{A.2.1a}$$

$$(1 - (1/p)\partial_x)C|_{x=0} = 1 \quad \text{and} \quad C_x|_{x=\varepsilon^{-1}} = 0, \tag{A.2.1b}$$

where $\hat{f}(x) = \sum_{j=1}^{N} \delta(x-j)$. Define a long lengthscale $X = \varepsilon x$ and allow the concentration to have two scale dependence with the short and long lengthscale x and X respectively. By treating x and X as independent variables, then derivatives transform by

$$\frac{\mathrm{d}}{\mathrm{d}x} = \frac{\partial}{\partial x} + \varepsilon \frac{\partial}{\partial X} \quad \text{and} \quad \frac{\mathrm{d}^2}{\mathrm{d}x^2} = \frac{\partial^2}{\partial x^2} + 2\varepsilon \frac{\partial^2}{\partial x \partial X} + \varepsilon^2 \frac{\partial^2}{\partial X^2}.$$

Expand C in powers of ε, i.e.

$$C(x, X) = C^{(0)}(x, X) + \varepsilon C^{(1)}(x, X) + \varepsilon^2 C^{(2)}(x, X) + \ldots,$$

where $C^{(n)}(x, X) = \mathcal{O}(1)$ for $n = 0, 1, 2, \ldots$ as $\varepsilon \to 0$ and allow

$$\mathcal{L}_x = (1/p)\partial_{x^2} - \partial_x \quad \text{and} \quad \mathcal{B}_x = \{(1 - (1/p)\partial_x)(\cdot)|_{X=0}, \partial_x(\cdot)|_{X=1}\}$$

to be a linear and boundary operator respectively, where the subscript here is to differentiate the operators from those in the main text. Now by using (A.2.1) and gathering terms of the same order, we obtain the following:

$$\mathcal{O}(1) \implies \begin{cases} \mathcal{L}_x C^{(0)} = 0 \\ \mathcal{B}_x C^{(0)} = \{1, 0\} \end{cases}, \tag{A.2.2a}$$

$$\mathcal{O}(\varepsilon) \implies \begin{cases} \mathcal{L}_x C^{(1)} = C^{(0)}_X - (2/p) C^{(0)}_{xX} + q\hat{f}(x) C^{(0)} \\ \mathcal{B}_x C^{(1)} = \{(1/p) C^{(0)}_X|_{X=0}, -C^{(0)}_X|_{X=1}\} \end{cases}, \tag{A.2.2b}$$

$$\mathcal{O}(\varepsilon^2) \implies \begin{cases} \mathcal{L}_x C^{(2)} = C^{(1)}_X - (2/p) C^{(1)}_{xX} + q\hat{f}(x) C^{(1)} - (1/p) C^{(0)}_{XX} \\ \mathcal{B}_x C^{(2)} = \{(1/p) C^{(1)}_X|_{X=0}, -C^{(1)}_X|_{X=1}\} \end{cases}, \tag{A.2.2c}$$

$$\vdots$$

Let us seek x-periodic solutions by considering a unit cell with the new coordinates $x' = x - \lfloor x + \frac{1}{2} \rfloor$, i.e. $-1/2 < x' < 1/2$ in each unit cell. By this choice of coordinates, each sink is located at $x' = 0$ for each cell. Also allow $\mathcal{L}_{x'} = \partial_{(x')^2} - p\partial_{x'}$ to be a linear operator in the new coordinates x', then each sub-problem of (A.2.2) can be solved in turn.

At $\mathcal{O}(1)$ we obtain

$$\mathcal{L}_{x'} C^{(0)} = 0, \tag{A.2.3a}$$

$$(C^{(0)} - (1/p) C^{(0)}_{x'})|_{X=0} = 1, \quad C^{(0)}_{x'}|_{X=0} = 0, \tag{A.2.3b}$$

$$[\![C^{(0)}]\!]_{x'=0} = 0, \quad [\![C^{(0)}_{x'}]\!]_{x'=0} = 0, \tag{A.2.3c}$$

$$x' - \text{periodicity of } C^{(0)}. \tag{A.2.3d}$$

From this, we find the leading order solution becomes independent of the short lengthscale with $C^{(0)} = C^{(0)}(X)$, where the boundary condition $C^{(0)}(0) = 1$ needs to be satisfied at the inlet.

At $\mathcal{O}(\varepsilon)$ we obtain

$$\mathcal{L}_{x'} C^{(1)} = C^{(0)}_X - (2/p) C^{(0)}_{x'X}, \tag{A.2.4a}$$

$$(C^{(1)} - (1/p) C^{(1)}_{x'})|_{X=0} = (1/p) C^{(0)}_X|_{X=0}, \quad C^{(1)}_{x'}|_{X=0} = -C^{(0)}_X|_{X=1}, \tag{A.2.4b}$$

$$[\![C^{(1)}]\!]_{x'=0} = 0, \quad [\![C^{(1)}_{x'}]\!]_{x'=0} = pq C^{(0)}|_{x'=0}, \tag{A.2.4c}$$

$$x' - \text{periodicity of } C^{(1)}, \tag{A.2.4d}$$

where terms involving $\hat{f}(x)$ are replace with a jump condition by integrating the differential equation inside a vanishing region about $x' = 0$ and imposing that $C^{(1)}$ is everywhere continuous. Now by performing a spatial average over a unit cell and using the jump conditions and periodicity assumption we obtain the macroscopic equation for the leading-order solution to be

$$C_X^{(0)} + qC^{(0)} = 0. \tag{A.2.5}$$

Solving this, along with the boundary condition $C^{(0)}(0) = 1$, gives the leading-order expression as

$$C^{(0)}(X) = e^{-qX}. \tag{A.2.6}$$

Substituting (A.2.6) into (A.2.4a) and solving yields the general solution to the correction term $C^{(1)}$ as

$$C^{(1)}(x', X) = \begin{cases} A_1(X) + B_1(X)e^{px'} + qx'C^{(0)}(X) & \text{for } -\frac{1}{2} \leq x' \leq 0 \\ A_2(X) + B_2(X)e^{px'} + qx'C^{(0)}(X) & \text{for } 0 \leq x' \leq \frac{1}{2} \end{cases}, \tag{A.2.7}$$

for some functions A_1, B_1, A_2 and B_2. Let $\langle C^{(1)} \rangle$ represent the slowly varying correction of $C(x)$, i.e. $\langle C^{(1)} \rangle = \int_{-1/2}^{1/2} C^{(1)}(x', X)\mathrm{d}x'$. Using this, along with both jump and periodicity conditions, yields

$$C^{(1)}(x', X) = \langle C^{(1)} \rangle + q\left(\frac{1}{p} + \upsilon(x')\right) C^{(0)}, \tag{A.2.8}$$

where $\upsilon(x')$ is the inter-sink corrections on the small scale and is given by

$$\upsilon(x') = \begin{cases} x' + \frac{1}{2} - \frac{1}{2}\mathrm{csch}\left(\frac{p}{2}\right) e^{p(x'+\frac{1}{2})} & \text{for } -\frac{1}{2} \leq x' \leq 0 \\ x' - \frac{1}{2} - \frac{1}{2}\mathrm{csch}\left(\frac{p}{2}\right) e^{p(x'-\frac{1}{2})} & \text{for } 0 \leq x' \leq \frac{1}{2} \end{cases}, \tag{A.2.9}$$

where $\mathrm{csch}(x) = 1/\sinh(x)$ is the hyperbolic cosecant. Note there that by using the $C^{(1)}$ inlet condition we obtain that $\langle C^{(1)} \rangle$ must satisfy

$$\langle C^{(1)} \rangle|_{X=0} = q\left(\frac{1}{2} - \frac{1}{p}\right). \tag{A.2.10}$$

At $\mathcal{O}(\varepsilon^2)$ we obtain

$$\mathcal{L}_{x'}C^{(2)} = C_X^{(1)} - (2/p)C_{x',X}^{(1)} - (1/p)C_{XX}^{(0)}, \tag{A.2.11a}$$

$$(C^{(2)} - (1/p)C_{x'}^{(2)})|_{X=0} = C_X^{(1)}|_{X=0}, \quad C_{x'}^{(2)}|_{X=0} = -C_X^{(1)}|_{X=1}, \tag{A.2.11b}$$

$$[C^{(2)}]_{x'=0} = 0, \quad [C_{x'}^{(2)}]_{x'=0} = pqC^{(1)}|_{x'=0}, \tag{A.2.11c}$$

$$x' - \text{periodicity of } C^{(2)}, \tag{A.2.11d}$$

where we have again replaced terms involving $\hat{f}(x)$ with a jump condition at $x' = 0$. Now by integration over a unit cell, whilst using the continuity, periodicity and jump conditions, (A.2.11a) gives

$$\langle C^{(1)} \rangle_X + q\langle C^{(1)} \rangle = \frac{q^2}{2} \coth\left(\frac{p}{2}\right) C^{(0)}. \tag{A.2.12}$$

Solving this, along with the use of (A.2.10), gives the slowly varying correction $\langle C^{(1)} \rangle$ as

$$\langle C^{(1)} \rangle = q\left[\frac{1}{2} - \frac{1}{p} + \frac{q}{2}\coth\left(\frac{p}{2}\right) X\right] C^{(0)},$$

which in turn gives

$$C^{(1)}(x', X) = q\left[\frac{1}{2} + \frac{q}{2}\coth\left(\frac{p}{2}\right) X + \upsilon(x')\right] C^{(0)}. \tag{A.2.13}$$

Therefore the classical approach approximates the concentration $C(x)$ for a periodic sink arrangement to be

$$C(x) \approx \left(1 + \mathrm{S}\left(\frac{1}{2} + \frac{\mathrm{S}}{2}\coth\left(\frac{\mathrm{Pe}}{2}\right) x + \upsilon(x')\right)\right) e^{-\mathrm{S}x} \tag{A.2.14}$$

where

$$\upsilon(x') = \begin{cases} x' + \frac{1}{2} - \frac{1}{2}\mathrm{csch}\left(\frac{\mathrm{Pe}}{2}\right) e^{\mathrm{Pe}(x'+\frac{1}{2})} & \text{for } -\frac{1}{2} \leq x' \leq 0 \\ x' - \frac{1}{2} - \frac{1}{2}\mathrm{csch}\left(\frac{\mathrm{Pe}}{2}\right) e^{\mathrm{Pe}(x'-\frac{1}{2})} & \text{for } 0 \leq x' \leq \frac{1}{2} \end{cases}$$

and $x' = x - \lfloor x + \frac{1}{2} \rfloor$. A plot of (A.2.14) can be seen in Figure 2.2, where the classic approach is compared to the numerical solution given by solving (A.1.6), the homogenized solution given in (2.2.5) and the combination of the homogenized solution and correction $\widehat{C}_a(x)$ given in (2.2.14). It is shown that the second-order correction for the classical approach includes the micro-scale perturbations on the inter-sink scale as it exhibits the wavy sink-to-sink structure. However, the approximation struggles to deal with the no diffusivity boundary condition at the downstream end due to only using the inlet condition from (A.2.10). This problem arises due to the ad-hoc assumption of two-scale dependence, as this prevents the multiscale structure within the boundary-layer at $x = \varepsilon^{-1}$ being accounted for.

A.3 Leading-order behaviour of the homogenized solution and Green's function

We will now establish expansions of the homogenized solution and Green's function in the limit where $\mathrm{Pe}_l = \mathcal{O}(1)$ and $\mathrm{S} = \mathcal{O}(\varepsilon)$. Define $X = \varepsilon x$, $\mathrm{Pe}_l = p$ and $\mathrm{S} = \varepsilon q$, where $X, p, q = \mathcal{O}(1)$. Note that ϕ can be Taylor expanded for $\varepsilon \ll 1$ to give

$$\phi = \frac{p}{2}\left(1 + \frac{4\varepsilon q}{p}\right)^{\frac{1}{2}} = \frac{p}{2} + \varepsilon q - \frac{\varepsilon^2 q^2}{p} + \mathcal{O}(\varepsilon^3). \tag{A.3.1}$$

So by setting $\alpha = \frac{p}{2\varepsilon}+q$ and using Taylor expansions the we obtain the leading-order expressions

$$e^{\phi x} = e^{\left(\alpha - \frac{\varepsilon q^2}{p}+\mathcal{O}(\varepsilon^2)\right)X} = e^{\alpha X}\left(1 - \frac{\varepsilon q^2}{p}X + \mathcal{O}(\varepsilon^2)\right), \tag{A.3.2a}$$

$$W(x) = 2p^2 e^{\alpha X} + 2\varepsilon pq\,(2 - qX)\,e^{\alpha X} + \mathcal{O}(\varepsilon^2), \tag{A.3.2b}$$

where $W(x)$ is approximated using (2.2.4). Note here that, in order to preserve any boundary-layers which appear in the system, terms involving α are not expanded since they are $\mathcal{O}(1)$ or larger in size. So using (2.2.3) and (2.2.10) we obtain the leading-order expansions of the homogenized solution and Green's function are

$$C_H(x) \approx \left(1 + \frac{\varepsilon q}{p}\left(qX - 1 + e^{(\frac{p}{\varepsilon}+2q)(X-1)}\right)\right)e^{-qX}, \tag{A.3.3}$$

and

$$\begin{aligned} G^-(x,y) &\approx \left(-1 + \frac{\varepsilon q}{p}\left(2 + q(X-Y) - e^{-(\frac{p}{\varepsilon}+2q)X} - e^{(\frac{p}{\varepsilon}+2q)(Y-1)}\right)\right)e^{(\frac{p}{\varepsilon}+q)(X-Y)}, \\ G^+(x,y) &\approx \left(-1 + \frac{\varepsilon q}{p}\left(2 + q(Y-X) - e^{-(\frac{p}{\varepsilon}+2q)Y} - e^{(\frac{p}{\varepsilon}+2q)(X-1)}\right)\right)e^{q(Y-X)}, \end{aligned} \tag{A.3.4}$$

respectively, where $\mathcal{O}(\varepsilon^2)$ terms are neglected. Due to the nature of which terms were expanded, both expansions remain uniformly valid throughout the domain, including within boundary-layers. These expansions are converted back into their original variables using $X = \varepsilon x$, $p = \mathrm{Pe}_l$ and $q = \varepsilon$ S and given in (2.2.5) and (2.2.11) respectively.

A.3.1 Useful calculations involving the product of the homogenized solution and Green's function

Note here that we can obtain a leading-order expressions for the composite term $(GC_H)|_{x,y} = G(x,y)C_H(y)$ as

$$\begin{aligned} (G^-C_H)|_{x,y} &\approx \left(-1 + \frac{\varepsilon q}{p}\left(3 + q(X-2Y) - e^{-(\frac{p}{\varepsilon}+2q)X} - 2e^{(\frac{p}{\varepsilon}+2q)(Y-1)}\right)\right)e^{(\frac{p}{\varepsilon}+q)(X-Y)-qY}, \\ (G^+C_H)|_{x,y} &\approx \left(-1 + \frac{\varepsilon q}{p}\left(3 - qX - e^{-(\frac{p}{\varepsilon}+2q)Y} - e^{(\frac{p}{\varepsilon}+2q)(X-1)} - e^{(\frac{p}{\varepsilon}+2q)(Y-1)}\right)\right)e^{-qX}, \end{aligned} \tag{A.3.5}$$

where $\mathcal{O}(\varepsilon^2)$ terms are neglected and we have used (A.3.3) and (A.3.4). This expansion is converted back into its original variables and stated in the main text in equation (2.3.3). Let us now evaluate the differential and definite integral of $(GC_H)|_{x,y}$ with respect to y. We can calculate the differential as $\frac{\mathrm{d}}{\mathrm{d}y}(GC_H)|_{x,y} = \varepsilon\frac{\mathrm{d}}{\mathrm{d}Y}(GC_H)|_{x,y}$, which gives

$$\begin{aligned} (G^-C_H)_y|_{x,y} &\approx \left(p - \varepsilon q\left(1 + q(X-2Y) - e^{-(\frac{p}{\varepsilon}+2q)X}\right)\right)e^{(\frac{p}{\varepsilon}+q)(X-Y)-qY}, \\ (G^+C_H)_y|_{x,y} &\approx \varepsilon q\left(e^{-(\frac{p}{\varepsilon}+2q)Y} - e^{(\frac{p}{\varepsilon}+2q)(Y-1)}\right)e^{-qX}. \end{aligned} \tag{A.3.6}$$

By noting that $\int_0^y (GC_H)|_{x,y}\mathrm{d}y = \varepsilon^{-1}\int_0^Y (GC_H)|_{x,y}\mathrm{d}Y$ we can integrate the expressions given in (A.3.5) explicitly using integration by parts when required to obtain

$$\begin{aligned}\int_0^y (G^- C_H)|_{x,y}\,\mathrm{d}y &= \frac{1}{p}\left(1 - 2qYe^{(\frac{p}{\varepsilon}+2q)(Y-1)}\right)e^{(\frac{p}{\varepsilon}+q)(X-Y)-qY},\\ \int_0^y (G^+ C_H)|_{x,y}\,\mathrm{d}y &= \left(-1 + \frac{\varepsilon q}{p}\left(3 - qX - e^{(\frac{p}{\varepsilon}+2q)(X-1)}\right)\right)\left(\frac{Y}{\varepsilon}\right)e^{-qX} + \mathcal{O}(\varepsilon^2),\end{aligned} \tag{A.3.7}$$

where the Taylor expansion

$$\left(\frac{p}{\varepsilon} + 2q\right)^{-1} = \frac{\varepsilon}{p} - \frac{2\varepsilon^2 q}{p^2} + \mathcal{O}(\varepsilon^3) \tag{A.3.8}$$

is used.

We can also obtain the leading-order expression for the square of $(GC_H)|_{x,y}$ to be

$$\begin{aligned}(G^- C_H)^2|_{x,y} &= \left(1 - \frac{2\varepsilon q}{p}\left(3 + q(X-2Y) - e^{-(\frac{p}{\varepsilon}+2q)X} - 2e^{(\frac{p}{\varepsilon}+2q)(Y-1)}\right)\right)e^{2(\frac{p}{\varepsilon}+q)(X-Y)-2qY},\\ (G^+ C_H)^2|_{x,y} &= \left(1 - \frac{2\varepsilon q}{p}\left(3 - qX - e^{-(\frac{p}{\varepsilon}+2q)Y} - e^{(\frac{p}{\varepsilon}+2q)(X-1)} - e^{(\frac{p}{\varepsilon}+q)(Y-1)}\right)\right)e^{-2qX},\end{aligned} \tag{A.3.9}$$

where $\mathcal{O}(\varepsilon^2)$ terms are neglected. This can be integrated to give

$$\begin{aligned}\int_0^y (G^- C_H)^2|_{x,y}\,\mathrm{d}y &= -\frac{1}{2p}e^{2(\frac{p}{\varepsilon}+q)(X-Y)-2qY},\\ \int_0^y (G^+ C_H)^2|_{x,y}\,\mathrm{d}y &= \left(\varepsilon^{-1} - \frac{2q}{p}\left(3 - qX - e^{(\frac{p}{\varepsilon}+2q)(X-1)}\right)\right)Ye^{-2qX}.\end{aligned} \tag{A.3.10}$$

A.4 Calculation of the covariance for normally-perturbed sink locations

We will now calculate an expression for the covariance $K(\widehat{C}_b(x_1), \widehat{C}_b(x_2))$. As σ is small, we can assume sink locations are independently and identically distributed (i.i.d) as sinks do not trade places. Therefore

$$\mathbb{E}[\widehat{\xi}_j\widehat{\xi}_l] = \mathbb{E}[\widehat{\xi}_j]\mathbb{E}[\widehat{\xi}_l], \quad \text{where } j \neq l. \tag{A.4.1}$$

This gives the covariance of $\widehat{\xi}_j$ and $\widehat{\xi}_l$ as

$$K(\widehat{\xi}_j, \widehat{\xi}_l) = \mathbb{E}[\widehat{\xi}_j\widehat{\xi}_l] - \mathbb{E}[\widehat{\xi}_j]\mathbb{E}[\widehat{\xi}_l] = \delta_{j,l}. \tag{A.4.2}$$

By (2.3.8), the expectation of $\widehat{C}_b(x)$ and $\widehat{C}_b(x_1)\widehat{C}_b(x_2)$ is given by

$$\mathbb{E}[\widehat{C}_b(x)] \approx \mathrm{S}\left(\sigma\sum_{j\neq k}(GC_H)|_{x,j}\mathbb{E}\left[\widehat{\xi}_j\right] + \mathbb{E}\left[[(GC_H)|_{x,y}]_{y=k}^{k+\sigma\widehat{\xi}_k}\right]\right) = \mathrm{S}\mathbb{E}\left[[(GC_H)|_{x,y}]_{y=k}^{k+\sigma\widehat{\xi}_k}\right] \tag{A.4.3}$$

and

$$\mathbb{E}[\widehat{C}_b(x_1)\widehat{C}_b(x_2)] \approx \mathbb{E}\Bigg[\mathrm{S}^2\left(\sigma\sum_{j\neq k_1}(GC_H)_y|_{x_1,j}\widehat{\xi}_j + [(GC_H)|_{x_1,y}]_{y=k_1}^{k_1+\sigma\widehat{\xi}_{k_1}}\right)\times \left(\sigma\sum_{l\neq k_2}(GC_H)_y|_{x_2,l}\widehat{\xi}_l + [(GC_H)|_{x_2,y}]_{y=k_2}^{k_2+\sigma\widehat{\xi}_{k_2}}\right)\Bigg] \tag{A.4.4}$$

respectively, where $\mathcal{O}(\sigma^2)$ terms are neglected. By expanding terms in (A.4.4), it can be seen that

$$\mathbb{E}[\widehat{C}_b(x_1)\widehat{C}_b(x_2)] \approx \mathrm{S}^2\left(\varphi_1(x_1,x_2)+\varphi_2(x_1,x_2)+\varphi_3(x_1,x_2)+\varphi_4(x_1,x_2)\right), \tag{A.4.5}$$

where

$$\begin{aligned}
\varphi_1(x_1,x_2) &= \Bigg\{\sigma^2\sum_{j\neq k_1}\sum_{l\neq k_2}(GC_H)_y|_{x_1,j}(GC_H)_y|_{x_2,l}\mathbb{E}\left[\widehat{\xi}_j\widehat{\xi}_l\right],\\
\varphi_2(x_1,x_2) &= \sigma\sum_{j\neq k_1}(GC_H)_y|_{x_1,j}\mathbb{E}\left[\widehat{\xi}_j[(GC_H)|_{x_2,y}]_{y=k_2}^{k_2+\sigma\widehat{\xi}_{k_2}}\right],\\
\varphi_3(x_1,x_2) &= \sigma\sum_{l\neq k_2}(GC_H)_y|_{x_2,l}\mathbb{E}\left[\widehat{\xi}_l[(GC_H)|_{x_1,y}]_{y=k_1}^{k_1+\sigma\widehat{\xi}_{k_1}}\right],\\
\varphi_4(x_1,x_2) &= \mathbb{E}\left[[(GC_H)|_{x_1,y}]_{y=k_1}^{k_1+\sigma\widehat{\xi}_{k_1}}[(GC_H)|_{x_2,y}]_{y=k_2}^{k_2+\sigma\widehat{\xi}_{k_2}}\right].
\end{aligned}$$

We will now evaluate each φ_i separately. As $\mathbb{E}[\widehat{\xi}_j\widehat{\xi}_l] = \mathbb{E}[\widehat{\xi}_j]\mathbb{E}[\widehat{\xi}_l] = 0$ when $j \neq l$, then $\varphi_1(x_1,x_2)$ becomes

$$\varphi_1(x_1,x_2) = \sigma^2\sum_{j\notin\{k_1,k_2\}}(GC_H)_y|_{x_1,j}(GC_H)_y|_{x_2,j}.$$

Also by noting

$$\mathbb{E}\left[\widehat{\xi}_j[(GC_H)|_{x_2,y}]_{y=k_2}^{k_2+\sigma\widehat{\xi}_{k_2}}\right] = \mathbb{E}\left[\widehat{\xi}_j\right]\mathbb{E}\left[[(GC_H)|_{x_2,y}]_{y=k_2}^{k_2+\sigma\widehat{\xi}_{k_2}}\right] = 0 \quad \text{if } j\neq k_2,$$

it can be seen that

$$\varphi_2(x_1,x_2) = \begin{cases}\sigma(GC_H)_y|_{x_1,k_2}\mathbb{E}\left[\widehat{\xi}_{k_2}[(GC_H)|_{x_2,y}]_{y=k_2}^{k_2+\sigma\widehat{\xi}_{k_2}}\right] & \text{if } k_1\neq k_2\\ 0 & \text{if } k_1 = k_2\end{cases}. \tag{A.4.6}$$

Similarly,

$$\varphi_3(x_1,x_2) = \begin{cases}\sigma(GC_H)_y|_{x_2,k_1}\mathbb{E}\left[\widehat{\xi}_{k_1}[(GC_H)|_{x_1,y}]_{y=k_1}^{k_1+\sigma\widehat{\xi}_{k_1}}\right] & \text{if } k_1\neq k_2\\ 0 & \text{if } k_1 = k_2\end{cases}. \tag{A.4.7}$$

We can also evaluate $\varphi_4(x_1, x_2)$ by considering different cases of k_1 and k_2 to obtain

$$\varphi_4(x_1,x_2) = \begin{cases} \mathbb{E}[\widehat{C}_b(x_1)]\mathbb{E}[\widehat{C}_b(x_2)] & \text{if } k_1 \neq k_2 \\ \mathbb{E}\left[[(GC_H)|_{x_1,y}]_{y=k}^{k+\sigma\widehat{\xi}_k}[(GC_H)|_{x_2,y}]_{y=k}^{k+\sigma\widehat{\xi}_k}\right] & \text{if } k \equiv k_1 = k_2 \end{cases}. \tag{A.4.8}$$

All φ_i can then be combined to give the covariance as

$$K(\widehat{C}_b(x_1),\widehat{C}_b(x_2)) = \begin{cases} \mathrm{S}^2\Big\{\sigma^2 \sum_{j\notin\{k_1,k_2\}}(GC_H)_y|_{x_1,j}(GC_H)_y|_{x_2,j} \\ \quad +\sigma(GC_H)_y|_{x_1,k_2}\mathbb{E}\left[\widehat{\xi}_{k_2}[(GC_H)|_{x_2,y}]_{y=k_2}^{k_2+\sigma\widehat{\xi}_{k_2}}\right] \\ \quad +\sigma(GC_H)_y|_{x_2,k_1}\mathbb{E}\left[\widehat{\xi}_{k_1}[(GC_H)|_{x_1,y}]_{y=k_1}^{k_1+\sigma\widehat{\xi}_{k_1}}\right]\Big\} & \text{if } k_1 \neq k_2 \\ \mathrm{S}^2\Big\{\sigma^2 \sum_{j\neq k}(GC_H)_y|_{x_1,j}(GC_H)_y|_{x_2,j} \\ \quad +\mathbb{E}\left[[(GC_H)|_{x_1,y}]_{y=k}^{k+\sigma\widehat{\xi}_k}[(GC_H)|_{x_2,y}]_{y=k}^{k+\sigma\widehat{\xi}_k}\right] \\ \quad -\mathbb{E}\left[[(GC_H)|_{x_1,y}]_{y=k}^{k+\sigma\widehat{\xi}_k}\right]\mathbb{E}\left[[(GC_H)|_{x_2,y}]_{y=k}^{k+\sigma\widehat{\xi}_k}\right]\Big\} & \text{if } k \equiv k_1 = k_2 \end{cases}.$$

A.5 Tracking the cumulative distribution function in the limit of advection-dominated transport

Consider the advection-dominated case where the concentration $C(x;\omega)$ for $x \in [0,1]$ is given by

$$C_x + \mathrm{S}(1+\hat{g}(x;\omega))C = 0 \tag{A.5.1}$$

and $\hat{g}(x;\omega)$ is a random function. Note the ω notation denotes that the function is a realisation drawn from a prescribed distribution, which in turn makes the concentration a random variable. For convenience, define

$$h(x) = \int_0^x \hat{g}(x;\omega)\,\mathrm{d}x. \tag{A.5.2}$$

Then by using an integrating factor obtain the exact solution of (A.5.1) to be

$$C(x;\omega) = \exp\left[-\mathrm{S}(x+h(x))\right]. \tag{A.5.3}$$

We will now consider tracking the cumulative distribution function (cdf) of the solute concentration. Define $\pi_C(\gamma, x)$ as the probability distribution function (pdf) of the concentration,

$F_C(\gamma, x) = \int_0^\gamma \pi_C(\mathcal{C}, x)\,\mathrm{d}\mathcal{C}$ as the cdf of the concentration and $\Pi(C, \gamma; x) = H(C - \gamma)$ (where H represents the Heaviside function). Then we can obtain the expectation of Π as

$$\mathbb{E}[\Pi(C, \gamma; x)] = \int_0^\infty H(\mathcal{C} - \gamma)\pi_C(\mathcal{C}, x)\,\mathrm{d}\mathcal{C} = 1 - F_C(\gamma, x). \tag{A.5.4}$$

By using the boundary condition $C(x = 0) = 1$ we obtain the relation

$$\mathbb{E}[\Pi(1, \gamma; 0)] = H(1 - \gamma) = 1 - F_C(\gamma, 0)$$

which gives

$$F_C(\gamma, 0) = H(\gamma - 1). \tag{A.5.5}$$

Consider multiplying the transport equation (A.5.1) by Π_γ, where subscript is used to notate partial differentiation. This gives

$$\frac{\partial \Pi}{\partial \gamma}\frac{\partial C}{\partial x} = -\mathrm{S}(1 + \hat{g})C\frac{\partial \Pi}{\partial \gamma}. \tag{A.5.6}$$

But we know $\Pi_x = \Pi_C C_x = -\Pi_\gamma C_x$ and $C\Pi_\gamma = -C\delta(C - \gamma) = -\gamma\delta(C - \gamma) = \gamma\Pi_\gamma$, therefore

$$\frac{\partial \Pi}{\partial x} = \mathrm{S}(1 + \hat{g})\gamma\frac{\partial \Pi}{\partial \gamma}. \tag{A.5.7}$$

The expression in (A.5.7) will only remain valid on a two-dimensional domain, where γ takes any potential concentration (i.e. $\gamma \in [0, \infty]$) and x remains within the domain (i.e. $x \in [0, 1]$). Set $\Pi(C, \gamma; x) = \mathbb{E}[\Pi(C, \gamma; x)] + \hat{\Pi}(C, \gamma; x)$, where $\mathbb{E}[\hat{\Pi}(C, \gamma; x)] = 0$, then using (A.5.4) with (A.5.7) gives

$$\frac{\partial \hat{\Pi}}{\partial x} - \mathrm{S}(1 + \hat{g})\gamma\frac{\partial \hat{\Pi}}{\partial \gamma} = \frac{\partial F_C}{\partial x} - \mathrm{S}(1 + \hat{g})\gamma\frac{\partial F_C}{\partial \gamma}. \tag{A.5.8}$$

Taking the expectation of (A.5.8) gives

$$\frac{\partial F_C}{\partial x} - \mathrm{S}\gamma\frac{\partial F_C}{\partial \gamma} = -\mathrm{S}Q(x, \gamma) \quad \text{where } Q(x, \gamma) = \mathbb{E}\left[\gamma\hat{g}\frac{\partial \hat{\Pi}}{\partial \gamma}\right], \tag{A.5.9}$$

which can be substituted back into (A.5.8) to give

$$\frac{\partial \hat{\Pi}}{\partial x} - \mathrm{S}(1 + \hat{g})\gamma\frac{\partial \hat{\Pi}}{\partial \gamma} = -\mathrm{S}\gamma\left(\hat{g}\frac{\partial F_C}{\partial \gamma} + Q(x, \gamma)\right). \tag{A.5.10}$$

We will now use the substitution $\mu = \log\gamma$, meaning (A.5.9) and (A.5.10) give

$$\frac{\partial F_C}{\partial x} - \mathrm{S}\frac{\partial F_C}{\partial \mu} = -\mathrm{S}Q(x, \mu), \quad \text{where } Q(x, \mu) = \mathbb{E}\left[\hat{g}\frac{\partial \hat{\Pi}}{\partial \mu}\right] \tag{A.5.11a}$$

and

$$\frac{\partial \hat{\Pi}}{\partial x} - \mathrm{S}(1 + \hat{g})\frac{\partial \hat{\Pi}}{\partial \mu} = -\mathrm{S}\left(\hat{g}\frac{\partial F_C}{\partial \mu} + Q(x, \mu)\right) \tag{A.5.11b}$$

respectively. If we use the change of variables

$$x \to x + \frac{\eta}{\mathrm{S}} \quad \text{and} \quad \mu \to \eta$$

then (A.5.11) can be reformulated along (deterministic) characteristics to give

$$\frac{\partial F_C}{\partial x} = -\mathrm{S}Q(x,\eta) \quad \text{where } Q(x,\eta) = \mathbb{E}\left[\hat{g}\frac{\partial \hat{\Pi}}{\partial \eta}\right] \tag{A.5.12a}$$

and

$$\frac{\partial \hat{\Pi}}{\partial x} - \mathrm{S}\hat{g}\frac{\partial \hat{\Pi}}{\partial \eta} = -\mathrm{S}\left(\hat{g}\frac{\partial F_C}{\partial \eta} + Q(x,\eta)\right). \tag{A.5.12b}$$

As in Boso et al. (2014) let us discard the $\hat{g}\hat{\Pi}_\eta$ term due to being quadratic in random quantities. So noting that $\hat{\Pi}(0,\eta) = 0$ then (A.5.12b) gives

$$\hat{\Pi}(x,\eta) = -\mathrm{S}\int_0^x \hat{g}(x')\frac{\partial F_C(x',\eta)}{\partial \eta} + Q(x',\eta)\,\mathrm{d}x'. \tag{A.5.13}$$

Applying $\hat{g}(x)\partial_\eta$ to both sides and taking the expectation yields

$$Q(x,\eta) = -\mathrm{S}\int_0^x \mathcal{K}_{\hat{g}}[x,x']\frac{\partial^2 F_C(x',\eta)}{\partial \eta^2}\,\mathrm{d}x', \tag{A.5.14}$$

where $\mathcal{K}_{\hat{g}}[x,x'] = \mathcal{K}[\hat{g}(x;\omega),\hat{g}(x';\omega)]$ is the covariance of the sink function $\hat{g}(x;\omega)$. Substituting this into (A.5.12a) gives

$$\frac{\partial F_C}{\partial x} = \mathrm{S}^2\int_0^x \mathcal{K}_{\hat{g}}[x,x']\frac{\partial^2 F_C(x',\eta)}{\partial \eta^2}\,\mathrm{d}x'. \tag{A.5.15}$$

So by restoring the μ dependence using $x \to x - \mu/\mathrm{S}$, $\eta \to \mu$ we obtain

$$\frac{\partial F_C}{\partial x} - \mathrm{S}\frac{\partial F_C}{\partial \mu} = \mathrm{S}^2\int_0^x \mathcal{K}_{\hat{g}}[x,x']\frac{\partial^2 F_C(x',\mu)}{\partial \mu^2}\,\mathrm{d}x', \tag{A.5.16}$$

where $F_C(x,\mu_L) = 0$, $F_C(x,\mu_R) = 1$ and $F_C(0,\mu) = H(\exp(\mu) - 1) = H(\mu)$. By solving the partial differential equation (PDE) given in (A.5.16) we can find the cdf of the concentration given by $F_C(\gamma,x)$.

In Boso et al. (2014) they consider the case where F_C varies over a lengthscale longer than the correlation length of the covariance function $\mathcal{K}_{\hat{g}}$. For this case we can write $\int_0^x \mathcal{K}_{\hat{g}}[x,x']\,\mathrm{d}x' \approx a \in \mathbb{R}$ and obtain

$$\frac{\partial F_C}{\partial x} - \mathrm{S}\frac{\partial F_C}{\partial \mu} \approx \mathrm{S}^2\frac{\partial^2 F_C(x,\mu)}{\partial \mu^2}\int_0^x \mathcal{K}_{\hat{g}}[x,x']\,\mathrm{d}x' = \mathrm{S}^2 a\frac{\partial^2 F_C(x,\mu)}{\partial \mu^2}. \tag{A.5.17}$$

We can solve (A.5.17) exactly to give

$$F_C(x,\mu) = \frac{1}{2}\left(1 + \operatorname{erf}\left(\frac{\mathrm{S}x + \mu}{2\mathrm{S}\sqrt{ax}}\right)\right). \tag{A.5.18}$$

However, in general $\int_0^x \mathcal{K}_{\hat{g}}[x,x']\,\mathrm{d}x'$ is not constant and the correlation length of the covariance function isn't asymptotically small. Therefore we require solving the full PDE given in (A.5.16) to track the concentration cdf for different values of x, though this is beyond the scope of this thesis.

Appendix B

Chapter 3 and 4 appendices

B.1 Exact Green's function in one dimension

The exact Green's function in one dimension can be calculated similar to in Chapter 2. Let $G(x_1, x_1')$ be the exact Green's function associated with the linear operator $\mathcal{L} = (\partial_{x_1})^2 - \mathrm{Pe}_L\,\partial_{x_1} - \mathrm{Da}$ under homogeneous boundary conditions such that

$$\mathcal{L}G = \delta(x_1 - x_1') \quad \text{and} \quad \mathcal{B}_1 G = \{0, 0\}, \tag{B.1.1}$$

where δ is the Dirac-delta function and $\mathcal{B}_1 = \{(1 - (1/\mathrm{Pe}_L)\partial_{x_1})(\cdot)|_{x_1=0}, \partial_{x_1}(\cdot)|_{x_1=1}\}$. The Green's function is a piecewise smooth and continuous function which satisfies the jump condition $[G_{x_1}]_{x_1'^-}^{x_1'^+} = 1$, which accounts for a point sink being located at $x_1 = x_1'$. This jump condition can be seen by integrating (B.1.1) inside a vanishing region about $x_1 = x_1'$ and using the fact that $G(x_1, x_1')$ is continuous. Define $G^-(x_1, x_1')$ and $G^+(x_1, x_1')$ such that

$$G(x_1, x_1') = \begin{cases} G^-(x_1, x_1') & \text{if } 0 \le x_1 \le x_1' \le 1 \\ G^+(x_1, x_1') & \text{if } 0 \le x_1' \le x_1 \le 1 \end{cases}.$$

Then by solving (B.1.1) we see that the two pieces of the Green's function are given by

$$\begin{aligned} G^-(x_1,x_1') &= -\left(\frac{1}{4\phi\psi(1)}\right)e^{\frac{\mathrm{Pe}_L}{2}(x_1-x_1')}\Bigg((2\phi+\mathrm{Pe}_L)^2e^{\phi(x_1-x_1'+1)} \\ &\qquad + (2\phi-\mathrm{Pe}_L)^2e^{-\phi(x_1-x_1'+1)} + 4\,\mathrm{Da}\left(e^{\phi(x_1+x_1'-1)}+e^{-\phi(x_1+x_1'-1)}\right)\Bigg), \\ G^+(x_1,x_1') &= -\left(\frac{1}{4\phi\psi(1)}\right)e^{\frac{\mathrm{Pe}_L}{2}(x_1-x_1')}\Bigg((2\phi+\mathrm{Pe}_L)^2e^{\phi(x_1'-x_1+1)} \\ &\qquad + (2\phi-\mathrm{Pe}_L)^2e^{-\phi(x_1'-x_1+1)} + 4\,\mathrm{Da}\left(e^{\phi(x_1+x_1'-1)}+e^{-\phi(x_1+x_1'-1)}\right)\Bigg). \end{aligned} \tag{B.1.2}$$

If we consider the limit where $\mathrm{Pe}_L^2 \gg \mathrm{Da}$ and are careful when expanding exponential terms we obtain

$$\begin{aligned} \phi &\approx \frac{\mathrm{Pe}_L}{2}+\frac{\mathrm{Da}}{\mathrm{Pe}_L}-\frac{\mathrm{Da}^2}{\mathrm{Pe}_L^3} \\ \exp(\phi x_1) &\approx \left(1-\frac{\mathrm{Da}^2}{\mathrm{Pe}_L^3}x_1\right)\exp\left(\left(\frac{\mathrm{Pe}_L}{2}+\frac{\mathrm{Da}}{\mathrm{Pe}_L}\right)x_1\right), \\ \exp(-\phi x_1) &\approx \left(1+\frac{\mathrm{Da}^2}{\mathrm{Pe}_L^3}x_1\right)\exp\left(-\left(\frac{\mathrm{Pe}_L}{2}+\frac{\mathrm{Da}}{\mathrm{Pe}_L}\right)x_1\right), \\ \psi(x_1) &\approx 2\,\mathrm{Pe}_L^2\left(1+\frac{\mathrm{Da}}{\mathrm{Pe}_L^2}\left(2-\frac{\mathrm{Da}}{\mathrm{Pe}_L}x_1\right)\right)\exp\left(\left(\frac{\mathrm{Pe}_L}{2}+\frac{\mathrm{Da}}{\mathrm{Pe}_L}\right)x_1\right). \end{aligned}$$

So in a similar fashion to Chapter 2 we obtain

$$\begin{aligned} \widetilde{G}^-(x_1,x_1') \approx &-\frac{1}{\mathrm{Pe}_L}\exp\left(\left(\mathrm{Pe}_L+\frac{\mathrm{Da}}{\mathrm{Pe}_L}\right)(x_1-x_1')\right) \\ &+\frac{\mathrm{Da}}{\mathrm{Pe}_L^3}\Bigg(\left(2+\frac{\mathrm{Da}}{\mathrm{Pe}_L}(x_1-x_1')\right)\exp\left(\left(\mathrm{Pe}_L+\frac{\mathrm{Da}}{\mathrm{Pe}_L}\right)(x_1-x_1')\right) \\ &-\exp\left(\mathrm{Pe}_L(x_1-1)+\frac{\mathrm{Da}}{\mathrm{Pe}_L}(x_1+x_1'-2)\right)-\exp\left(-\mathrm{Pe}_L\,x_1'-\frac{\mathrm{Da}}{\mathrm{Pe}_L}(x_1+x_1')\right)\Bigg), \\ \widetilde{G}^+(x_1,x_1') \approx &-\frac{1}{\mathrm{Pe}_L}\exp\left(\frac{\mathrm{Da}}{\mathrm{Pe}_L}(x_1'-x_1)\right) \\ &+\frac{\mathrm{Da}}{\mathrm{Pe}_L^3}\Bigg(\left(2+\frac{\mathrm{Da}}{\mathrm{Pe}_L}(x_1'-x_1)\right)\exp\left(\frac{\mathrm{Da}}{\mathrm{Pe}_L}(x_1'-x_1)\right) \\ &-\exp\left(\mathrm{Pe}_L(x_1-1)+\frac{\mathrm{Da}}{\mathrm{Pe}_L}(x_1+x_1'-2)\right)-\exp\left(-\mathrm{Pe}_L\,x_1'-\frac{\mathrm{Da}}{\mathrm{Pe}_L}(x_1+x_1')\right)\Bigg). \end{aligned} \tag{B.1.3}$$

From the first term in G^- (G^+) we see a boundary layer of width approximately $1/\,\mathrm{Pe}$ ($\mathrm{Da}\,/\,\mathrm{Pe}$) exists upstream (downstream) of $x_1 = x_1'$. The final two terms in G^- and G^+ account for the boundary conditions, which gives a boundary layer of width approximately $1/\,\mathrm{Pe}$ at the x_1-outlet and x_1'-inlet.

B.2 Finite-difference scheme

B.2.1 One dimension

In one dimension let x_1, $C(x_1;\omega)$ and $\hat{g}(x_1;\omega)$ be represented by vectors of dimension $K+1$, where $x_1 = x_1^i$, $C(x_1^i;\omega) = C^i$ and $\hat{g}(x_1^i;\omega) = \hat{g}^i$ for $i = 1,\ldots,K+1$ and $K \in \mathbb{Z}$. By setting $h = 1/K$ to be the interval width, a second order finite-different scheme can be used with (3.1.2) to give

$$(2\,\mathrm{Pe}_L\,h+3)C^1 - 4C^2 + C^3 = 2\,\mathrm{Pe}_L\,h, \tag{B.2.1}$$

$$(1+\mathrm{Pe}_L\,h/2)C^{i-1} - (2+\mathrm{Da}\,h^2(1+\hat{g}^i))C^i + (1-\mathrm{Pe}_L\,h/2)C^{i+1} = 0 \quad \text{and} \tag{B.2.2}$$

$$C^{K-1} - 4C^K + 3C^{K+1} = 0, \tag{B.2.3}$$

where $i = 2,\ldots,K$. Here, a mixture of second-order forward, central and backward difference schemes are used to calculate differentials. Chapter 3 and 4 will use LU factorisation to produce any figures which involve using this finite difference scheme.

B.2.2 Two dimensions

In two dimensions we consider a semi-infinite-domain $\mathcal{D}_2 = [0,1]\times(-\infty,\infty)$. In order to apply a finite-difference scheme, consider instead the reduced domain $\mathcal{D}_2^r = [0,1]\times(-L_r,L_r)$. Represent x_1, x_2, $C(x_1,x_2;\omega)$ and $\hat{g}(x_1,x_2;\omega)$ by $x_1 = x_1^i$, , x_2^j $C(x_1^i,x_2^j;\omega) = C^{i,j}$ and $\hat{g}(x_1^i,x_2^j;\omega) = \hat{g}^{i,j}$ for $i = 1,\ldots,K_1+1$, $j = 1,\ldots,K_2+1$ and $K_1,K_2 \in \mathbb{Z}$. By setting $h = 1/K_1 = 2L_r/K_2$ as the interval width a second order finite-different scheme can be used with (3.1.2) to give

$$(2\,\mathrm{Pe}_L\,h+3)C^{1,j} - 4C^{2,j} + C^{3,j} = 2\,\mathrm{Pe}_L\,h, \tag{B.2.4}$$

$$C^{K_1-1,j} - 4C^{K_1,j} + 3C^{K_1+1,j} = 0 \tag{B.2.5}$$

$$-3C^{i,1} + 4C^{i,2} - C^{i,3} = 0 \tag{B.2.6}$$

$$C^{i,K_2-1} - 4C^{i,K_2} + 3C^{i,K_2+1} = 0 \tag{B.2.7}$$

$$(2+\mathrm{Pe}_L\,h)C^{i-1,j} + 2C^{i,j-1} - (8+2h^2\,\mathrm{Da}(1+\hat{g}^{i,j}))C^{i,j} + 2C^{i,j+1} + (2-\mathrm{Pe}_L\,h)C^{i+1,j} = 0 \tag{B.2.8}$$

where (B.2.4) and (B.2.5) use $j = 1,\ldots,K_2+1$, (B.2.6) and (B.2.7) use $i = 2,\ldots,K_1$ and (B.2.8) uses $i = 2,\ldots,K_1$ and $j = 2,\ldots,K_2$. As for the one-dimensional solver we have used a mixture of second-order forward, central and backward difference schemes to calculate differentials of x_1 and x_2. Chapter 3 and 4 will use LU factorisation to produce any figures which involve using this finite difference scheme. Sparsity of matrices are exploited by storing matrices using the MATLAB sparse function with vector triplets.

B.3 Integral solver

When solving integrals in n dimensions, the integral solver given in Hosea (2021) is used. This allows one-, two-, three-, four-, five- and six-dimensional functions to be integrated using the INTEGRAL, INTEGRAL2 and INTEGRAL3 adaptive quadrature functions in MATLAB. When integrating with infinite limits, these limits are instead replaced with suitably high values which allow the integral to converge.

B.4 Evaluating useful integrals

Here, we will solve integrals analytically which are used throughout the chapter. Firstly, consider solving

$$\int_{x^-}^{x^+} \exp\left(-ax^2 - bx + c\right) \mathrm{d}x$$

where $a, b, c, x^-, x^+ \in \mathbb{R}$. By completing the square of the quadratic in the exponential we obtain

$$\int_{x^-}^{x^+} \exp\left(-ax^2 - bx + c\right) \mathrm{d}x = \exp\left(\frac{b^2}{4a} + c\right) \int_{x^-}^{x^+} \exp\left(-a\left(x + \frac{b}{2}\right)^2\right) \mathrm{d}x.$$

The error function (also known as the Gauss error function) is defined to be

$$\mathrm{erf}(x) = \frac{2}{\sqrt{\pi}} \int_0^x \exp\left(-t^2\right) \mathrm{d}t,$$

so by using the substitution $u = \sqrt{a}(x + b/(2a))$ we obtain

$$\int_{x^-}^{x^+} \exp\left(-ax^2 - bx + c\right) \mathrm{d}x = \frac{1}{2}\sqrt{\frac{\pi}{a}} \exp\left(\frac{b^2}{4a} + c\right) \left(\mathrm{erf}\left(\sqrt{a}x^+ + \frac{b}{2\sqrt{a}}\right) - \mathrm{erf}\left(\sqrt{a}x^- + \frac{b}{2\sqrt{a}}\right)\right). \tag{B.4.1}$$

In the limit $b, c \to 0$ the integral in (B.4.1) converges to

$$\int_{x^-}^{x^+} \exp\left(-ax^2 - bx + c\right) \mathrm{d}x \to \frac{1}{2}\sqrt{\frac{\pi}{a}} \left(\mathrm{erf}\left(\sqrt{a}x^+\right) - \mathrm{erf}\left(\sqrt{a}x^-\right)\right). \tag{B.4.2}$$

Next, we will consider the integral

$$\int_{x^-}^{x^+} x \exp\left(-ax^2\right) \mathrm{d}x$$

where $a, x^-, x^+ \in \mathbb{R}$. To solve this integral, we should first note that $\mathrm{d}/\mathrm{d}x(\exp(-ax^2)) = -2ax\exp(-ax^2)$. Therefore the integral can be solved to give

$$\int_{x^-}^{x^+} x \exp\left(-ax^2\right) \mathrm{d}x = -\frac{1}{2a}\left(\exp\left(-a(x^+)^2\right) - \exp\left(-a(x^-)^2\right)\right). \tag{B.4.3}$$

For $x^- = 0$ and $x^+ \to \infty$ we obtain

$$\int_0^\infty x \exp\left(-ax^2\right) \mathrm{d}x = \frac{1}{2a}. \tag{B.4.4}$$

For the next integral we will combine the previous two integrals using integration by parts to obtain

$$\begin{aligned}\int_{x^-}^{x^+} x^2 \exp\left(-ax^2\right) \mathrm{d}x &= \left[-\frac{1}{2a} x \exp\left(-ax^2\right)\right]_{x^-}^{x^+} + \frac{1}{2a}\int_{x^-}^{x^+} \exp\left(-ax^2\right) \mathrm{d}x \\ &= \frac{1}{4a}\sqrt{\frac{\pi}{a}}\left(\operatorname{erf}\left(\sqrt{a}x^+\right) - \operatorname{erf}\left(\sqrt{a}x^-\right)\right) \\ &\quad - \frac{1}{2a}\left(x^+ \exp\left(-a(x^+)^2\right) - x^- \exp\left(-a(x^-)^2\right)\right),\end{aligned} \tag{B.4.5}$$

where $a, x^-, x^+ \in \mathbb{R}$. Finally, let us consider solving

$$\int_{x^-}^{x^+} x \log(bx) \exp\left(-ax^2\right) \mathrm{d}x$$

where $a, b, x^-, x^+ \in \mathbb{R}$. By using the substitution $\hat{x} = \sqrt{a}x$ we obtain

$$\int_{x^-}^{x^+} x \log(bx) \exp\left(-ax^2\right) \mathrm{d}x = \frac{1}{a}\int_{\hat{x}^-}^{\hat{x}^+} \hat{x} \log(\hat{x}) \exp\left(-\hat{x}^2\right) \mathrm{d}\hat{x} + \frac{1}{a}\log\left(\frac{b}{\sqrt{a}}\right)\int_{\hat{x}^-}^{\hat{x}^+} \hat{x} \exp\left(-\hat{x}^2\right) \mathrm{d}\hat{x}.$$

where $\hat{x}^- = \sqrt{a}x-$ and $\hat{x}^+ = \sqrt{a}x+$. The second integral in this expression can be solved using (B.4.3). For the first integral, note that

$$\begin{aligned}\int_0^{\hat{x}} \hat{x} \log(\hat{x}) \exp\left(-\hat{x}^2\right) \mathrm{d}\hat{x} &= \int_{\hat{x}^-}^{\hat{x}^+} -\frac{1}{2}\frac{\mathrm{d}}{\mathrm{d}\hat{x}}\left(\log(\hat{x}) \exp\left(-\hat{x}^2\right)\right) + \frac{1}{2\hat{x}} \exp\left(-\hat{x}^2\right) \mathrm{d}\hat{x} \\ &= -\frac{1}{2}\log(\hat{x}) \exp\left(-\hat{x}^2\right) + \frac{1}{4}\int_{\hat{x}^-}^{\hat{x}^+} \frac{1}{\hat{x}^2} \exp\left(-\hat{x}^2\right) \mathrm{d}(\hat{x}^2).\end{aligned}$$

So by using the definition of an exponential integral Ei, where $Ei(z) = -\int_{-z}^{\infty} e^{-t}/t \, \mathrm{d}t$, we obtain

$$\begin{aligned}\int_{x^-}^{x^+} x \log(bx) \exp\left(-ax^2\right) \mathrm{d}x = &-\frac{1}{2a}\log\left(\frac{b}{\sqrt{a}}\hat{x}^+\right) \exp\left(-(\hat{x}^+)^2\right) + \frac{1}{4a} Ei\left(-(\hat{x}^+)^2\right) \\ &+ \frac{1}{2a}\log\left(\frac{b}{\sqrt{a}}\hat{x}^-\right) \exp\left(-(\hat{x}^-)^2\right) - \frac{1}{4a} Ei\left(-(\hat{x}^-)^2\right).\end{aligned} \tag{B.4.6}$$

Consider when $x^- = 0$ and $x^+ \to \infty$, which gives

$$\begin{aligned}\int_0^\infty x \log(bx) \exp\left(-ax^2\right) \mathrm{d}x = &-\frac{1}{2a}\lim_{x\to\infty}\left(\log\left(\frac{b}{\sqrt{a}}x\right) \exp\left(-x^2\right)\right) + \frac{1}{4a}\lim_{\hat{x}\to\infty}\left(Ei\left(-x^2\right)\right) \\ &+ \lim_{x\to 0}\left(\frac{1}{2a}\log\left(\frac{b}{\sqrt{a}}x\right) \exp\left(-x^2\right) - \frac{1}{4a}\left(Ei\left(-x^2\right)\right)\right).\end{aligned}$$

The first limit can be solved using L'Hôpital's rule to give

$$\lim_{\hat{x}\to\infty}\left(\frac{\log\left(\frac{b}{\sqrt{a}}x\right)}{\exp\left(x^2\right)}\right) = \lim_{\hat{x}\to\infty}\left(\frac{1}{2x^2 \exp\left(x^2\right)}\right) = 0.$$

For the second limit, by the definition of Ei we see that $Ei\left(-x^2\right) \to 0$ as $x \to \infty$. To calculate the third limit we must consider the Puiseux series

$$\log x \exp\left(-x^2\right) = \log x + \mathcal{O}(x^2 \log x) \quad \text{and} \quad Ei(-x^2) = \gamma + \log(x^2) + \mathcal{O}(x^2),$$

where γ represents the Euler-Mascheroni constant and the second expansion can be found in Van Heemert (1957). This gives

$$\lim_{\hat{x}\to 0}\left(\frac{1}{2a}\log\left(\frac{b}{\sqrt{a}}x\right)\exp\left(-x^2\right) - \frac{1}{4a}\left(Ei\left(-x^2\right)\right)\right) = \frac{1}{2a}\log\left(\frac{b}{\sqrt{a}}\right) + \frac{\gamma}{4a}$$

and so

$$\int_0^\infty x\log(bx)\exp\left(-ax^2\right)\,\mathrm{d}x = \frac{1}{2a}\log\left(\frac{b}{\sqrt{a}}\right) + \frac{\gamma}{4a}.$$

Gradshteyn and Ryzhik (2014) gives

$$\int_0^\infty t^n \log(t)\exp\left(-\mu t\right)\,\mathrm{d}t = \frac{n!}{\mu^{n+1}}\left(1 + \frac{1}{2} + \cdots + \frac{1}{n} - \gamma - \log(\mu)\right),$$

which can be used with $t = R$, $n = 1$ and $\mu = 1$ to give

$$\int_0^\infty R\log R\exp\left(-R\right)\,\mathrm{d}r = 1 - \gamma. \tag{B.4.7}$$

B.5 Integrating the homogenized solution combined with the one-dimensional free-space Green's function

We can solve

$$\int_{\mathcal{D}_1} \mathcal{G}_1(x_1 - x_1')C_H(x_1')\,\mathrm{d}x_1',$$
$$\int_{\mathcal{D}_1} \mathcal{G}_1(x_1 - x_1')\mathcal{G}_1(x_1' - x_1'')C_H(x_1'')\,\mathrm{d}x_1'\,\mathrm{d}x_1'' \quad \text{and}$$
$$\int_{\mathcal{D}_1} \mathcal{G}_1(x_1 - x_1')^2 C_H(x_1')^2\,\mathrm{d}x_1'$$

using the homogenized solution and one-dimensional free-space Green's function given in (3.2.2) and (3.4.9) respectively. For the first integral, by considering $x_1 \leq x_1'$ and $x_1 \geq x_1'$ separately we obtain

$$\int_{\mathcal{D}_1} \mathcal{G}_1(x_1 - x_1')C_H(x_1')\,\mathrm{d}x_1' = -\frac{\mathrm{Pe}_L}{2\phi^2\psi(1)}e^{\frac{\mathrm{Pe}_L}{2}x_1}\Bigg(\left(\phi(2\phi - \mathrm{Pe}_L)(1 - x_1) - \mathrm{Pe}_L\right)e^{\phi(x_1-1)}$$
$$+ \left(\frac{\mathrm{Pe}_L}{2} + \phi\right)(1 + 2\phi x_1)\,e^{\phi(1-x_1)} + \left(\frac{\mathrm{Pe}_L}{2} - \phi\right)e^{-\phi(x_1+1)}\Bigg),$$

where ψ was previously defined for $C_H(x_1)$ in (3.2.2). By considering $x_1 \leq x_1'$ and $x_1 \geq x_1'$ separately this can then be used to obtain the second integral, which is given by

$$\begin{aligned}\int_{\mathcal{D}_1}\int_{\mathcal{D}_1} \mathcal{G}_1(x_1-x_1')\mathcal{G}_1(x_1'-x_1'')C_H(x_1'')\,\mathrm{d}x_1'\,\mathrm{d}x_1'' \\ = \frac{\mathrm{Pe}_L}{4\phi^4\psi(1)}e^{\frac{\mathrm{Pe}_L}{2}x_1}\Bigg(\left(\mathrm{Pe}_L+\phi\left(\phi-\frac{\mathrm{Pe}_L}{2}\right)(x_1-1)\right)\phi(x_1-1)e^{\phi(x_1-1)} \\ + \frac{1}{4}\left(\mathrm{Pe}_L(2\phi+3)-2\phi(2\phi+1)\right)e^{-\phi(x_1+1)} \\ + \frac{1}{4}\left(2\phi(\mathrm{Pe}_L-2\phi)(x_1-1)+2\phi-3\,\mathrm{Pe}_L\right)e^{\phi(x_1-1)} \\ + \left(\frac{\mathrm{Pe}_L}{2}+\phi\right)\left((1+\phi x_1)^2e^{\phi(1-x_1)}-(1+\phi)e^{\phi(x_1-1)}\right) \\ + \frac{1}{2}\left(\frac{\mathrm{Pe}_L}{2}-\phi\right)\left((1+2\phi x_1)e^{-\phi(x_1+1)}-e^{-\phi(3-x_1)}\right)\Bigg).\end{aligned}$$

For the third integral we can again use the same technique to obtain

$$\begin{aligned}\int_{\mathcal{D}_1} G(x_1,x_1')^2C_H(x_1')^2\,\mathrm{d}x_1' \\ = \left(\frac{\mathrm{Pe}_L^2}{4\phi^3\psi(1)^2}\right)e^{\mathrm{Pe}_L\,x_1}\Bigg(\left(\phi(2\phi-\mathrm{Pe}_L)^2(1-x_1)+\mathrm{Pe}_L^2-2\phi\,\mathrm{Pe}_L-4\phi^2\right)e^{2\phi(x_1-1)} \\ + \left(\phi+\frac{\mathrm{Pe}_L}{2}\right)^2(4\phi x_1+1)e^{2\phi(1-x_1)} \\ + \left(4\phi^2-\mathrm{Pe}_L^2\right)\left(2-e^{-2\phi x_1}\right)+\left(\phi-\frac{\mathrm{Pe}_L}{2}\right)^2e^{-2\phi(x_1+1)}\Bigg)\end{aligned}$$

To find a leading-order expression for these integrals, note that $e^{-\phi(x_1+1)}$, $e^{-2\phi(x_1+1)}$ and $e^{-\phi(3-x_1)}$ remain exponentially small throughout the domain. As $e^{\phi(x_1-1)}$ is asymptotically small for large ϕ except when $x_1 \approx 1$, we find $(1-x_1)e^{\phi(x_1-1)}$ and $(1-x_1)e^{2\phi(x_1-1)}$ also remain asymptotically small throughout the domain. Therefore we can approximate theses integrals as

$$\int_{\mathcal{D}_1}\mathcal{G}_1(x_1-x_1')C_H(x_1')\,\mathrm{d}x_1' \approx \frac{\mathrm{Pe}_L}{4\phi^2\hat{\psi}(1)}e^{\frac{\mathrm{Pe}_L}{2}x_1}\left(2\,\mathrm{Pe}_L\;e^{\phi(x_1-1)}-(2\phi+\mathrm{Pe}_L)\,(1+2\phi x_1)\,e^{\phi(1-x_1)}\right), \tag{B.5.1}$$

$$\begin{aligned}\int_{\mathcal{D}_1}\int_{\mathcal{D}_1}\mathcal{G}_1(x_1-x_1')\mathcal{G}_1(x_1'-x_1'')C_H(x_1'')\,\mathrm{d}x_1'\,\mathrm{d}x_1'' \approx \frac{\mathrm{Pe}_L}{8\phi^4\hat{\psi}(1)}e^{\frac{\mathrm{Pe}_L}{2}x_1}\Bigg((2\phi+\mathrm{Pe}_L)\,(1+\phi x_1)^2e^{\phi(1-x_1)} \\ + \left(-\frac{5\,\mathrm{Pe}_L}{2}-\phi(1+\mathrm{Pe}_L+2\phi)\right)e^{\phi(x_1-1)}\Bigg).\end{aligned} \tag{B.5.2}$$

and

$$\int_{\mathcal{D}_1} G(x_1,x_1')^2 C_H(x_1')^2\,\mathrm{d}x_1' \approx \left(\frac{\mathrm{Pe}_L^2}{16\phi^3\hat{\psi}(1)^2}\right) e^{\mathrm{Pe}_L\, x_1}\Bigg((2\phi+\mathrm{Pe}_L)^2\,(4\phi x_1+1)e^{2\phi(1-x_1)} + 4\left(4\phi^2-\mathrm{Pe}_L^2\right)\left(2-e^{-2\phi x_1}\right) - 4\left(4\phi^2+2\phi\,\mathrm{Pe}_L-\mathrm{Pe}_L^2\right)e^{2\phi(x_1-1)}\Bigg), \tag{B.5.3}$$

with $\hat{\psi}$ being the approximation of ψ near $x_1 = 1$, which is given by $\hat{\psi}(x_1) = (2\,\mathrm{Pe}_L\,\phi + \mathrm{Pe}_L^2 + 2\,\mathrm{Da})e^{\phi x_1}$. The order of each integral can be obtained for $\mathrm{Pe}_L \gg \max(1,\sqrt{\mathrm{Da}})$ by neglect the impact of boundary layers and use $\phi \approx \mathrm{Pe}_L/2$, $\hat{\psi}(x_1) \approx 2\,\mathrm{Pe}_L^2\, e^{(\mathrm{Pe}_L/2)x_1}$ and $x_1 = \mathcal{O}(1)$, which gives

$$\int_{\mathcal{D}_1} \mathcal{G}_1(x_1-x_1')C_H(x_1')\,\mathrm{d}x_1' = \mathcal{O}\left(1/\mathrm{Pe}_L\right), \tag{B.5.4a}$$

$$\int_{\mathcal{D}_1}\int_{\mathcal{D}_1} \mathcal{G}_1(x_1-x_1')\mathcal{G}_1(x_1'-x_1'')C_H(x_1'')\,\mathrm{d}x_1'\,\mathrm{d}x_1'' = \mathcal{O}\left(1/\mathrm{Pe}_L^2\right), \tag{B.5.4b}$$

$$\int_{\mathcal{D}_1} G(x_1,x_1')^2 C_H(x_1')^2\,\mathrm{d}x_1' = \mathcal{O}\left(1/\mathrm{Pe}_L^3\right). \tag{B.5.4c}$$

B.6 Eigenvalue decomposition

Let the three-dimensional sink function $\hat{g}(\mathbf{x};\omega)$ have a mean, variance and correlation length of zero, ℓ and σ^2 respectively. Then we can calculate an eigenvalue decomposition by separating the domain into $\hat{N}$ subintervals of width $h_{\hat{N}} = 1/\hat{N}$ in the x_1 direction and $\hat{M}$ subintervals of width $h_{\hat{M}} = 1/\hat{M}$ in the x_2 and x_3 directions. First, let the Gaussian and exponential covariance functions from (4.1.2) and (4.1.3) be decomposed into (Lord et al., 2014)

$$\Sigma^G_{(\mathbf{i}_3,\mathbf{j}_3)} = \sigma^2\exp\left(-\frac{(\mathbf{x}_{\mathbf{i}_3}-\mathbf{y}_{\mathbf{j}_3})^2}{\ell^2}\right) \quad \text{and} \quad \Sigma^E_{(\mathbf{i}_3,\mathbf{j}_3)} = \sigma^2\exp\left(-\frac{|\mathbf{x}_{\mathbf{i}_3}-\mathbf{y}_{\mathbf{j}_3}|}{\ell}\right) \tag{B.6.1}$$

respectively, where $\mathbf{i}_3 = (i,j,k)$ and $\mathbf{j}_3 = (i',j',k')$ such that $i,i' = 1,\ldots,\hat{N}$ and $j,j',k,k' = 1,\ldots,\hat{M}$. Define U and Λ to be the eigenvectors and eigenvalues of $\Sigma_{(\mathbf{i}_3,\mathbf{j}_3)}$ respectively, where $\Lambda = [\lambda_1,\ldots,\lambda_{\hat{N}\hat{M}\hat{M}}]$ and $\lambda_1 \geq \cdots \geq \lambda_{\hat{N}\hat{M}\hat{M}} \geq 0$. Then the sink function can be decomposed and given by

$$\hat{g}_{\mathbf{i}_3} = \hat{g}(\mathbf{x}_{\mathbf{i}_3}) = (U\Lambda^{1/2}\xi)_{\mathbf{i}_3} = \sum_{i'=1}^{\hat{N}}\sum_{j'=1}^{\hat{M}}\sum_{k'=1}^{\hat{M}} \lambda_{\mathbf{i}_3} U_{\mathbf{i}_3\mathbf{j}_3}\xi_{\mathbf{j}_3}, \tag{B.6.2}$$

where $\xi_{\mathbf{j}_3} \sim \mathcal{N}(\mathbf{0},I)$. This approach can be used to produce realisations of the sink function, which can in turn be used to give realisations of the solute concentration.

Analogous definitions can be used when finding eigenvalue decompositions in one and two dimensions, which is done in one dimension to calculate sample moments and two dimensions

to produce Figure 4.1. It is worth noting that the eigenvalue decomposition can become costly in higher dimensions, meaning producing multiple realisations for finding sample moments can become infeasible. Alternative approaches do exist which reduce the computational cost for producing realisations, which include the stochastic Galerkin method among others (Lord et al., 2014).

B.7 Considering a log-normal Gaussian process in one dimension

Consider when the sink function is given by a one-dimensional log-normal Gaussian process. This will be represented by

$$\hat{g}(x_1;\omega) = \exp\left(z(x_1) - \sigma^2/2\right) - 1 \tag{B.7.1}$$

such that $z(x_1)$ is a Gaussian process with mean, variance and correlation length of zero, σ^2 and ℓ respectively. By properties of log-normal distributions (Johnson et al., 1995) the expectation of $\exp(z(x_1))$ is given by $\exp(\sigma^2/2)$, meaning the expectation of the sink function remains zero. This is demonstrated by the two realisations of $1 + \hat{g}(x_1;\omega)$ shown in Figure B.1(a) and B.1(c) having a mean of one, which use a Gaussian and exponential covariance function respectively for $z(x_1)$.

By using 10^4 realisations of the sink function we can use the finite difference scheme from Section B.2 to produce realisations of the concentration profile. These are shown in Figures B.1(b) and B.1(d), which use $\sigma = 1$ and $\ell = 0.1$ for the variance and correlation length respectively. Due to the form of (B.7.1) we know $1 + \hat{g}(x_1;\omega)$ remains positive for all x_1, which allows for a larger value of σ to be used in comparison to the Gaussian process used in Section 4.1. This, coupled with the distribution being log-normal, causes any spikes in the sink function to be more exaggerated and leads to large drops in concentration at certain points within the domain. Figure B.1(b) and (d) both show a non-Gaussian distribution of concentration profiles about the mean, which shows moments offering a poor prediction of disorder in solute concentration. However, the sample credible-intervals (plotted in cyan) in Figures B.1(b) and (d) show an improvement when capturing disorder caused due to the continuous sink distribution. These credible-intervals could potentially be calculated using similar methodology to that presented in Section 2.2.3, where cdf credible-intervals could be found using the tracking of the cdf from Appendix A.5.

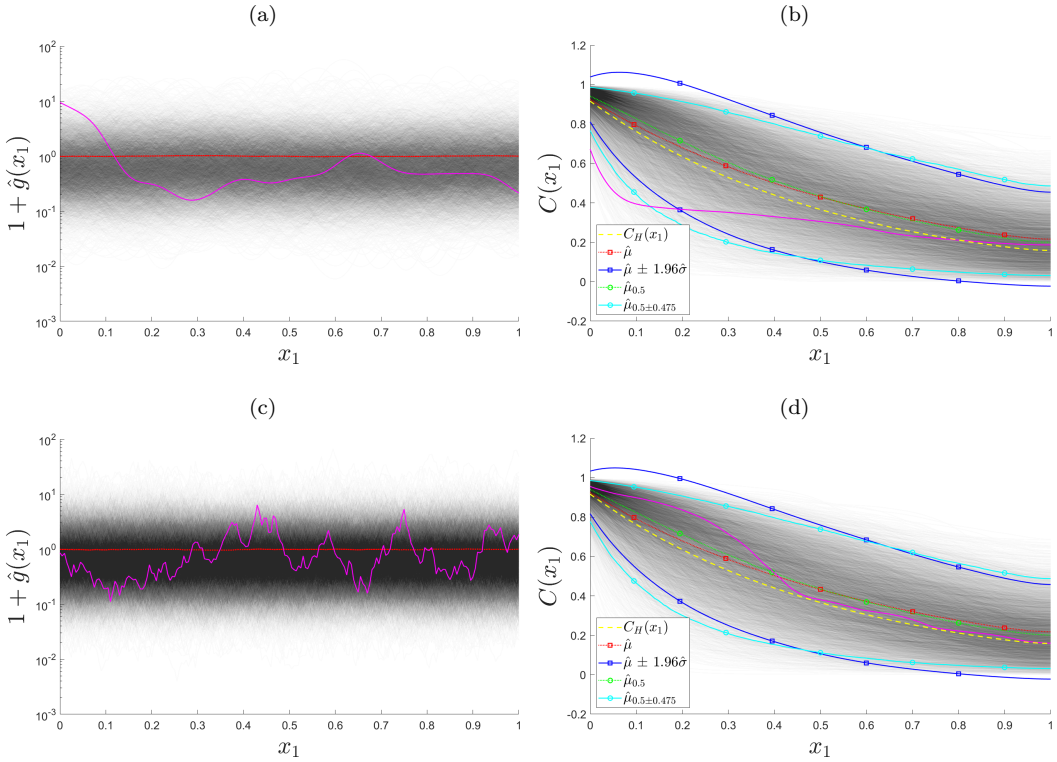

Figure B.1: (a) & (c) Realisations of one plus the sink function on a log-scale [grey] with the sample mean [dashed red] and a single realisation [solid magenta]. (b) & (d) Realisations of concentration profiles [grey] with the sample mean [$\hat{\mu}$, dashed red], sample Gaussian-based 95% credible-intervals [$\hat{\mu} \pm 1.96\hat{\sigma}$ (where $\hat{\sigma}$ represents the sample standard deviation), solid blue], sample median [$\hat{\mu}_{0.5}$, dashed green], sample 95% credible-intervals [$\hat{\mu}_{0.5\pm0.475}$, solid cyan] and one single realisation [solid magenta]. Figures (a)-(b) and (c)-(d) use a Gaussian and exponential covariance function for $z(x_1)$ in (B.7.1) respectively. All figures use 10^4 Monte Carlo simulation with $(\mathrm{Pe}_L, \mathrm{Da}) = (10, 40)$, $\sigma = 1$ and $\ell = 0.1$.

Bibliography

Abramowitz, M. and Stegun, I. A. (1964). *Handbook of mathematical functions with formulas, graphs, and mathematical tables*, volume 55. U.S. Government printing office.

Adam, M. S. and Sibert, J. R. (2002). Population dynamics and movements of skipjack tuna (Katsuwonus pelamis) in the Maldivian fishery: analysis of tagging data from an advection-diffusion-reaction model. *Aquat. Living Resour.*, 15(1):13–23.

Aifantis, E. C. (1978). Towards a rational modeling for the human placenta. *Math. Biosci.*, 40(3-4):281–301.

Alim, K., Parsa, S., Weitz, D. A., and Brenner, M. P. (2017). Local pore size correlations determine flow distributions in porous media. *Phys. Rev. Lett.*, 119(14):144501.

Alpkvist, E., Picioreanu, C., Van Loosdrecht, M. C. M., and Heyden, A. (2006). Three-dimensional biofilm model with individual cells and continuum EPS matrix. *Biotechnol. Bioeng.*, 94(5):961–979.

Anantharaman, A. and Le Bris, C. (2011). A numerical approach related to defect-type theories for some weakly random problems in homogenization. *Multiscale Model. Simul.*, 9(2):513–544.

Arnold, B. C., Balakrishnan, N., and Nagaraja, H. N. (1992). *A first course in order statistics*, volume 54. SIAM.

Auriault, J.-L. and Adler, P. M. (1995). Taylor dispersion in porous media: Analysis by multiple scale expansions. *Adv. Water Res.*, 18(4):217–226.

Auriault, J.-L. and Sanchez-Palencia, E. (1977). Study of the macroscopic behavior of a saturated porous elastic medium. *J. de Mec.*, 16(4):575–603.

Bakhvalov, N. S. (1975). Averaged characteristics of bodies with periodic structure. In *Soviet Physics Doklady*, volume 19, page 650.

Bal, G. (2011). Convergence to homogenized or stochastic partial differential equations. *Appl. Math. Res. eXpress*, 2011(2):215–241.

Balhoff, M., Mikelić, A., and Wheeler, M. F. (2010). Polynomial filtration laws for low Reynolds number flows through porous media. *Transp. Porous Med.*, 81(1):35–60.

Banerjee, R. K., Kwon, O., Vaidya, V. S., and Back, L. H. (2008). Coupled oxygen transport analysis in the avascular wall of a coronary artery stenosis during angioplasty. *J. Biomech.*, 41(2):475–479.

Bear, J. (2013). *Dynamics of fluids in porous media*. Courier Corporation.

Beech, I. B. and Sunner, J. (2004). Biocorrosion: towards understanding interactions between biofilms and metals. *Curr. Opin. Biotechnol.*, 15(3):181–186.

Beliaev, A. Y. and Kozlov, S. M. (1996). Darcy equation for random porous media. *Commun. Pure Appl. Math.*, 49(1):1–34.

Bensoussan, A., Lions, J.-L., and Papanicolaou, G. (1978). *Asymptotic analysis for periodic structures*, volume 5. Elsevier North-Holland,, studies in mathematics and its applications edition.

Berdichevsky, V. L. (1975). Spatial averaging of periodic structures. In *Doklady Akademii Nauk*, volume 222, pages 565–567. Russian Academy of Sciences.

Berkowitz, B., Cortis, A., Dentz, M., and Scher, H. (2006). Modeling non-Fickian transport in geological formations as a continuous time random walk. *Rev. Geophys.*, 44(2).

Bhattacharya, R. N. (1982). On the functional central limit theorem and the law of the iterated logarithm for Markov processes. *Z. Wahr. v. Geb.*, 60(2):185–201.

Biot, M. A. (1941). General theory of three-dimensional consolidation. *J. Appl. Phys.*, 12(2):155–164.

Bolster, D. and Dentz, M. (2012). Anomalous dispersion in chemically heterogeneous media induced by long-range disorder correlation. *J. Fluid Mech.*, 695:366–389.

Boso, F., Broyda, S. V., and Tartakovsky, D. M. (2014). Cumulative distribution function solutions of advection–reaction equations with uncertain parameters. *Proc. R. Soc. A*, 470(2166):20140189.

Brenner, H. (1980). Dispersion resulting from flow through spatially periodic porous media. *Philos. Trans. R. Soc. A*, 297(1430):81–133.

Brenner, H. (2013). *Macrotransport processes*. Elsevier.

Brinkman, H. C. (1949). A calculation of the viscous force exerted by a flowing fluid on a dense swarm of particles. *Flow Turbul. Combust.*, 1(1):27–34.

Burridge, R. and Keller, J. B. (1981). Poroelasticity equations derived from microstructure. *J. Acoust. Soc. Am.*, 70(4):1140–1146.

Chapman, S. J. and McBurnie, S. E. (2011). A unified multiple-scales approach to one-dimensional composite materials and multiphase flow. *SIAM J. Appl. Math.*, 71(1):200–217.

Chernyavsky, I. L., Dryden, I. L., and Jensen, O. E. (2012). Characterizing the multiscale structure of fluctuations of transported quantities in a disordered medium. *IMA J. Appl. Math.*, 77(5):697–725.

Chernyavsky, I. L., Jensen, O. E., and Leach, L. (2010). A mathematical model of intervillous blood flow in the human placentone. *Placenta*, 31(1):44–52.

Chernyavsky, I. L., Leach, L., Dryden, I. L., and Jensen, O. E. (2011). Transport in the placenta: Homogenizing haemodynamics in a disordered medium. *Philos. Trans. R. Soc. A*, 369(1954):4162–4182.

Chunsheng, M. (1992). Moments of functions of order statistics. *Stat. Probab. Lett.*, 15(1):57–62.

Costerton, J. W. (1999). Introduction to biofilm. *Int. J. Antimicrob. Agents*, 11(3-4):217–221.

Craine, J. M. (2006). Competition for nutrients and optimal root allocation. *Plant Soil*, 285(1-2):171–185.

Cushman, J. H., Bennethum, L. S., and Hu, B. X. (2002). A primer on upscaling tools for porous media. *Adv. Water Res.*, 25(8-12):1043–1067.

Dagan, G. (1984). Solute transport in heterogeneous porous formations. *J. Fluid Mech.*, 145:151–177.

Dalwadi, M. P., Bruna, M., and Griffiths, I. M. (2016). A multiscale method to calculate filter blockage. *J. Fluid Mech.*, 809:264–289.

Dalwadi, M. P., Griffiths, I. M., and Bruna, M. (2015). Understanding how porosity gradients can make a better filter using homogenization theory. *Proc. R. Soc. A*, 471(2182):20150464.

Dalwadi, M. P. and King, J. R. (2020). A systematic upscaling of nonlinear chemical uptake within a biofilm. *SIAM J. Appl. Math.*, 80(4):1723–1750.

Dalwadi, M. P., Wang, Y., King, J. R., and Minton, N. P. (2018). Upscaling diffusion through first-order volumetric sinks: a homogenization of bacterial nutrient uptake. *SIAM J. Appl. Math.*, 78(3):1300–1329.

Darcy, H. (1856). *Les fontaines publiques de la ville de Dijon: exposition et application...* Victor Dalmont.

Datta, S. and Redner, S. (1998). Gradient clogging in depth filtration. *Phys. Rev. E*, 58:R1203–R1206.

David, H. A. and Nagaraja, H. N. (2004). *Order statistics*. John Wiley & Sons.

Davit, Y., Bell, C. G., Byrne, H. M., Chapman, L. A. C., Kimpton, L. S., Lang, G. E., Leonard, K. H. L., Oliver, J. M., Pearson, N. C., Shipley, R. J., et al. (2013). Homogenization via formal multiscale asymptotics and volume averaging: How do the two techniques compare? *Adv. Water Res.*, 62:178–206.

De Anna, P., Le Borgne, T., Dentz, M., Tartakovsky, A. M., Bolster, D., and Davy, P. (2013). Flow intermittency, dispersion, and correlated continuous time random walks in porous media. *Phys. Rev. Lett.*, 110(18):184502.

Del Pozo, J. L., Rouse, M. S., and Patel, R. (2008). Bioelectric effect and bacterial biofilms. a systematic review. *Int. J. Artif. Organs*, 31(9):786–795.

Delgado-Buscalioni, R. and Coveney, P. V. (2003). Continuum-particle hybrid coupling for mass, momentum, and energy transfers in unsteady fluid flow. *Phys. Rev. E*, 67(4):046704.

Deo, S. (2004). Stokes flow past a swarm of porous circular cylinders with Happel and Kuwabara boundary conditions. *Sadhana*, 29(4):381–387.

Dillon, R., Fauci, L., and Gaver III, D. (1995). A microscale model of bacterial swimming, chemotaxis and substrate transport. *J. Theor. Biol.*, 177(4):325–340.

Du, X. and Ostoja-Starzewski, M. (2006). On the size of representative volume element for Darcy law in random media. *Proc. R. Soc. A*, 462(2074):2949–2963.

Du Plessis, J. P. and Masliyah, J. H. (1991). Flow through isotropic granular porous media. *Transp. Porous Med.*, 6(3):207–221.

Dumontet, H. (1986). Study of a boundary layer problem in elastic composite materials. *ESIAM: Math. Model. Numer. Anal.*, 20(2):265–286.

Edwards, D. A., Shapiro, M., Brenner, H., and Shapira, M. (1991). Dispersion of inert solutes in spatially periodic, two-dimensional model porous media. *Transp. Porous Med.*, 6(4):337–358.

Erian, F. F., Corrsin, S., and Davis, S. H. (1977). Maternal, placental blood flow: a model with velocity-dependent permeability. *J. Biomech.*, 10(11-12):807–814.

Erlich, A., Nye, G. A., Brownbill, P., Jensen, O. E., and Chernyavsky, I. L. (2019a). Quantifying the impact of tissue metabolism on solute transport in feto-placental microvascular networks. *Interface Focus*, 9(5):20190021.

Erlich, A., Pearce, P., Mayo, R. P., Jensen, O. E., and Chernyavsky, I. L. (2019b). Physical and geometric determinants of transport in fetoplacental microvascular networks. *Sci. Adv.*, 5(4):eaav6326.

Fick, A. (1855). V. on liquid diffusion. *Philos. Mag.*, 10(63):30–39.

Flekkøy, E. G., Wagner, G., and Feder, J. (2000). Hybrid model for combined particle and continuum dynamics. *Europhys. Lett.*, 52(3):271.

Flemming, H.-C. (1993). Biofilms and environmental protection. *Water Sci. Technol.*, 27(7-8):1–10.

Fomin, S. A., Chugunov, V. A., and Hashida, T. (2011). Non-Fickian mass transport in fractured porous media. *Adv. Water Res.*, 34(2):205–214.

Forchheimer, P. (1901). Wasserbewegung durch boden. *Z. Ver. Deutsch, Ing.*, 45:1782–1788.

Ford, R. M. and Harvey, R. W. (2007). Role of chemotaxis in the transport of bacteria through saturated porous media. *Adv. Water Res.*, 30(6-7):1608–1617.

Freitas, R. K. and Schröder, W. (2008). Numerical investigation of the three-dimensional flow in a human lung model. *J. Biomech.*, 41(11):2446–2457.

Garcia, R. E. and Chiang, Y.-M. (2007). Spatially resolved modeling of microstructurally complex battery architectures. *J. Electrochem. Soc.*, 154(9):A856.

Gardiner, C. (2009). *Stochastic methods*, volume 4. Springer Berlin.

Gillespie, D. T. (1976). A general method for numerically simulating the stochastic time evolution of coupled chemical reactions. *J. Comput. Phys.*, 22(4):403–434.

Gillespie, D. T. (1977). Exact stochastic simulation of coupled chemical reactions. *J. Phys. Chem.*, 81(25):2340–2361.

Gillespie, D. T. (2007). Stochastic simulation of chemical kinetics. *Annu. Rev. Phys. Chem.*, 58:35–55.

Gradshteyn, I. S. and Ryzhik, I. M. (2014). *Table of integrals, series, and products*. Academic press.

Gray, H. (1918). *Anatomy of the human body*. (20th ed.). Philadelphia, PA: Lea & Febiger.

Hall-Stoodley, L., Costerton, J. W., and Stoodley, P. (2004). Bacterial biofilms: from the natural environment to infectious diseases. *Nat. Rev. Microbiol.*, 2(2):95–108.

Hasimoto, H. (1959). On the periodic fundamental solutions of the Stokes equations and their application to viscous flow past a cubic array of spheres. *J. Fluid Mech.*, 5(2):317–328.

Hassanizadeh, M. and Gray, W. G. (1979). General conservation equations for multi-phase systems: 1. averaging procedure. *Adv. Water Res.*, 2:131–144.

Hassanizadeh, M. and Gray, W. G. (1980). General conservation equations for multi-phase systems: 3. constitutive theory for porous media flow. *Adv. Water Res.*, 3(1):25–40.

Havlin, S. and Ben-Avraham, D. (2002). Diffusion in disordered media. *Adv. Phys.*, 51(1):187–292.

Higham, N. J. (2002). *Accuracy and stability of numerical algorithms*. SIAM.

Hosea, M. (2021). integralN.m (https://www.mathworks.com/matlabcentral/fileexchange/47919-integraln-m). *MATLAB Central File Exchange. Retrieved May 26, 2021.*

Hunt, M. J., Planella, F. B., Theil, F., and Widanage, W. D. (2020). Derivation of an effective thermal electrochemical model for porous electrode batteries using asymptotic homogenisation. *J. Eng. Math.*, 122(1):31–57.

Iliev, O., Mikelić, A., Prill, T., and Sherly, A. (2020). Homogenization approach to the upscaling of a reactive flow through particulate filters with wall integrated catalyst. *Adv. Water Res.*, 146:103779.

Jensen, O. E. and Chernyavsky, I. L. (2019). Blood flow and transport in the human placenta. *Annu. Rev. Fluid Mech.*, 51(25-47).

Jin, C., Langston, P. A., Pavlovskaya, G. E., Hall, M. R., and Rigby, S. P. (2016). Statistics of highly heterogeneous flow fields confined to three-dimensional random porous media. *Phys. Rev. E*, 93(1):013122.

Johnson, B., Davoudi, A., Chapman, P., and Sauer, P. (2011). A unified dynamic characterization framework for microgrid systems. *Electr. Pow. Compo. Sys.*, 40(1):93–111.

Johnson, N. L., Kotz, S., and Balakrishnan, N. (1995). *Continuous univariate distributions, volume 2*, volume 289. John wiley & sons.

Jones, G. W. and Chapman, S. J. (2012). Modeling growth in biological materials. *SIAM Rev.*, 54(1):52–118.

Keller, J. B. (1964). Viscous flow through a grating or lattice of cylinders. *J. Fluid Mech.*, 18(1):94–96.

Keller, J. B. (1977). Effective behavior of heterogeneous media. In *Statistical Mechanics and Statistical Methods in Theory and Application*, pages 631–644. Springer.

Keller, J. B. (2001). Flow in random porous media. *Transp. Porous Med.*, 43(3):395–406.

King, J. R., Köry, J., and Ptashnyk, M. (2021). Multiscale analysis of nutrient uptake by plant roots with sparse distribution of root hairs: nonstandard scaling. *SIAM J. Appl. Math.*, 81(4):1361–1388.

Kleinstreuer, C. and Zhang, Z. (2010). Airflow and particle transport in the human respiratory system. *Annu. Rev. Fluid Mech.*, 42:301–334.

Kozlov, S. M. (1979). Averaging of random operators. *Mat. Sb.*, 151(2):188–202.

Kuwahara, F., Sano, Y., Liu, J., and Nakayama, A. (2009). A porous media approach for bifurcating flow and mass transfer in a human lung. *J. Heat Transfer*, 131(10).

Lakshmi, K. R., Nagesh, Y., and Krishna, M. V. (2014). Performance comparison of three data mining techniques for predicting kidney dialysis survivability. *Int. J. Adv. Eng. Technol.*, 7(1):242.

Lande, B. and Mitzner, W. (2006). Analysis of lung parenchyma as a parametric porous medium. *J. Appl. Physiol.*, 101(3):926–933.

Lighthill, M. J. and Whitham, G. B. (1955). On kinematic waves II. a theory of traffic flow on long crowded roads. *Proc. R. Soc. A*, 229(1178):317–345.

Lin, M., Mauroy, B., James, J. L., Tawhai, M. H., and Clark, A. R. (2016). A multiscale model of placental oxygen exchange: The effect of villous tree structure on exchange efficiency. *J. Theor. Biol.*, 408:1–12.

Lord, G. J., Powell, C. E., and Shardlow, T. (2014). *An introduction to computational stochastic PDEs*, volume 50. Cambridge University Press.

Mahiout, L. A., Panasenko, G., and Volpert, V. (2020). Homogenization of the diffusion equation with a singular potential for a model of a biological cell network. *Z. Angew. Math. Phys.*, 71(6):1–20.

Marciniak-Czochra, A. and Ptashnyk, M. (2008). Derivation of a macroscopic receptor-based model using homogenization techniques. *SIAM J. Math. Anal.*, 40(1):215–237.

Mei, C. C. and Auriault, J.-L. (1991). The effect of weak inertia on flow through a porous medium. *J. Fluid Mech.*, 222:647–663.

Miguel, A. F. (2012). Lungs as a natural porous media: architecture, airflow characteristics and transport of suspended particles. In *Heat and Mass Transfer in Porous Media*, pages 115–137. Springer.

Montroll, E. W. and Weiss, G. H. (1965). Random walks on lattices. II. *J. Math. Phys.*, 6(2):167–181.

Morse, P. M. and Ingard, K. U. (1986). *Theoretical acoustics*. Princeton university press.

Nield, D. A., Bejan, A., et al. (2006). *Convection in porous media*, volume 3. Springer.

Noetinger, B., Hume, L., Chatelin, R., and Poncet, P. (2018). Effective viscosity of a random mixture of fluids. *Phys. Rev. Fluids*, 3(1):014103.

Ochs, M., Nyengaard, J. R., Jung, A., Knudsen, L., Voigt, M., Wahlers, T., Richter, J., and Gundersen, H. J. G. (2004). The number of alveoli in the human lung. *Am. J. Resp. Crit. Care*, 169(1):120–124.

Panasenko, G. and Volpert, V. (2016). Homogenization of a one-dimensional diffusion-discrete absorption equation with feedback. *Appl. Anal.*, 95(7):1507–1516.

Papanicolaou, G. C. (1979). Boundary value problems with rapidly oscillating random coefficients. In *Colloquia Math. Soc., Janos Bolyai*, volume 27, pages 853–873.

Papanicolau, G., Bensoussan, A., and Lions, J.-L. (1978). *Asymptotic analysis for periodic structures*. North-Holland Publishing, Amsterdam.

Pavliotis, G. and Stuart, A. (2008). *Multiscale methods: averaging and homogenization*. Springer Science & Business Media.

Pedretti, D., Fernàndez-Garcia, D., Bolster, D., and Sanchez-Vila, X. (2013). On the formation of breakthrough curves tailing during convergent flow tracer tests in three-dimensional heterogeneous aquifers. *Water Resour. Res.*, 49(7):4157–4173.

Penta, R. and Ambrosi, D. (2015). The role of the microvascular tortuosity in tumor transport phenomena. *J. Theor. Biol.*, 364:80–97.

Pereira, V. E., Dalwadi, M. P., Ruiz-Trejo, E., and Griffiths, I. M. (2021). Optimising the flow through a concertinaed filtration membrane. *J. Fluid Mech.*, 913.

Petrovskii, S. and Li, B.-L. (2003). An exactly solvable model of population dynamics with density-dependent migrations and the Allee effect. *Math. Biosci.*, 186(1):79–91.

Piatnitski, A. and Ptashnyk, M. (2017). Homogenization of biomechanical models for plant tissues. *Multiscale Model. Simul.*, 15(1):339–387.

Quintard, M. and Whitaker, S. (1988). Two-phase flow in heterogeneous porous media: The method of large-scale averaging. *Transp. Porous Med.*, 3(4):357–413.

Rektor, A. and Vatai, G. (2004). Application of membrane filtration methods for must processing and preservation. *Desalination*, 162:271–277.

Roose, T. and Schnepf, A. (2008). Mathematical models of plant–soil interaction. *Philos. Trans. R. Soc. A*, 366(1885):4597–4611.

Rubin, Y. (2003). *Applied stochastic hydrogeology*. Oxford University Press.

Rubinstein, J. and Torquato, S. (1988). Diffusion-controlled reactions: Mathematical formulation, variational principles, and rigorous bounds. *J. Chem. Phys.*, 88(10):6372–6380.

Rubinstein, J. and Torquato, S. (1989). Flow in random porous media: mathematical formulation, variational principles, and rigorous bounds. *J. Fluid Mech.*, 206:25–46.

Russell, M. J. (2017). *Transport processes in spatially disordered systems*. PhD thesis, The University of Manchester.

Russell, M. J. and Jensen, O. E. (2020). Homogenization approximations for unidirectional transport past randomly distributed sinks. *IMA J. Appl. Math.*, 85(2):161–189.

Russell, M. J., Jensen, O. E., and Galla, T. (2016). Stochastic transport in the presence of spatial disorder: Fluctuation-induced corrections to homogenization. *Phys. Rev. E*, 94(4):042121.

Sahimi, M. (1993). Flow phenomena in rocks: from continuum models to fractals, percolation, cellular automata, and simulated annealing. *Rev. Mod. Phys.*, 65(4):1393.

Sahimi, M. (2011). *Flow and transport in porous media and fractured rock: from classical methods to modern approaches*. John Wiley & Sons.

Salles, J., Thovert, J.-F., Delannay, R., Prevors, L., Auriault, J.-L., and Adler, P. M. (1993). Taylor dispersion in porous media. Determination of the dispersion tensor. *Phys. Fluids A*, 5(10):2348–2376.

Sánchez-Palencia, E. (1980). Non-homogeneous media and vibration theory. *Lect. Notes Phys.*, 127.

Scher, H. and Montroll, E. W. (1975). Anomalous transit-time dispersion in amorphous solids. *Phys. Rev. B*, 12(6):2455.

Serov, A. S., Salafia, C., Grebenkov, D. S., and Filoche, M. (2015). The role of morphology in mathematical models of placental gas exchange. *J. Appl. Physiol.*, 120(1):17–28.

Shackelford, C. D. and Redmond, P. L. (1995). Solute breakthrough curves for processed kaolin at low flow rates. *J. Geotech. Eng.*, 121(1):17–32.

Shampine, L. F. (2008). Vectorized adaptive quadrature in MATLAB®. *J. Comput. Appl. Math.*, 211(2):131–140.

Shewmon, P. G. (1963). *Diffusion in solids*. McGraw-Hill Book Company.

Shipley, R. J. and Chapman, S. J. (2010). Multiscale modelling of fluid and drug transport in vascular tumours. *Bull. Math. Biol.*, 72(6):1464–1491.

Sibert, J. R., Hampton, J., Fournier, D. A., and Bills, P. J. (1999). An advection–diffusion–reaction model for the estimation of fish movement parameters from tagging data, with application to skipjack tuna (Katsuwonus pelamis). *Can. J. Fish. Aquat. Sci.*, 56(6):925–938.

Smith, C. A. and Yates, C. A. (2018). Spatially extended hybrid methods: a review. *J. R. Soc. Interface*, 15(139):20170931.

Taylor, G. I. (1953). Dispersion of soluble matter in solvent flowing slowly through a tube. *Proc. R. Soc. London*, 219(1137):186–203.

Tikhonov, A. N. and Samarskiĭ, A. A. (2013). *Equations of mathematical physics*. Courier Corporation.

Tsunoda, S., Fukaya, H., Sugihara, T., Martin, C. J., and Hildebrandt, J. (1974). Lung volume, thickness of alveolar walls, and microscopic anisotropy of expansion. *Resp. Physiol.*, 22(3):285–296.

Tun, W. M., Poologasundarampillai, G., Bischof, H., Nye, G., King, O. N. F., Basham, M., Tokudome, Y., Lewis, R. M., Johnstone, E. D., Brownbill, P., et al. (2021). A massively multi-scale approach to characterizing tissue architecture by synchrotron micro-CT applied to the human placenta. *J. R. Soc. Interface*, 18(179):20210140.

Vafai, K. (2015). *Handbook of porous media*. Crc Press.

Van Heemert, A. (1957). Cyclic permutations with sequences and related problems. *J. Reine Angew. Math.*, 1957(198):56–72.

Van Kampen, N. G. (1992). *Stochastic processes in physics and chemistry*, volume 1. Elsevier.

Van Noorden, T. L. and Muntean, A. (2011). Homogenisation of a locally periodic medium with areas of low and high diffusivity. *Eur. J. Appl. Math.*, 22(5):493–516.

Vasin, S. I. and Filippov, A. N. (2009). Cell models for flows in concentrated media composed of rigid impenetrable cylinders covered with a porous layer. *J. Colloid Sci.*, 71(2):141–155.

Wang, Y. (2010). Vascular biology of the placenta. In *Colloquium Series on Integrated Systems Physiology: From Molecule to Function*, volume 2, pages 1–98. Morgan & Claypool Life Sciences.

Whitaker, S. (1986). Flow in porous media I: A theoretical derivation of Darcy's law. *Transp. Porous Med.*, 1(1):3–25.

Whitaker, S. (1999). Theory and applications of transport in porous media: The method of volume averaging. *Kluwer Academic Publishers*.

Zhang, Z. and Kleinstreuer, C .and Kim, C. S. (2001). Flow structure and particle transport in a triple bifurcation airway model. *J. Fluids Eng.*, 123(2):320–330.

Zhikov, V. V., Kozlov, S. M., Oleinik, O. A., and Ngoan, K. T. (1979). Averaging and G-convergence of differential operators. *Russ. Math. Surv.*, 34(5):69–147.

Zularisam, A. W., Ismail, A. F., and Salim, R. (2006). Behaviours of natural organic matter in membrane filtration for surface water treatment–a review. *Desalination*, 194(1-3):211–231.